Synthesis and Surface Modifications of Graphene Oxide and its Derivative Two-dimensional Materials for Various Sensing Applications

A Thesis Submitted to

Indian Institute of Technology Guwahati

For the degree of

Doctor of Philosophy

By

Ningthoujam Somorjit Singh

Centre for Nanotechnology
Indian Institute of Technology Guwahati
Guwahati-781039, India
July 2022

Dedicated to my departed father

Department of Physics
Indian Institute of Technology Guwahati
Guwahati-781039, India

STATEMENT

The work contained in the thesis entitled "**Synthesis and Surface Modifications of Graphene Oxide and its Derivative Two-dimensional Materials for Various Sensing Applications**" has been carried out by me at the Indian Institute of Technology Guwahati, under the supervision of Prof. P. K. Giri, Professor, Department of Physics and Centre for Nanotechnology, and Prof. H.B. Nemade, Professor, Department of Electronics and Electrical Engineering and Centre for Nanotechnology, Indian Institute of Technology Guwahati. This work has not been submitted elsewhere for the award of any degree.

Ningthoujam Somorjit Singh
Roll no. 136153005
Senior Research Fellow
Centre for Nanotechnology
Indian Institute of Technology Guwahati
Guwahati-781039, India

Prof. P. K. Giri
Professor
Department of Physics
And Centre for nanotechnology
Indian Institute of Technology Guwahati
Guwahati-781039, India
Phone: +91-361-2583072, Fax: +91-361-2690762
Email: giri@iitg.ac.in

CERTIFICATE

This is to certify that the work contained in the thesis entitled "**Synthesis and Surface Modifications of Graphene Oxide and its Derivative Two-dimensional Materials for Various Sensing Applications**" has been carried out by **Mr. Ningthoujam Somorjit Singh** at the Indian Institute of Technology Guwahati, under my supervision. This work has not been submitted elsewhere for the award of any degree.

Prof. P. K. Giri

Thesis Supervisor

ACKNOWLEDGEMENT

It is my honor to be able to acknowledge everyone who contributed to the successful completion of this Ph. D. thesis.

First and foremost, I would like to convey my sincerest thanks to my Ph. D. Supervisors, Prof. P. K. Giri and Prof. H.B. Nemade, for allowing me to work under their guidance. Their vast scientific expertise and passion for Nanotechnology are genuinely inspiring. I am grateful to have had the chance to work closely with them, observe them and engage in prolific discussions throughout this journey. Their skills and overall approach towards research in the field of new-age semiconductors and their applications have helped shape my perception of research in the field, identifying opportunities, and preparing for challenges. I am indebted to them for providing me with all the essential requirements and laboratory facilities and for believing in me by giving me complete freedom in my work towards fulfilling the goal.

I want to thank the members of my Doctoral Committee, Prof. Girish Sampath Setlur**,** Prof. Roy Paily Palathinkal, and Prof. Ashwini Kumar Sharma, for their valuable insights, constructive criticism, and constant encouragement.

I extend my sincere thanks to the Head of the Centre for Nanotechnology (CFN) and other faculty members and staff of the CFN, as well as the Central Instruments Facility (CIF), for providing me with a research-friendly environment and state-of-the-art research infrastructure. I especially want to thank Dr. Franco Mayanglambam, Indrajit Talukdar, Dr. Pranjoli Das, Kaustubh Acharya, Sandhan Sarma, Sayanika Das, Tenison Basumatary, Madhurjya Borah for their help and co-operation throughout my Ph.D.

I am grateful to the Indian Institute of Technology Guwahati for providing financial assistance, good facilities, and a safe and enjoyable working environment. I am thankful to the Central Workshop, Department of Mechanical Engineering, for fabricating essential components used in my experimental setup. I also acknowledge the help from my collaborators Prof. Minoru Fujii and Prof. H. Sugimoto from Kobe University, Japan, for providing the opportunity to access some of their laboratory facilities.

The support of my lab-mates and seniors has been vital in completing my work. I have been blessed with some of the best colleagues. I thank my seniors - Dr. Ramesh Ghosh, Dr. Sk. Md. Obaidulla, Dr. Rajendra Gone, Dr. Jitendra Kumar, and my fellow lab-mates Dr. Kamal Kumar Paul, Dr. Larionette Mawlong, Dr. Sumana Paul, Dr. Joydip Ghosh, Dr. Ruma Das, Dr. Sumaiya Parveen, Abhilasha Bora, Tarik, Ravinder, Abdul, Tadasha, Koushik, Sirsendu, Ghanashyam, and Sanju for their help and valuable insights in research. They enlivened the

laboratory work environment. I am thankful to my seniors and friends Dr. Disco, Royal, Alex, Yaifarenba, Bale, Jiten, Kisan, Dr. Lenin, Dr. Gyanendro, Dr. Gishan, Dr. Namami, Dr. Monica, Sophia, Kasturi, Paromita, Roson, Karnajit, Richard, and Himaskhi for always being there in my corner, during my research journey. Their constant support and cheer played a significant role in bringing this thesis into reality.

Lastly, I would like to express my immense thankfulness for my family, to whom I owe everything. I am grateful to my parents, Late Ningthoujam Komol Singh and Ningthoujam Manaotombi Devi, for teaching me the values of patience, innocent, humility, determination, and kindness. I intend to thank my sisters Ningthoujam Romita Devi, Ningthoujam Ranjita Devi, Ningthoujam Radheshana Devi, and my brother Ningthoujam Rajesor Singh for being my pillars. I want to thank my niece Jessica for playing beside me during writing my thesis. I desire to mention my nieces Macha and Tombi and my nephews Thoithoiba and Sana for playing with me during my research period.

Ningthoujam Somorjit Singh

IIT Guwahati

CONTENTS

SYNOPSIS

Graphene oxide (GO) and its derivative materials are potential candidates for various sensing applications due to their spectacular and significant properties. There are several unique properties of the GO materials. 1. It has a large surface area (2630 m^2g^{-1}); every atom present in the materials is exposed to the analytes for interaction. 2. The charge carrier in graphene materials has high mobility; it is a ballistic transport, meaning electrons can travel up to the speed of light at room temperature (~200000 cm^2 V^{-1} s^{-1}). 3. Graphene is a highly sp^2 crystalline structure, a single electron change in the materials can have a noticeable change in the material's conductivity. 4. The analyte molecules and the materials can interact by physisorption reaction, also known as Van der week interaction, and chemisorption reaction (strong interaction). 5. Graphene is a 2D and very strong material in the nanoscale, which is 100 times stronger than steel. 6. Derivatives of graphene can be synthesized using the well-known modified Hummer's method, which can be produced on a large scale and is easily soluble in water and other organic solutions. 7. It can be functionalized by doping using a chemical method or gas plasma treatment, 8. It changes its electronic properties using nanocomposite or heterostructure with other metal oxide materials. Due to the wide range of properties of graphene materials, it is used in surface-enhanced Raman scattering (SERS), photodetector, gas sensing, water splitting, bio-medical, super capacitor, etc. applications.

Exfoliation from GO is cost-effective, and the attached functional groups can control their properties. Several top-down exfoliation techniques have been reported emphasizing the lateral size of GO, their functional property, their scale-up practicality, and their viable applications. Several methods are used for exfoliation of GO using electrochemical exfoliation, ultrasonic exfoliation, microwave-assisted exfoliation, shear-mechanical exfoliation, hydrothermal, thermal techniques, and freezing-thawing based exfoliation, etc. Furthermore, extreme care is needed during exfoliation for the latter synthesis protocol to obtain high quality and large lateral size graphene-based sheets to implement in wide-scale electronic applications. The increase of material resistance due to the flakes' discontinuity increases the potential barrier for charge carriers to flow in the material. The fabrication of the interdigitated electrode (IDE) on the RGO required a new method to synthesize large lateral-size GO sheets. We demonstrated a facile and simple technique at minimal cost to exfoliate large GO sheets based on a mild temperature hydrothermal process at ambient conditions. Subsequently, a large lateral-size RGO was synthesized by chemical reduction/ deoxygenation.

Recently, trace detection for the various analyte (dyes, pesticides, food adulterants, etc.) has been enabled by employing the SERS technique. In the SERS technique, metal-based nanomaterial has been widely used as a substrate onto which a low concentration analyte is placed for detection or analysis. In most cases, gold or silver nanoparticles/nanostructured substrates are used to enhance the analyte's Raman signal in the SERS technique. However, the instability of the metals, susceptible to oxidation and sulfidation, could hinder the efficiency and consistency of the substrate for creating a plasmonic hotspot, thereby decreasing the sensitivity of the target molecules. Besides the metal NPs, several semiconductors have also been used as SERS sensing materials, such as TiO_2 nanostructures, CuTe nanocrystals, Cu_2O nanospheres, InAs/GaAs quantum dots, and graphene and its derivatives. However, the SERS sensitivity of semiconductors is relatively low compared to that of metal NPs. Graphene-based materials are promising applications in SERS sensors because of their low cost, abundantly available raw materials (graphite), biocompatibility, tunable sheet layers, controllable lateral size, and tunable electronic properties. Furthermore, graphene exhibits a uniform surface, high absorptivity, and high stability.

The SERS signal of an analyte on the graphene substrate is primarily contributed by the interaction of π-π stacking layers and inter-band charge transfer. Further, defects and functional groups in the graphene assist in more interaction with the analytes, enhancing the intensity of Raman signals. Additionally, plasma treatment has been used to modify the properties of the graphene oxide for functionalization, etching, creating defects, and reduction of GO. Plasma treatment is a simple, cost-effective, efficient, energy and time-saving, and clean process. The most commonly used gases in the plasma treatment system are N_2, O_2, H_2, CH_4, NH_3, and F. However, there are very few studies on modifying the GO materials using plasma treatment, specifically for SERS application. Based on the nature of gases in the plasma treatment, the effectiveness of GO is changed owing to its defects, doping, electrical conductivity, and n/p - type nature. The role of functional groups and defects on the SERS application of GO is little understood, and it is worth exploring since it enables a metal-free platform for cost-effective and reliable SERS detection.

The development of modern ultraviolet photodetectors is necessary because the human body is sensitive to UV radiation that may cause different diseases, including cataracts and skin cancer. The UV spectrum can be classified into three bands (according to the International Commission on Illumination), which include the UVA wavelength range from 320 to 400 nm, UVB from 280 to 300 nm, and UVC from 10 to 280 nm, where the content of UVA is the greatest in the

solar spectrum. The working mechanism of UV photodetector is mainly based on the photoconductivity effect. Under UV illumination on a wide band gap semiconductor, the absorption of UV light occurs, generating electron-hole pairs when the photon energy is larger or equal to the bandgap. The photo-generated electrons and holes are collected in the external circuit as a photocurrent. GO-based materials offer a low-cost fabrication of photodetectors, and we study the GO-based photodetectors in different hybrid configurations.

In the last few decades, many researchers have been interested in the cause, monitoring, and solution for the change of environment in the world. The factors which changed the world's climate are using hydrocarbons, exfoliation of mineral resources, deforestation for modernization and wars, etc. The above factors cause increased global warming, climatic change, sea level increase, acid rains, green housed effect, extinction of flora and fauna, etc. The major challenge in the near future is the control of global warming by reducing or controlling the production of harmful gases like CO_2, NO_2, and CO, which are significant contributors to the greenhouse effect. The sensing and monitoring of carbon dioxide gas are beneficial to various applications like human health care, detection of human or animal captive inside a room, air quality control room which safe more electrical wastage, etc. Therefore, developing a durable, simplified, cheap, reusable, highly sensing, fast response CO_2 gas sensor device is essential. The CO_2 gas sensing in the typical atmospheric environment is complicated due to the contribution of sensing response from many gas species like NO_2, CO, and humidity which are considered low selectivity of gases.

This thesis presents a systematic study on synthesizing super large lateral size GO using a simplified Hummer's method and then exfoliated by mild heating. In addition, the synthesis of the other derivatives of the GO, such as RGO using chemical and thermal process, graphene quantum dots (GQDs) using hydrothermal method insisted by the tip- sonication from the GO are reported. Further, the surface structures of GO and RGO are modified using different gas plasma treatments. The synthesized GO, RGO, and GQDs are used in various applications such as SERS, photodetector, and gas sensing purposes. Different dyes such as Rhodamine B (RhB), Methylene blue (MB), Methyl orange (MO), and Rose Bengal (RB) are studied on large area GO/RGO for their SERS effect without and with gas plasma treatment. The photodetector device based on the GO, surface modified GO, and nano-composite of SnO_2 NPs is analyzed for their photo-response and detectivity. Next, the composites of RGO/GQDs with SnO_2 nanoparticles were used as CO_2 sensors, and their gas sensing responses were measured. The complete thesis work has been organized into seven chapters, as detailed below.

Chapter 1 briefly introduces GO and its derivative materials (RGO, GQDs). The history of GO and the evolution of the synthesized method of GO are presented in this chapter. The unique properties of the GO, the various methods for synthesizing the GO, and its exfoliation techniques are presented. Multiple GO-based applications, such as gas sensors, photodetectors, and SERS, are discussed. We discuss the significant challenges related to the synthesis of large lateral-size GO/RGO for practical applications and present a brief account of the experimental techniques used. A brief discussion on the importance of the SERS effect on the bio-sensing application, trace detection, non-destructive sensing, etc., using the various materials is presented. An evolution of the gas sensor device made using semiconductor materials to 2D and 0D materials are studied. The challenge related to the detection of highly stable CO_2 draws the attention of many environmentalists; indoor air quality management, greenhouse effect, global warming, etc., are presented. The importance of the photodetector using the 2D material is studied. The motivation and focus of the thesis work are presented at the end of the chapter.

Chapter 2 presents a systematic study of the simplified Hummers method for synthesizing graphite oxide and exfoliating graphite oxide to large lateral-size GO sheets using mild heating. The pictorial representation of each synthesis step is presented with the well-known reaction mechanism of graphite oxide. The systematic steps with images for the exfoliation of graphite oxide to GO using the newly proposed method named "a mild heating method" are presented along with the proposed mechanism. The reduction of the oxygen functional groups from the GO is illustrated using a chemical (hydrazine) process and shows the commonly accepted reduction mechanism. The large lateral size of the GO and RGO is confirmed by the optical microscopy and FESEM image. The oxidative graphite structure of GO is studied using XRD and Raman spectroscopy. GQDs are synthesized from the GO using hydrothermal and assisted with the tip-sonication process. The quality of GQDs is analyzed using various characterization techniques. The synthesis of GO, RGO, and GQDs and their characterization are discussed in detail.

Chapter 3 studied the optimization of exfoliation GO using a mild heating technique and a detailed analysis of as-prepared large-area GO. It is a facile and simple technique at a minimal cost (about 10 times lower than the commonly used ultrasonic technique). Moreover, it requires ~80 °C to exfoliate GO, which is 3 times lower than the conventional hydrothermal method, eliminating the need for high temperature in the high-pressure hydrothermal method. Subsequently, RGO was synthesized by chemical reduction/ deoxygenation. An optical microscope, FESEM, and AFM investigated the morphology and lateral dimensions of the GO

and RGO. The structural quality and characteristics of GO and RGO were further analyzed using Raman spectroscopy, XRD, XPS, FTIR, UV-vis absorption spectroscopy, PL, Thermo gravimetric analysis (TGA), and Brunauer-Emmett-Teller (BET) analysis. The electronic and electrochemical behaviors were investigated from current-voltage (I-V) characterization and electrochemical impedance spectra. Furthermore, the sensing application of large area GO and RGO was also explored using Rhodamine B at low concentrations to test the surface-enhanced Raman spectroscopy (SERS) effect.

In **Chapter 4**, we employ a plasma treatment method on large lateral-size GO and RGO sheets to modify the surface, leading to structural change in the carbon skeleton. Various gas plasma environments were used, such as Ar, N_2, O_2, and H_2 (diluted with Ar) during the treatment processes. The resulting substrates were used to investigate the structural disorder and characteristics using Raman and FTIR spectroscopy. The surface morphology of the synthesized GO and RGO was studied using FESEM, AFM, and FETEM. The functionality of the GO and RGO (with or without plasma treatments) in terms of their sensitivity to various dyes such as MO, MB, RB, and RhB was explored using the surface-enhanced Raman spectroscopy technique. Further, the addition of noble metal (Au NPs) was examined to form a composite with GO and RGO, and its SERS performance to detect various dyes was studied.

Chapter 5 focuses on the fabrication of inter-digitated electrodes (IDE) on GO sheets and GO-based photodetector devices. Each step for the fabrication of IDE pattern is presented, from software design to metal lift-off. The 10 µm IDE pattern was analyzed using the FESEM imaging, and the metal thickness is 30 nm. The role of oxygen functional groups attached to the GO in the electrical properties of GO is analyzed. The various temperature annealed GO shows changed structural properties of GO, as confirmed by the Raman, XRD, and FTIR analyses. The significant change in the electrical conductivity of the GO after 230 ˚C anneal is observed in the IV characteristics. The photoresponsivity (R) for GO, nano-composite of GO and SnO_2 NPs (SO-GO), and Ar plasma treated on GO (Ar-GO) is 0.39 mAW^{-1}, 1.07 mAW^{-1}, and 3.7 mAW^{-1}, respectively. And the detective (D) for GO, SO-GO, and Ar-GO are 0.22×10^{10} Jones, 0.37×10^{10} Jones, and 1.22×10^{10} Jones, respectively. The Ar-GO has improved the R and D compared to others.

Chapter 6 concentrates on the fabrication and optimization of gas sensing devices using the nano-composite of RGO/GQDs with SnO_2 NPs. The schematic illustration of the mechanism of CO_2 sensing on the composite material is presented. The sensing materials are analyzed for

their IV characteristics. Sensing response of the fabricated gas sensors is measured for CO_2 gas at different concentrations, such as 250 ppm, 500 ppm, 1000 ppm, and 5000 ppm. Interestingly, CO_2 content in the atmosphere is 410 ppm; if the concentration exceeds 5000 ppm, it is harmful. The sensing properties such as response time and sensitivity are studied in this chapter. The nano-composite of RGO and SnO_2 NPs (SO-RGO) sensitivity (S) is 9% and 4% for 5000 ppm and 1000ppmof CO2. The response and recovery time for SO-RGO is the 20s and 40s at 5000 ppm of CO_2. The SO-RGO exhibits improved sensing response up to 50% as compared to SnO_2. Further, the nano-composite of GQDs and SnO_2 NPs (GQDs-SO) improved their sensitivity by 2 times and 3 times as compared to SO-RGO and SnO_2 NPs, respectively.

Chapter 7 summarizes the work done in this thesis and highlights its contributions to the study of GO and its derivative materials. Our studies have demonstrated that it is an active material for SERS applications, photodetectors, and CO_2 sensors. In the end, we discuss the scope for future works in this field.

LIST OF PUBLICATIONS:

A. In Peer-Reviewed Journals:

1. **N. Somorjit Singh**, F. Mayanglambam, H.B. Nemade and P.K. Giri, "Facile synthetic route to exfoliate high quality and super large lateral size of graphene-based sheets and their applications in SERS and CO_2 gas sensing", **RSC advance 11, 9488-9504 (2021).**

2. **N. Somorjit Singh**, F. Mayanglambam, H.B. Nemade and P.K. Giri," Plasma-treated graphene surface for trace dye detection using surface-enhanced Raman spectroscopy" **ACS Applied Nano Materials, 2022, 5,5, 6352-6364**.

3. **Ningthoujam Somorjit Singh**, H.B. Nemade and P.K. Giri, Effect of annealing temperature on the photo-response study on GO based materials used as a photodetector device **(under preparation)**

4. **Ningthoujam Somorjit Singh**, H.B. Nemade and P.K. Giri, Nano-composite of RGO/GQDs with SnO_2 NPs used as an active material for CO_2 gas sensing applications **(under preparation)**

B. Conference Papers Presented:

1. **N. Somorjit Singh**, H.B. Nemade and P.K. Giri, "Synthesis and characterization of reduced graphene oxide" in National conference on Recent Advance in Nanoscience and Nanotechnology (NCRANNT-2016), NEHU, Shillong on 8 & 9 Sept. 2016 (**oral**)

2. **N. Somorjit Singh**, H.B. Nemade and P.K. Giri, "Synthesis of ultrasmall graphene quantum dots using tip sonication CO_2 gas sensing application", ICANN 2019, IIT Guwahati on 18-21 Dec. 2019

3. **N. Somorjit Singh**, H.B. Nemade and P.K. Giri, "CO_2 gas sensing enhancement by coated rGO material on SnO_2 sensor" ICFM 2020, IIT Kharagpur, 6-8 Jan. 2020

4. **N. Somorjit Singh**, H.B. Nemade and P.K. Giri, "Large area graphene oxide and reduced graphene oxide sheets for high efficiency SERS application" ICEE2020, IIT Delhi, on 26-28 Nov. 2020

5. **N. Somorjit Singh**, H.B. Nemade and P.K. Giri, "Facile Low-cost synthesis of Monolayer reduced graphene oxide with super large lateral size and its application in SERS" IWSPD 2021, IIT Delhi, on 14-17 Dec. 2021

6. **N. Somorjit Singh**, H.B. Nemade and P.K. Giri, "Temperature-dependent study of graphene oxide and use in photodetector applications" NERC, IIT Guwahati, on 20-22 May 2022 (**oral**)

C. Short-term project/ hands-on-training workshop

1. INUP Hands-on training workshop certificate on "Nanofabrication Technologies" at the Centre for Nano Science and Engineering, Indian Institute of Science (IISC), Bangalore, from 7th - 16th October 2014.

2. Short course on "Modeling, Simulation and Characterization of Nano-Transistor" at the Department of Electrical Engineering, IIT Kanpur, from 26th – 30th, October 2015.

LIST OF ABBREVIATIONS

Abbreviation	Description
0D	Zero dimension
2D	Two dimensions
AFM	Atomic force microscopy
Au NPs	Gold nanoparticles
Ar-GO	Argon plasma treated GO
Ar-RGO	Argon plasma treated RGO
BET	Brunauer-Emmett-Teller
CuTe	Copper telluride
D	Detectivity
EDS/EDX	Energy dispersive X-ray spectroscopy
FESEM	Field emission scanning electron microscopy
FETEM	Field emission transmission electron microscopy
FTIR	Fourier transform infrared
GO	Graphene oxide
GQDs	Graphene quantum dots
GQDs-SO	Nano-composite of SnO_2 and GQDs
HRTEM	High-resolution Transmission electron microscopy
H-GO	Diluted H_2 plasma-treated GO
H-RGO	Diluted H_2 plasma-treated RGO
I-V	Current-voltage
IDE	Interdigitated electrode
MB	Methylene blue
MO	Methyl orange
N-GO	N_2 plasma-treated GO
O-GO	O_2 plasma-treated GO
O-RGO	O_2 plasma-treated RGO

PL	Photoluminescence
R	Responsivity
RB	Rose Bengal
RGO	Reduced GO
S	Sensitivity
SAED	Selected area electron diffraction
SERS	Surface-enhanced Raman Scattering
SO-GO	Nano-hybrid of SnO_2 NPs and GO
SO-RGO	Nano-hybrid of SnO_2 and RGO
TiO_2	Titanium oxide
TGA	Thermo gravimetric analysis
XPS	X-ray photoelectron spectroscopy
XRD	X-ray diffraction
UV	Ultra-violet
τ_{res}	Response time
τ_{rec}	Recovery time

Chapter 1

Introduction

Graphene is an assembly of carbon atoms arranged in a honeycomb lattice; carbon means Charcol in Latin. Carbon is the 15th most abundant element in the earth's crust and the 4th most abundant element in the universe by mass, and the 2nd rich element in our human body after oxygen by mass. Graphene oxide (GO) was popularised after the discovery of graphene by Geim and Novoselov in 2004[1]. GO is a 2D material that consists of sp^2 and sp^3 carbon atoms and various oxygen functional groups. In other words, it is another form of graphene (**Fig. 1.1(a)**) that contains oxygen functional groups. It is composed of oxygen functional groups such as hydroxyl (-OH), carboxyl (-COOH), carbonyl (C=O), ether (C-O-C), and epoxy (O-C=O)[2]. The schematic structure of GO is shown in **Fig. 1.1(b)**. The oxygen functional groups bonded with the carbon atoms, change the hybridized sp^2 to sp^3 carbon atoms, and interrupt the delocalized π system. The electrical properties of GO can change by the degree of oxidation in the in-plane and out-of-plane of the skeleton layer. It has garnered interest in the research community due to its semi-conducting nature and usefulness in various applications. GO is synthesized from the exfoliation of graphite oxide, and graphite oxide is obtained from the oxidation of graphite flakes. GO is one of the cheapest 2D materials. Moreover, its source materials, such as graphite flakes, charcoals, plants, and leaves, are readily abundant in our environment, mass-producible, and the synthesis process is well known[3].

There are several unique properties of GO that make it an ideal candidate for a wide range of applications: (i) It has a large surface area; every atom present in the material can be exposed to the analyte molecules; (ii) An electron can change the material's conductivity; (iii) An analyte molecule can interact with GO by van der Waals (weak) and chemisorption (strong) reactions; (iv) It is readily dispersible in water and other organic solvents; (v) Its surface structure can be modified by gas plasma treatment, doping of atoms, functionalization, etc.; (vi) The electronic properties can be altered by forming nano-composite and heterostructures with other materials[4–6]. The extraordinary properties of the GO and its derivative materials are applied in various applications such as surface-enhanced

Raman scattering (SERS), photodetection, gas sensing, in batteries and supercapacitors, electrochemical water splitting, bio-medical areas, etc[7–12].

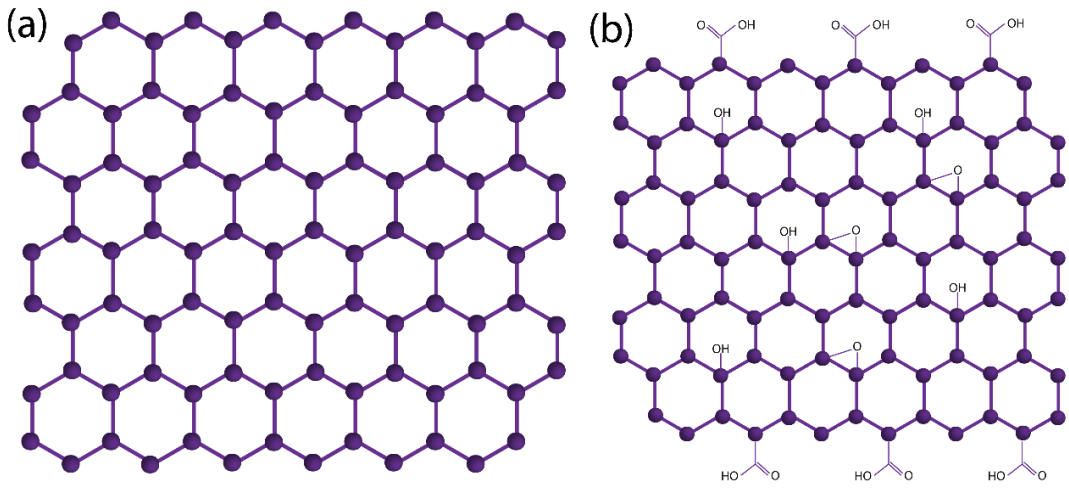

Fig. 1.1: Schematic structure of (a) pristine graphene; (b) GO.

1.1. History of graphene oxide and its evolution

The evolution of graphitic materials can be traced back to the Neolithic age (4000 B.C.), where graphite was used to paint for decorating pottery ceramic by Martia culture in Europe. British used graphite for marking sheep in 1500 A.D. In the year 1859, B.C. Brodie was the first person who synthesized the graphite oxide from graphite from the chemical reaction with potassium chlorate ($KClO_3$) and fuming nitric acid (HNO_3) for three or four days at a temperature of 60 ˚C until yellow vapors cases to be evolved[13]. The synthesized graphite oxide contained 61.74% of carbons, 1.85% of Hydrogen, and 37.41% of oxygen after repeating the oxidation process four times. He used graphite oxide as graphic acid because of its non-dispersability in acidic media. Further, the oxygen functional groups in the graphite oxide were reduced by thermal treatment at 250 ˚C for three to four hours until all perceptible gas evolution had ceased. After heat treatment, 1.024g of graphite oxide was reduced to 0.684g; the concentration of its elemental composition such as 80.19% of carbon, 0.52% of Hydrogen, and 19.29% of oxygen. Thus, Brodie showed a way to convert graphite to graphite oxide for the first time.

In 1898, L. Staudenmaier boosted the oxidation reaction in the process by adding chlorate ($KClO_3$ or $NaClO_3$) and concentrated sulfuric acid to increase the acidity in the solution[14]. Thus, he was able to increase the concentration of the oxygen in the graphite oxide to the ratio of 2:1 of carbon and oxygen, respectively, in one reaction. However, using HNO_3 produced hazardous gases such as nitrogen dioxide (NO_2) and dinitrogen tetroxide (N_2O_4)

gases, known as yellow vapor. Moreover, the potassium chlorate being an explosive material. Therefore, the usage of both nitric acid and potassium chlorate was extremely dangerous.

In the year 1958, Hummers synthesized graphite oxide by using less harmful chemicals such as potassium permanganate ($KMnO_4$), sodium nitrate ($NaNO_3$), and highly concentrated sulfuric acid (H_2SO_4)[15]. He achieved a high degree of oxidation of graphite oxide from the reaction of graphite flakes with $KMnO_4$, $NaNO_3$, and H_2SO_4. Subsequently, most groups adopted synthesis processes following what came to be known as the "Hummers method." Nevertheless, modifications were made to the Hummers method to obtain high-quality graphite oxide by adding an extra chemical[16,17] or a different source of carbon or adding a few additional steps, thus, following a "modified Hummers method" or "simplified Hummers method"[18].

Further, GO is synthesized from the exfoliation of graphite oxide. Various proposed techniques exist to exfoliate graphite oxide to obtain GO, such as ultrasonication, electrochemical, microwave-assisted, shear-mechanical, hydrothermal, and freezing-thawing-based exfoliation. More detail on the exfoliation technique is discussed in **section 1.7.1**. In this thesis, we use a simplified Hummers method for the synthesis of graphite oxide of larger domain sizes by modifying a few of the experimental steps to achieve a higher degree of oxidation, following which an optimized heating treatment yielded high-quality graphene oxide of large later size.

1.2. Structure of graphene oxide

Interestingly, the identical structural model of the GO does not exist, even though many proposals have been presented. Since graphite oxide was synthesized 150 years ago, the distinct chemical structure is not well defined due to the presence of sp^3 hybridized carbon and the irregular attachment of various oxygen functional groups[19]. This complexity is caused by multiple factors such as the degree of oxidation that cannot be specified, distribution of oxygen functional groups, oxidizing sites on the graphite material, practical drawbacks, and lack of analytical techniques. However, the structure of GO has been proposed by various models such as Hofmann, Ruess, Scholz-Boehm, Nakajima-Matsuo, and Lerf-Klinowki models, as shown in **Fig. 1.2**. Hofmann proposed a structural model of GO, which attached the epoxy functional groups on the basal plane of the hexagonal honeycomb structure of the carbon atoms[20].

He arranged the epoxy groups randomly, perpendicular to the basal plane of the graphitic structure. The net molecular formula of GO is C_2O. In the Hofmann model, the functionalized carbon atoms are arranged in sp^2 hybridized configuration. Further, Ruess proposed a model that improved upon the Hofmann model by adding hydroxyl and epoxy functional groups on the basal plane. The functionalized carbon atoms are converted from sp^2 to sp^3 hybridized structure. Similarly, the proposed oxygen functional groups are attached perpendicular to the basal plane of the graphitic system. In the Ruess model, a unit structure of GO contains 25% of oxygen functional groups; 1/3rd are hydroxyl groups, and 2/3rd are epoxy groups. Whereas in the Scholz-Boehm model, quinoidal species are attached on the basal plane instead of epoxide and ether functional groups.

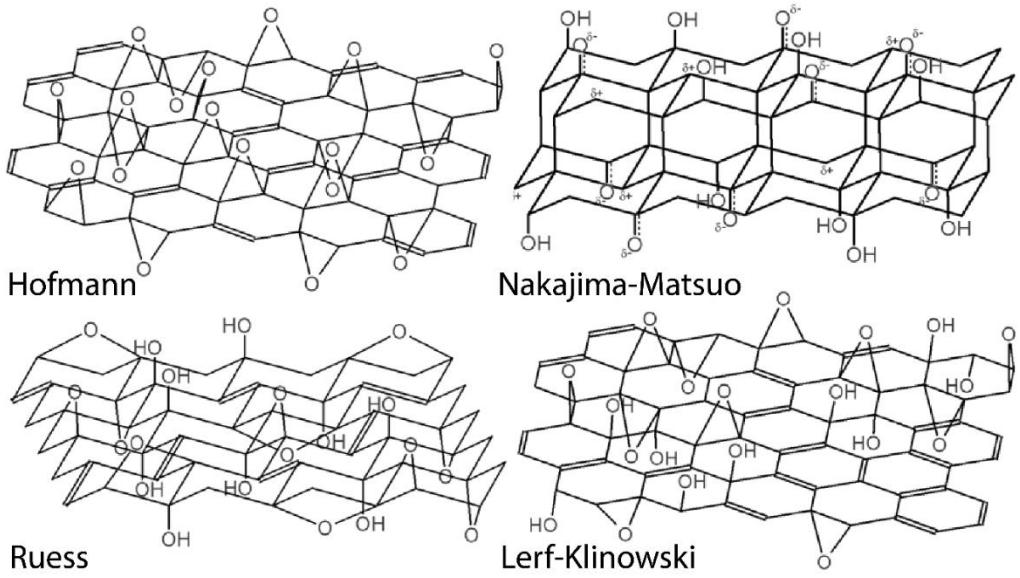

Fig. 1.2: Structural models of GO (adopted from ref.[21]).

Nakajima and Matsu proposed a structural graphite oxide model named graphite intercalation compound (GIC). He explained the oxidation mechanism of GO and the nonstoichiometric and amorphous structure that constructs the GO structure. The Mermoux model is made by the tertiary alcohols, epoxy (1,2-ether) groups, and a mixture of alkenes is attached to the basal plane of the graphitic structures. In addition, he explored the hydrogen with the alcohols and epoxy functional groups linked to the structural bonding between the stacking GO layers. Lerf-Klinowski model is based on the reactivity, composition of elements, and experimental studies. In his proposed model, ether, epoxide, carboxylic, and hydrogen attach to the graphitic structure, bonding between the stacking layers of GO. And carboxyl and carbonyl groups are attached at the edge of the graphitic structure, and epoxide groups are attached to the basal plane of the structure. Further, GO is contained by the attached functional groups

such as lactols on the edge, esters and tertiary alcohols on the surface, and epoxy and alcohol groups on the plane of GO which is characterized by the nuclear magnetic resonance spectroscopy (NMR)[22].

The structure of the GO is a rough surface due to the oxygen functional groups attached above and below the graphitic structure and the presence of sp^3 hybridized carbon atoms. The structure of the GO is studied via various techniques such as high-resolution annular dark field (ADF), Scanning transmission electron microscope (STEM), NMR, and Scanning tunneling microscopy (STM), to investigate the sp^2 and sp^3 hybridized carbon atoms in a nano-scale, presence of oxygen functional groups, defects on the planar structure, and retained size of the unit cell of GO.

1.3. Mechanism of formation of graphene oxide

Dimiev et al. studied the mechanism for the formation of graphite oxide. He explained the formation of GO in three stages: graphite interaction compound (GIC), pristine graphite oxide (PGO), and GO[23]. GIC stage is a dark green color solution formed within 3-5 minutes after the reaction of source graphite flakes with highly concentrated H_2SO_4. The stoichiometry of the GIC stage is represented by a formula $C_{(21\text{-}28)}{}^{+}.HSO_4{}^{-}$ 2.5 H_2SO_4. H_2SO_4 and $HSO_4{}^{-}$ ions occupy the interlayer corridors in the GIC stage. To oxidize the graphite flakes, the oxidizing agents must insert in-between the stacking graphene layers or replace the existing intercalated molecules. PGO is formed after GIC; when the specified amount of $KMnO_4$ is added to the GIC solution, $KMnO_4$ is dissolved in the acidic solution and slowly changes the colour of the solution to dark brown from dark green. The chemical reaction of $KMnO_4$ and H_2SO_4 has obtained manganese heptaoxide (Mn_2O_7), the potent oxidizing agent. Thus, the chemical reaction to form oxidizing agent is given in below:

$$KMnO_4 + 3H_2SO_4 \rightarrow K^+ + MnO_3{}^+ + H_3O^+ + 3HSO_4{}^-$$

$$MnO_3{}^+ + MnO_4{}^- \rightarrow \mathbf{Mn_2O_7\ (highly\ reactive)}$$

In the solution, permanganyl ($MnO_3{}^+$) ion is the cation, and hydrogen sulphate ($HSO_4{}^-$) and sulphate ($SO_4{}^{2-}$) ions are the anions present in the form of MnO_3HSO_4, or $(MnO_3)2SO_4$. If 100% H_2SO_4 is used as the solvent, the given compound is obtained in non-ionized form, while in dilute H_2SO_4 used as the solvent, the given compound is obtained in ionized form. PGO stage is determined by the rate of oxidation in graphite flakes and a diffusive-controlled where the oxidant replaces the acid intercalant. The rate of diffusion of the oxidizing agent into the interlayer of stacking graphene is slower than the rate of the chemical reaction. And

the movement of the reaction on the various graphite flakes is varied in an oxidation reaction. The oxidized graphite flakes are identified from the optical microscope in both the light modes; graphite oxides are observed in semi-transparent light brown in transmitted light mode and light-yellow pearl in reflected light mode. However, the unoxidized graphite flakes are obtained with dark color in transmitted light mode and blue color in reflected light mode. The oxidized graphite and un-oxidized graphite flakes are detected in the Raman analysis from the emergence of D band for oxidized graphite and this is the most promising characterization technique used for the study of GO and its derivative materials.

Further, Kang et al. suggested another oxidation reaction of graphite flake after adding water into the dark-brown solution (PGO)[24]. After adding water to the solution, the color of the solution is changed to dark from dark brown, which is an exothermic reaction. Similarly, the subsequent oxidation stage by MnO_4^- in the acidic aqueous condition is determined by Kang et al. This exothermic reaction is stopped by adding diluted H_2O_2 into the solution, and the color of the solution is changed to bright yellow from the dark. The oxidizing agent is converted into Mn^{2+} ions and manganese sulfate (colorless soluble).

1.4. Derivatives of graphene oxide

GO can be developed into various materials such as reduced graphene oxide (RGO) and graphene quantum dots (GQDs) based on the degree of oxygen functional groups attached to it, size of the particles, presence of defects, structural arrangement, etc. The properties of each derivative material are unique due to the changes in structure, size, and shape.

1.4.1. Reduced graphene oxide

RGO is the derived material of GO, where a negligible amount of oxygen functional groups is presented. The accurate value of C/O to determine RGO is not regulated but can reduce to 14.5:1 of C/O by chemical treatment[25]. Due to the reduction of oxygen functional groups, the propertied of the RGO is drastically changed from GO. RGO improves from GO in the mobility of charge carrier, electrochemical properties, optical transparency, thermal conductivity, more flexibility and ease to functionalize with foreign analytes, etc. Due to the controllable and rich property of RGO, it is used in various applications such as biosensors[26], gas sensors[27], photodetectors[28], SERS[8], field-effect transistors[29], solar cells[30], etc.

1.4.2. Graphene quantum dots

GQDs or graphene quantum dots, that can also be derived from GO, are popular materials for sensing applications. They are zero-dimensional (0D) with lateral sizes less than ~15 nm, have significant defects, and highly luminescent. A negligible amount of oxygen functional groups is attached. The unique optical and electrical properties of GQDs can be utilized in various applications such as SERS, bio-imaging, bio-sensing, optical sensing, gas sensor, optoelectronic devices, etc.[31] The properties of GQDs can be tuned by doping and functionalization[31,32].

1.5. Properties of graphene oxide

GO has been applied in various applications due to its large surface area, unique physical and chemical properties, cheapness, and ease to modified its structure. Some of the properties of GO are electronic properties, mechanical properties, thermal properties, nonlinear optics, etc.[33]

1.5.1. Electronic properties

The electronic properties of GO are heavily dependent on the degree of oxygen functional groups attached to the graphitic structure, the creation of surface defects, and the presence of sp^3 carbon atoms. The energy band structure of GO is adjustable by controlling the oxygen functional groups and structural defects on it. The band gap of GO can be 0.02 eV to 3.39 eV. The band gap of GO ranges from 3.39 eV to 1.44 eV to 0.22 eV to 0.02 eV depending directly upon the degree of oxygen functional groups present - from 50% to 25% to 16.7% to 12.5%, respectively. Also, the tuning of the band gap (2.4 eV to 0.9 eV) of GO can be achieved by exposure to a laser with different incident powers. A higher laser power reduces the degree of oxygen functional groups attached to GO. The band gap formation in GO is due to the bonding between the *p*-orbital electrons of the attached functional groups and graphitic carbon atoms, which leads to two bands – the *p*-bonding and *p*-antibonding bands. The increase in the functional groups reduces the width of the π band disturbing the electron transfer among the carbon atoms. The functional groups increase the localized electronic state density due to the incorporation of oxygen atoms into the graphitic structure. The band gap varies noticeably on addition of the relative fraction of epoxy and hydroxyl groups. Functionalization of the graphitic structure using epoxy groups leads to C:O ratios of 0.094 and 0.063 reducing the band gap to 1.58 and 1.19 eV, respectively. Lian et al.[34] studied the variation of band gap by changing the degree of oxygen attached to the GO maintaining the ratio of epoxy and hydroxyl groups at 2:1 and then by varying the ratio from 0.5 to 8.0

without changing the degree of oxygen attached to GO. The electronic band structure of GO is often ambiguous due to the heavy dependence on the degree of oxidation, type of functional groups, and distribution of GO. However, the tuneable band gap of GO is useful in various applications.

A higher density of oxygen functional groups on GO makes it behave like an insulator due to the breaking of π conjugate networks of graphitic structure. The electrical conductivity of GO is of the order of 10^{-3} S/m, whereas for GO with reduced functional groups (RGO) it reaches up to 0.05 S/m, comparable to pristine graphene[35]. The electrical conductivity of RGO reduces by 100 times when temperature is varied from 298 K to 4 K. At higher temperatures of ~2750 K, the electrical conductivity of RGO increased up to 3112 S/m[36]. Thus, the electrical conductivity of the GO is also affected by the presence of oxygen functional groups, structural defects, and ambient temperature. The electronic properties of the GO and its derivative materials depend on the degree of oxidation, defect, and functional groups that enhance the SERS effect, photodetector, and gas sensing applications.

1.5.2. Transparent-conductor properties

Transparency is one of the interesting properties of a material due to its demand in various applications such as touch screens, displays, solar cells, and light emitting diodes (LEDs). GO is a highly transparent material owing to its atomic layer thickness. Moreover, the conductivity of the GO can be tuned to an order comparable to disordered graphene, simply by controlling the degree of oxygen functional groups. Thus, RGO can be used as a transparent electrode in various applications. Zhu et al.[37] studied the properties of thermally reduced RGO thin film and observed 80% optical transparency for 550 nm and 10^2–10^3 Ω/ cm^2, which lays potential as a transparent conductor. Though single-layer GO has 96% optical transmittance, it has low electrical conductivity. Again, Eda et al.[38] studied the optical transmittance and the respective sheet resistance of RGO samples, which have been synthesized using various procedures. However, they concluded that a compromise between the optical transparency and electrical conductivity of GO needs to be made depending on the required application.

The optical transparency and conductivity of GO can be improved by various approaches: tuning the degree of functional groups, surface defects, doping, and formation of GO based hybrid materials. The electrical conductivity of GO/RGO can be enhanced by increasing the lateral size of the GO/RGO to avoid the loss of the resistance that occurs on overlapping of small-size GO/RGO. Zhao et al.[39] have improved upon the properties of RGO

film by using a larger lateral size, which acquired 78% of optical transparency at 550 nm and 840 Ω/ cm^2. Doping of GO can improve the electrical conductivity by means of increasing the charge carrier concentration. Doping can be done by surface charge transfer and substitutional doping. $SOBr_2$ doped on the GO has increased the electrical conductivity and optical transmittance of GO up to 1600 Ω/cm^2 and 82%, respectively[40].

1.5.3. Mechanical properties

Graphene is an extraordinary material due to its unique atomic arrangement. The sp^2 hybridized graphitic structure is formed by σ bonding with three adjacent carbon atoms and a 2D honeycomb structure. Thus, graphene becomes one of the most robust materials in the nanoscale owing to 1 TPa of in-plane Young's modulus and intrinsic strength of 130 GPa. On the other hand, dissimilarity, due to oxygen functional groups and structural defects in GO, weakens its mechanical properties. However, the mechanical properties of GO can be tuned by controlling the degree of oxidation, its stacking orientation, water contained intercalated molecules/ions, and structural defects. Varying the oxidation degrees of GO from 0 to 0.7 altered the in-plane Young modulus from 495 to 294 GPa and the intrinsic strength of the GO from 48 GPa to 28 GPa, respectively[41].

GO is a highly flexible material owing to the attachment of oxygen functional groups and structural defects, which attracts various futuristic devices like touch screens, bio-compatible sensors, transistors, solar cells, wearable devices etc. He et al.[42] demonstrated a flexible RGO-based transistor, which can retain its stability after testing its flexible properties for more than 6000 cycles by bending its radius up to 4 mm. GO/RGO–based flexible devices are fabricated by drop-casting on the flexible, transparent, and bendable substrate (ITO), which retained its conductivity up to 150 S/cm for GO, and 5.51×10^5 S/cm for RGO.

1.5.4. Thermal conductivity properties

The thermal conductivity of graphene is exceptionally high, up to 2000 W/mK at room temperature. For GO, its thermal conductivity can be tuned by controlling the degree of oxidation and structural defects. Because of the thermal conductivity of graphene, it has the potential to drain the excess heat from electronic devices. Thermal conductivity of the GO thin film is obtained up to 10 W/mK, owing to the phonon scattering at the sheets interface, which is much lower than pristine graphene[43]. Thus, the reduction of thermal conductivity after increased oxidation in GO is due to oxygen defect scattering that decreases the phonon's mean free path.

Interestingly, external strain applied on the GO can increase its thermal conductivity up to 12%, while for graphene, the thermal conductivity decreased to 28.4%, under similar conditions. The mean free path of phonon on GO increases when stress is applied on GO which causes the vertical displacement of sp^3 carbons and flattens the GO structure. Whereas, in case of RGO, the mean free path of phonon is reduced on application of pressure, causing a reduction of thermal conductivity on RGO.

1.5.5. Optical properties

The optical properties of GO can be tuned by controlling the degree of oxygen functional groups and structural defects[44,45]. As discussed earlier, GO is highly optically transparent due to its atomic layer thickness. GO is a fluorescent material over a wide range of wavelengths from ultraviolet to near-infrared region, but pristine graphene does not have this property due to zero bandgap. GO is used in non-linear optics due to a small cluster of sp^2 hybridized carbons with sp^3 hybridized carbon atoms. Due to its remarkable optical features, GO can is a potential candidate in several applications, such as in-display due to its transparency, in biosensing due to its fluorescence, and in laser technology due to its non-linear optics properties.

1.6. Surface modification using gas plasma treatment

The surface structure of the GO/RGO can be modified by using gas plasma treatment. Gas plasma treatment is a simple, cheap, efficient, eco-friendly, energy-saving, and clean process that is carried out at room temperature. It is used to modify the properties of GO by functionalization, etching, creating defects, and reducing oxygen functional groups.

Gases such as N_2, O_2, H_2, CH_4, NH_3, and F (fluorine) are used for gas plasma treatment systems[46–49]. The modification of GO depends on the use of the gas in the plasma treatment- it may change its defects, doping, and electrical conductivity. The effect of the plasma treatment depends on the chemical activities of ions, electrons, and other active species of plasma activated by the RF power. Most researchers have accepted the tailoring of the physical and chemical properties of GO by treating with the gas plasma.

The treatment of Ar plasma can modify the narrow near-surface region of the GO and cause reduction of the oxygen functional groups from the surface of the GO. Iqbal et al.[49] have demonstrated the graphene-based field-effect transistor (GFET), in which its charge density was controlled by introducing oxygen functional groups and reduction of functional groups from the surface of graphene using exposure to the O_2 and Ar gas environment,

respectively. N_2 plasma introduced nitrogen atoms into the GO and RGO up to 1.35% and 3%, respectively. GO can also be nitrogen doped using NH_3 plasma treatment. The oxygen functional groups such as epoxy, hydroxyl, carbonyl, and carboxyl, which are attached to the GO, are removed and persuaded by the C-N functional groups. The elemental composition ratio of the O/C was gradually reduced. In contrast, the N/C was increased by nitrogen gas plasma treatment. In addition, N_2 plasma led to formation of various nitrogen-based functional groups such as pyridine (pyridinic-N), pyrrole (pyrrolic-N), and graphitic-N. O_2 plasma aggressively modifies the surface of GO which leads to a change in the electronic and chemical properties of GO. The process can functionalize GO, etch the GO surface, induce disorder in the GO lattice, and oxidize the reduced GO or graphene. It can also carbon atoms from the lattice and functionalize GO with oxygen functional groups. RGO can be functionalized with oxygen-containing functional groups such as epoxy (C-O-C), and carboxyl (C-OH), using oxygen plasma treatment. The properties of graphene-based materials such as graphene, GO, RGO, and GQDs have been altered by modifying their chemical and structures to suit specific applications, using plasma treatments. However, the number of studies in this field is limited.

1.7. Synthesis of graphene oxide and its derivative materials

The properties of GO are sensitive to the synthesis process, and also GO is the source material for its derivative materials (RGO and GQDs). A comprehensive understanding of the synthesis of GO is required and essential for use in its potential applications. The evolution of the GO synthesis process has been discussed in **section 1.1**. The production of GO and graphene (RGO) on an industrial scale can be done using the top-down approach. Its mass production can be carried out at a low cost.

1.7.1. Synthesis of graphene oxide

Graphite oxide can be synthesized using the modified or simplified Hummers method. Graphite/ expanded graphite flakes as source material, concentrated H_2SO_4, H_3SO_4, or mixture are used as a protonated solvent, and $KMnO_4$ as an oxidizing agent is used for synthesis of graphite oxide. Adding H_2O_2 to end the oxidation reaction, filtration and centrifugation processes are used to obtain purified graphite oxide after oxidation. Various proposed techniques exist to exfoliate graphite oxide to obtain GO, such as ultrasonication, electrochemical, microwave-assisted, shear-mechanical, hydrothermal, and freezing-thawing-based exfoliation.

Table 1.1 collates various exfoliation techniques for graphene-based sheets, the nature of the solvent used, the resulting lateral size, and their applications. Although several approaches have been reported to exfoliate graphene derivatives into a few layers of large

Table 1.1: *Various techniques for graphene-based sheet exfoliation, nature of solvent used, their resulting lateral dimension and applications*

Exfoliation method	Nature of solvent	Lateral size	Applications	Reference
Electrochemical	Aq. Ammonium sulfate	>30 µm	-	[50]
Ultrasonic	Imidazole	10 µm	Supercapacitor	[51]
Ultrasonic	Pyridine	<1 µm	Mechanical	[52]
Ultrasonic	Water	>30 µm	Highly conductive thin film	[53]
Ultrasonic	Aq. salt	Up to 30 µm	Thin film devices	[54]
Ultrasonic	Aq. PTCA	10 – 12 µm	Conductive wire	[55]
Ultrasonic	Aq. salt	5 – 10 µm	Electrochemical sensors	[56]
Ultrasonic	Aq.salt	10 µm	Li-battery electrode	[57]
Ultrasonic	Water/SL/DDAC /DDBAC	100 nm – 1 µm	-	[58]
Ultrasonic	Aq. salt	100 nm– 6 µm	Ultracapacitor	[59]
Microwave	Water	30 µm	-	[60]
Microwave	CHP/DMF/NMP/ionic liquid	2 – 7 µm	3D Printing	[61]
Electrochemical	Aq. Ammonium sulfate	>30 µm	-	[50]
Shear force	Water	50 µm	Energy storage	[62]
Freeze-thaw	Anhy. THF/DMSO	4 µm	Electronics and energy storage	[63]
Hydrothermal	Aq. Glucose	20 – 100 µm	Photodetector	[28]

lateral size, the hydrothermal method has shown to be a promising technique exhibiting its relative cost-effectiveness, producing excellent yield with controllable and large lateral size

with outstanding electrical properties. However, this method requires additional autoclave equipment and the exfoliation processes at high temperatures up to 220 °C. Therefore, there is a further demand for a simpler and more cost-effective approach to exfoliate huge lateral dimension graphene-based sheets, exhibiting high electrical and sensing performances.

1.7.2. Synthesis of reduced graphene oxide

RGO is one of the derivative materials of GO where the presence of oxygen functional groups is minimal, and its atomic structures have resorted to sp^2 hybridized graphitic structure from sp^3. The applications of GO and RGO are vastly different due to the difference in their properties, even though both are the similar derivative materials. The conversion process from GO to RGO can be achieved using various chemical reactions, thermal treatment, and electrochemical methods. The above techniques are used to remove the oxygen functional groups and restore the graphitic structure of GO. However, the RGO exhibits difference in surface morphology, and structural, electronic, and physical properties. The conversion from GO to RGO can be observed by change in the colour to black from bright yellow, its hydrophobic nature, increase in the C/O ratio, high electrical conductivity, etc.

***Table 1.2**: The list of chemically reducing agents and its details to synthesise RGO*

Reducing agent	C/O ratio	Conductivity (S/m)	Expt. parameters	Reference
Hydrazine	10.3	2420	100 °C, 24 hrs	[64]
NH_3BH_3	14.2	19300	80 °C, 12 hrs	[65]
$LiAlH_4$	12	----	70 °C, 24 hrs	[66]
HI	12	29800	100 °C, 1 hr	[67]
Thiourea dioxide	14.5	----	90 °C, 1 hr	[68]
Methanol	4	3.2×10^{-5}	100 °C, 5 days	[69]
Thiophene	10.9	----	80 °C, 24 hrs	[70]

GO can be reduced to RGO chemically using hydrazine, borohydrides, aluminum hydride, hydrohalic acid, thiourea dioxide, methanol, etc. The list of chemically reducing agents and their details for synthesized RGO are mentioned in **Table 1.2**. Reduction of GO by using a chemical method has its limitations, such as a) it cannot retain the same lateral size

of RGO as similar to GO, b) it is challenging to exfoliation into mono-layer, c) it becomes hydrophobic nature leads to agglomerate in a water solvent, d) this process produces harmful bi-products causes environmental hazard and e) unwanted doping on RGO, etc.

The thermal treatment process is the simplest and has overcome most of the limitations caused by chemical methods such as retaining the lateral size and monolayer RGO, which are significant for various applications, especially to fabricate 2-D devices with two-electrode terminals or transistors. In thermally reduced RGO, oxygen functional groups from the GO are removed in the form of CO_2 and CO gas during heat treatment. Zhao et al.[44] studied the thermal treatment of GO in a range of temperatures from 200 to 900 °C. They analysed the transformation of GO to RGO by using Raman and FTIR analysis and studied its capacitance properties.

1.7.3. Synthesis of graphene quantum dots

GQDs are another derivative material of GO. They have significant edge defects due to the breaking down from a large size to a small size (down to 1.53 nm), exhibit quantum confinement effect, offer large surface area, high photoluminescence, and minimum oxygen functional groups.

***Table 1.3**: List of GQDs synthesis methods and obtained sizes.*

Techniques	Source material	Size (nm)	Reference
Electrochemical	Graphite rods	14	[72]
Pulsed laser ablation	GO	3.4	[73]
Chemical reaction	GO	5.6	[74]
Microwave	Triethanolamine	5.6	[75]
Hydrothermal	Citric acid	15	[76]

They are potentially used in various applications such as a photodetector, bio-medical sensors, solar cell, super capacitor, memory device, catalysis, etc.[45] GQDs can be synthesized using both top-down and bottom-up approaches. GQDs can be synthesized from GO by using various methods such as hydrothermal, high-power sonication, chemical reactions, electrochemical processes, pulsed laser ablation, etc. The list of some of the protocols adopted for synthesis of GQDs is summarized in **Table 1.3**. The hydrothermal method is one of the most well-known and standardized methods to synthesize GQDs from ~~the~~ critic acid,

1,5-dinitronaphalene, 1,3,6-trinitropyrene, GO, etc. This process is time-consuming (12-24 hours), costly, requires high temperature and pressure. Moreover, it yields QDs with a non-uniform size distribution, that agglomerate after removal of oxygen functional groups from GO.

1.8. Applications of graphene oxide

1.8.1. Surface-enhanced Raman Scattering

SERS is a Raman spectroscopy technique that can detect the low concentration of analytes molecules by increasing the intensity of the Raman signal for molecules with the help of a plasmonic surface shown in **Fig. 1.3**. Many techniques can enhance the Raman signal by using the stimulated Raman process, electronic resonance enhancement, and SERS; SERS is the most promising technique[71].

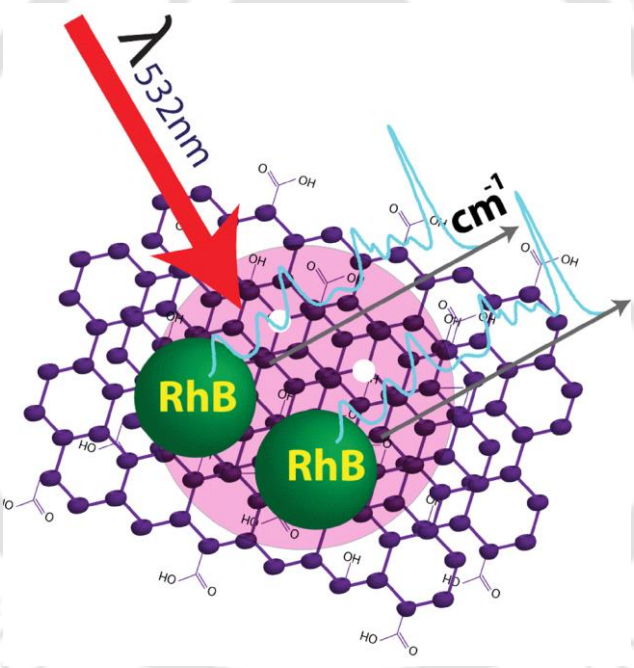

Fig. 1.3: Schematic illustration of RhB detection on GO using the SERS technique.

The enhancement of the Raman signal is due to the generation of the electromagnetic field by the excitation of the surface plasmons around the analytes. It may be assisted by the charge transfer between the analytes and the substrate. Today, SERS can be studied in many ways like UV-SERS, Tip-enhanced Raman spectroscopy, and ultrafast SERS. From the first observation of the SERS in 1974 to present day, SERS has been used in pollutant sensing, single-molecule, ultrahigh vacuum, trace detection for the various analytes (dyes, pesticides, food contaminants, etc.), and ultrafast science. In the SERS technique, metal-based nanomaterial has been widely used as a substrate onto which low concentration analyte is

placed for detection or analysis[77]. In most cases, gold or silver nanoparticles/nanostructured substrates are used to enhance the Raman signal of the analyte molecule.

Silver is a relatively better choice due to its lower cost than gold. However, the instability of the metal NPs properties in short duration, susceptibility to oxidation and sulfidation, could hinder the efficiency and consistency of the substrate for creating a plasmonic hotspot, thereby decreasing the sensitivity of the target molecules. Besides the metal NPs, several semiconductors have also been used as SERS sensing materials, such as TiO_2 nanostructures, CuTe nanocrystals, Cu_2O nanospheres, InAs/GaAs quantum dots, and graphene and its derivatives[78]. However, the SERS sensitivity of semiconductors is relatively low compared to that of metal NPs.

Graphene-derivatives are promising candidates as SERS materials because they are low-cost, synthesized from abundantly available raw materials (graphite), of large surface area and are biocompatible. Moreover, they exhibit adjustable electronic properties. Ling et al.[79] first observed the effect of graphene in Raman signals in which many unknown peaks emerged when the graphene substrate was treated with organic solvent as compared to that of SiO_2/Si substrate. Several other studies have reported the sensing efficiency of the graphene-based sheet through enhancement of Raman signal[80–83]. Jin-Ha Choi et al.[84] demonstrated the reliability of graphene-hybrid (gold array) as a SERS sensing substrate developed by laser interference lithography and electrochemical deposition method for detecting 10^{-4} to 10^{-9} M concentration of dopamine.

A single molecule (10^{-15} M) of Rhodamine 6G was detected using a graphene-oxide quantum sensor (GOQS) with an enhancement factor of 10^{14} times[85].Graphene-based SERS substrates are enhanced predominantly by the chemical enhancement (CE) mechanism through charge transfer processes. Monolayer and a few layers of graphene were found to be more efficient in strengthening the Raman signals, and the intensities decrease as the number of layers increases. Ling et al.[79] reported the enhancement of SERS signals for phthalocyanine (Pc), R6G, protoporphyrin (PPP), and crystal violet (CV) dyes by using graphene as substrates. A composite of GO, silicon pyramid arrays, and Ag NPs has improved the SERS signals of R6G compared to GO, as demonstrated by Zhang et al.[86]. A comparative analysis of the SERS enhancement factor (EF) for RhB dye on the modified GO/RGO using various methods is shown in **Table 1.4**. It is apparent that most of the EFs are of the order of 10^3 or lower for non-metal substrates, and there is enormous scope for improvement of the EF factor for practical applications.

The SERS signal of an analyte on the graphene substrate is primarily contributed by the interaction of π-π stacking layers and interband charge transfer[68–71]. Further, defects and functional groups present in the graphene assist in more interaction with the analytes, enhancing the intensity of Raman signals[72]. In most of the reports, the smaller lateral size of the graphene-based substrates was used for the SERS analysis. The effect of the large lateral dimension of graphene on the SERS enhancement is not reported yet. Moreover, it is challenging to locate the small-dimension graphene sheets using micro Raman spectroscopy due to their high optical transparency.

***Table 1.4**: Summary of SERS enhancement factors (EF) for GO/RGO reported.*

Substrate	Conc. of RhB	Peak position (cm^{-1})	Intensity (Counts)	EF	Reference
Mildy reduced GO	-	1597	-	~6×10^2	[80]
2pH of GO solution	2×10^{-5}	1648	-	40	[87]
Ozone plasma-treated graphene	1×10^{-5} M	1648	-	2.5×10^4	[88]
AgGO	1×10^{-4} M	1648	12000	2×10^3	[83]
Graphene Nanocolloids	1×10^{-4} M	-	-	40	[89]

1.8.2. Photodetector

GO and its derivative materials are prospective for photodetector applications due to their large surface area, surface defects, transparency, high charge carrier mobility, flexibility, ease of fabricating the device, self-bias, etc. Further, the photodetector can be used in remote control devices, self-driving cars, military applications, night surveillance, etc[90]. The current photodetector device made of semiconductor materials show several limitations such as high cost, required high operational temperature, toxicity, opaque, and rarity. The recent interest in the RGO and its application on the photodetector is shown as a graphical representation in **Fig. 1.4**. The change in the resistance of the device/ material during exposure to light leads to ~~a~~ generation of excess charge carriers in the material, shown in **Fig. 1.4(b)**. Lin et al.[91] has improved 50% of the external quantum efficiency (EQC) of the RGO after nanocomposite with CdSe by increasing the absorbance. Shao et al. has enriched the photo response time up to 9 ms of the RGO by composite with ZnO[92]. Furthermore, the photo response of the RGO is

further enhanced 4 times after composite with perovskite[93]. The quality of the GO-based photodetector can be improved by nanocomposite with other materials. As a result, it is required to obtain high performance GO-based materials by a simple modification process. The performance of the photodetector can be determined by studying the photo-response, spectral responsivity, reproducibility, power dependent response, time response, repeatability, and consistency of a device.

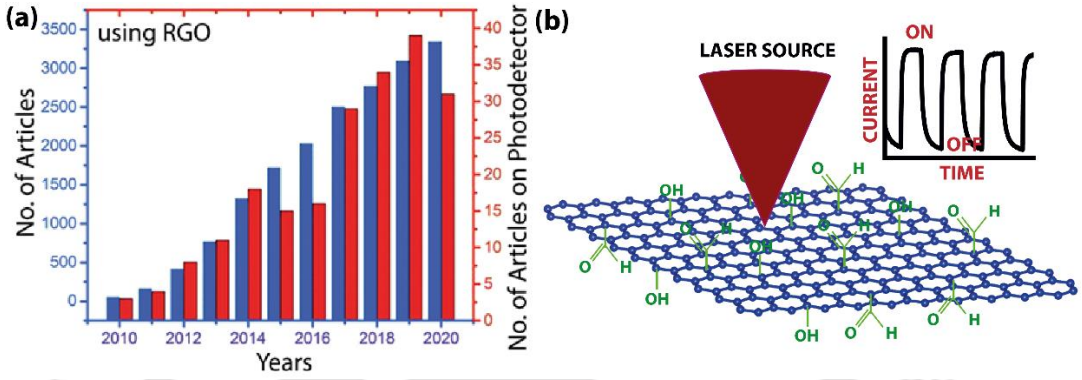

Fig. 1.4: (a) List of publication based on RGO and its photodetector device are emerging in recent years (reprinted from[90]); (b) Schematic illustration of GO based photodetector device and with photo-response.

1.8.3. CO_2 gas sensor

The CO_2 gas sensor is one of the emerging applications to monitor the continuously changing environment of the world. We are faced with a plethora of severe problems, like climate change, global warming, deterioration of flora and fauna, rising sea levels, and melting of icebergs, unusual floods, etc. The average concentration of CO_2 in the atmosphere is increasing from 300 ppm to 408 ppm since the pre-industrial revolution. However, the requirement of the CO_2 sensor is not limited to the environment, but extends into military, betterment for the human being, monitoring indoor air quality (IAQ), bio-engineering, cell culture, rescue operations for natural calamities, etc. Many CO_2 sensors based on optical, solid electrolyte, surface acoustic, and metal oxide-based sensors[74] are costly, require high operational temperature, and are not easy to fabricate.

Fabrication of high quality, low-cost, energy-efficient, easy-to-fabricate, reliable, and highly accurate CO_2 sensor is essential. A GO/RGO based-CO2 sensor can fulfil the above requirements. The room temperature-based CO2 sensor can be made from GO based material, as-shown in **Fig. 1.5**.

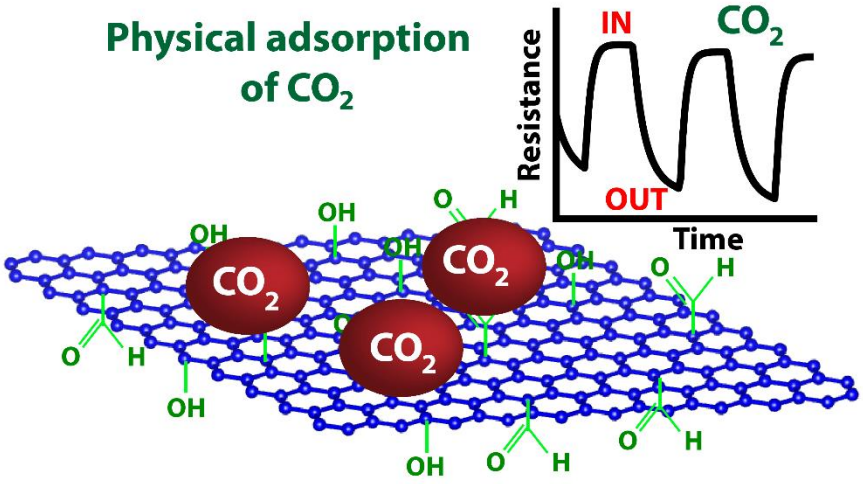

Fig. 1.5: Schematic illustration of CO_2 gas sensor device using GO based materials

GO and its derivative materials are one of the prospective materials due to the easily adjustable surface defects, presence of oxygen functional groups, and easy synthesis and fabrication process. GO/RGO can detect various gases such as CO_2, NO_2, NH_3, N_2, O_2, NO, CO, SO_2, etc. and can also be used as humidity sensors[74].

***Table 1.5**: Summary of performance of GO-based CO_2 sensors reported in the literature.*

Active material	Detection (ppm)	Time response/recovery (s)	Reference
H_2 plasma RGO	300-1500	240/240	[94]
GO	200-1000	150/250	[95]
Porous GO	250-1000	25/675	[96]
Graphene	400-2000	5.5/8.5	[10]
GO	400-4000	3/5	[97]
RGO-PEI	1000-15000	43/120	[98]

The proposed interaction sites of the oxygen functional groups with the suitable analyte gas molecules are obtained, such as -COOH for CO and NO, -OH for NH_3, and NO_2 for oxygen functional groups[75]. CO_2 is highly stable, has a high contribution to global warming, and has fewer studies for its detection. Thus, the change in the conductivity of the GO/RGO after the interaction leads to detection of the analyte gas. A comparative survey of the CO_2 sensors using GO and its derivative materials used is shown in **Table 1.5**.

In general, gas sensors can be calibrated using various characteristics such as sensitivity, selectivity, stability, detection limit, resolution, response time, recovery time, working temperature, life cycle, etc. Sensitivity is the change in resistance/conductivity of the material per unit of analyte gas molecules; selectivity is the ability to detect a particular analyte gas among other gases; stability is the ability of a device to provide reproducible results; detection limit is the minimum concentration of analyte gas can be detected by the device; response time is defined as the required time taken by the sensor device to detect the analyte gas molecules; recovery time is defined as the time taken by device to returned to its initial state after exposer of gas.

1.9. Focus of the Present Thesis

Although the synthesis of GO has been optimized since 1958, any repeatable and low cost methodology to achieve the sizeable lateral size GO is not established. Thus, the utilization of GO in applications sensitive to the large lateral size has been somewhat hampered. In the present thesis, we have introduced a new methodology to exfoliate the large lateral size GO using the easiest and simplest method of mild heating. Further, the properties of the GO can be enhanced by gas plasma-treatment. It is the simplest, dry, effective, and low-cost method to obtain the structural defects and modify the functional groups attached to the graphitic plane of GO. The application of the GO is vast to all disciplines such as electronics, mechanical, civil engineering, bio-medical, nanotechnology, material science, etc. Further, GO-based derivative materials such as RGO and GQDs are synthesized; RGO is synthesized using chemical and thermal treatment, and uniformed size GQDs are synthesized using a two-step process, hydrothermal and tip-sonication methods. We have presented GO/RGO/GQDs and structurally modified GO-based applications such as (a) detection of residue dye molecules in water at low concentrations using SERS technique, (b) photodetector, and (c) CO_2 gas sensor.

1.10. Organization of the Thesis

The present thesis is divided into seven chapters, and the chapter-wise descriptions are given below:

Chapter 1 briefly introduces GO and its derivative materials (RGO, GQDs). The history of GO, its unique properties, the various methods for synthesizing the graphite oxide, the mechanism of formation of graphite oxide, and its exfoliation techniques are discussed. The synthesized RGO and GQDs are studied. The GO applications such as gas sensor,

photodetector, SERS are studied. The motivation and focus of the present thesis work are described at the end of the chapter.

Chapter 2 focuses on synthesizing GO and other 2D materials such as RGO and GQDs. A systematic study of the simplified Hummer's method for synthesizing graphite oxide and exfoliating graphite oxide to large lateral-size GO sheets using sonication and a mild heating technique. The reduction of the oxygen functional groups from the GO is illustrated using a chemical (hydrazine) process and thermal treatment. The characterization of the GO and RGO is studied using FESEM, AFM, Raman spectroscopy, XRD, etc. A comparative study analyzed the GO synthesized from sonication and mild heating processes. Similarly, the RGO synthesized from hydrazine and thermal treatment is analyzed using various characterization techniques. Further, GQDs are synthesized using a two-step process: hydrothermal and Tip-sonication; the in-detail analysis of the GQDs is done by XRD, Raman, and FETEM with size distribution analysis.

Chapter 3 concentrates on the brief characterization of the GO exfoliated mild heating and its applications. The GO synthesized from the mild heating technique is analyzed using various characterization techniques. The GO layers are analyzed using Raman spectroscopy coordinate with FETEM and AFM images. The electronic and electrochemical behaviour of the large area GO and RGO is studied. The enhancement of Raman signals of RhB on the large area GO, UGO, and RGO are presented using the SERS technique. The study of this chapter is published in "***RSC advance 2021, 11, 9488-9504***".

Chapter 4 elucidates the brief concentration on the effect of gas plasma treatment, SERS effect of various dyes (MB, MO, RB, and RhB) on large area GO and RGO, and SERS effect of RhB enhanced on the surfaced modified GO and RGO. The characterization of the modified GO and RGO is briefly studied by Raman spectroscopy of various parameters such ID/IG, shifting peak position of D, G, and D', etc. The mapping of the SERS effect of the RhB on the GO and SiO2 substrate is illustrated. The EF of the Raman signals of RhB is calculated for all the samples and compared among them. The SERS effect of RhB is analyzed on the AU NPs, AuRGO, and AuGO substrates. This study is reported in "**ACS Applied Nano Materials 2022, 5, 5, 6352-6364**".

Chapter 5 focuses on the fabrication of a photodetector device based on the GO and its modified materials. At first, we have illustrated the fabrication of 10 µm IDE pattern on the SiO_2/Si substrate by using the UV lithography technique; each step for fabrication of IDE pattern is explained, from software design to metal lift-off. GO-based photodetector devise is made by drop-casting on IDE pattern and analyzing its photo-electric characteristics.

Furthermore, measured the photo-electric properties of the various temperature annealed GO, which shows changed structural properties of GO, as confirmed by the Raman, XRD, and FTIR analyses. Further, the photodetector characteristics such as photocurrent ON/OFF ratio, response and recovery time, responsivity (R), and detectivity (D) are measured for gas plasma-treated GO/RGO with gas plasma-treated samples.

Chapter 6 concentrates on the fabrication and optimization of gas sensing devices using RGO/GQDs with SnO_2 NPs. The schematic illustration of the RGO solution drop cast on the SnO_2 thin film and the mechanism of CO_2 sensing on the composite material is presented. The IV characteristics of the sensing material are measured, and the change of current with an increase in temperature is analyzed. The sensing properties such as response time, responsivity, working temperature, repeatability, etc., are studied in this chapter.

Chapter 7 summarizes the work done in this thesis and highlights its contributions to the study of GO and its derivative materials. It is an active material for SERS applications, photodetectors, and CO_2 sensors. In the end, we discuss the scope for future works in this field.

Reference

(1) Geim, A. K.; Novoselov, K. S. The Rise of Graphene. *Nat. Mater.* **2007**, *6* (3), 183–191. https://doi.org/10.1038/nmat1849.

(2) Dikin, D. A.; Stankovich, S.; Zimney, E. J.; Piner, R. D.; Dommett, G. H. B.; Evmenenko, G.; Nguyen, S. T.; Ruoff, R. S. Preparation and Characterization of Graphene Oxide Paper. *Nature* **2007**, *448*, 457.

(3) Saha, J. K.; Dutta, A. *A Review of Graphene: Material Synthesis from Biomass Sources*; Springer Netherlands, 2022; Vol. 13. https://doi.org/10.1007/s12649-021-01577-w.

(4) Venugopal, G.; Krishnamoorthy, K.; Mohan, R.; Kim, S. J. An Investigation of the Electrical Transport Properties of Graphene-Oxide Thin Films. *Mater. Chem. Phys.* **2012**, *132* (1), 29–33. https://doi.org/10.1016/j.matchemphys.2011.10.040.

(5) Kang, D.-W.; Shin, H.-S. Control of Size and Physical Properties of Graphene Oxide by Changing the Oxidation Temperature. *Carbon Lett.* **2012**, *13* (1), 39–43. https://doi.org/10.5714/cl.2012.13.1.039.

(6) Smith, A. T.; LaChance, A. M.; Zeng, S.; Liu, B.; Sun, L. Synthesis, Properties, and Applications of Graphene Oxide/Reduced Graphene Oxide and Their Nanocomposites. *Nano Mater. Sci.* **2019**, *1* (1), 31–47. https://doi.org/10.1016/j.nanoms.2019.02.004.

(7) Dideikin, A. T.; Vul', A. Y. Graphene Oxide and Derivatives: The Place in Graphene Family. *Front. Phys.* **2019**, *6* (JAN). https://doi.org/10.3389/fphy.2018.00149.

(8) Cheng, J.; Zhang, S.; Wang, S.; Wang, P.; Su, X. O.; Xie, J. Rapid and Sensitive Detection of Acrylamide in Fried Food Using Dispersive Solid-Phase Extraction Combined with Surface-Enhanced Raman Spectroscopy. *Food Chem.* **2019**, *276* (October 2018), 157–163. https://doi.org/10.1016/j.foodchem.2018.10.004.

(9) Zheng, L.; Zhongzhu, L.; Guozhen, S.; Zhang, K.; Zhang, L.; Han, L.; Wang, L.; Chen, Z.; Xing, H.; Chen, X.; Qiao, H.; Huang, Z.; Ren, X.; Liu, S.; Zhang, Y.; Qi, X.; Zhang, H.; Long, M.; Wang, P.; Fang, H.; Hu, W.; Jiang, J.; Wen, Y.; Wang, H.; Yin, L.; Cheng, R.; Liu, C.; Feng, L.; He, J.; Huo, N.; Konstantatos, G.; Ezhilmaran, B.; Patra, A.; Benny, S.; M. R., S.; V. V., A.; Bhat, S. V.; Rout, C. S. Recent Progress and Future Prospects of 2D-Based Photodetectors. *Adv. Funct. Mater.* **2021**, *7* (19), 1–27. https://doi.org/10.1088/1674-4926/37/9/091001.

(10) Zhou, Y.; Jiang, Y.; Xie, G.; Wu, M.; Tai, H. Gas Sensors for CO2 Detection Based on RGO–PEI Films at Room Temperature. *Chinese Sci. Bull.* **2014**, *59* (17), 1999–2005. https://doi.org/10.1007/s11434-014-0253-2.

(11) Fu, C.; Zhao, G.; Zhang, H.; Li, S. Evaluation and Characterization of Reduced Graphene Oxide Nanosheets as Anode Materials for Lithium-Ion Batteries. *Int. J. Electrochem. Sci.* **2013**, *8* (5), 6269–6280.

(12) Ray, S. C. Application and Uses of Graphene Oxide and Reduced Graphene Oxide. *Appl. Graphene*

Graphene-Oxide Based Nanomater. **2015**, No. December 2015, 39–55. https://doi.org/10.1016/b978-0-323-37521-4.00002-9.

(13) Brodie, B. C. On the Atomic Weight of Graphite. *Philos. Trans. R. Soc. London Ser. I* **1859**, *149*, 249–259.

(14) Staudenmaier, L. Verfahren Zur Darstellung Der Graphitsäure. *Berichte der Dtsch. Chem. Gesellschaft* **1898**, *31* (2), 1481–1487. https://doi.org/https://doi.org/10.1002/cber.18980310237.

(15) Hummers, W. S.; Offeman, R. E. Preparation of Graphitic Oxide. *J. Am. Chem. Soc.* **1958**, *80* (6), 1339. https://doi.org/10.1021/ja01539a017.

(16) Mowry, M. N. In Situ Raman Spectroscopy Study of the Formation of Graphene from Urea and Graphite Oxide. **2012**, 107.

(17) Marcano, D. C.; Kosynkin, D. V; Berlin, J. M.; Sinitskii, A.; Sun, Z.; Slesarev, A.; Alemany, L. B.; Lu, W.; Tour, J. M. Improved Synthesis of Graphene Oxide. *ACS Nano* **2010**, *4* (8), 4806–4814. https://doi.org/10.1021/nn1006368.

(18) Zhu, Y.; Murali, S.; Cai, W.; Li, X.; Suk, J. W.; Potts, J. R.; Ruoff, R. S. Graphene and Graphene Oxide: Synthesis, Properties, and Applications. *Adv. Mater.* **2010**, *22* (35), 3906–3924. https://doi.org/10.1002/adma.201001068.

(19) Pei, S.; Cheng, H.-M. The Reduction of Graphene Oxide. *Carbon N. Y.* **2012**, *50* (9), 3210–3228. https://doi.org/https://doi.org/10.1016/j.carbon.2011.11.010.

(20) Poh, H. L.; Šaněk, F.; Ambrosi, A.; Zhao, G.; Sofer, Z.; Pumera, M. Graphenes Prepared by Staudenmaier, Hofmann and Hummers Methods with Consequent Thermal Exfoliation Exhibit Very Different Electrochemical Properties. *Nanoscale* **2012**, *4* (11), 3515–3522. https://doi.org/10.1039/c2nr30490b.

(21) Szabó, T.; Berkesi, O.; Forgó, P.; Josepovits, K.; Sanakis, Y.; Petridis, D.; Dékány, I. Evolution of Surface Functional Groups in a Series of Progressively Oxidized Graphite Oxides. *Chem. Mater.* **2006**, *18* (11), 2740–2749. https://doi.org/10.1021/cm060258+.

(22) Siklitskaya, A.; Gacka, E.; Larowska, D.; Mazurkiewicz-Pawlicka, M.; Malolepszy, A.; Stobiński, L.; Marciniak, B.; Lewandowska-Andrałojć, A.; Kubas, A. Lerf–Klinowski-Type Models of Graphene Oxide and Reduced Graphene Oxide Are Robust in Analyzing Non-Covalent Functionalization with Porphyrins. *Sci. Rep.* **2021**, *11* (1), 1–14. https://doi.org/10.1038/s41598-021-86880-1.

(23) Dimiev, A. M.; Tour, J. M. Mechanism of Graphene Oxide Formation. *ACS Nano* **2014**, *8* (3), 3060–3068. https://doi.org/10.1021/nn500606a.

(24) Kang, J. H.; Kim, T.; Choi, J.; Park, J.; Kim, Y. S.; Chang, M. S.; Jung, H.; Park, K. T.; Yang, S. J.; Park, C. R. Hidden Second Oxidation Step of Hummers Method. *Chem. Mater.* **2016**, *28* (3), 756–764. https://doi.org/10.1021/acs.chemmater.5b03700.

(25) Chua, C. K.; Pumera, M. Chemical Reduction of Graphene Oxide: A Synthetic Chemistry Viewpoint. *Chem. Soc. Rev.* **2014**, *43* (1), 291–312. https://doi.org/10.1039/c3cs60303b.

(26) Huang, H. N.; Wang, S. Y.; Chiang, W. H. Microplasma-Engineered Ag/GONR-Based Nanocomposites for Selective and Label-Free SERS-Sensitive Detection of Dopamine. *ACS Appl. Nano Mater.* **2021**, *4* (10), 10360–10369. https://doi.org/10.1021/acsanm.1c01867.

(27) Mi, W.; Chiu, S. W.; Xue, T.; Chen, Y.; Qi, H.; Yang, Y.; Tang, K. T.; Ren, T. L. Highly Sensitive and Portable Gas Sensing System Based on Reduced Graphene Oxide. *Tsinghua Sci. Technol.* **2016**, *21* (4), 435–441. https://doi.org/10.1109/TST.2016.7536721.

(28) Tang, L.; Li, X.; Ji, R.; Teng, K. S.; Tai, G.; Ye, J.; Wei, C.; Lau, S. P. Bottom-up Synthesis of Large-Scale Graphene Oxide Nanosheets. *J. Mater. Chem.* **2012**, *22* (12), 5676–5683. https://doi.org/10.1039/c2jm15944a.

(29) Kotchey, G. P.; Allen, B. L.; Vedala, H.; Yanamala, N.; Kapralov, A. A.; Tyurina, Y. Y.; Klein-Seetharaman, J.; Kagan, V. E.; Star, A. The Enzymatic Oxidation of Graphene Oxide. *ACS Nano* **2011**, *5* (3), 2098–2108. https://doi.org/10.1021/nn103265h.

(30) Li, P.; Chen, C.; Zhang, J.; Li, S.; Sun, B.; Bao, Q. Graphene-Based Transparent Electrodes for Hybrid Solar Cells. *Front. Mater.* **2014**, *1* (November), 1–7. https://doi.org/10.3389/fmats.2014.00026.

(31) Das, R.; Parveen, S.; Bora, A.; Giri, P. K. Origin of High Photoluminescence Yield and High SERS Sensitivity of Nitrogen-Doped Graphene Quantum Dots. *Carbon N. Y.* **2020**, *160*, 273–286. https://doi.org/10.1016/j.carbon.2020.01.030.

(32) Biroju, R. K.; Rajender, G.; Giri, P. K. On the Origin and Tunability of Blue and Green Photoluminescence from Chemically Derived Graphene: Hydrogenation and Oxygenation Studies. *Carbon N. Y.* **2015**, *95*, 228–238. https://doi.org/10.1016/j.carbon.2015.08.036.

(33) Huang, X. M.; Liu, L. Z.; Zhou, S.; Zhao, J. J. Physical Properties and Device Applications of Graphene Oxide. *Front. Phys.* **2020**, *15* (3). https://doi.org/10.1007/s11467-019-0937-9.

(34) Lian, K. Y.; Ji, Y. F.; Li, X. F.; Jin, M. X.; Ding, D. J.; Luo, Y. Big Bandgap in Highly Reduced Graphene Oxides. *J. Phys. Chem. C* **2013**, *117* (12), 6049–6054. https://doi.org/10.1021/jp3118067.

(35) Gómez-Navarro, C.; Weitz, R. T.; Bittner, A. M.; Scolari, M.; Mews, A.; Burghard, M.; Kern, K. Electronic Transport Properties of Individual Chemically Reduced Graphene Oxide Sheets. *Nano Lett.* **2007**, *7* (11), 3499–3503. https://doi.org/10.1021/nl072090c.

(36) Chen, Y.; Fu, K.; Zhu, S.; Luo, W.; Wang, Y.; Li, Y.; Hitz, E.; Yao, Y.; Dai, J.; Wan, J.; Danner, V. A.; Li, T.; Hu, L. Reduced Graphene Oxide Films with Ultrahigh Conductivity as Li-Ion Battery Current Collectors. *Nano Lett.* **2016**, *16* (6), 3616–3623. https://doi.org/10.1021/acs.nanolett.6b00743.

(37) Zhu, Y.; Cai, W.; Piner, R. D.; Velamakanni, A.; Ruoff, R. S. Transparent Self-Assembled Films of Reduced Graphene Oxide Platelets. *Appl. Phys. Lett.* **2009**, *95* (10). https://doi.org/10.1063/1.3212862.

(38) Eda, G.; Chhowalla, M. Chemically Derived Graphene Oxide: Towards Large-Area Thin-Film Electronics and Optoelectronics. *Adv. Mater.* **2010**, *22* (22), 2392–2415. https://doi.org/10.1002/adma.200903689.

(39) Zhao, J.; Pei, S.; Ren, W.; Gao, L.; Cheng, H. M. Efficient Preparation of Large-Area Graphene Oxide Sheets for Transparent Conductive Films. *ACS Nano* **2010**, *4* (9), 5245–5252. https://doi.org/10.1021/nn1015506.

(40) Zheng, Q. Bin; Gudarzi, M. M.; Wang, S. J.; Geng, Y.; Li, Z.; Kim, J. K. Improved Electrical and Optical Characteristics of Transparent Graphene Thin Films Produced by Acid and Doping Treatments. *Carbon N. Y.* **2011**, *49* (9), 2905–2916. https://doi.org/10.1016/j.carbon.2011.02.064.

(41) Papageorgiou, D. G.; Kinloch, I. A.; Young, R. J. Mechanical Properties of Graphene and Graphene-Based Nanocomposites. *Prog. Mater. Sci.* **2017**, *90*, 75–127. https://doi.org/10.1016/j.pmatsci.2017.07.004.

(42) He, Q.; Wu, S.; Gao, S.; Cao, X.; Yin, Z.; Li, H.; Chen, P.; Zhang, H. Transparent, Flexible, All-Reduced Graphene Oxide Thin Film Transistors. *ACS Nano* **2011**, *5* (6), 5038–5044. https://doi.org/10.1021/nn201118c.

(43) James, D. K.; Tour, J. M. Graphene: Powder, Flakes, Ribbons, and Sheets. *Acc. Chem. Res.* **2013**, *46* (10), 2307–2318. https://doi.org/10.1021/ar300127r.

(44) Liu, Z.; Wang, Y.; Zhang, X.; Xu, Y.; Chen, Y.; Tian, J. Nonlinear Optical Properties of Graphene Oxide in Nanosecond and Picosecond Regimes. *Appl. Phys. Lett.* **2009**, *94* (2), 1–4. https://doi.org/10.1063/1.3068498.

(45) Huo, N.; Konstantatos, G. Recent Progress and Future Prospects of 2D-Based Photodetectors. *Adv. Mater.* **2018**, *30* (51), 1–27. https://doi.org/10.1002/adma.201801164.

(46) Wang, Y.; Shao, Y.; Matson, D. W.; Li, J.; Lin, Y. Nitrogen-Doped Graphene and Its Biosensing. *ACS Nano* **2010**, *4* (4), 1790–1798. https://doi.org/10.1063/1.4870424.

(47) Felten, A.; Eckmann, A.; Pireaux, J. J.; Krupke, R.; Casiraghi, C. Controlled Modification of Mono- and Bilayer Graphene in O2, H2 and CF4 Plasmas. *Nanotechnology* **2013**, *24* (35). https://doi.org/10.1088/0957-4484/24/35/355705.

(48) Zhao, H.; Fan, S.; Chen, Y.; Feng, Z.; Zhang, H.; Pang, W.; Zhang, D.; Zhang, M. Oxygen Plasma-Treated Graphene Oxide Surface Functionalization for Sensitivity Enhancement of Thin-Film Piezoelectric Acoustic Gas Sensors. *ACS Appl. Mater. Interfaces* **2017**, *9* (46), 40774–40781. https://doi.org/10.1021/acsami.7b09547.

(49) Iqbal, M. Z.; Rehman, A.; Siddique, S. Ultraviolet-Light-Driven Carrier Density Modulation of Graphene Based Field Effect Transistors under Oxygen- and Argon Atmosphere. *Appl. Surf. Sci.* **2018**, *451*, 40–44. https://doi.org/10.1016/j.apsusc.2018.04.222.

(50) Achee, T. C.; Sun, W.; Hope, J. T.; Quitzau, S. G.; Sweeney, C. B.; Shah, S. A.; Habib, T.; Green, M. J.

High-Yield Scalable Graphene Nanosheet Production from Compressed Graphite Using Electrochemical Exfoliation. *Sci. Rep.* **2018**, *8* (1), 1–8. https://doi.org/10.1038/s41598-018-32741-3.

(51) Chen, J.; Shi, X.; Qi, S.; Mohai, M.; Bertóti, I.; Gao, Y.; Dong, H. Reducing and Multiple-Element Doping of Graphene Oxide Using Active Screen Plasma Treatments. *Carbon N. Y.* **2015**, *95*, 338–346. https://doi.org/https://doi.org/10.1016/j.carbon.2015.08.046.

(52) Kim, J.; Kim, J.; Song, S.; Zhang, S.; Cha, J.; Kim, K.; Yoon, H.; Jung, Y.; Paik, K. W.; Jeon, S. Strength Dependence of Epoxy Composites on the Average Filler Size of Non-Oxidized Graphene Flake. *Carbon N. Y.* **2017**, *113*, 379–386. https://doi.org/10.1016/j.carbon.2016.11.023.

(53) Deemer, E. M.; Paul, P. K.; Manciu, F. S.; Botez, C. E.; Hodges, D. R.; Landis, Z.; Akter, T.; Castro, E.; Chianelli, R. R. Consequence of Oxidation Method on Graphene Oxide Produced with Different Size Graphite Precursors. *Mater. Sci. Eng. B Solid-State Mater. Adv. Technol.* **2017**, *224* (March 2019), 150–157. https://doi.org/10.1016/j.mseb.2017.07.018.

(54) Niu, L.; Li, M.; Tao, X.; Xie, Z.; Zhou, X.; Raju, A. P. A.; Young, R. J.; Zheng, Z. Salt-Assisted Direct Exfoliation of Graphite into High-Quality, Large-Size, Few-Layer Graphene Sheets. *Nanoscale* **2013**, *5* (16), 7202–7208. https://doi.org/10.1039/c3nr02173d.

(55) Narayan, R.; Lim, J.; Jeon, T.; Li, D. J.; Kim, S. O. Perylene Tetracarboxylate Surfactant Assisted Liquid Phase Exfoliation of Graphite into Graphene Nanosheets with Facile Re-Dispersibility in Aqueous/Organic Polar Solvents. *Carbon N. Y.* **2017**, *119*, 555–568. https://doi.org/10.1016/j.carbon.2017.04.071.

(56) Tung, T. T.; Yoo, J.; Alotaibi, F. K.; Nine, M. J.; Karunagaran, R.; Krebsz, M.; Nguyen, G. T.; Tran, D. N. H.; Feller, J. F.; Losic, D. Graphene Oxide-Assisted Liquid Phase Exfoliation of Graphite into Graphene for Highly Conductive Film and Electromechanical Sensors. *ACS Appl. Mater. Interfaces* **2016**, *8* (25), 16521–16532. https://doi.org/10.1021/acsami.6b04872.

(57) Geng, X.; Guo, Y.; Li, D.; Li, W.; Zhu, C.; Wei, X.; Chen, M.; Gao, S.; Qiu, S.; Gong, Y.; Wu, L.; Long, M.; Sun, M.; Pan, G.; Liu, L. Interlayer Catalytic Exfoliation Realizing Scalable Production of Large-Size Pristine Few-Layer Graphene. *Sci. Rep.* **2013**, *3*, 1–6. https://doi.org/10.1038/srep01134.

(58) Hu, Y.; Su, M.; Xie, X.; Sun, C.; Kou, J. Few-Layer Graphene Oxide with High Yield via Efficient Surfactant-Assisted Exfoliation of Mildly-Oxidized Graphite. *Appl. Surf. Sci.* **2019**, *494* (February), 1100–1108. https://doi.org/10.1016/j.apsusc.2019.07.111.

(59) Zhu, Y.; Stoller, M. D.; Cai, W.; Velamakanni, A.; Piner, R. D.; Chen, D.; Ruoff, R. S. Exfoliation of Graphite Oxide in Propylene Carbonate and Thermal Reduction of the Resulting Graphene Oxide Platelets. *ACS Nano* **2010**, *4* (2), 1227–1233. https://doi.org/10.1021/nn901689k.

(60) Kim, H. R.; Lee, S. H.; Lee, K. H. Scalable Production of Large Single-Layered Graphenes by Microwave Exfoliation 'in Deionized Water.' *Carbon N. Y.* **2018**, *134*, 431–438. https://doi.org/10.1016/j.carbon.2018.04.014.

(61) Wu, W.; Xu, J.; Tang, X.; Xie, P.; Liu, X.; Xu, J.; Zhou, H.; Zhang, D.; Fan, T. Two-Dimensional Nanosheets by Rapid and Efficient Microwave Exfoliation of Layered Materials. *Chem. Mater.* **2018**, *30* (17), 5932–5940. https://doi.org/10.1021/acs.chemmater.8b01976.

(62) Park, W. K.; Yoon, Y.; Song, Y. H.; Choi, S. Y.; Kim, S.; Do, Y.; Lee, J.; Park, H.; Yoon, D. H.; Yang, W. S. High-Efficiency Exfoliation of Large-Area Mono-Layer Graphene Oxide with Controlled Dimension. *Sci. Rep.* **2017**, *7* (1), 1–9. https://doi.org/10.1038/s41598-017-16649-y.

(63) Ogino, I.; Yokoyama, Y.; Iwamura, S.; Mukai, S. R. Exfoliation of Graphite Oxide in Water without Sonication: Bridging Length Scales from Nanosheets to Macroscopic Materials. *Chem. Mater.* **2014**, *26* (10), 3334–3339. https://doi.org/10.1021/cm501305c.

(64) Stankovich, S.; Dikin, D. A.; Piner, R. D.; Kohlhaas, K. A.; Kleinhammes, A.; Jia, Y.; Wu, Y.; Nguyen, S. T.; Ruoff, R. S. Synthesis of Graphene-Based Nanosheets via Chemical Reduction of Exfoliated Graphite Oxide. *Carbon N. Y.* **2007**, *45* (7), 1558–1565. https://doi.org/https://doi.org/10.1016/j.carbon.2007.02.034.

(65) Pham, V. H.; Hur, S. H.; Kim, E. J.; Kim, B. S.; Chung, J. S. Highly Efficient Reduction of Graphene Oxide Using Ammonia Borane. *Chem. Commun.* **2013**, *49* (59), 6665–6667. https://doi.org/10.1039/c3cc43503b.

(66) Ambrosi, A.; Chua, C. K.; Bonanni, A.; Pumera, M. Lithium Aluminum Hydride as Reducing Agent for Chemically Reduced Graphene Oxides. *Chem. Mater.* **2012**, *24* (12), 2292–2298. https://doi.org/10.1021/cm300382b.

(67) Pei, S.; Zhao, J.; Du, J.; Ren, W.; Cheng, H. M. Direct Reduction of Graphene Oxide Films into Highly Conductive and Flexible Graphene Films by Hydrohalic Acids. *Carbon N. Y.* **2010**, *48* (15), 4466–4474. https://doi.org/10.1016/j.carbon.2010.08.006.

(68) Chua, C. K.; Ambrosi, A.; Pumera, M. Graphene Oxide Reduction by Standard Industrial Reducing Agent: Thiourea Dioxide. *J. Mater. Chem.* **2012**, *22* (22), 11054–11061. https://doi.org/10.1039/c2jm16054d.

(69) Dreyer, D. R.; Murali, S.; Zhu, Y.; Ruoff, R. S.; Bielawski, C. W. Reduction of Graphite Oxide Using Alcohols. *J. Mater. Chem.* **2011**, *21* (10), 3443–3447. https://doi.org/10.1039/c0jm02704a.

(70) Some, S.; Kim, Y.; Yoon, Y.; Yoo, H.; Lee, S.; Park, Y.; Lee, H. High-Quality Reduced Graphene Oxide by a Dual-Function Chemical Reduction and Healing Process. *Sci. Rep.* **2013**, *3* (Figure 1), 1–5. https://doi.org/10.1038/srep01929.

(71) Sharma, B.; Frontiera, R. R.; Henry, A.; Ringe, E.; Duyne, R. P. Van. SERS : Materials , Applications , and the Future Surface Enhanced Raman Spectroscopy (SERS) Is a Powerful Vibrational. *Mater. Today* **2012**, *15* (1–2), 16–25. https://doi.org/10.1016/S1369-7021(12)70017-2.

(72) Zhang, M.; Bai, L.; Shang, W.; Xie, W.; Ma, H.; Fu, Y.; Fang, D.; Sun, H.; Fan, L.; Han, M.; Liu, C.; Yang, S. Facile Synthesis of Water-Soluble, Highly Fluorescent Graphene Quantum Dots as a Robust

Biological Label for Stem Cells. *J. Mater. Chem.* **2012**, *22* (15), 7461–7467. https://doi.org/10.1039/c2jm16835a.

(73) Santiago, S. R. M.; Lin, T. N.; Chang, C. H.; Wong, Y. A.; Lin, C. A. J.; Yuan, C. T.; Shen, J. L. Synthesis of N-Doped Graphene Quantum Dots by Pulsed Laser Ablation with Diethylenetriamine (DETA) and Their Photoluminescence. *Phys. Chem. Chem. Phys.* **2017**, *19* (33), 22395–22400. https://doi.org/10.1039/c7cp03993j.

(74) Maiti, S.; Kundu, S.; Roy, C. N.; Das, T. K.; Saha, A. Synthesis of Excitation Independent Highly Luminescent Graphene Quantum Dots through Perchloric Acid Oxidation. *Langmuir* **2017**, *33* (51), 14634–14642. https://doi.org/10.1021/acs.langmuir.7b02611.

(75) Ren, Q.; Ga, L.; Ai, J. Rapid Synthesis of Highly Fluorescent Nitrogen-Doped Graphene Quantum Dots for Effective Detection of Ferric Ions and as Fluorescent Ink. *ACS Omega* **2019**, *4* (14), 15842–15848. https://doi.org/10.1021/acsomega.9b01612.

(76) Dong, Y.; Shao, J.; Chen, C.; Li, H.; Wang, R.; Chi, Y.; Lin, X.; Chen, G. Blue Luminescent Graphene Quantum Dots and Graphene Oxide Prepared by Tuning the Carbonization Degree of Citric Acid. *Carbon N. Y.* **2012**, *50* (12), 4738–4743. https://doi.org/10.1016/j.carbon.2012.06.002.

(77) Lightcap, I. V.; Kosel, T. H.; Kamat, P. V. Anchoring Semiconductor and Metal Nanoparticles on a Two-Dimensional Catalyst Mat. Storing and Shuttling Electrons with Reduced Graphene Oxide. *Nano Lett.* **2010**, *10* (2), 577–583. https://doi.org/10.1021/nl9035109.

(78) Almohammed, S.; Zhang, F.; Rodriguez, B. J.; Rice, J. H. Electric Field-Induced Chemical Surface-Enhanced Raman Spectroscopy Enhancement from Aligned Peptide Nanotube-Graphene Oxide Templates for Universal Trace Detection of Biomolecules. *J. Phys. Chem. Lett.* **2019**, *10* (8), 1878–1887. https://doi.org/10.1021/acs.jpclett.9b00436.

(79) Ling, X.; Xie, L.; Fang, Y.; Xu, H.; Zhang, H.; Kong, J.; Dresselhaus, M. S.; Zhang, J.; Liu, Z. Can Graphene Be Used as a Substrate for Raman Enhancement? *Nano Lett.* **2010**, *10* (2), 553–561. https://doi.org/10.1021/nl903414x.

(80) Yu, X.; Cai, H.; Zhang, W.; Li, X.; Pan, N.; Luo, Y.; Wang, X.; Hou, J. G. Tuning Chemical Enhancement of SERS by Controlling the Chemical Reduction of Graphene Oxide Nanosheets. *ACS Nano* **2011**, *5* (2), 952–958. https://doi.org/10.1021/nn102291j.

(81) Wang, Y.; Polavarapu, L.; Liz-marza, L. M. Reduced Graphene Oxide-Supported Gold Nanostars for Improved SERS Sensing and Drug Delivery. **2014**. https://doi.org/10.1021/am501382y.

(82) Jalani, G.; Cerruti, M. Nano Graphene Oxide-Wrapped Gold Nanostars as Ultrasensitive and Stable SERS Nanoprobes. *Nanoscale* **2015**, *7* (22), 9990–9997. https://doi.org/10.1039/c4nr07473d.

(83) Gough, J. J.; Siewerska, K. E.; Mehigan, S.; Hanlon, D.; Backes, C.; Gholamvand, Z.; Szydłowska, B. M.; Blau, W. J.; McCabe, E.; Bradley, A. L. Influence of Graphene Oxide/Ag Nanoparticle Composites on the Fluorescence Properties of Organic Dyes. *J. Nanosci. Nanotechnol.* **2017**, *17* (12), 8901–8911.

https://doi.org/10.1166/jnn.2017.13889.

(84) Choi, S. H.; Kim, Y. L.; Byun, K. M. Graphene-on-Silver Substrates for Sensitive Surface Plasmon Resonance Imaging Biosensors. *Opt. Express* **2011**, *19* (2), 458. https://doi.org/10.1364/oe.19.000458.

(85) Ganesh, S.; Venkatakrishnan, K.; Tan, B. Tailoring Carbon for Single Molecule Detection – Broad Spectrum 3D Quantum Sensor. *Sensors Actuators, B Chem.* **2020**, *317* (April), 128216. https://doi.org/10.1016/j.snb.2020.128216.

(86) Zhang, C.; Jiang, S. Z.; Huo, Y. Y.; Liu, A. H.; Xu, S. C.; Liu, X. Y.; Sun, Z. C.; Xu, Y. Y.; Li, Z.; Man, B. Y. SERS Detection of R6G Based on a Novel Graphene Oxide/Silver Nanoparticles/Silicon Pyramid Arrays Structure. *Opt. Express* **2015**, *23* (19), 24811. https://doi.org/10.1364/oe.23.024811.

(87) Liu, Z.; Li, S.; Hu, C.; Zhang, W.; Zhong, H.; Guo, Z. PH-Dependent Surface-Enhanced Raman Scattering of Aromatic Molecules on Graphene Oxide. *J. Raman Spectrosc.* **2013**, *44* (1), 75–80. https://doi.org/10.1002/jrs.4142.

(88) Huh, S.; Park, J.; Kim, Y. S.; Kim, K. S.; Hong, B. H.; Nam, J. M. UV/Ozone-Oxidized Large-Scale Graphene Platform with Large Chemical Enhancement in Surface-Enhanced Raman Scattering. *ACS Nano* **2011**, *5* (12), 9799–9806. https://doi.org/10.1021/nn204156n.

(89) Sun, S.; Zhang, Z.; Wu, P. Exploring Graphene Nanocolloids as Potential Substrates for the Enhancement of Raman Scattering. *ACS Appl. Mater. Interfaces* **2013**, *5* (11), 5085–5090. https://doi.org/10.1021/am400938z.

(90) Khan, M. A.; Kumar, A.; Zhang, J.; Kumar, M. Recent Advances and Prospects in Reduced Graphene Oxide-Based Photodetectors. *J. Mater. Chem. C* **2021**, *9* (26), 8129–8157. https://doi.org/10.1039/d1tc01306h.

(91) Lin, Y.; Zhang, K.; Chen, W.; Liu, Y.; Geng, Z.; Zeng, J.; Pan, N.; Yan, L.; Wang, X.; Hou, J. G. Dramatically Enhanced Photoresponse of Reduced Graphene Oxide with Linker-Free Anchored CdSe Nanoparticles. *ACS Nano* **2010**, *4* (6), 3033–3038. https://doi.org/10.1021/nn100134j.

(92) Shao, D.; Yu, M.; Sun, H.; Hu, T.; Lian, J.; Sawyer, S. High Responsivity, Fast Ultraviolet Photodetector Fabricated from ZnO Nanoparticle-Graphene Core-Shell Structures. *Nanoscale* **2013**, *5* (9), 3664–3667. https://doi.org/10.1039/c3nr00369h.

(93) Yifan Li, 1 Yating Zhang, 1; *Zhiliang Chen, 1; Qingyan Li, 1; Tengteng Li, 1; Mengyao Li, 1; Hongliang Zhao, 1 Quan Sheng, 1; Wei Shi, 1; YAO, A. J.; 1. Ultraviolet-Terahertz Photodetector Based on a Laser-Reduced Graphene Oxide / CsPbBr 3 Composite. *Photonics Res.* **2020**, *8* (8), 1–8.

(94) Zaki, S. E.; Basyooni, M. A.; Shaban, M.; Rabia, M.; Eker, Y. R.; Attia, G. F.; Yilmaz, M.; Ahmed, A. M. Role of Oxygen Vacancies in Vanadium Oxide and Oxygen Functional Groups in Graphene Oxide for Room Temperature CO2 Gas Sensors. *Sensors Actuators, A Phys.* **2019**, *294*, 17–24. https://doi.org/10.1016/j.sna.2019.04.037.

(95) Fan, X.; Elgammal, K.; Smith, A. D.; Östling, M.; Delin, A.; Lemme, M. C.; Niklaus, F. Humidity and

CO2 Gas Sensing Properties of Double-Layer Graphene. *Carbon N. Y.* **2018**, *127*, 576–587. https://doi.org/10.1016/j.carbon.2017.11.038.

(96) Smith, A. D.; Elgammal, K.; Fan, X.; Lemme, M. C.; Delin, A.; Råsander, M.; Bergqvist, L.; Schröder, S.; Fischer, A. C.; Niklaus, F.; Östling, M. Graphene-Based CO2 Sensing and Its Cross-Sensitivity with Humidity. *RSC Adv.* **2017**, *7* (36), 22329–22339. https://doi.org/10.1039/c7ra02821k.

(97) Akhter, F.; Alahi, M. E. E.; Siddiquei, H. R.; Gooneratne, C. P.; Mukhopadhyay, S. C. Graphene Oxide (GO) Coated Impedimetric Gas Sensor for Selective Detection of Carbon Dioxide (CO2) with Temperature and Humidity Compensation. *IEEE Sens. J.* **2021**, *21* (4), 4241–4249. https://doi.org/10.1109/JSEN.2020.3035795.

(98) Yu, C. H.; Huang, C. H.; Tan, C. S. A Review of CO2 Capture by Absorption and Adsorption. *Aerosol Air Qual. Res.* **2012**, *12* (5), 745–769. https://doi.org/10.4209/aaqr.2012.05.0132.

Chapter 2

Synthesis and Characterization of Large Lateral-size Graphene Oxide and its Derivative Materials

In this **chapter**, we have focused on synthesizing large lateral-size graphene oxide (GO) and its derivative materials (reduced graphene oxide (RGO) and graphene quantum dots (GQDs)). Graphite oxide was synthesized using the simplified Hummers method. The large lateral size of the GO sheet can be obtained by changing the process steps of Hummers method, which are discussed in this chapter. We have compared the two exfoliation techniques for obtaining GO from graphite oxide: sonication and a mild heating technique. In these, a mild-heating technique is our proposed technique that can exfoliate the large flake size of the GO sheets. We have characterized and analyzed GO exfoliated from the bath sonicated GO and mild-heating GO, showing the advantage of mild-heating GO. The synthesis of RGO is obtained from the reduction of oxygen functional groups from the GO. Various characterizations such as FESEM, XRD, and Raman are analyzed for large lateral size GO, oxidation of GO, reduction of functional groups from RGO, etc. Finally, GQDs are synthesized from GO using a two-step process: hydrothermal and Tip-sonication methods. The optimization of the size distribution of GQDs by exposing various duration of ultrasonic signals on the GQDs is studied. The successful synthesis of the GQDs is confirmed by the FETEM, XRD, Raman, and PL.

2.1. Introduction

Since the discovery of graphene[1], immense efforts have been focused on GO since it is the most promising precursor for obtaining large quantities of this unique material. GO can be visualized as individual sheets of graphene decorated with oxygen functional groups on both basal planes and edges, prepared by oxidative exfoliation of graphite. The presence of oxygen makes GO amenable to chemical functionalization; however, it extends the sp^2 network of the graphene hexagonal lattice[2]. To convert GO back to graphene, the chemical[3]/thermal reduction[4] of GO is the most attractive procedure because of its simplicity, reliability, high yield, and low cost. Chemical treatment, especially exposure to hydrazine, is the most widely used route to reduce GO in solution. Hydrazine treatment leads to the formation of nitrogen-functional groups and hydrazine's inherent toxicity.

It is a low-temperature deoxygenating process but not completely effective in reducing GO. This process is amenable to electronic applications of graphene patterned onto glass or plastic substrates. Finally, a wide range of functional hybrids is synthesized for polymer composites, biosensors, gas sensors, photodetectors, and conversion technologies. There is very little knowledge on how the oxygen content of graphene oxide evolves during thermal reduction. Theoretical and experimental studies have shown the formation of thermodynamically stable carbonyl and ether groups by transforming the initial nearby hydroxyl and epoxy groups during thermal annealing. Still, little is known about the survival of the persistent residual oxygen groups.

Further, GQD is a zero-dimensional (0D) carbon material; it has large edge defects sites and a low oxygen-containing functional group. It has a lateral diameter of less than ~10 nm with a few numbers of stacking layers known as quantum dots. The edge defects are more active than the basal plane of carbon atoms; quantum dots has more edge defect sites due to the smaller lateral size. The edge defect and a few functional groups could be used as the trapping sites for various applications such as dye detection[5], sensor[6], bio-sensing[7] etc.. Other advantages of the GQD are cheap source material, water used as a solvent, a simple synthesis process, no toxicity, etc. Due to the extreme expediency of the GQDs, we have synthesized the size-controllable GQDs using the simple method known as the hydrothermal method and further insisting on the tip-sonication technique to reduce the average size of the GQDs materials. The synthesis details and its characterization will be studied in the following sections.

2.2. Synthesis of grapene oxide and its derivative materials

2.2.1. Synthesis of graphene oxide

Graphite was oxidized to obtain graphite oxide using a simplified Hummers method. A brief synthesis process is explained using each step in **Fig. 2.1**. A 150 ml borosilicate conical flask is placed on the hot plate; 4g of solid $KMnO_4$ is added into the flask and added 0.5g of graphite flakes (supplied from *Asbury Carbon*); mixing the chemicals by shaking the flasks by hand. Surrounded the flask on the ice, poured 100ml of 98% conc. of H_2SO_4 into the flask in drop by drop. This process is an exothermic reaction; extra care is required when adding acids to the $KMnO_4$. The solution is stirred using a glass rod, and a further 0.5g of $NaNO_3$ is added slowly; the solution's temperature is kept at <30 ˚C. After adding all $NaNO_3$, the solution was heated up to 60 ˚C for 14 hours; in between, the solution was stirred by a glass rod. During this

time, the solution became highly viscous and turned dark brown. The reaction flask was then cooled in a block of ice, and ultrapure deionized water (100 mL) was slowly added to the solution, ensuring that the temperature remained below 40 ˚C. Subsequently, the color of the solution is changed from dark brown to black. Still, the oxidation reaction continues in the solution, which is observed from the increased temperature of the solution. The second oxidation process[8] is explained in the previous **section 1.3**. The resulting diluted black mixture was poured into ultrapure deionized water (700 mL) and quenched with 30 % hydrogen peroxide (4 mL), yielding a light-yellow suspension of graphite oxide. The change of light yellow in the solution is shown the stop of chemical reaction in the solution.

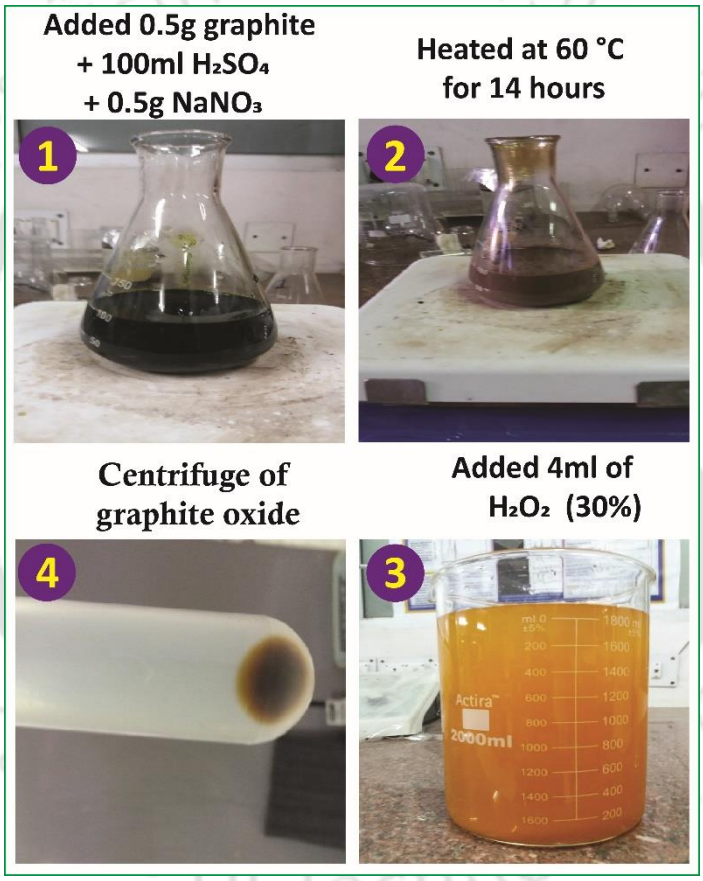

Fig. 2.1: Digital images of products obtained in each steps of the simplified Hummers method.

The residue was allowed to settle overnight. The supernatant liquid was discarded, and fresh de-ionized water was added again and diluted to make up to 2 L. pH was about 1.8. The solution was allowed to settle overnight, and the supernatant liquid was discarded. Approximately 400 mL of the sediment solution was left at the bottom. The sediment solution was taken out for centrifugation (*Legend X1R Centrifuge, Thermo Scientific*) at 9000 rpm for 30 min using 30 mL centrifuge tubes. The supernatant liquid was discarded, and de-ionized

water was added to the tubes (pH was 3.6). The solution was washed several times to attain neutral pH using de-ionized water and filtered using vacuum filtration (grade 1, *Whatman* filter paper). The as-obtained graphitic oxide was dried on the hot plate at 35 °C for 48 h. All Chemicals ($KMnO_4$, H_2SO_4, $NaNO_3$, and H_2O_2) were procured from *Merck*. Finally, graphite oxide is exfoliated into GO sheets using sonication and a mild heating technique.

The synthesized graphite oxide flakes were exfoliated using two techniques; (a) mild-heating technique and (b) ultrasonication. For mild heating exfoliation, 3 mg of graphite oxide was added into a 250 mL beaker containing 100 mL of de-ionized water (*Milli-Q*) and heated at a constant temperature of 80 °C for two hours in a typical environment using a hot plate (*Anitech*). Notably, the separation of smaller flakes was visible. The schematic diagram for exfoliation of GO from graphite oxide using a mild heating technique is shown in **Fig. 2.2.**

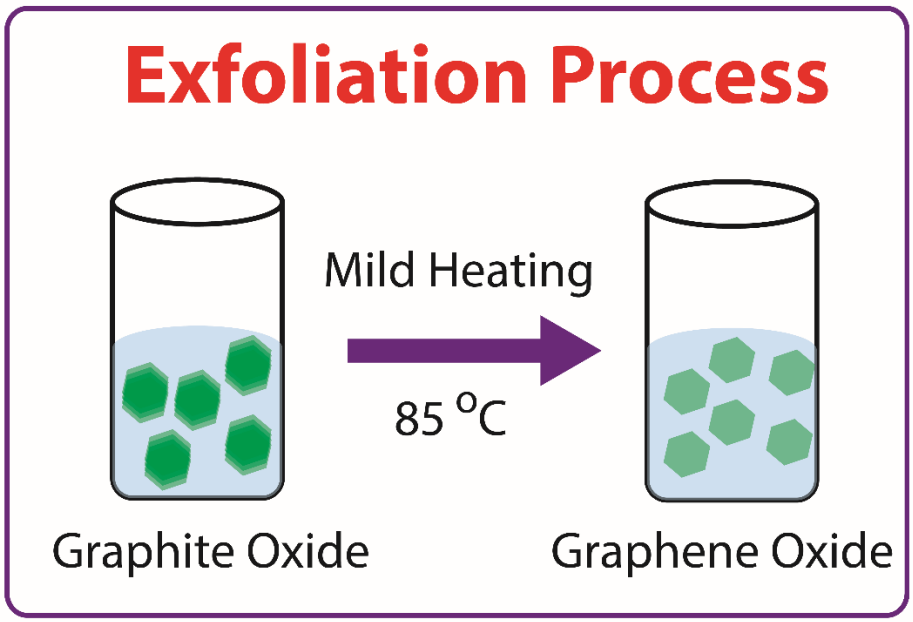

Fig.2.2: Schematic illustration of exfoliation of GO using mild heating technique.

It was cooled down to room temperature. The impurities or dissolved metal ions during the oxidation process are presented in the solution. These impurities are removed from the GO solution using a centrifugation process. The solution was centrifuged at 9000 rpm for 15 minutes, 3000 rpm for 15 minutes, and 300 rpm for 45 minutes. Each step is followed by discarding the supernatant liquid and refilling it with de-ionized water. However, after the last step (300 rpm), the supernatant liquid was used for further characterization and analysis.

Moreover, ultrasonic exfoliation of GO was performed using 3 mg of graphite oxide in a 100 mL beaker containing 50 mL de-ionized water. The solution was sonicated using a conventional water-bath sonicator (*LMUC 2, Labman*) for 15 min at a power of 50 W. After uniform dispersion of GO flakes, it was centrifuged with the same parameters. Similarly, each step is followed by discarding the supernatant liquid and refilling it with de-ionized water. The supernatant liquid was used for further characterization and studies.

2.2.2. Synthesis of reduced graphene oxide (RGO)

RGO was synthesized from the exfoliated GO using hydrazine treatment (chemical reduction process), and thermal treatment. In RGO, the presence of oxygen functional groups on GO sheets are removed, which leads to restoring the graphitic structure of RGO. The hydrazine treatment performed the reduction process of the GO samples, and an illustrated schematic diagram for the reduction process is shown in **Fig. 2.3**. The chemical reactions on the drop-casted GO samples on SiO_2 to retained the original size of GO sheets. The exfoliated GO solution was drop cast onto SiO_2 substrate and dried in a hot air oven (*ICON instrument*) at 85 °C for 5 h. This step is more simplified and easier to obtain the mono-layer RGO as compared to the commonly used methods, like hydrazine treatment in the GO solution then drop-casted on the substrate for further analysis.

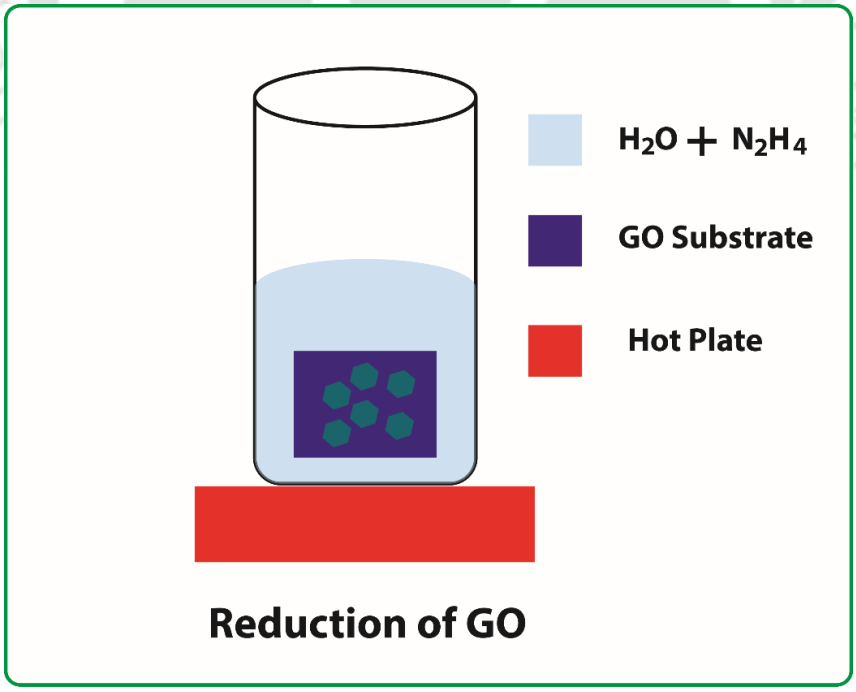

Fig. 2.3: Schematic illustration of the reduction of GO using hydrazine treatment.

The dried substrate was immersed inside a 250 mL beaker containing 10 µl of hydrazine monohydrate in 100 mL de-ionized water, heating at 95 °C for three hours using a hot plate (*Anitech*). This process is performed inside the fume-hood, and extra precautions are required to handle hazardous chemicals (hydrazine). The hydrazine-treated samples are removed from the beaker after being disposed of in the solution. The samples are cleaned with de-ionized water and air-dry the samples for further characterizations.

Thermal treatment is another simplest process to obtain RGO from GO without losing the lateral size of GO sheets; the schematic diagram is shown in **Fig.2.4**. Similarly, the exfoliated GO solution was drop cast onto SiO_2 substrate and dried in a hot air oven at 85 °C for 5 h. The substrates are placed inside the quartz boat and inserted into the quartz tube, which diameter is 2 inches. One size of the quartz tube is closed after inserting samples. A rotary vacuum pump reduces the pressure inside the quartz tube to 2.5×10^{-2} mbar.

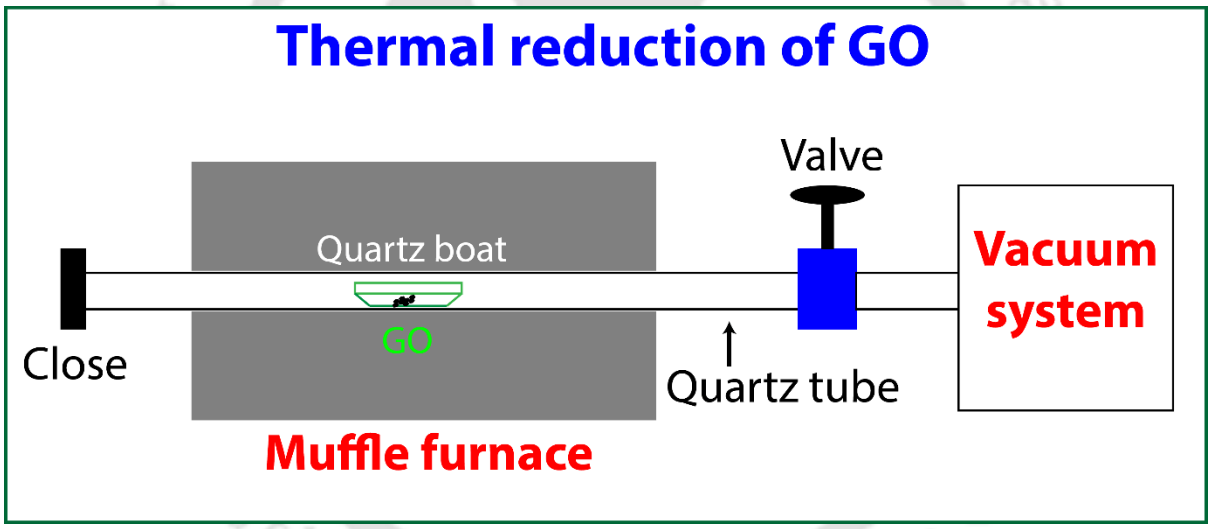

Fig. 2.4: The schematic diagram of thermal treatment on GO to obtain RGO using vacuum annealing.

Subsequently, the muffle furnace's temperature increases at 8 ˚C/min until the set temperature reaches 360 ˚C. The GO samples are exposed to the heat treatment for 3 h. Then, the temperature of the quartz tube is reduced to room temperature at the same rate of 8 ˚C/min. Removed the samples from the quartz tube after shut down the vacuum system. The thermal treatment RGO samples are characterized using FESEM imaging, XRD, and Raman spectroscopy.

2.2.3. Synthesis of graphene quantum dots (GQDs)

The high-quality GQDs are synthesized using the hydrothermal method's optimized parameters. An amount of 3 mg of GO, synthesized using the simplified Hummers method

(explained in **section 2.2.1**), is dispersed into the 50 ml of highly pure de-ionized water in a 100 ml beaker (Borosil). It is sonicated for 30 minutes at 180 watts using a bath-sonicator (Telsonic AG) to uniformly and highly disperse the GO in a water solution. The solution is poured into the Teflon tube of a hydrothermal system (Berghof high-pressure reactor) and sealed the tube air-tight with screws and nuts. The system is heated at 220 ˚C for 36 hours inside the fume hood; the schematic diagram is shown in **Fig. 2.5**. Then, it is cooled down the system at room temperature, and removed the samples from the Teflon tube for further analyses. The first observation changed the dark color GO solution to a semi-transparent solution with small, dark color particles floating after the hydrothermal treatment. The solution analyzed the size of particles using the FETEM image and size distribution method and observed the non-uniformed distribution of various size particles from 40 nm to 3 nm scales, shown in the following **Fig. 2.13a**.

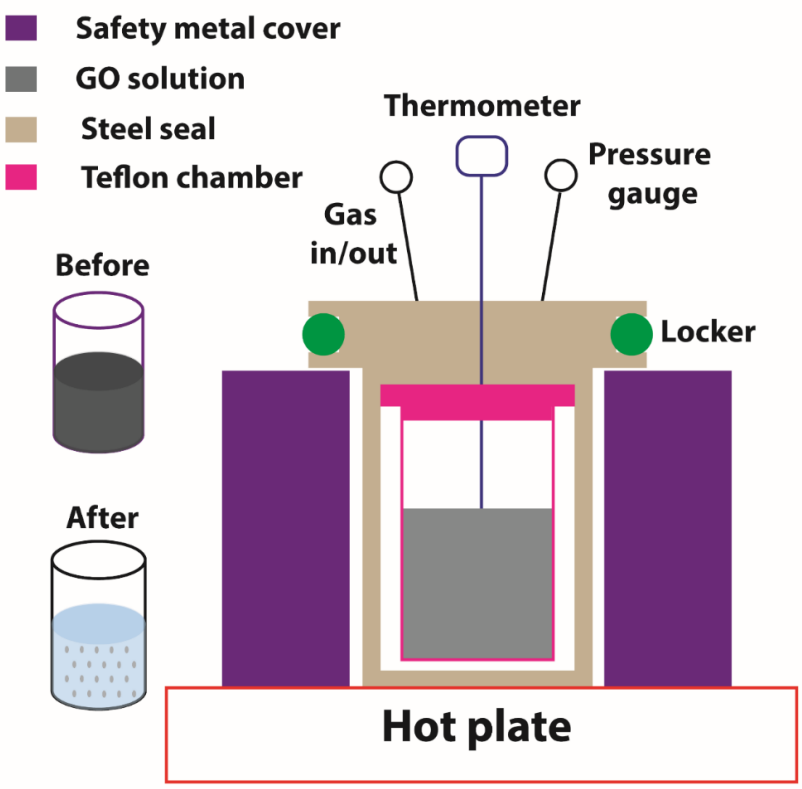

Fig. 2.5: Schematic illustration of synthesis GQDs using hydrothermal process.

Further, the size of the GQDs is reduced by using Tip-sonicator (Sonic ruptor 250) in two different durations (30 and 60 minutes) by applying a constant power (100 watts) and pulse (50%). The solution is transferred into a 50 ml beaker and placed on a sample (beaker) holder in the Tip-sonicator, which is placed inside a soundproof chamber. A 4 mm diameter micro tip is depth into the solution (inside the beaker) up to 70% submerged in the solution. The high-

energy sonic wave is applied into the GQDs solution for 30 minutes by applying two cycles of 15 minutes between 5 minutes of break. Then, 10 ml of the treated solution is removed for analysis of its particle size by using FETEM imaging and size distribution technique.The remaining sample is exposed to another 30 minutes (60 minutes in total) of high-energy sonic waves using a 4 mm micro tip in the same process; the treated sample is analyzed using a FETEM image and its size distribution technique. The tip-sonicator technique is the easiest and simplest method to reduce the particle size to 1.5 nm; however, it is a noisy technique that disturbs the surrounding environments. The large lateral-sized particle was removed using centrifugation at 15000 RPM for 15 minutes, and the residue was discarded.

Further, the temperature of the hydrothermal reactor is controlled by a hotplate (AnTech) which can be heated up to 280 ˚C. The hotplate's temperature is retained and monitored constantly throughout the experiment's completion to achieve reproducible results. Moreover, the Teflon tube is cleaned using de-ionized water for 24 hours at 220 ˚C to remove the residue impurities from the previous experiments. The capacity of the GO solution is less than 50% of the Teflon tube's total capacity to avoid complications and safe the instruments. The characterization of the GQD is done using a FETEM, XRD analysis, Raman analysis, XPS, FTIR, UV absorption spectrum, and PL spectrum.

2.3. Characterization techniques

Microstructural features were studied using a field emission scanning electron microscope (FESEM, *JEOL, JSM-7610F).* The high magnification morphology of GQDs was examined using a field emission transmission electron microscopy (FETEM, *JEOL JEM-2100F*), operated at an accelerating voltage of 200 kV. The thickness and dimension of the sheets were further examined by AFM (*Bruker, Innova series*) in tapping mode. The crystalline nature and the interlayer spacing of graphite, GO, and RGO were studied from X-ray diffraction (XRD), *Rigaku RINT 2500 TTRAX-III*, using CuKα radiation. The functional groups on the basal plane and edge of GO and RGO were analyzed by Raman spectrometer (*Horiba Jobin, LabRam HR*). Before the measurement, the samples drop-cast onto a Si substrate were focused using a 100X optical microscope with a spatial resolution of ~1 μm. A 532 nm laser was used to excite the sample.

Fourier transforms infrared (FTIR) spectroscopy (*Perkin Elmer, Spectrum BX)* was used to analyze the functional groups of GO and RGO. Sample preparation involved mixing graphene-based materials and KBr powder, and thin circular pellets were made using the KBr pellet machine. X-ray photoelectron spectroscopy (XPS) analysis was performed using an XPS

microprobe (*PHI X-tool, ULVAC-PHI INC.*) with Al Kα as an X-ray source at 20 kV and 54 W. Commercial UV-visible spectrophotometers (*Shimadzu, UV3101PC)* were used to obtain the UV-visible absorption spectra. Photoluminescence measurement was conducted using a commercial fluorimeter (*Fluromax-4, Horiba)* with a Xenon lamp source. GO, and RGO samples were excited at 360 nm wavelength.

2.4. Results and discussions

2.4.1. Morphological and microstructural

The morphology of the exfoliated GO sheet using sonication and mild heating is shown in **Fig. 2.6**. This analysis focuses on the lateral size of the GO sheets obtained using the mentioned two techniques. In **Fig. 2.6a**, the GO sheet is observed, which only has a lateral size of up to 10 µm. Moreover, the GO sheet is rested on the SiO_2/ Si substrate with numerous wrinkles and folded shapes[9].

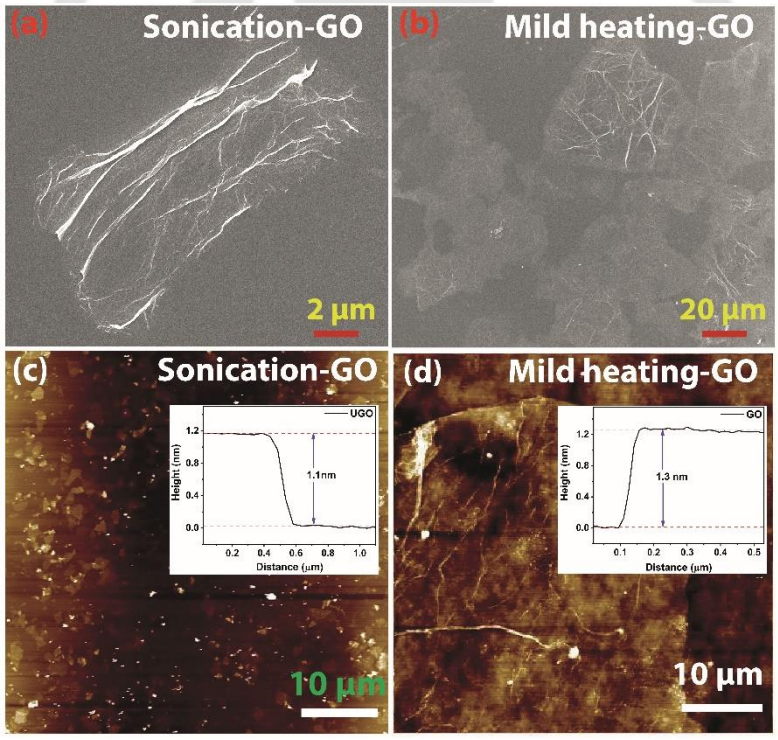

Fig. 2.6: FESEM image of GO sheet exfoliated from (a) bath-sonication; (b) mild heating; AFM images (inset: AFM height profiles) of GO obtained from (c) bath-sonication; and (d) mild heating.

In **Fig. 2.6(b)**, the GO sheets are spread across the substrate by overlapping; the large lateral size GO sheets were exfoliated from the mild heating technique. Most of the GO sheets obtained their lateral size up to 80 µm, and the lateral size of the GO sheets is varied. Similarly, wrinkles are observed on this GO. The AFM image of sonicated GO, and mild heating GO are shown in **Fig. 2.6c** and **Fig. 2.6d**, respectively. The extensive distribution of small sheets is

observed in the sonicated GO, whereas a part of the GO sheet is observed in the mild heating-based exfoliation GO. Therefore, the particle size of the GO is significantly reduced after bath-sonication; this technique can exfoliate the GO sheets from graphite oxide and break down the GO sheets into small pieces. The thickness of the ultrasonicated-GO (**Fig. 2.5c (inset)**) and mild heating-GO (**Fig. 2.5d (inset)**) are measured using the height profile of the AFM data and obtained at 1.1 nm and 1.3 nm, respectively. The thickness variation may be due to oxygen functional groups attached to it. Moreover, mild heating is the simplest technique to exfoliate the large lateral size GO without reducing their sizes.

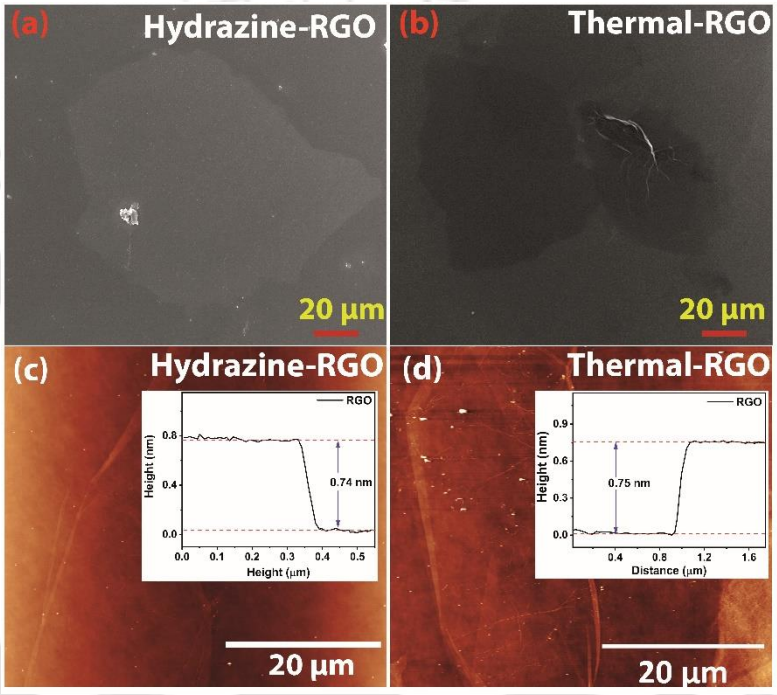

Fig. 2.7: FESEM image of RGO obtained from (a) chemical treatment; (b) thermal treatment; AFM image of RGO (inset: height profile) achieved from (c) chemical and (d) thermal treatment.

The FESEM and AFM images of chemically and thermally obtained RGO are shown in **Fig. 2.7**. The large lateral size GO sheets obtained from the mild heating technique are used to synthesize the RGO from both the reduction treatments. In **Fig. 2.7a**, RGO has observed a large lateral size up to 100 µm after chemical treatment for three hours at 95 ˚C. Small bright spots on the samples, which may be the dust particle, fall during the characterizations. Similarly, the large lateral size of RGO sheets is detected after thermal treatment (**Fig. 2.7b**). The AFM images of RGO sheets from chemical treatment (**Fig.2.7c**) and thermal treatment (**Fig.2.7d**) confirmed the large lateral size of RGO. The thickness of the chemical treatment RGO (**Fig.2.7c (inset)**) and thermal treatment RGO (**Fig.2.7d(inset)**) are 0.74 nm and 0.75 nm,

respectively. Hence, mild heating-based exfoliation of GO will be used for various applications which are required a large surface area of GO. Furthermore, thermally produced RGO will be a suitable method compared to chemically reduced RGO due to the less hazard, generation of toxic fumes, unwanted contaminations, etc.

The mechanism for the mild temperature exfoliation is presented in **Fig. 2.8**. It is proposed that the water molecules gain kinetic energy owing to the gradual heat supply, which facilitates entering and adsorbing or intercalating between GO layers. The entrance of the intercalating molecules could orient towards the electrostatic interaction with the opposite charge of the oxygen attached as a functional group onto the basal GO plane and edge sites, thereby weakening the $\pi - \pi$ interlinkage between the layers, which eventually decreases the van der Waal forces between the layers. On attaining sufficient heat energy, the intercalated molecules forming hydrogen bonding with the oxygen-containing functional group enhance susceptibility to exfoliate large lateral size sheets due to reduced van der Waal force between the two layers of GO as compared to graphite.

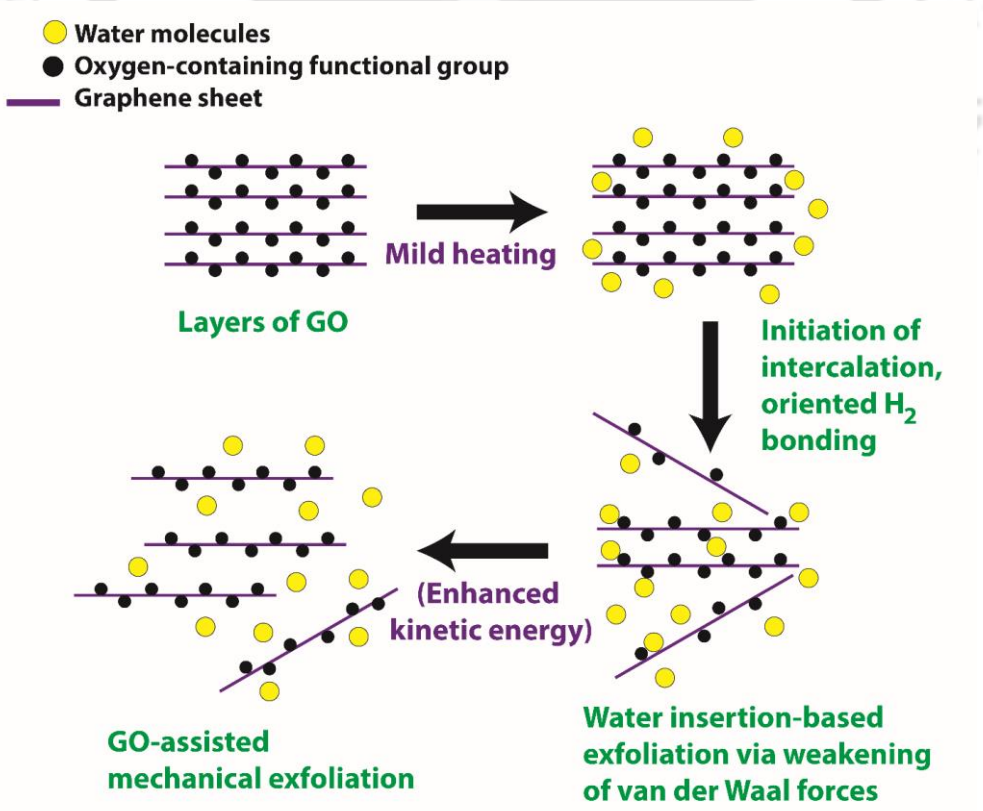

Fig. 2.8: Proposed mechanism for the mild heating and mechanical-assisted exfoliation of GO.

Besides, exfoliated GO could also augment further exfoliation for other thicker flakes, as evidenced from physical observation during the process wherein fragmented thinner flakes

rise on gaining kinetic energy and subsequently strike other thicker flakes. This GO mediated-exfoliation occurs mechanically, arising from temperature-assisted momentum. Chong et al.[3] reported on the GO-assisted mechanical exfoliation of graphite using the hydrothermal method. However, we adopted the ambient pressure mild heating condition without using high-temperature and high-pressure autoclave reactions. Hence, the present simplified exfoliation technique could be a combination of mild temperature heating, augmenting the intercalation between GO layers, and the fragmented GO-mediated mild mechanical exfoliation.

Stankovich et al.[10] have well explained the deoxygenation of GO by hydrazine treatment. GO contains mostly hydroxyl or epoxide of oxygen functional groups, lactones, anhydrides, and quinones[11–13]. The epoxide-containing GO has reacted with hydrazine and formed hydrazino alcohols[14]. Further, the bi-product of the solution is diazene, water, and reduced oxygen functional groups GO (RGO). Thus, hydrazine treatment reduced the oxygen functional groups of GO to form RGO. However, hydrazine is a toxic and expositive chemical[15].

2.4.2. Structural analysis of graphene oxide and reduced graphene oxide

The structural properties of the GO and RGO is analysed using the **Fig. 2.9** and **Fig. 2.10.**

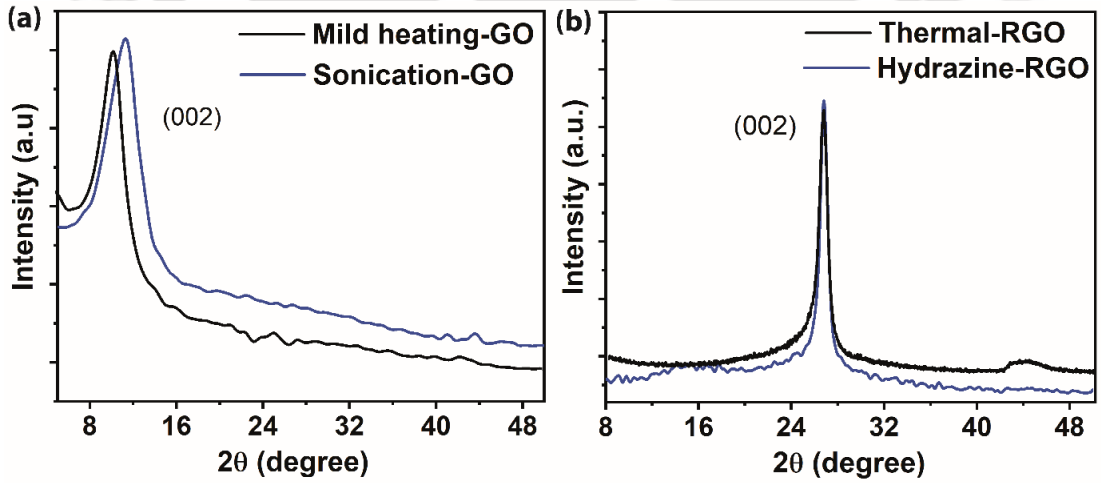

Fig. 2.9: Comparative XRD pattern of (a) exfoliated GO from mild heating and sonication, (b) RGO obtained from thermal treatment and hydrazine treatment.

In **Fig. 2.9a**, a prominent diffraction peak of (002) plane for the GO exfoliated by using mild heating and sonication are persuaded at 2θ peak of 10.4˚ and 11.4˚ for, respectively. The shifting of the peak position from the original graphite peak centred at 26.5˚ to 10.4˚ and 11.4˚ shows the oxidation of graphite or formation of graphite oxide[16]. The interplanar/lattice spacing

for mild heating GO and sonicated GO, calculated using Bragg's law ($n\lambda=2d\sin\theta$), are 0.85 nm and 0.78 nm, respectively. The observed peak is from the reflection of the basal plane (0 0 2), which is the characteristic of π—π stacking of the graphite layers[17]. More shifting of the peak position towards the left (lower) or increased lattice spacing indicates a higher degree of oxidation occurs on the graphite flakes. This shift is due to the intercalation of oxygen functional groups on the graphitic structure[18,19]. The new shifted XRD pattern infers that the long-range periodicity and orderliness are modified along the c-axis[8] due to distorted intrinsic structure and defects created during the oxidation. Furthermore, the peak becomes broader owing to the decrease in crystallite size, according to the Scherrer equation, which defines the crystallite size as the reciprocal of the full width at half maximum.

Whereas, after reducing oxygen functional groups from the GO using chemical and thermal treatment, the position of the 2θ peak for RGO is shifted to 26.5˚, shown in **Fig. 2.9b**. The interplanar spacing is reduced to 0.335 nm after the removing oxygen functional groups. Interestingly, the peak position of the RGO synthesized from the chemical and thermal treatments is the same at 26.5˚; it is shown that both processes can reduce the oxygen functional groups from the GO. A hump peak at 45˚ is observed in the thermally reduced RGO, which is related to the (102) plane of RGO structure[18]. It is worthy to note that although the peak position in RGO changes towards a higher 2θ, the broadness of the peak does not change significantly compared to GO, suggesting that the sheet sizes do not vary substantially. However, the restoration of the sp^2 carbon skeleton occurs in RGO.

The Raman spectroscopy analysis of GO and RGO are studied in **Fig. 2.10**. In **Fig. 2.10a**, the Raman spectra of the GO obtained from mild heating and sonication are analyzed; two prominent bands for D and G[20] are observed at 1350 cm^{-1} and 1600 cm^{-1}. G-band is due to the in-plane lattice vibration of sp^2 carbon atoms, mainly arising from E_{2g} phonon at the Brillouin zone centre. The increase in intensity for D-band in GO compared to graphite is attributed to oxidation-induced distortion of the continuous sp^2 plane. There is a slight shift of the G-band towards the higher side owing to the stress formed by bonding with the functional group during the oxidation process. D band is related to the presence of oxygen functional groups, structural defects, disorder, and presence of sp^3 carbon atoms[21] etc. In contrast, the G band results from sp^2 carbon atoms, the signature peak for the graphitic structure[22]. The structural defects of the GO can be calculated by using I_D/I_G[23]; the I_D/I_G of the GO and UGO are 1.6 and 0.9. As correlated to XRD analysis, mild heating-GO has a higher degree of oxidation which changes the structural properties of GO as compared to the sonicated GO.

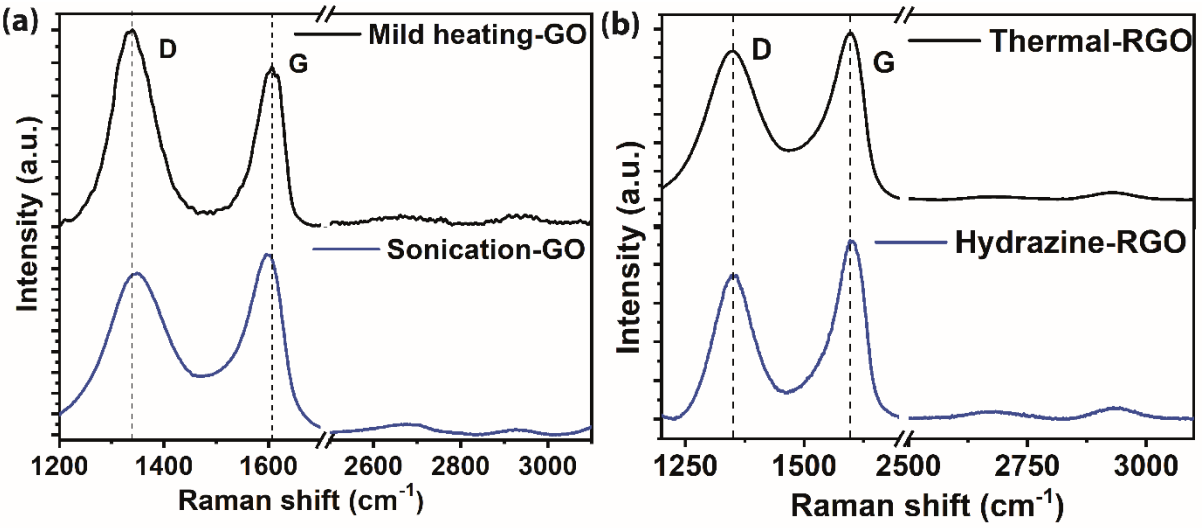

Fig. 2.10: Raman analysis of (a) exfoliated GO using mild heating and sonication; (b) RGO synthesised from thermal and hydrazine treatment.

Further, the Raman spectra of the RGO synthesized from thermal and hydrazine are shown in **Fig. 2.10b**. Similarly, the D and G bands appear in the RGO; the presence of the D band may be due to the donation of structural defects after removing oxygen functional groups from the graphitic structure[2,24,25]. The intensity ratio I_D/I_G measures the degree of defects in graphene materials; I_D/I_G of the thermally and chemically reduced RGO are 0.8 and 0.7, respectively. The detailed study of the presence of oxygen functional groups and structural defects is demonstrated in the following **chapters 3** and **4**.

2.4.3. Optimization of graphene quantum dots size

The size and uniformity of the GQDs are important parameters for determining the quality of the GQDs, and their analysis is shown in **Fig. 2.11**. The mean particle sizes synthesized from the hydrothermal method are obtained at 15.7 nm, which is acquired from data analysis and extraction using the ImageJ and further fitted by log-normal. From **Fig. 2.11a**, the size of the GQDs particles are dispersed non-uniformly and varied sizes downwards from 40 nm, which is observed from the FETEM imaging. The average particle size of the GQDs is reduced to 3.2 nm after high energy sonicated using the tip-sonicator for 30 minutes (**Fig. 2.11b**). In this process, the uniformity of the size distribution is improved to 3.2 nm by removing the bigger particles using the centrifugation technique. The FETEM imaging of the particles is done on the supernatant particles of the GQDs after centrifuging at 15000 RMP for 15 minutes at 3 ˚C. Further, the average size of the GQDs particles (**Fig. 2.11c**) is reduced up to 1.53 nm by sonicating the solution for another 30 minutes upon the previous sample. The fringe width is

0.25 nm in the high-resolution TEM (HRTEM) of GQDs after 60 minutes of sonication, shown in **Fig. 2.11c**, and the size distribution is uniformly dispersed across the substrate.

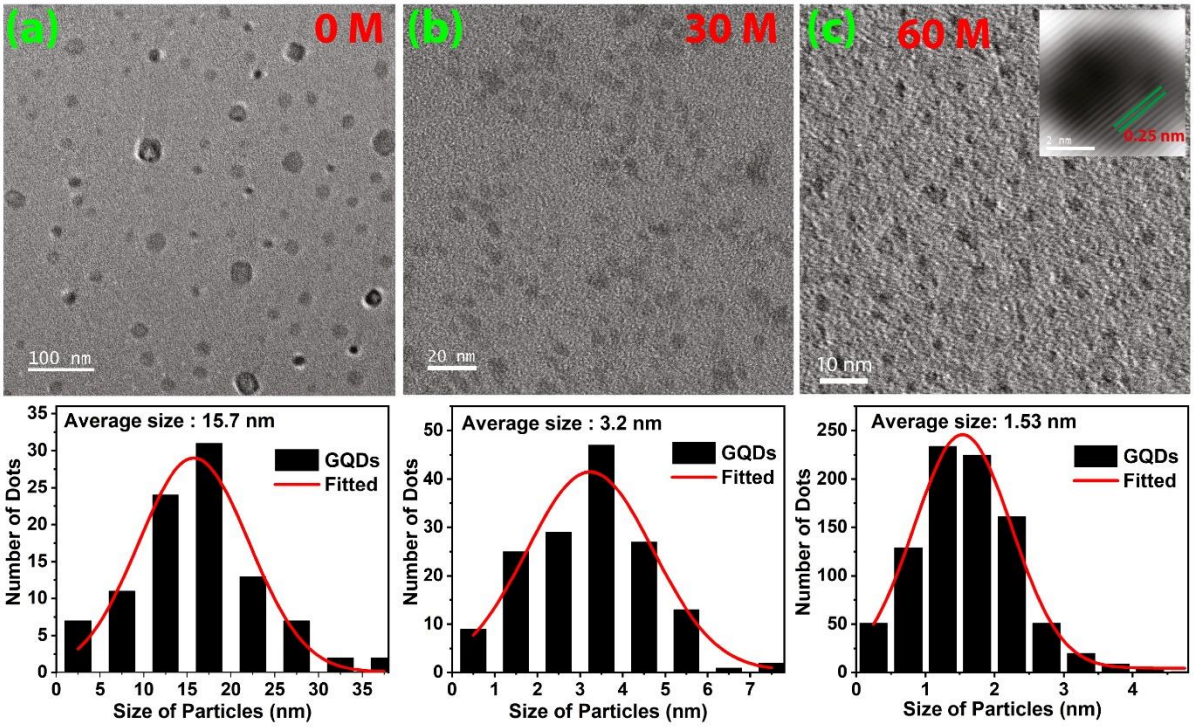

Fig. 2.11: Surface morphology of GQDs: (a) as synthesized; (b) after 30 minutes of tip sonicated (HRTEM image: inset); and (c) after 60 minutes of tip sonicated with respected size distribution as below the figures, respectively.

2.4.4. Structural analysis of graphene quantum dots

The structure of the optimized GQDs is analyzed using XRD and Raman spectroscopy which is shown in **Fig. 2.12**. The XRD analysis of GQDs obtained a prominent broad peak at 22˚, which is expected and shown in **Fig. 2.12a**; the shifting of peak position from the 11.4˚ of GO to 22˚ is due to the removal of oxygen functional groups during the hydrothermal process. Moreover, the peaking board may be due to the polycrystalline nature of the GQDs. The Raman spectra of the GQDs are shown in **Fig. 2.12b-d**; the signature peaks of the GQDs are D band, G band, 2D, D+G, and 2G peaks whereas, D and G bands are observed in the GO[26]. The Raman spectrum of the GQDs is measured from 1200 cm^{-1} to 3300 cm^{-1} to acquire detailed information on GQD. The D band centered at 1350 cm^{-1} is obtained due to structural defects and a small percentage of stable oxygen functional groups, which will be discussed later.

The G band centered at 1596 cm^{-1} is attributed to sp^2 hybridized carbon atoms stretching. The blue shift of its peak position towards the pristine peak position at 1589 cm^{-1} shows the returning of a graphitic structure after high oxidization. The detailed study of the G and D band

for Raman spectra of GQDs is fitted with five Gaussian peaks. Interestingly, another three peaks such as 2D, D+G, and 2G peaks, emerged in GQDs, centered at 2676 cm^{-1}, 2926 cm^{-1}, and 3202 cm^{-1}; these correspond to the combination modes or overtones[26]. Lastly, the structural analysis of the XRD and Raman spectra of GQDs concluded the restoration of sp^2 hybridized carbon bonds (graphitic structure) after distortion into sp^3 carbon bonds during the oxidation process in GO synthesis.

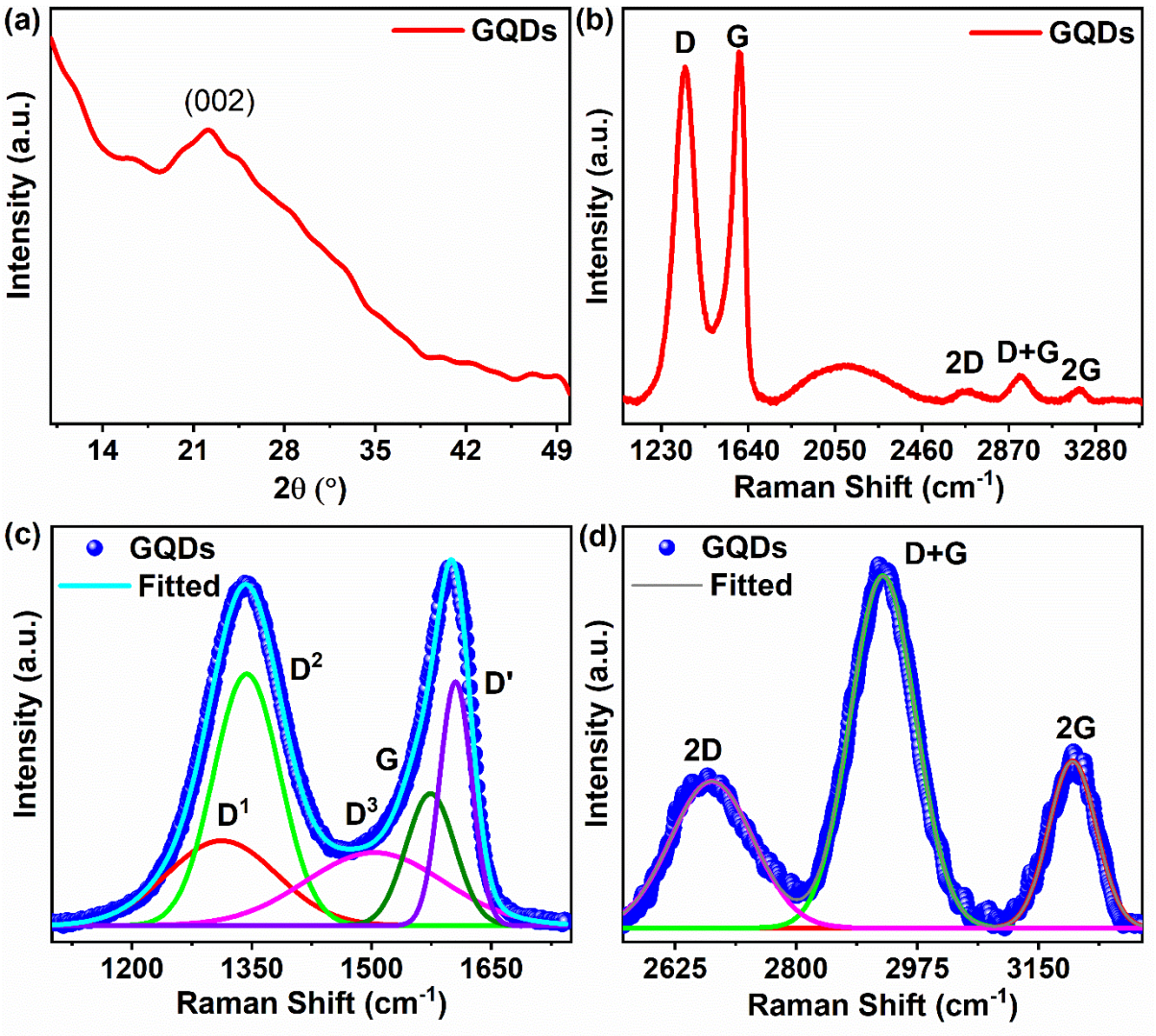

Fig. 2.12: Structural analysis of GQDs using (a) XRD; (b) Raman; (c) Fitted of D and G bands; and (d) analysis of 2D, D+G, and 2G peaks.

2.4.5. XPS and FTIR analysis of graphene quantum dots

The elemental composition of the GQDs is analyzed using XPS and FTIR spectra shown in **Fig. 2.13**. In **Fig. 2.13a**, the XPS spectra are measured from 295 eV to 280 eV, which corresponds to C1s, and 545 eV to 520 eV, which corresponds to O1s. Similar to the reported data5, the intensity of the C1s is much lower than the O1s. The C1s peak of the GQDs is

detailed from 280 eV to 290 eV, and the peak is de-convoluted with three Gaussian peaks centered at 283.4 eV, 285 eV, and 287.2 eV. The prominent peak at 283.4 eV of the sp^2 hybridized carbon-carbon bonds is dominated in the C1s peaks. Further, the peaks corresponding to the C-O and C=O are presented in the GQDs, which are highly stable oxygen functional groups attached to the basal plane of carbon atoms.

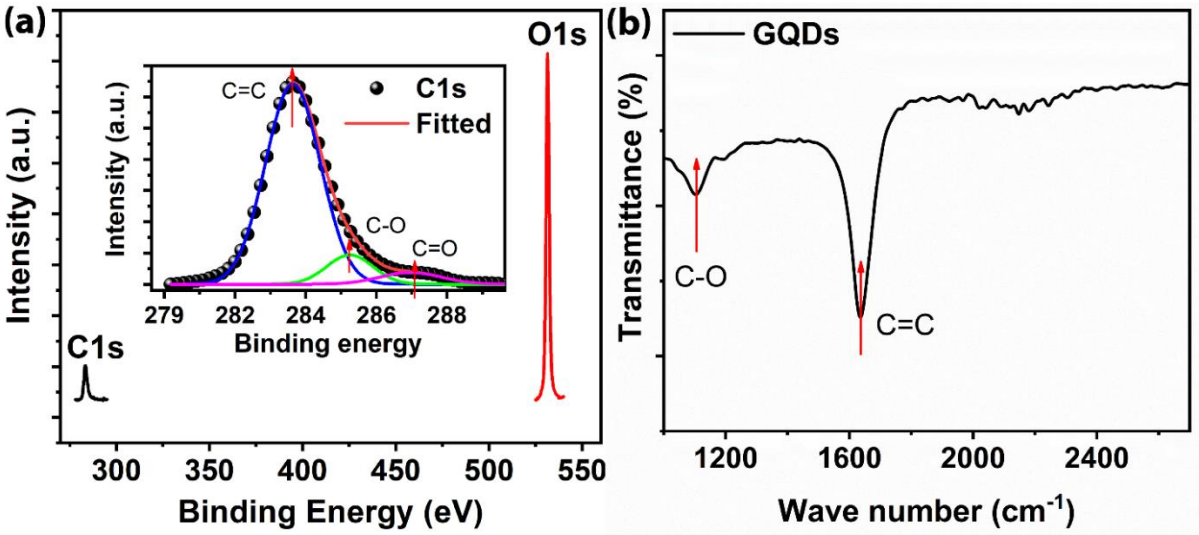

Fig. 2.13: (a) XPS spectrum of GQDs, the inset shows the fitted of C1s spectrum; and (b) FTIR spectrum of GQDs.

Since the GQDs are synthesized from the highly functionalized oxygen functional groups of GO, the presence of tiny oxygen functional groups in GQDs is expected and observed in other reported results[27].

Similarly, the presence of minimal oxygen functional in GQDs is analyzed using FTIR, a fast, simple, and most commonly used characterization technique. The FTIR spectroscopy measured the GQDs dispersed in the de-ionized water and observed two prominent peaks at 1153 cm^{-1} and 1630 cm^{-1} corresponded to the C-O and C=C (sp^2), respectively, which is shown in **Fig. 2.13b**. Unlike the GO/RGO spectra of FTIR, only two peaks are observed in the GQDs, showing that the presence of functional groups is extremely reduced in GQDs, and restoration of the sp^2 hybridized carbon is restored atoms after hydrothermal treatment at 220 ˚C. Finally, the elemental composition of the GQDs is analyzed by using XPS and FTIR spectra, confirming the heavily reduced oxygen functional groups in GQDs, and identifying the elemental structures.

2.4.6. UV absorption and PL analysis of graphene quantum dots

The optical properties of the GQDs are unique to other derivatives of graphene materials such as GO and RGO due to the change of structural arrangement and quantum confinement effect. In **Fig. 2.14a**, the UV absorbance of the GQDs spectra is shown, and the spectrum is measured from 200 nm to 330 nm. The two prominent peaks are perceived at 230 nm and 275 nm, which are corresponded to the π–π* and π–n, respectively[7]. The UV absorbance peak for the GQDs may be due to a high degree of daggling bonds at the edge/ more structural defects at the edge after reducing its size. The hydrothermal method reduced the size and created more defects in the edges, which helped trap the external molecules or charge transfer with foreign particles. The corresponding peak of π–n is shifted from 330nm to 275 nm for the GO/RGO to GQDs. Furthermore, the corresponding peak of π– π* of GQDs is swollen compared to the RGO peak.

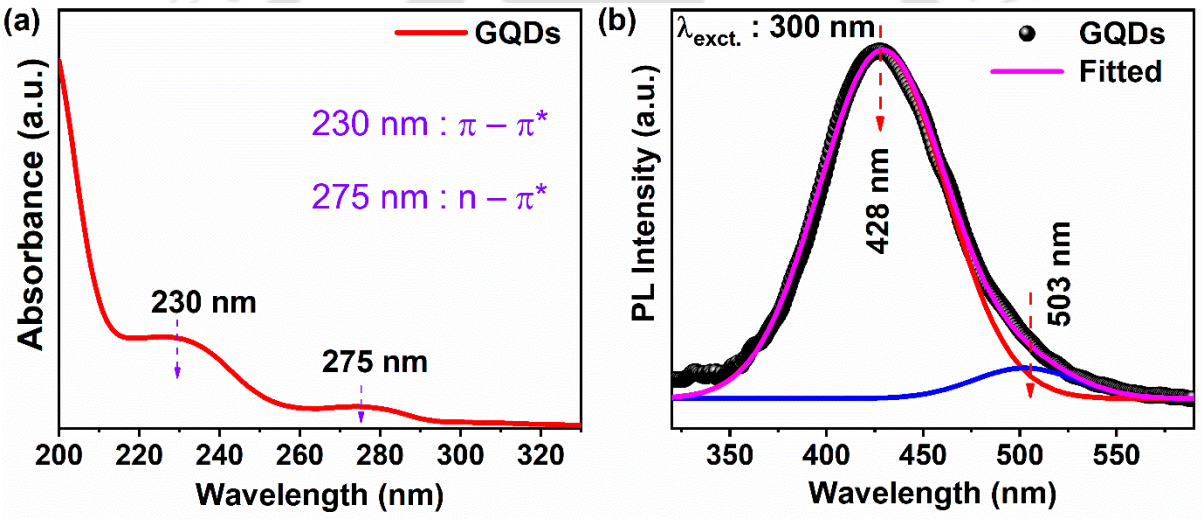

Fig. 2.14: (a) UV absorption spectrum and (b) PL spectrum of GQDs fitted with two peaks.

In **Fig. 2.14b**, the PL spectrum of the GQDs is measured from 330 nm to 600 nm by exposing the excitation wavelength of 300 nm from a laser power source to the GQDs solution. The PL spectrum of the GQDs is de-convoluted with two peaks centered at 428 nm and 503 nm[27,28]. The blue emission (428 nm) is a prominent peak, generated from the intrinsic state emission consisting of quantum confinement of electrons inside the pi-conjugated C domains, electron-hole recombination, and zig-zag edge effect. In contrast, the 503 nm peak may be exhibited by the presence of highly stable oxygen functional groups retained in the GQDs. The PL spectra of GQDs are more significant than RGO due to defects at the edge and quantum confinement effect. The synthesized GQD contains the minimal oxygen functional groups, which contribution is negligible to the PL peak. The main contributor to the PL peak in GO is

obtained from the attached oxygen functional groups. The PL intensity of RGO is suppressed due to the removal of oxygen functional groups; however, GQDs attained PL peak due to the structural defects at the edges and quantum confinement effect. From the UV absorption and PL analysis of GQDs, the optical properties of the GO and its derivative materials are changed/ varied based on the arrangement of the graphitic configurations.

2.5. Conclusion

Graphite oxide is synthesized using the simplified Hummers method; we have omitted continuous stirring of solution during the oxidation process, which leads to breaking the graphite oxide into small pieces. We have oxidized the graphite flakes to a high degree of oxidation, which is visually confirmed by the change of solution color into dark brown and later light yellow. Further, it is confirmed from the XRD and Raman analysis of GO. We have demonstrated a cost-effective and facile approach using mild heating to exfoliate graphene oxide (GO) sheets with ultra-large lateral sizes up to 104 μm using a simplified technique, superior to the commonly used ultrasonic method. Ultrasonication of GO breaks the GO sheets apart from exfoliation, leading to reduced flake sizes observed from the FESEM and AFM image. Subsequently, the reduction of GO sheets was carried out to obtain graphene sheets (RGO) with fewer defects as indicated by the I_D/I_G ration from Raman analysis. The highly uniformed and small size distribution of the GQDs after 60 minutes of tip-sonication is validated from the FETEM imaging and its size distribution analysis. Further, the structure of GQDs is analyzed using XRD and Raman spectroscopy. Thus, we successfully synthesized high-quality, super large lateral size GO sheets of thickness ~1.3 nm and its derivative materials such as RGO and GQDs.

Reference

(1) Geim, A. K.; Novoselov, K. S. The Rise of Graphene. *Nat. Mater.* **2007**, *6* (3), 183–191. https://doi.org/10.1038/nmat1849.

(2) Pei, S.; Cheng, H. M. The Reduction of Graphene Oxide. *Carbon N. Y.* **2012**, *50* (9), 3210–3228. https://doi.org/10.1016/j.carbon.2011.11.010.

(3) Lonkar, S. P.; Deshmukh, Y. S.; Abdala, A. A. Recent Advances in Chemical Modifications of Graphene. *Nano Res.* **2015**, *8* (4), 1039–1074. https://doi.org/10.1007/s12274-014-0622-9.

(4) Acik, M.; Chabal, Y. J. A Review on Reducing Graphene Oxide for Band Gap Engineering. *J. Mater. Sci. Res.* **2012**, *2* (1), 101–112. https://doi.org/10.5539/jmsr.v2n1p101.

(5) Das, R.; Parveen, S.; Bora, A.; Giri, P. K. Origin of High Photoluminescence Yield and High SERS Sensitivity of Nitrogen-Doped Graphene Quantum Dots. *Carbon N. Y.* **2020**, *160*, 273–286. https://doi.org/10.1016/j.carbon.2020.01.030.

(6) Li, M.; Chen, T.; Gooding, J. J.; Liu, J. Review of Carbon and Graphene Quantum Dots for Sensing. *ACS Sensors* **2019**, *4* (7), 1732–1748. https://doi.org/10.1021/acssensors.9b00514.

(7) Chen, W.; Lv, G.; Hu, W.; Li, D.; Chen, S.; Dai, Z. Synthesis and Applications of Graphene Quantum Dots: A Review. *Nanotechnol. Rev.* **2018**, *7* (2), 157–185. https://doi.org/10.1515/ntrev-2017-0199.

(8) Kang, J. H.; Kim, T.; Choi, J.; Park, J.; Kim, Y. S.; Chang, M. S.; Jung, H.; Park, K. T.; Yang, S. J.; Park, C. R. Hidden Second Oxidation Step of Hummers Method. *Chem. Mater.* **2016**, *28* (3), 756–764. https://doi.org/10.1021/acs.chemmater.5b03700.

(9) Saafi, M.; Tang, L.; Fung, J.; Rahman, M.; Sillars, F.; Liggat, J.; Zhou, X. Graphene/Fly Ash Geopolymeric Composites as Self-Sensing Structural Materials. *Smart Mater. Struct.* **2014**, *23* (6). https://doi.org/10.1088/0964-1726/23/6/065006.

(10) Stankovich, S.; Dikin, D. A.; Piner, R. D.; Kohlhaas, K. A.; Kleinhammes, A.; Jia, Y.; Wu, Y.; Nguyen, S. T.; Ruoff, R. S. Synthesis of Graphene-Based Nanosheets via Chemical Reduction of Exfoliated Graphite Oxide. *Carbon N. Y.* **2007**, *45* (7), 1558–1565. https://doi.org/https://doi.org/10.1016/j.carbon.2007.02.034.

(11) He, H.; Riedl, T.; Lerf, A.; Klinowski, J. Solid-State NMR Studies of the Structure of Graphite Oxide. *J. Phys. Chem.* **1996**, *100* (51), 19954–19958. https://doi.org/10.1021/jp961563t.

(12) He, H.; Klinowski, J.; Forster, M.; Lerf, A. A New Structural Model for Graphite Oxide. *Chem. Phys. Lett.* **1998**, *287* (1–2), 53–56. https://doi.org/10.1016/S0009-2614(98)00144-4.

(13) Lerf, A.; He, H.; Forster, M.; Klinowski, J. Structure of Graphite Oxide Revisited. *J. Phys. Chem. B* **1998**, *102* (23), 4477–4482. https://doi.org/10.1021/jp9731821.

(14) Lázár, L.; Szakonyi, Z.; Forró, E.; Palkó, M.; Zalán, Z.; Szatmári, I.; Fülöp, F. [Synthesis of hydrazino alcohols with anti-inflammatory activity]. *Acta Pharm. Hung.* **2004**, *74* (1), 11–18.

(15) Fernández-Merino, M. J.; Guardia, L.; Paredes, J. I.; Villar-Rodil, S.; Solís-Fernández, P.; Martínez-Alonso, A.; Tascón, J. M. D. Vitamin C Is an Ideal Substitute for Hydrazine in the Reduction of Graphene Oxide Suspensions. *J. Phys. Chem. C* **2010**, *114* (14), 6426–6432. https://doi.org/10.1021/jp100603h.

(16) Dash, P.; Dash, T.; Rout, T. K.; Sahu, A. K.; Biswal, S. K.; Mishra, B. K. Preparation of Graphene Oxide by Dry Planetary Ball Milling Process from Natural Graphite. *RSC Adv.* **2016**, *6* (15), 12657–12668. https://doi.org/10.1039/c5ra26491j.

(17) Deemer, E. M.; Paul, P. K.; Manciu, F. S.; Botez, C. E.; Hodges, D. R.; Landis, Z.; Akter, T.; Castro, E.; Chianelli, R. R. Consequence of Oxidation Method on Graphene Oxide Produced with Different Size Graphite Precursors. *Mater. Sci. Eng. B Solid-State Mater. Adv. Technol.* **2017**, *224* (March 2019), 150–157. https://doi.org/10.1016/j.mseb.2017.07.018.

(18) Gupta, B.; Kumar, N.; Panda, K.; Kanan, V.; Joshi, S.; Visoly-Fisher, I. Role of Oxygen Functional Groups in Reduced Graphene Oxide for Lubrication. *Sci. Rep.* **2017**, *7*, 1–14. https://doi.org/10.1038/srep45030.

(19) Yuan, R.; Yuan, J.; Wu, Y.; Chen, L.; Zhou, H.; Chen, J. Efficient Synthesis of Graphene Oxide and the Mechanisms of Oxidation and Exfoliation. *Appl. Surf. Sci.* **2017**, *416*, 868–877. https://doi.org/10.1016/j.apsusc.2017.04.181.

(20) Aliahmad, M.; Dehbashi, M. Synthesis and Characterization of Thermally-Reduced Graphene. *Iran. J. Energy Environ.* **2013**, *4* (1), 53–59. https://doi.org/10.5829/idosi.ijee.2013.04.01.

(21) Panchakarla, L. S.; Subrahmanyam, K. S.; Saha, S. K.; Govindaraj, A.; Krishnamurthy, H. R.; Waghmare, U. V.; Rao, C. N. R. Synthesis, Structure, and Properties of Boron- and Nitrogen-Doped Graphene. *Adv. Mater.* **2009**, *21* (46), 4726–4730. https://doi.org/10.1002/adma.200901285.

(22) Konstantin N. Kudin, †; Bulent Ozbas, ‡; Hannes C. Schniepp, ‡; Robert K. Prud'homme, ‡; Ilhan A. Aksay, ‡ and; Roberto Car*, †. Raman Spectra of Graphite Oxide and Functionalized Graphene Sheets. *Nano Lett.* **2008**, *8* (1), 36–41. https://doi.org/10.1021/NL071822Y.

(23) Tung, T. T.; Yoo, J.; Alotaibi, F. K.; Nine, M. J.; Karunagaran, R.; Krebsz, M.; Nguyen, G. T.; Tran, D. N. H.; Feller, J. F.; Losic, D. Graphene Oxide-Assisted Liquid Phase Exfoliation of Graphite into Graphene for Highly Conductive Film and Electromechanical Sensors. *ACS Appl. Mater. Interfaces* **2016**, *8* (25), 16521–16532. https://doi.org/10.1021/acsami.6b04872.

(24) Lee, A. Y.; Yang, K.; Anh, N. D.; Park, C.; Lee, S. M.; Lee, T. G.; Jeong, M. S. Raman Study of D* Band in Graphene Oxide and Its Correlation with Reduction. *Appl. Surf. Sci.* **2021**, *536* (September 2020), 147990. https://doi.org/10.1016/j.apsusc.2020.147990.

(25) Zhou, Y.; Lin, X.; Huang, Y.; Guo, Y.; Gao, C.; Xie, G.; Jiang, Y. Impact of Further Thermal Reduction on Few-Layer Reduced Graphene Oxide Film and Its n-p Transition for Gas Sensing. *Sensors Actuators, B Chem.* **2016**, *235*, 241–250. https://doi.org/10.1016/j.snb.2016.05.078.

(26) Dervishi, E.; Ji, Z.; Htoon, H.; Sykora, M.; Doorn, S. K. Raman Spectroscopy of Bottom-up Synthesized

Graphene Quantum Dots: Size and Structure Dependence. *Nanoscale* **2019**, *11* (35), 16571–16581. https://doi.org/10.1039/c9nr05345j.

(27) Das, R.; Parveen, S.; Bora, A.; Giri, P. K. Origin of High Photoluminescence Yield and High SERS Sensitivity of Nitrogen-Doped Graphene Quantum Dots. *Carbon N. Y.* **2020**, *160*, 273–286. https://doi.org/10.1016/j.carbon.2020.01.030.

(28) Ghaffarkhah, A.; Hosseini, E.; Kamkar, M.; Sehat, A. A.; Dordanihaghighi, S.; Allahbakhsh, A.; van der Kuur, C.; Arjmand, M. Synthesis, Applications, and Prospects of Graphene Quantum Dots: A Comprehensive Review. *Small* **2022**, *18* (2), 1–48. https://doi.org/10.1002/smll.202102683.

Chapter 3

A Detailed Study of Layer Dependent Properties of Large Lateral-size Graphene Oxide and Reduced Graphene Oxide

Chapter 3 studied a facile and simple technique at a minimal cost (substantially lower than the commonly used ultrasonic technique) to exfoliate GO based on mild temperature heating (up to 80 °C) at ambient conditions, which is 3 times lower than the conventional hydrothermal method, eliminating the need of high temperature used in the high-pressure hydrothermal method. Subsequently, RGO was synthesized by chemical reduction/ deoxygenation. The morphology and lateral dimensions of the GO and RGO were investigated by optical microscope, FESEM, and AFM. The structural quality and characteristics of GO and RGO were further analyzed using Raman spectroscopy, XRD, XPS, FT-IR, UV-vis absorption spectroscopy, PL, Thermo gravimetric analysis (TGA), and Brunauer-Emmett-Teller (BET) analysis. The electronic and electrochemical behaviors were investigated from current-voltage (I-V) characterization and electrochemical impedance spectra. Furthermore, the sensing application of large area GO and RGO was also explored using Rhodamine B at low concentrations to test the surface-enhanced Raman spectroscopy (SERS) effect.

3.1. Introduction

After the finding of graphene[1], derivatives of graphene are intensely appealing to numerous research domains owing to their distinctive behaviors, such as tunable electrical conductivity[2–5], excellent mechanical properties[6–8], high corrosion resistance[9–11], extremely efficient electrocatalytic activity[12,13] and so forth[10]. These unique properties depend on the lateral dimension and thickness of the synthesized graphene sheets[14]. Besides, the limitation for mass production lies in the complexities involved, related to the requirement of high-cost equipment for bottom-up synthesis protocol, rigorous exothermic reactions, and also several steps associated with the top-down synthesis method despite having the better potential to scale up for the latter process than the former synthesis route. Furthermore, the need for extreme care during exfoliation for the top-down synthesis protocol to obtain high quality and large lateral size graphene-based sheets is of significant concern to implement in wide-scale electronic applications, in particularly its sensing applications.

Exfoliation from chemically synthesized graphene oxide is cost-effective and most functional properties can be tailored to the degree of oxidation-reduction processes. Several top-down exfoliation techniques have been reported emphasizing the lateral size of graphene sheets, their functional property, practicality to scale up, and their viable applications. There are reports on electrochemical exfoliation[3,15–20], ultrasonic exfoliation[5,21–29], microwave-assisted exfoliation[30–32], and a few studies on shear-mechanical exfoliation[33–35], hydrothermal[4] and thermal techniques[36], and freezing-thawing based[37] exfoliation, etc. Table 1 collates various exfoliation techniques for graphene-based sheets, nature of solvent used, the resulting lateral size, and their applications.

Several techniques have been reported to exfoliate graphite oxide into large lateral size GO. Among them, the hydrothermal method has shown to be a promising technique exhibiting its relative cost-effectiveness, producing excellent yield with controllable and large lateral size with outstanding electrical properties. However, this method requires additional autoclave equipment and the exfoliation processes at high temperatures up to 220 °C. Therefore, there is a further demand for a simpler and more cost-effective approach to exfoliate very large lateral dimension graphene-based sheets, exhibiting high electrical and sensing performances.

3.2. Synthesis of graphene oxide and reduced graphene oxide

3.2.1. Synthesis of graphene oxide

The brief procedure of the synthesis process for graphite oxide is explained in previous chapter 2 (**section 2.2.1**).

Further, GO sheets are exfoliated from the graphite oxide using a mild heating technique. The snapshots for the exfoliation stages from 1 to 5 are shown in **Fig. 3.1.** The graphene oxide sheets exfoliated using ultrasonication and mild heating-based methods are named UGO and GO, respectively.

3.2.2. Synthesis of reduced graphene oxide (RGO)

RGO is synthesized by a chemical process using hydrazine monohydrate. Large lateral size GO was drop-casted on the SiO_2/Si substrate and is used to synthesize RGO. The synthesis process and generalized mechanism for reduction of GO using hydrazine is explained in chapter 2 (**section 2.3.2**). In this chapter, chemically reduced graphene oxide is named RGO.

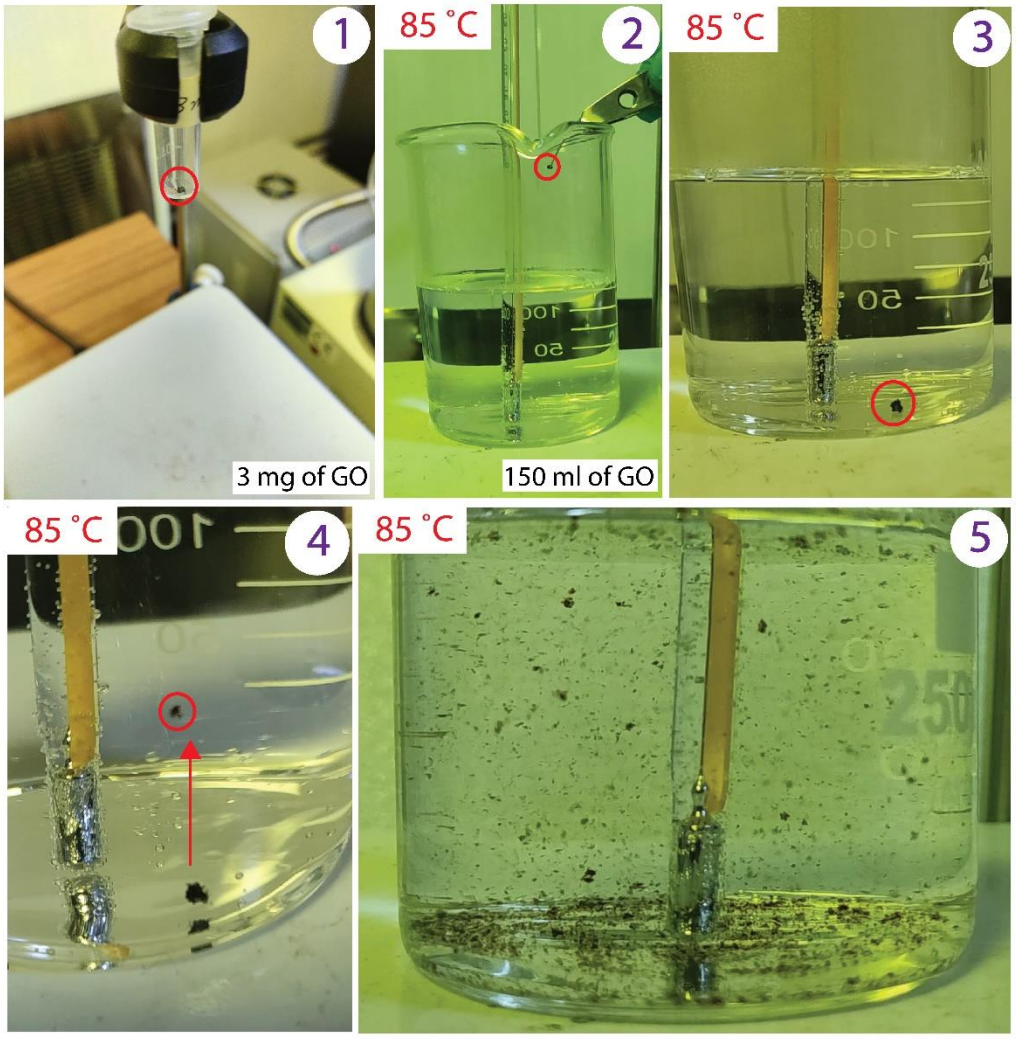

Fig. 3.1: Snapshots showing stages of exfoliation during the mild heating condition. The temperature is carefully adjusted to maintain a constant value. The rise of the initial exfoliated flake is observed at stage 4 driven by mild temperature. At stage 5, numerous fragmented flakes assist in mechanical exfoliation within the flakes owing to the gained kinetic energy.

3.3. Characterization techniques

In reflection mode, the lateral dimension of UGO, GO, and RGO sheets were observed using an optical microscope (*Leica DM 2500M*). Thermogravimetric analysis was performed using *HITACHI STA7200*, a thermal analyzer with a heating rate of 5 °C/min. The surface area and pore volume of graphene-based material was studied using the BET (Brunauer-Emmett-Teller) method using *Micromeritics, TriStar II* instrument at 77 K. The specific surface area and pore volume were calculated from the N_2 adsorption/desorption isotherm data. Prior to the experiment, the graphene-based material was heated at 50 °C for 24 h in an oven.

I-V measurements were performed using a microprobe station (ECOPIA) and a source measure unit (*Keithley 2400*, Germany), and the data were retrieved using *KickStart* Instrument

control software (version 1.9.8). Electrochemical impedance spectra were obtained using a *Gamry* potentiostat instrument (*Model: Reference 600+*) in a three-electrode system (Ag/AgCl as a reference, a platinum wire as counter, and graphene-based materials drop-cast onto a platinum disk of 3 mm diameter as a working electrode). 0.5 M H_2SO_4 was used as the electrolyte. For drop-casting, the graphene-based ink was prepared using 5 mg of GO/RGO and mixed with 87 µl of Nafion, 261 µl of ethanol, and 652 µl of de-ionized water. The frequency range was between 0.1 Hz and 10^6 Hz with a sinusoidal ac amplitude of 10 mV. Chemical sensing application of UGO, GO, and RGO was studied using various concentrations of Rhodamine B (RhB, 10^{-4} M, 10^{-5} M, 10^{-6} M, 10^{-7} M, and 10^{-8} M). A comparative study of different substrates such as UGO, GO, RGO, and bare SiO_2 was conducted to test the surface-enhanced Raman spectroscopy (SERS) effect for RhB detection using the above Raman spectrometer.

3.4. Results and discussions

3.4.1. Morphological and microstructural

The GO's typical surface-rippling and wrinkle-shaped structures have been seen in the optical microscopic, FESEM, FETEM, and AFM images. **Fig. 3.2** shown the optical images of UGO obtained from conventional ultrasonication (**Fig. 3.2a (inset)**), GO from mild-heating process (**Fig. 3.2b (inset)**), and chemically reduced GO (RGO) (**Fig. 3.2c (inset)**) and their corresponding statistical lateral size distribution, as represented in **Figs. 3.2a, 3.2b & 3.2c**, respectively. For the samples prepared by ultrasonication process (**Fig. 3.2a (inset)**), UGO sheets appear smaller in lateral size, and some are broken further into several smaller pieces. Asymmetric distribution with a mixture of bigger and smaller flakes, exhibiting irregular shapes, appears staking and overlapping on each other.

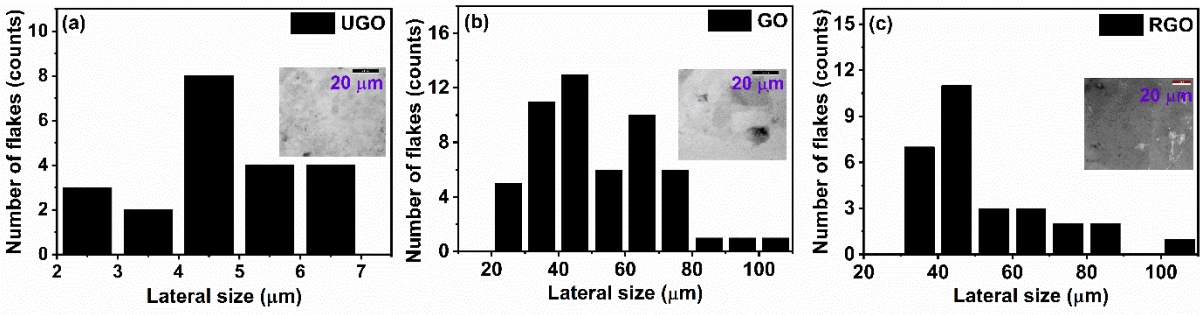

Fig. 3.2: Histogram depicting the statistical distribution of various lateral sizes for (a) GO exfoliation from ultrasonication, (b) GO exfoliation from mild heating, and (c) RGO from chemical reduction with an optical image shown in the inset, respectively.

The lateral size distribution, as shown in **Fig. 3.2a**, indicates that most of the lateral dimensions are 4–5 µm.

In the case of GO prepared by mild heating conditions **Fig. 3.2b**), the lateral size of the few layers of sheets is remarkably more significant than that of sheets obtained from the ultrasonic process. The maximum size obtained is ~104 µm, which is the largest lateral size of GO reported to date, to our knowledge, using such kind of a facile and simplified mild condition exfoliation route. However, more miniature sheets of thicker with many stacked layers, illustrated by darker shades overlapping the large dimensional flake, are also seen.

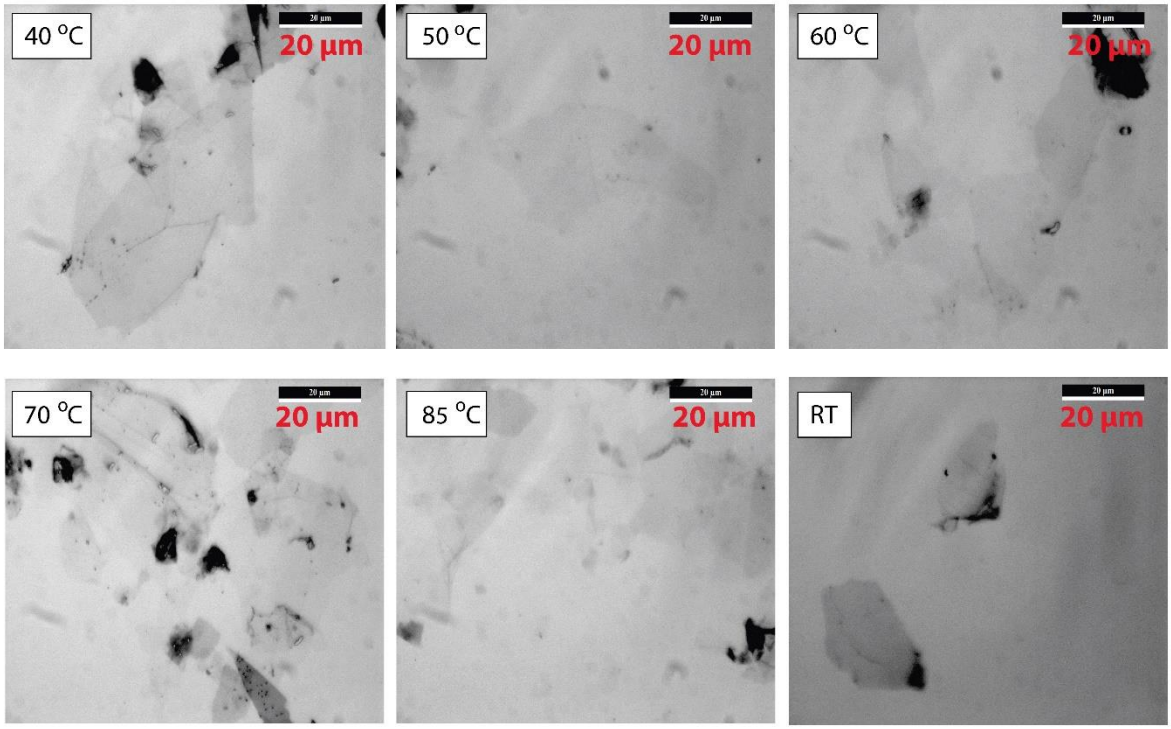

Fig. 3.3: Optical images of exfoliated GO obtained from mild heating at different temperatures (RT stands for room temperature, 23 °C). Darker patches correspond to the thicker sheets, which are not efficiently exfoliated.

The corresponding statistical distribution of flake size evaluated from 54 flakes using an optical microscope is presented (**Fig. 3.2b (inset)**). The majority of the flakes are in the range of 40–50 µm. The statistics indicate that the flakes are well separated and distinguishable, enabling the size measurement of the lateral dimension by end-to-end demarcation. **Fig. 3.2c** exhibits the flakes for RGO and their lateral size. An immense lateral size in the range of 100–110 µm is obtained, as seen in the inset of the optical image. However, the smaller flakes appear relatively thicker, as depicted by the darker patches. Most lateral

dimensions are 40-50 µm (**Fig. 3.2c (inset)**). Some of the layers are found to be folded and stacked in all the images.

The exfoliation of the GO is studied at different operating temperatures; room temperature (RT, 25 ˚C), 40 ˚C, 50 ˚C, 60 ˚C, 70 ˚C, and 85 ˚C. The optical images of the exfoliated GO sheets are shown in **Fig. 3.3**. GO flakes are seen to be exfoliated at all temperatures, and the optimum temperature for GO exfoliation is 85 ˚C. At 85 ˚C, a large number of GO flakes are exfoliated, and the super large size of the GO sheets is obtained. If the operating temperature increases beyond 85 ˚C, it is expected that the evaporation of the solvent will occur with more kinetic energy, leading to the breakdown of the GO sheets.

For the ultrasonic technique, the exfoliation for different sonication times (5 minutes, 15 minutes, 30 minutes, 60 minutes, and 180 minutes) is analyzed as shown in **Fig. 3.4**. The

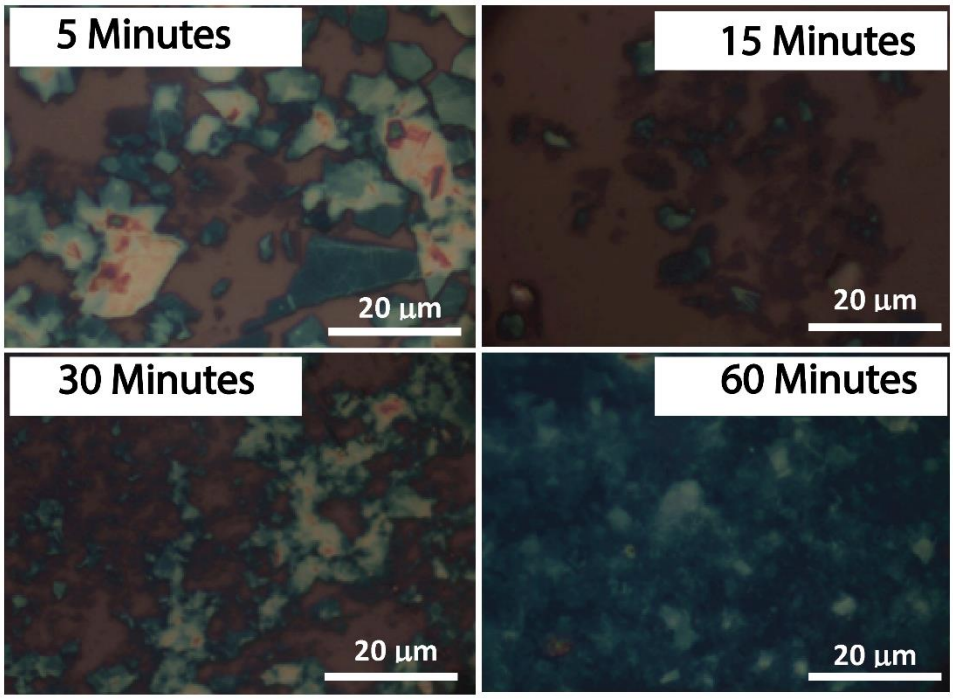

Fig. 3.4: Optical images of GO flakes obtained from exfoliation using ultrasonication at different time intervals at 50 W. Flakes fragmentation and layer exfoliation occur simultaneously wherein fragmentation predominates over-exfoliation as indicated by the presence of several smaller lateral size flakes.

optical microscopic analysis reveals that it is difficult to control the size and thickness of the UGO flakes using the ultrasonication technique. For 5 minutes of exfoliation of UGO using ultrasonication, most of the graphite oxide flakes are not exfoliated. After 15 and 30 minutes, the GO flakes break down into smaller pieces, which mainly existed with multi-layered GO flakes. After 60 and 180 minutes of ultrasonication, the UGO sheets are almost broken down.

GO sheet with super large size and presence of wrinkles on it is observed from the optical image shown in **Fig. 3.5a**. A closer observation in TEM from the portion of the large lateral size GO sheet shows that the sheet has high optical transparency, suggesting the thin graphitic nanostructure (**Fig. 3.5b**). The selected area electron diffraction (SAED) pattern in **Fig. 3.5b (inset)** shows bright diffraction spots, which indicate the crystalline structure of GO has a (002) plane. However, the blurry/ less sharp spots suggest the presence of functional groups. The wrinkled nano feature is also preserved in the few layers of RGO, as observed in TEM images (**Fig. 3.5c**). SAED pattern shows polycrystalline nature for RGO having (0 0 2) plane (**Fig. 3.5c (inset)**). However, in the case of RGO, the well-defined bright and sharp six-fold spots are the hexagonal honeycomb framework of the graphene skeleton, indicating the restoration of the sp2 character of carbon structure after the removal of oxygen-containing functional groups during the reduction process. The distinct lines confirm the crystallinity from diffraction with an interlayer spacing of 0.355 nm (**Fig. 3.5d**).

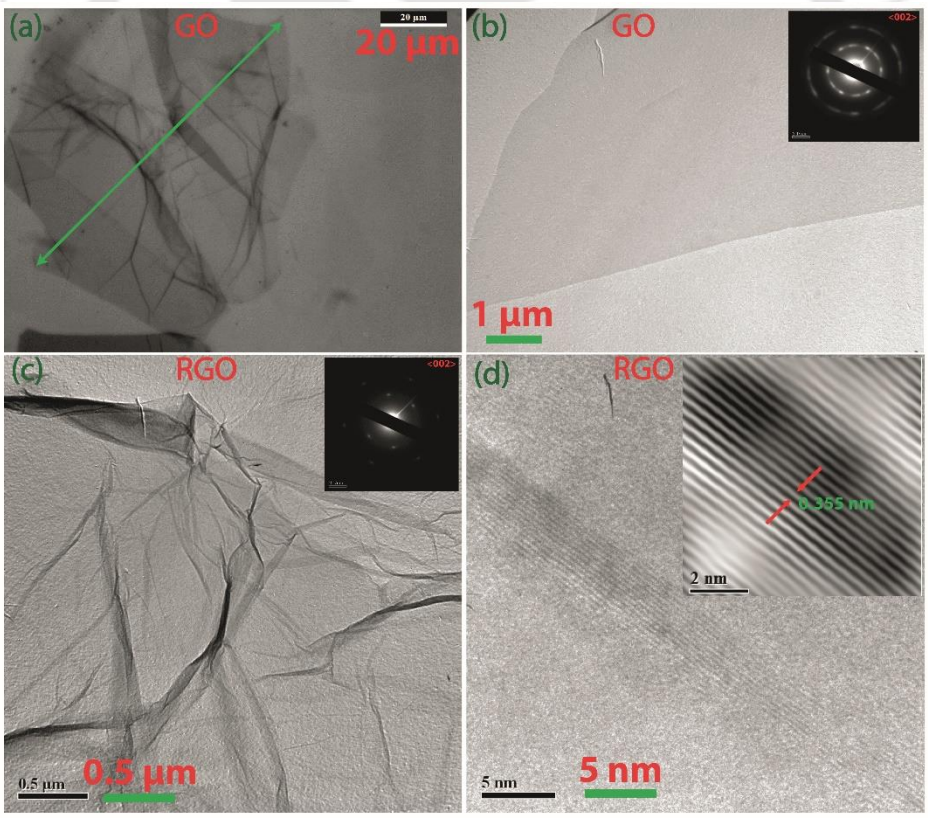

Fig. 3.5: Higher magnification images of GO and RGO showing the nano-/micro features and diffraction of graphene-based sheets; (a) optical image showing the dimensions of the GO sheet; (b) TEM image for large-area GO sheet with SAED pattern(inset); (c) TEM image for RGO sheet with SAED pattern (inset); (d) HRTEM monographs showing the interlayer spacing of RGO and magnified pattern for the interlayer spacing of RGO (inset).

3.2.2. Structural and chemical features of graphene oxide and reduced graphene oxide

The evolution of disorder-induced Raman spectra of carbons along an amorphization trajectory can be classified into three stages: (1) graphite to nanocrystalline graphite; (2) nanocrystalline graphite to low sp^3 amorphous carbon; (3) low sp^3 amorphous carbon to high sp^3 (tetrahedral) amorphous carbon[9,11]. In the present study for GO and RGO, stage 1 and stage 2 are more relevant. In stage 1 and stage 2 (a) appearance of D-band occurs; consequently, I_D/I_G increases; (b) D-band and G-band broaden; (c) emergence of oxygen-terminated nanocrystalline carbon band within D-band and amorphous sp^2 carbon merged with G-band as represented in fitted spectra in **Fig. 3.6a**. Detailed analysis of bands by fitting the Raman spectra for the GO sample shows the D^1 band at 1238 cm^{-1} corresponds to an oxygen-terminated nanocrystalline diamond. D^2 band at 1355 cm^{-1} relates to the symmetric breakdown of structure. D^3 band at 1541 cm^{-1} correlates with amorphous sp^2 carbon, and G-band at ~1603 cm^{-1} is attributed to sp^2 bonded carbon atoms. In the case of RGO, the absence of D^1 indicates the elimination of the oxygen group, which eventually restores the ordered hybridized sp^2 carbon framework (**Fig. 3.6a**). Reduction of the D peak intensity in RGO compared to GO indicates the reduction/removal of oxygen-containing functional groups or healing of structural defects during exfoliation.

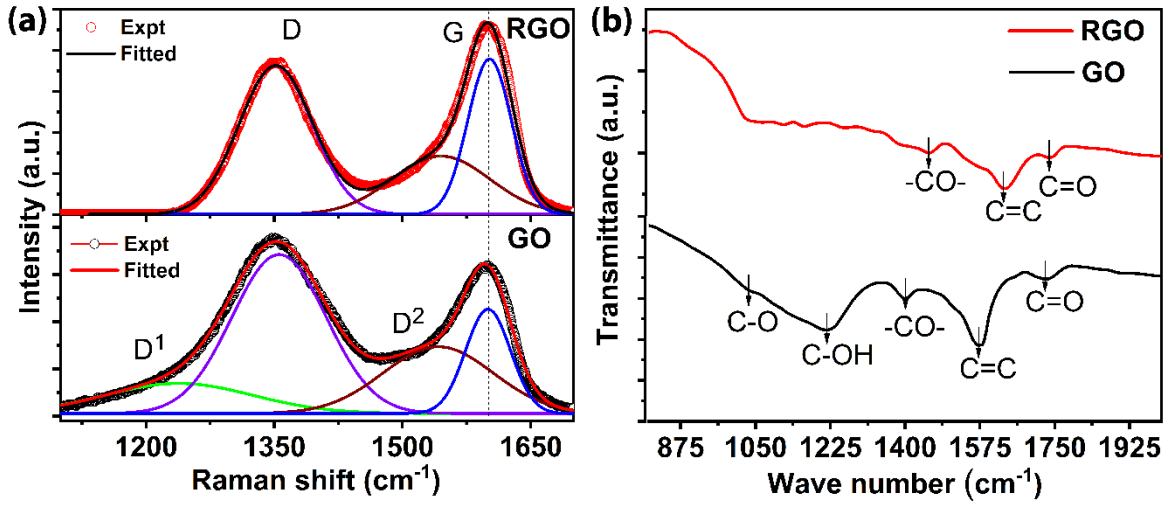

Fig. 3.6: Characteristics of GO and RGO from various analyses: Gaussian and Lorentzian fitting for (a) and RGO; (b) FTIR absorption spectra for different samples showing different bonds.

The FTIR analysis further confirms the identification of various in-plane and edge oxygen functional groups in GO and RGO. **Fig. 3.6b** represents the FTIR spectra of GO and RGO. Most of the peaks are concentrated in the range from 1000 to 2000 cm^{-1}, revealing the

characteristic absorption bands of GO and RGO formation. The bands associated with the various oxygen functional groups and sp^2 carbons can be distinguished from the FTIR spectrum. In the case of GO, a weak shoulder at 1035 cm^{-1} correlates with carbon-oxygen (alkoxyl); a distinctive band appeared at 1226 cm^{-1} corresponds to the carbon-oxygen vibration, 1403 cm^{-1} band is assigned to the ─OH in-plane bends (deformation), 1564 cm^{-1} band corresponds to the sp^3 C-C stretching, low-intensity band at 1593 cm^{-1} corresponds to the sp^2 C=C and 1753 cm^{-1} band is due to the presence of the carbonyl group. Carbon – hydrogen bond character is shown in the band centered at 2363 cm^{-1}. In the case of RGO, the significant reduction of the band between 1000 cm^{-1} and 1500 cm^{-1}, as compared to GO spectra, suggests the removal of weakly bonded carbon-oxygen groups, which indicates the effectiveness of nullifying the defects. Shoulder correlated to alkoxyl at 1035 cm^{-1} is absent, and a significant band corresponding to carbon-oxygen vibration at 1226 cm^{-1} is missing. However, there are weakly absorbed bands at 1108 cm^{-1} due to C─O stretching; the band at 1160 cm^{-1} is attributed to C─O─C stretching; the band at 1453 cm^{-1} is due to C─OH; 1564 cm^{-1} band corresponds to the sp^3 C-C stretching, and the clear band at 1634 cm^{-1} corresponds to C═C stretching, and the weak band of the carbonyl group is found at 1743 cm^{-1}. Thus, the weak bands in RGO compared to GO indicate the removal of defects induced by the oxygen functional groups, which corroborate with the results from XRD and Raman analyses

Furthermore, a slight shifting of the G-band towards the lower frequency side occurs due to the emergence of the graphitic sp^2 order. The quantitative confirmation of the degree of oxygen removal comes from the decrease in the value of I_D/I_G (0.8 for RGO) compared to GO. The Raman scattering mapping for RGO is shown in **Fig. 3.7**. The Raman scattering was measured on the large surface area of the RGO sheet (50 × 50 μm^2) (**Fig. 3.7a**). The cumulative Raman scattering signals (**Fig. 3.7b**) for the RGO sheet were obtained from the D and G bands. The uniform distribution of the intensity of Raman signals (D and G) was acquired, shown in **Fig. 3.7c & 3.7d**, respectively.

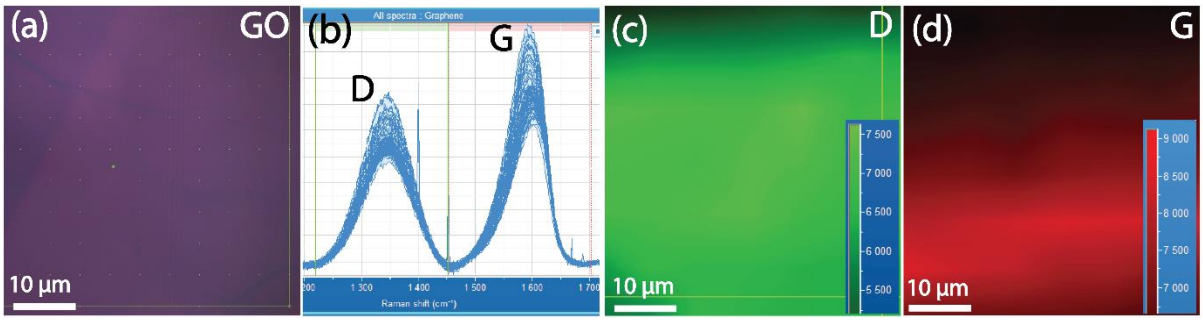

Fig. 3.7: (a) Optical image of RGO sheet (b) Raman mapping spectrum on the 50 × 50 µm size RGO sheet; (c) mapping of D band; and (d) mapping of G band.

The intensity of the D band ranges from 5,500 to 7,500 counts, and the intensity of the G band ranges from 7,000 to 9,000 counts. The Raman mapping measurement confirmed RGO sheets of high quality and super large lateral size.

Bonding characteristics are further supplemented by XPS analysis, as shown in **Fig. 3.8**. The bonding elements are predominantly carbon and oxygen, as indicated by two pronounced peaks exclusively from C 1s and O 1s (**Fig. 3.8a & b**). The raw data mainly consists of two peaks; the carbon basal plane and the oxygen-containing functional groups. However, the deconvoluted spectra contain several peaks corresponding to C═C, C─O, C═O, and O─C═O. For GO (**Fig. 3.8a (inset)**), the peak centered at 283.8 eV is assigned to C═C. The second peak (raw data) centered at ~286.5 eV, containing C─O (epoxy and hydroxyl groups), C═O and O─C═O bond characteristics, has high intensity (precisely, C─O → 286.3 eV, C═O → 288 eV, and O─C═O → 288.9 eV).

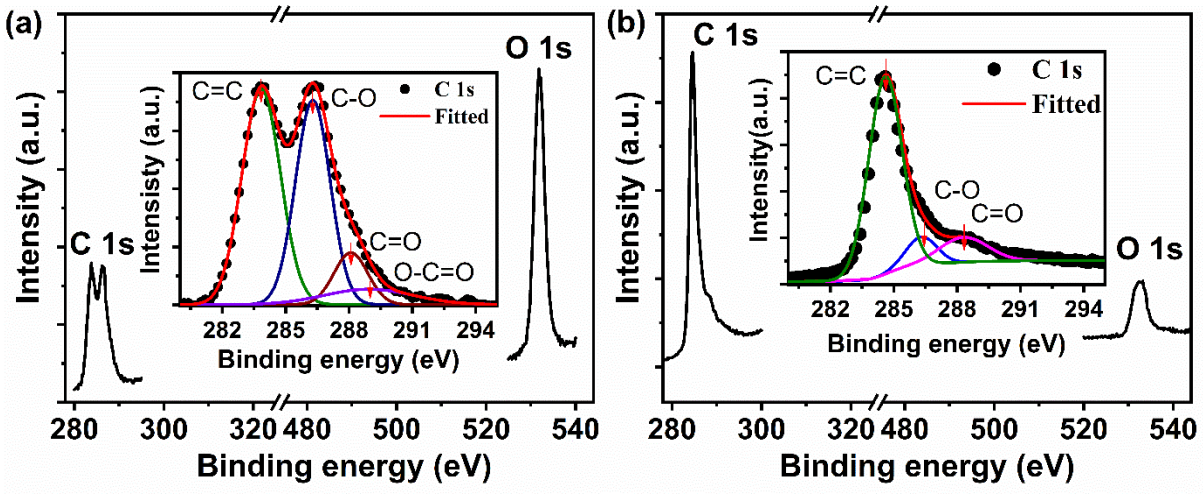

Fig. 3.8: XPS spectra indicating (a) C 1s and O 1s for GO with deconvoluted C 1s spectra for GO (inset), and (b) C 1s and O 1s for RGO with deconvoluted C 1s spectra for RGO (inset).

In contrast, in the case of RGO (**Fig. 3.8b (inset)**), a sharp decrease in the second peak, correlated to combined peaks for C─O and C═O at 286.3 eV and 288.3 eV, respectively, infers

the reduced state of RGO by removing the significant oxygen-containing functional groups attached to the carbon framework. Besides, the peak for O─C═O is suppressed in RGO, indicating the removal of the labile carboxylic group completely during the reduction process. Furthermore, the sp^2 character for carbon in RGO is revealed from the peak corresponding to C═C at 284.5 eV, which confirms the efficacy of the reduction. The C/O ratio for RGO is 3.66, which is much larger than that of GO (0.417) as calculated from peak relative maxima of C 1s and O 1s, suggesting the minimal oxygen content in the reduced state of RGO, which agrees with the comparative analysis for the presence of oxygen-containing functional groups by the other techniques.

The UV-visible absorption spectra for GO and RGO are shown in **Fig. 3.9a**. For GO, a strong absorption peak at 230 nm can be assigned to $\pi \rightarrow \pi^*$ transition or π-plasmon resonance common for extended sp^2 conjugated carbon sheet (C═C present within the aromatic sp^2 hybridized carbon framework)[12]. A slight hump-like shoulder is also seen at 303 nm, corresponding to $n \rightarrow \pi^*$ from oxygen-containing functional groups. The presence of oxygen-containing functional groups is evident from the absorption spectra of GO.

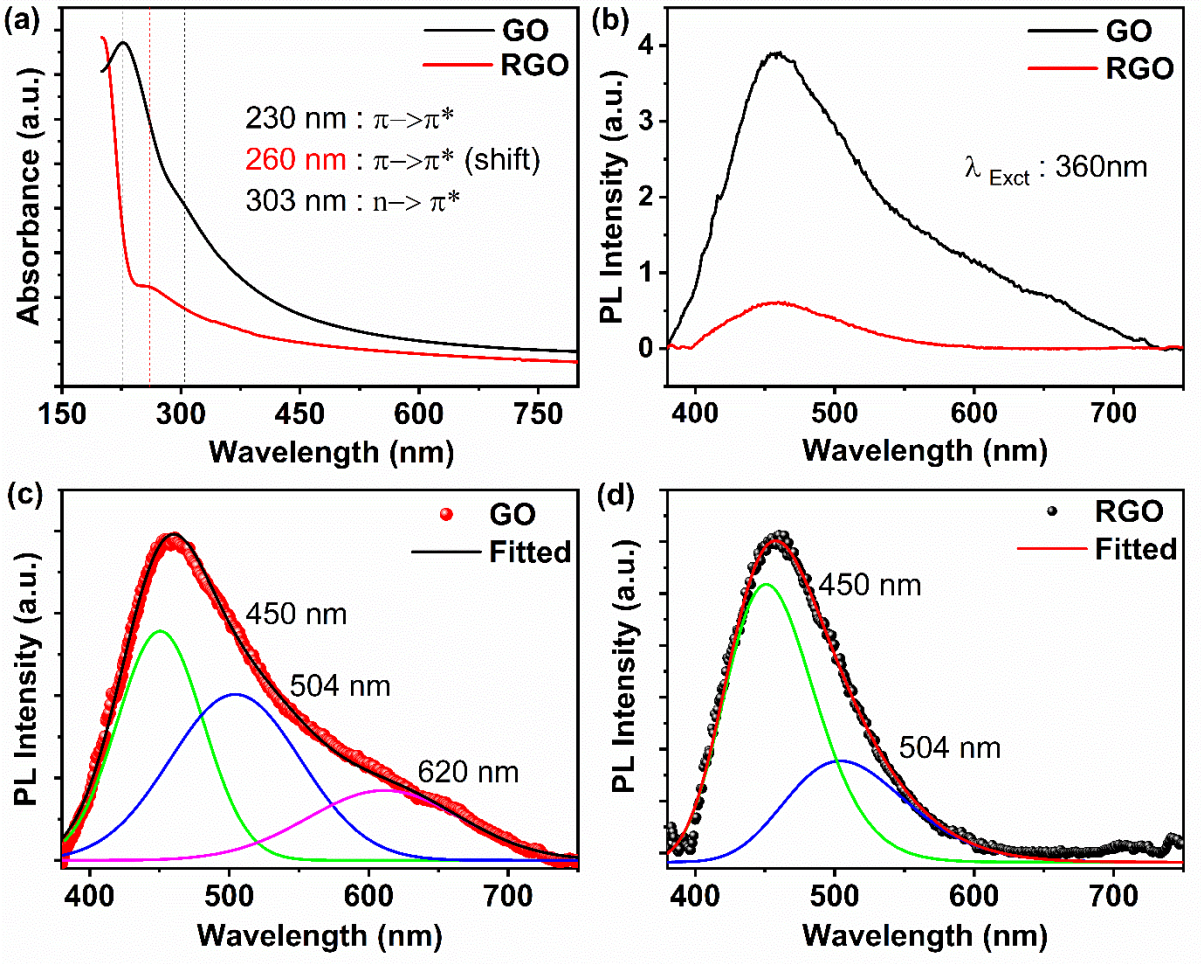

Fig. 3.9: a) UV-vis absorption spectra of GO and RGO showing bands attributed to π / π* and n / π* transitions. Photoluminescence emission behavior showing the degree of defect states for (b) GO and RGO, (c) fitted plot for GO, and (d) fitted plot for RGO.

The redshift of the peak at 260 nm for RGO shows restoration of sp^2 character predominantly from π → π* transition of C═C without the presence of oxygen-containing absorption peak, as compared to GO spectrum, suggesting the deoxygenated RGO. The low energy transition corroborates with the previous results, indicating the reduction of defects, thereby decreasing the energy bandgap.

The PL spectra of GO and RGO are shown in **Fig. 3.9b, 3.9c & 3.9d**. A significant difference in the spectra evolution is observed between the two samples, GO and RGO (**Fig. 3.9b**). GO has a broad peak, and the fitted spectra consist of three peaks centered at 620 nm, 504 nm, and 450 nm (**Fig. 3.9c**), arising from the disorder-induced defect states due to the sp^3 character of carbon with oxygen-containing functional groups attached to graphene carbons. The presence of oxygen can increase the number of (C─OH) and (C─O─C) bonds due to the rearrangement of oxygen and oxygen-containing functional groups with carbons. This consequently enhances the transfer of resonance energy from O sites to the sp^2 clusters in the graphene lattice, contributing to a broad PL emission[13].

The significant number of defect states present in the GO sample within the π → π* results in the broad PL spectrum. It should be noted that these defect states are distributed broadly at lower energy and higher energy within the bandgap between π (analogous to valence band) and π* (analogous to conduction band). Theoretically, the transition within π → π* is caused by Piz states oriented perpendicular to the planar graphene. On reduction, oxidized sp^3 carbon responsible for the distortion is transformed to sp^2 carbon clusters, thereby decreasing the number of defect states in RGO, which results in the decrease in intensity (**Fig. 3.9b**) as well as the absence of PL peak at 620 nm (**Fig. 3.9d**), as compared to GO spectrum. The increased cluster-like states from the newly formed sp^2 domain have higher energy than the defect states, which correspond to the emission peak at a shorter wavelength, i.e., the higher energy of 450 nm. This phenomenon is consistent with the mechanism explained by Chuang et al.[13] and Chien et al.[14]. A significant drop of the intensity of 450 nm peak confirms the reduction of several defect states in RGO attributed to more sp^2 character in the carbon skeleton. The drastic decrease in the PL intensity from GO to RGO confirms that the present reduction process is more potent than other photoreduction techniques.

TGA/DTG profiles of GO and RGO further provide evidence for the presence of functional groups and their thermal response to weight change, as shown in **Fig. 3.10a & 3.10b**. The TGA/DTG data were acquired with a heating rate of 5 °C/min in the presence of nitrogen gas. For the GO sample (**Fig. 3.10a**), three stages can be assigned in the thermogram; the first stage corresponds to evaporation of water (below 100 °C) adsorbed onto the GO or intercalated between GO layers; secondly, the loss of more labile carbon oxide-based gas (100─220 °C) and thirdly, the removal of relatively more inert carbon oxide-based gas (220─290 °C). DTG peaks show pronounced bands centered at 60 °C, 191 °C, and 242 °C.

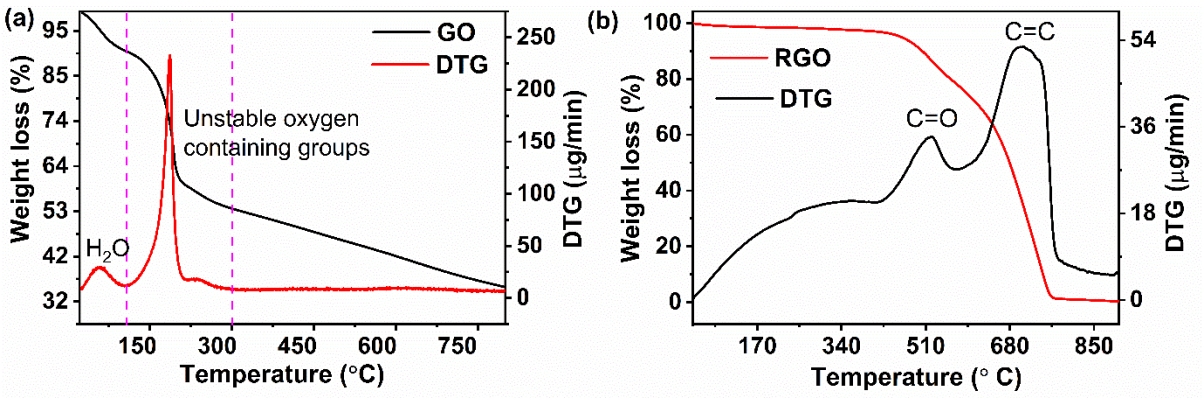

Fig. 3.10: TGA/DTG analysis for (a) GO and (a) RGO.

The DTG peaks at 60 °C, 91 °C, and 242 °C correlate to the first, second, and third stages, respectively, due to the loss of moisture and decomposition of unstable oxygen-containing functional groups (hydroxyl and epoxy groups). In the first stage/zone, a weight loss of 9 % of the initial weight in the form of water is observed. In the second zone, 32 wt. % is lost, which is attributed to the escape of CO_2 and CO gases. Subsequently, 5 wt.% is lost in the third zone due to the release of CO_2 and CO. These results are consistent with the reported works[6,7,15], which describe the three zones for weight reduction owing to loss of water, loosely bound oxygen, and relatively inert oxygen. Tang et al.[6] explained that the weight loss in the second stage originated from the decomposition of the oxygen-containing group, resulting in a mixture of CO_2 and CO where CO_2 dominates. However, in the third stage, CO dominates during the weight reduction process, originating from CO_2 and CO. In RGO (**Fig. 3.10b**), the weight loss is gradual up to 410 °C and only 4 wt. % is lost over this wide temperature window. The broad DTG band at 100─400 °C represents the negligible loss of adsorbed water, in-plane oxygen functional groups, and COOH-related groups.

Interestingly, compared to the GO, DTG for RGO peaks at 522 °C and 706 °C are due to the removal of more stable carbonyl groups and breaking of sp^2 carbon bonds, respectively.

A similar observation was reported by Sundramoorthy et al.[16], describing the two major weight loss features attributed to the decomposition of the dangling oxygenated compounds and the graphene itself. The DTG profile of RGO reveals the removal of many oxygen functional groups and the restoration of the graphitic sp^2 carbon framework, which is subsequently broken on further heating. It appears that RGO has lower thermal stability than GO, as seen by the rapid decrease in weight at elevated temperatures. E.M. Deemer et al.[7] reported that the weight losses above 625 °C are due to the rapid combustion of the carbon skeleton. Hence, the removal of the labile oxygen-containing group is confirmed in both GO and RGO.

To understand the surface area of the graphene-based materials rendering active sites for gas interaction with large area GO and RGO, BET analysis was conducted, as shown in **Fig. 3.11** depicting the adsorption/desorption isotherm in the N_2 environment. RGO sheets exhibit the typical Type IV characteristics with slight hysteresis (**Fig. 3.11b**), indicating its mesoporous nature with more active sites available for gas to interact. At the same time, the GO shows a comparatively flat curve (**Fig. 3.11a**). The calculated surface areas for GO and RGO are 0.0993 m^2/g and 87.256 m^2/g, respectively. Thus, the specific surface area of RGO is much higher than the GO. Pore size distributions for GO and RGO are shown as insets **Fig. 3.11a and 3.11b**, respectively. The majority of pore width for GO and RGO is 2.6 nm and 3.5 nm, respectively. However, the RGO contains additional pores of larger sizes. Micropore volumes analyzed from BET for GO and RGO are 0.000254 cm^3/g and 0.024595 cm^3/g, respectively. More interaction sites are evidenced by the larger surface area of RGO compared to GO. The low surface area of GO shows a highly interrupted flow of electrons; thus, GO is electrically less conductive material[17] as compared to RGO, which is further discussed in **section 3.2.4**.

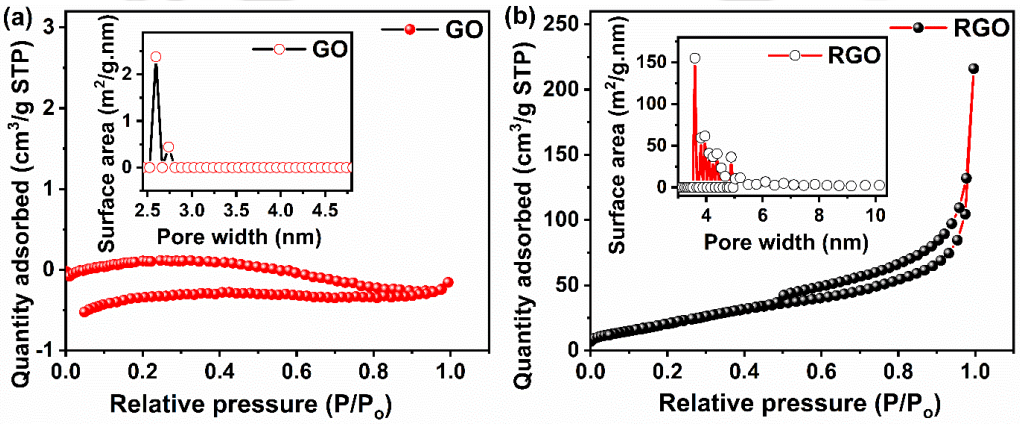

Fig. 3.11: Adsorption/desorption isotherms in N_2 environment and pore size distribution (inset) for (a) GO and (b) RGO.

3.2.3. Layer analysis of graphene oxide: Correlation of FETEM, AFM and Raman spectral analyses

The thickness of the GO sheet determined from the FETEM and AFM imaging is shown in **Fig. 3.12**. The number of layers in each sheet can be obtained from the thickness mentioned earlier. The correlation between the number of layers and Raman spectra was analyzed. The Raman spectra were measured on the known thickness of GO sheets using the same sample.

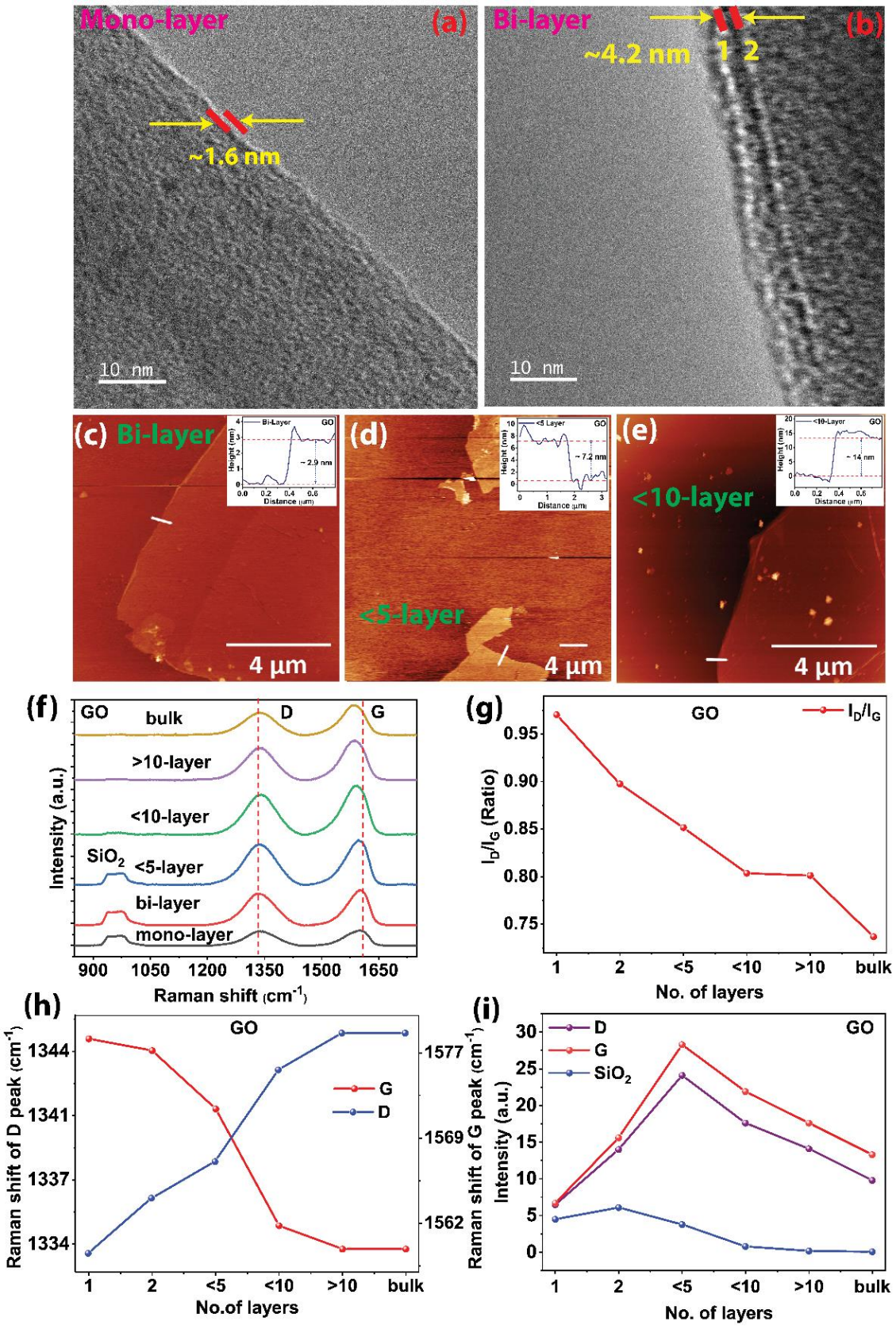

Fig. 3.12: FETEM images of (a) mono-layer and (b) bi-layer GO sheets. AFM images and the height profiles (inset) of (c) bi-layer, (d) (~ 1603 cm^{-1}), and the corresponding ratio of I_D/I_G, redshift of G peak, and blue shift of D peak, as shown in Fig. 14(f ─ i).

The monolayer and bi-layers of the exfoliated large area GO are shown in FETEM images (**Fig. 3.12a & 3.12b**, respectively). The thickness of the monolayer and bi-layers of GO are calculated using the ImageJ analyzer (~1.6 nm and ~4.2 nm, respectively). Further, the thickness of the monolayer and bi-layer GO are obtained from the AFM imaging and height profile measurement as shown in **Fig. 2.5e & Fig. 3.12c** (~1.6 nm and ~2.9 nm, respectively). The monolayer's thickness is consistent in the FETEM and AFM analyses.

However, the bi-layer does not show exact values in FETEM, possibly due to the instrumental error. The different thicknesses corresponding to layers of GO sheets as obtained from AFM, such as monolayer (~1.6 nm, **Fig. 3.12g**), bi-layers (~2.9 nm, **Fig. 3.12c**), <5 layers (~7.2 nm, **Fig. 3.12d**), <10 layers (~14 nm, **Fig. 3.12e**), >10 layers (~20 nm), and graphite oxide (Gt) are analyzed in correlation with Raman spectra using intensities of SiO2 peak (~950 cm^{-1}), D peak (~ 1333 cm^{-1}), and G peak. The cumulative Raman spectra for the different layers of GO sheets are plotted in **Fig. 3.12f** in the range 850 cm^{-1} to 1750 cm^{-1}, and the changes in Raman spectra based on no of layers are shown. In agreement with the reported analyses on the graphene layers[18–21], when the number of GO layers increases, the I_D/I_G ratio decreases linearly from 0.97 to 0.73 (**Fig. 3.12g**), in which G peak has a redshift from 1602 cm^{-1} to 1586 cm^{-1}, whereas the D peak has a blue shift from 1333 cm^{-1} to 1345 cm^{-1} (**Fig. 3.12h**). The intensities of the D and G peaks increase from monolayer up to <5 layers and then decrease afterward, whereas the intensity of the SiO_2 peak ~ 950 cm^{-1} gradually decreases (**Fig. 3.12i**) as the thickness of the GO layer increases[22,23]. From the analysis, it can be concluded that the mild heating-based exfoliation of GO has exfoliated various thicknesses of large-area GO sheets.

3.2.4. Electronic and electrochemical behaviors of large-area graphene oxide and reduced graphene oxide

I-V characteristics for large area GO and RGO is shown in **Fig. 3.13a & 3.13b**. The I-V characteristic of the GO and RGO sheets are measured by using the interdigital electrode (IDE) pattern on the sheets. The IDE patterning on the GO and RGO sheets is fabricated using the lithography technique shown as a schematic diagram in **Fig. 3.13a (inset)**. The channel width of the IDE pattern is 1mm, shown in **Fig. 3.13b (inset)**. Non-linear ohmic characteristic is exhibited for GO due to the non-ohmic contact formation. This is primarily attributed to the reduction of electron flow rate due to the functional group's presence. The sp^3 character bonds and defects arising from the oxidation disrupt the transport of charge carriers through graphene

sp^2 networks and discontinuities between the sp^2 domains, reducing electron mobility and electrical conductivity[38]. The electron transport is more of a hopping type than ballistic

***Table 3.1**: Electrochemical impedance spectroscopy parameters for as grown large-area GO and RGO sheets*

Samples	R_s (Ω)	C_p (μF)	R_p (Ω)	C_{ct} (μF)	R_{ct} (Ω)
GO	9.71	0.51	148.7	1.4	958.3
RGO	11.86	1.06	69.19	1.56	193.2

transport. For RGO, the current flow rate is significantly improved from mA to milliampere, which is three orders ofmagnitude higher, arising from the good ohmic contact formation of

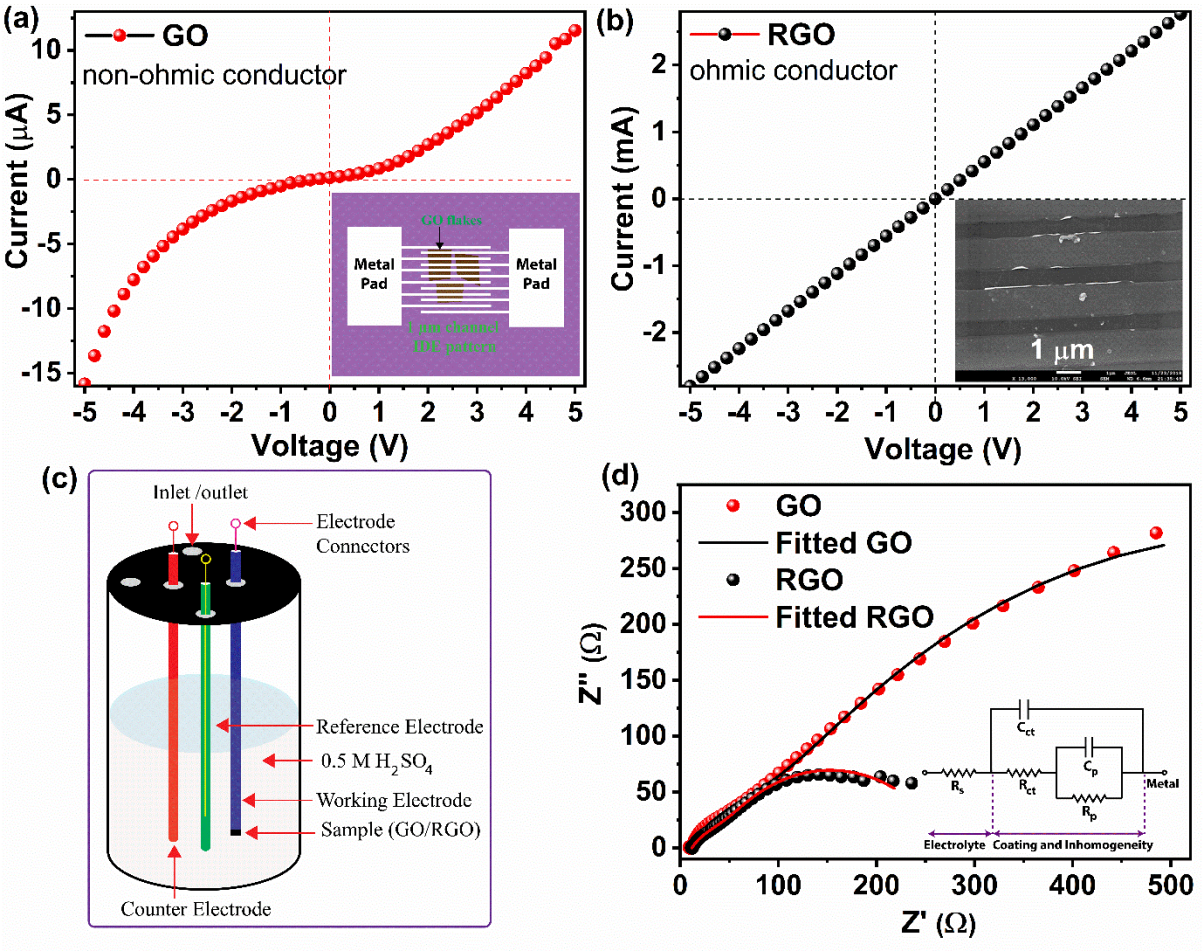

Fig. 3.13: (a) I–V characteristics for GO showing the schematic device contact (inset); (b) I–V characteristics for RGO showing device contact (inset); (c) schematic diagram of a three-electrode system for acquiring electrochemical impedance data; (d) Nyquist plot from electrochemical impedance spectroscopy presenting the

comparison of impedance dimensions (the parameters from the fitted equivalent circuit (inset) is shown in **Table 3.1**).

RGO as confirmed by the linear I-V curve. The recovery of the sp^2 graphitic plane with increasing the delocalization of electrons in C═C, thereby augmenting the electron flow rate by removing the functional groups during the reduction process, is evidenced by the I-V curve. The I-V characteristic of RGO is comparable to that of pristine graphene and other reported literature[22].

The schematic diagram for the three-electrode system used to acquire the electrochemical impedance data is shown in **Fig. 3.13c**. The electrochemical impedance spectra for GO and RGO are demonstrated in **Fig. 3.13d**. The large dimension of the impedance curve in the Nyquist plot for GO as compared to RGO reveals the significant resistance to charge transfer at the interface of the graphene-based electrode and electrolyte (impeding the flow of electrons). The smaller impedance arc for RGO indicates higher conductivity in RGO than the GO. The charge transfer resistance (Rct) for RGO is 193.2 Ω, five times lower than the GO (958.3 Ω). Suggesting the high conductivity of RGO across the interface, subsequently transferring the charge along with the carbon frame and through the base substrate of the working electrode. The Nyquist plot for both GO and RGO is obtained as half of a semicircle curve. It may be due to experimental errors; By the non-uniform distribution of current at the electrode surface and ohmic contact at the interface of the metal and solution. Similar curves are reported in the literature[39–41].

The EIS results are tabulated in **Table 3.1** as obtained from the fitting using the equivalent circuit (inset in **Fig. 3.13d**). Solution resistance (Rs) is nearly consistent when immersed with RGO and GO samples as working electrodes. However, pore resistance (Rp) of RGO (69.19 Ω) and GO (148.7 Ω) are slightly different, which could be attributed to the inherent surface inhomogeneity and unavoidable variation in the localized nano/micropores created during the process drying of the drop-casted electrode. ‘Cct’ and ‘Cp’ represent the respective capacitance for Rct and Rp. Overall, RGO prepared in this investigation has demonstrated excellent electronic and electrochemical properties as depicted from the results of I-V characteristics and electrochemical impedance responses.

3.4.5. SERS-based sensing applications of large-area graphene oxide and reduced graphene oxide for Rhodamine B detection

Surface-enhanced Raman spectroscopy (SERS) is a highly-sensitive and promising Raman spectroscopy technique, enabling significant enhancement of Raman signals of adsorbed analyte molecules on an engineered surface[42]. Usually, metallic nanoparticles, such as Au, Ag coated glass / SiO_2 substrates are used as SERS substrate to enhance the Raman signal of analytes, which have very weak Raman signal. More recently, semiconductors have also been used as SERS substrates, where the enhancement factor is much lower than that of metallic SERS substrates. Rhodamine B (RhB) molecules are highly fluorescent in nature and have a very weak Raman signal. The intensity of the Raman signal for RhB molecule can be enhanced on the GO and RGO by using SERS technique. The efficacy of UGO, GO, and RGO in sensing the low concentration of RhB is studied using the SERS technique, as represented by **Fig. 3.14a, 3.14b,** and **Fig. 3.15a**, respectively.

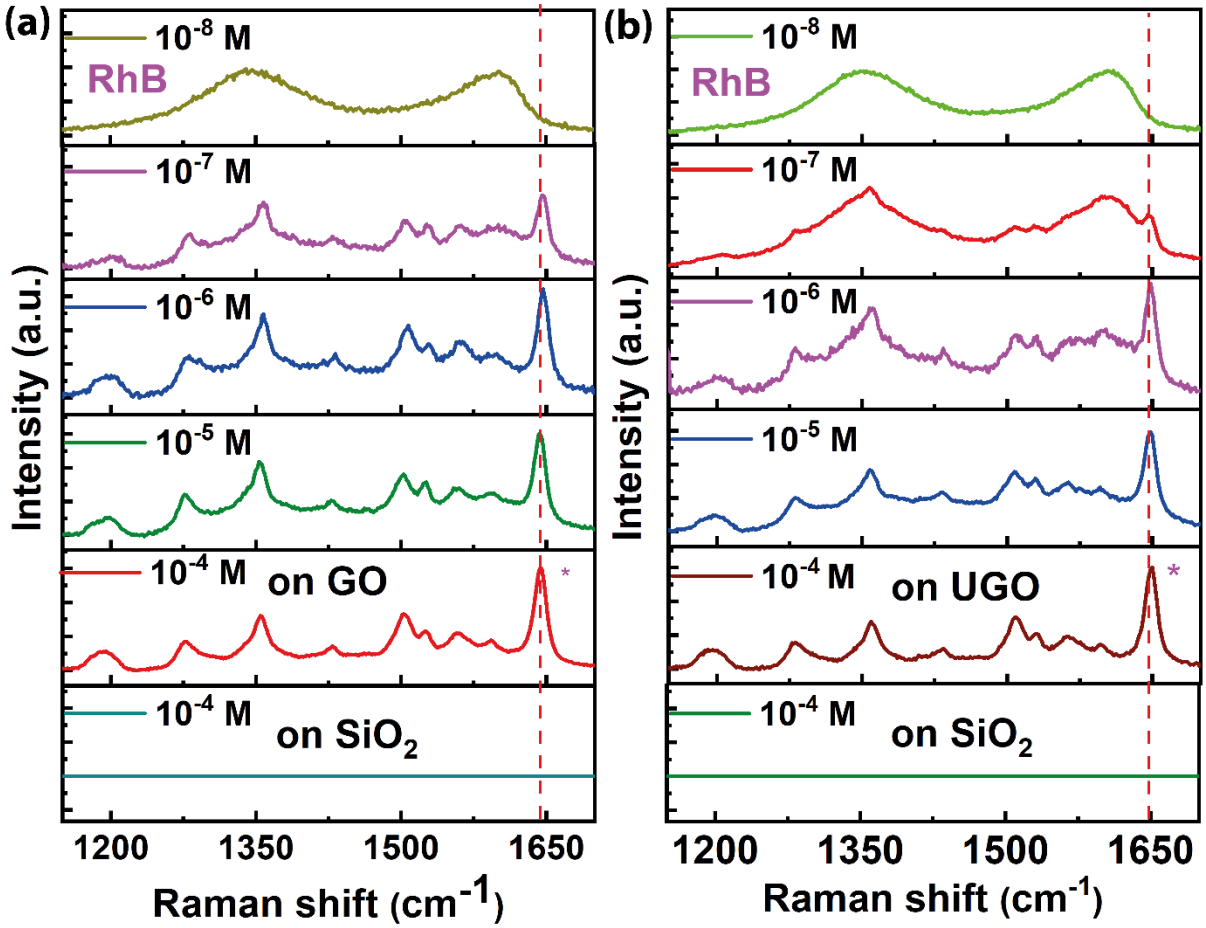

Fig. 3.14: (a) Raman spectra of different concentrations of RhB on GO; (b) Raman spectra of different concentrations of RhB on UGO

RhB at a concentration of 10^{-4} M has no Raman signal when placed on SiO_2/Si substrate. However, with GO and RGO as substrates, the enhancement of Raman intensity is observed, indicating the detection of RhB on the substrates. The corresponding seven peak positions of the RhB is explained in **Table 3.2**. The prominent peak at 1647 cm^{-1} is taken as the detection signal for the UGO, GO, and RGO materials. With the initial concentration of 10^{-4} M of RhB, the sharp peak at 1647 cm^{-1} is observed for all the substrates of UGO, GO, and RGO. The peaks with indexing values of relevant Raman shifts of the GO substrate is shown in **Fig. 3.15b**. On diluting the RhB to 10^{-5} M there is a decrease in the peak intensity, showing the change in the intensity of the peak at 1647 cm^{-1} as a function of the concentration of RhB for all the three substrates. On further diluting to 10^{-6} M, there is still detection of RhB with lower intensity of the peak. Furthermore, significant detection is observed down to the concentration of 10^{-7} M for GO and UGO. Interestingly, the detection is observed down to a concentration of 10^{-8} M RhB for RGO substrate. However, the peak at 1647 cm^{-1} disappears on subsequent dilution to 10^{-8} M for both GO and UGO substrates. Thus, the GO, and UGO have better Raman signal for the lower concentrations of RhB down to 10^{-7} M. And, Raman spectra of 10^{-2} M concentration of RhB on SiO_2/Si is measured to analysed the enhancement factor (*EF*) of other substrates (GO, UGO, and RGO), or used as a reference for EF of other substrates, which is shown in **Fig. 3.15c**.

Table 3.2. *Raman peak positions for RhB molecule*[43]

Raman Peak Position (cm^{-1})	**Bond details**
1647	C-C stretching
1595	C-C stretching
1560	C-C stretching
1508	C-C stretching
1358	C-C stretching
1281	C-O-C stretching
1199	C-H Bending

The mild heating-based exfoliated GO sheets exhibit a high enhancement of the Raman signal compared to the ultrasonic-based UGO. It is observed that there is a sudden enhancement of the Raman signal for the 10^{-7} M of the RhB molecules on the UGO substrate. The detection of RhB on GO and RGO substrates even at lower concentrations indicated by the amplification of the Raman signal is contributed by the π-π stacking and from the local electric field generated

by sp^2 carbon domains. The enhancement of the Raman signal is also explained when LUMO levels of the RhB are aligned or closer to the Fermi Energy level of the graphene-based substrates[44]. Recently, Das et al. demonstrated high SERS sensitivity of nitrogen-doped graphene quantum dots[45].

The mechanism of the SERS is mainly contributed by two components; electromagnetic enhancement and chemical enhancement[45]. he electromagnetic enhancement arises from the localized electromagnetic field of metallic nature. The chemical enhancement factor is due to the charge transfer phenomenon. In the present case, the electromagnetic enhancement is negligible due to the semiconducting nature of GO and RGO. The primary reason for the enhancement is the charge transfer between the GO or RGO and the RhB molecules. The $\pi - \pi$ stacking between GO or RGO and RhB molecules could assist in better interaction, increasing the charge transfer from the substrate to the adsorbed molecules. In the SERS measurement on the GO substrate, the enhancement of the signal is obtained in all the peaks, including G-band and D-band. However, the G-band and D-band are subtracted to illustrate the Raman pattern for RhB. GO, which has several defects due to functional groups, has higher enhancement in the Raman peak as the interaction sites increase to combine with more RhB molecules than RGO.

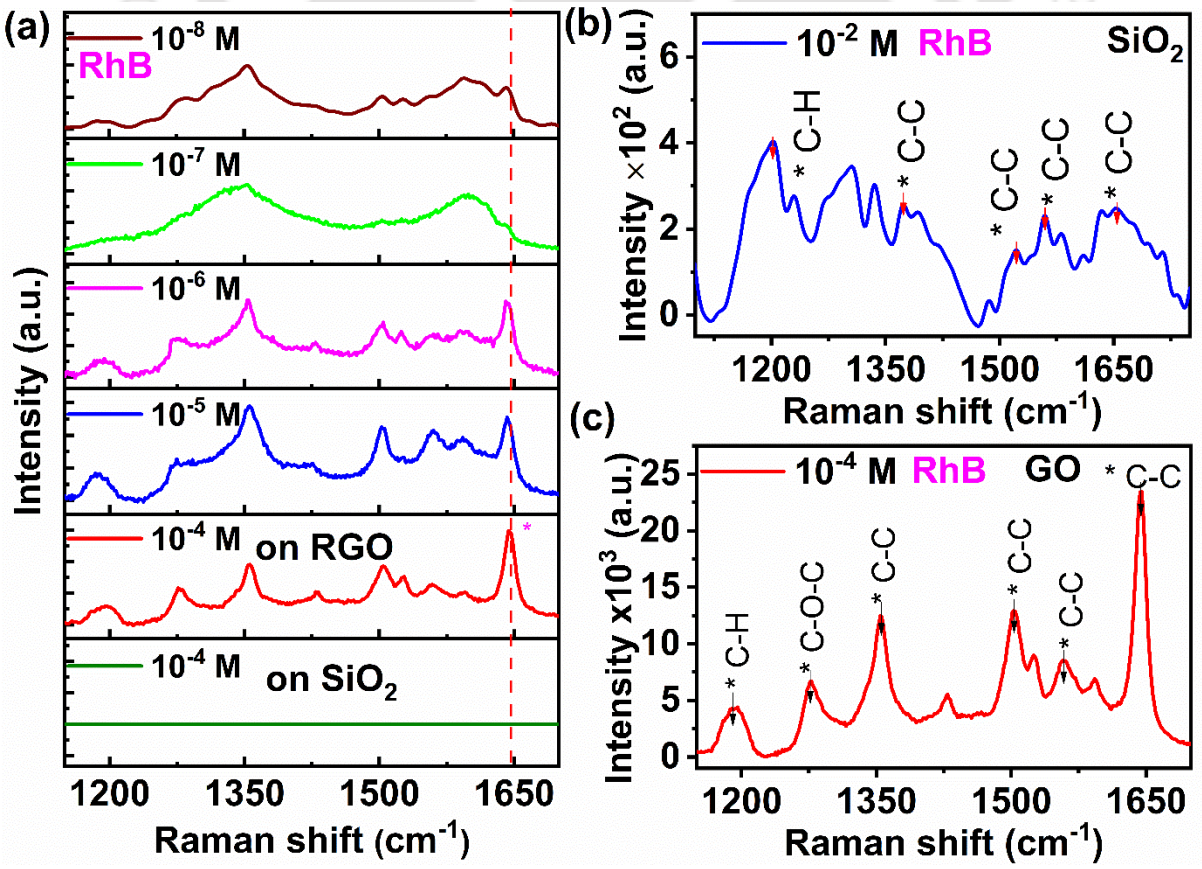

Fig. 3.15: (a) Raman spectra of different concentrations of RhB on RGO; (b)Raman spectrum of 10^{-2} M concentration of RhB on SiO_2/Si substrate; (c) Raman spectrum analysis of 10^{-4} M concentration of RhB on GO substrate.

During the SERS technique, if different substrate samples are used with different Raman characterization parameters such as laser power and accumulation time, then the formula for the enhancement factor is below,

$$EF = \frac{I_{SERS}}{I_R} \times \frac{C_R}{C_{SERS}} \times \frac{P_R}{P_{SERS}} \times \frac{T_R}{T_{SERS}}$$

Whereas, P_{SERS} is the laser excitation power in SERS measurement on GO/RGO substrate, T_{SERS} is the accumulation time of the SERS measurement on GO/RGO substrate, P_R is the laser excitation power of the Raman signal on base SiO_2 substrate, and T_R is the accumulation time of the Raman signal on base SiO_2 substrate.

If the volume of the sample solution is used differently in Raman characterization measurement, then the EF formula[46] is given below,

$$EF = \frac{I_{SERS}}{I_R} \times \frac{C_R}{C_{SERS}} \times \frac{P_R}{P_{SERS}} \times \frac{T_R}{T_{SERS}} \times \frac{N_R}{N_{SERS}}$$

Whereas, N_{SERS} is the volume of the concentration solution used for SERS signal on GO/RGO substrate, and N_R is the volume of the concentration solution used for the Raman signal on base SiO_2 substrate.

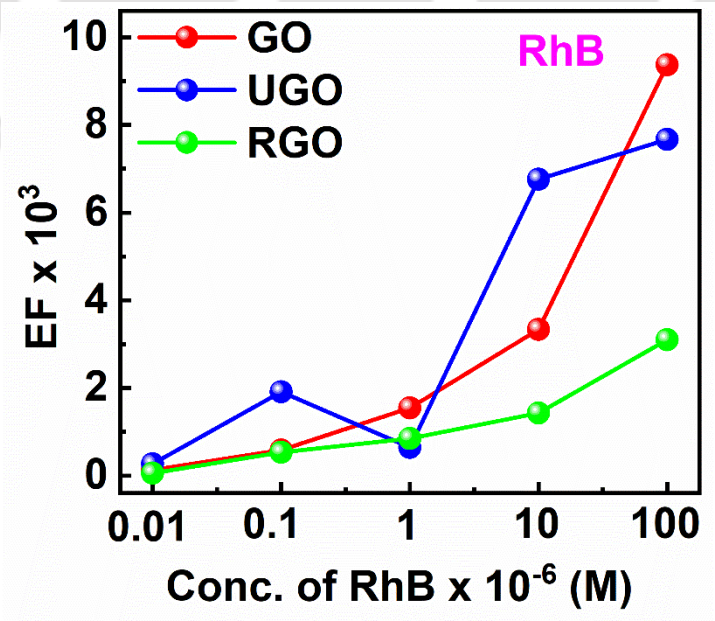

Fig. 3.16: Raman intensity for RhB (1647 cm^{-1}) peak for UGO, GO, and rGO substrates at different concentrations.

The *EF* for SERS is a valuable parameter for studying the effect of substrates for SERS on a material. It is commonly defined as the ratio of the SERS signal intensity to the intensity of the Raman signal under identical conditions (e.g., laser power, data accumulation time, the concentration of the analyte) on different substrates[47]. The most acceptable mathematical formula for the calculation of *EF* is given below, with varying concentrations of the analyte studied on different substrates:

$$EF = \frac{I_{SERS}}{I_R} \times \frac{C_R}{C_{SERS}}$$

Where, I_{SERS} is the peak intensity of the SERS signal on GO/RGO substrate at 1647 cm^{-1}, C_{SERS} is the concentration of the RhB for measuring SERS signal on GO/RGO substrate, I_R is the peak intensity of the Raman signal for RhB on SiO_2 base substrate, C_R is the higher concentration of the RhB up to which Raman signal is detected on SiO_2 base substrate.

To simplify the calculation of the *EF*, the same volume of solution and experimental parameters are maintained, such as laser excitation wavelength (532 nm) and laser power (5 mW), accumulation time (10 seconds). The concentration of RhB for SERS measurement is 10^{-4} M and the higher concentration of RhB up to which Raman signal is detected on SiO_2 base substrate is 10^{-2} M, shown in **Fig.3.15b**. The volume of the solution used to drop-cast on both substrate samples is 5 μL.

So, the value of the EF for RGO at 10^{-4} M concentration of RhB is given by,

$$EF = \frac{7750/10^{-4}}{247/10^{-2}} = 3137$$

So, the *EF* value of the RGO substrate for RhB is 3.137 $\times 10^3$ at 1647 cm^{-1} for 10^{-4} M concentration of RhB using laser excitation of 532 nm. The *EF* value of the GO and UGO substrates are calculated to be 9.482 $\times 10^3$ and 7.759 $\times 10^3$ for 10^{-4} M concentration of RhB at 1647 cm^{-1} using the same laser excitation; a relative comparison of *EF* with substrate is shown in **Fig.3.16**. Thus, the *EF* value for GO is about three times higher than that of RGO, and about 1.22 times higher than UGO. *EF* values for various substrates at different Raman peaks are shown in **Table 3.3**. Thus, the GO has better enhanced the Raman signal of the RhB molecules as compared to that of RGO. This enhancement of the Raman signal may be due to the interaction between the RhB molecules and functional groups present on the GO sheets. Interestingly, the EF value calculated here is the highest among the reported values for GO. Usually, the reported EF corresponding to the chemical enhancement is only ~10^3, about one

order of magnitude lower than the value observed for GO. Thus, the large area GO, and RGO flakes developed in this work by the simplified technique can be applied as substrates in sensing low concentration molecules using SERS/ graphene-enhanced Raman spectroscopy (GERS) technique.

***Table 3.3**. Raman intensity and Enhancement Factors for various substrates at different Raman shifts.*

Peak position (cm^{-1})	**Raman intensity for RhB on SiO_2 substrate (a.u.)**	**Raman intensity for RhB on RGO substrate (a.u.)**	**EF of RGO substrate**	**Raman intensity for RhB on GO substrate (a.u.)**	**EF of GO substrate**
1647	247	7750	3137	23423	9482
1596	188	3261	1734	8571	4559
1505	150	4829	3219	12946	8630
1356	255	4806	1884	12158	4767
1286	344	3042	884	6642	1930
1196	403	1474	365	4277	790

3.5. Conclusion

In summary, we have demonstrated a cost-effective and facile approach using mild heating to exfoliate graphene oxide (GO) sheets with ultra-large lateral size up to 104 µm, the largest size reported to date, using a simplified technique with varied layers (mono, bi, and few layers), superior to commonly used ultrasonic technique. Subsequently, the reduction was carried out to obtain less defective graphene sheets (RGO) as indicated by I_D/I_G from Raman studies. Correlation between the number of GO layers and the I_D/I_G ratio was obtained from Raman spectra in which the I_D/I_G ratio decreases linearly (from 0.97 to 0.73) with an increase in the number of layers in GO (mono, bi, <5, <10 and > 10 layers). Results from FTIR, XPS, UV-vis, PL, and TGA/DTG confirmed the removal of oxygen-containing functional groups in RGO, suggesting the minimization of defect-induced disorder in graphene carbon framework, which results in restoration of sp^2 hybridized honeycomb skeleton. In RGO, the current flow was significantly improved from micro-ampere to milli-ampere, which is 3 orders of magnitude change, arising from the good ohmic contact formation on RGO as confirmed from the linear I-V curve, indicating the high quality of the graphene-based sheets. The electrochemical impedance results corroborate with the I-V characteristics, exhibiting much lower charge transfer resistance (R_{ct}=193.2 Ω) for RGO than that of GO (R_{ct}=958.3 Ω), which depicts the

higher conductivity across the liquid/solid interface for the former as compared to the latter electrode materials. The large area GO and RGO sheets have been utilized for SERS application for detecting Rhodamine B (RhB) down to a concentration of 10 nM, and a large SERS enhancement factor of 10^4 is reported. Thus, the present simplified and economical approach of large-area graphene oxide could potentially open up a new strategy for industrial-scale production for cutting-edge sensing applications.

Reference

(1) Novoselov, K. S.; Geim, A. K.; Morozov, S. V; Jiang, D.; Zhang, Y.; Dubonos, S. V.; Grigorieva, I. V; Firsov, A. A. Electric Field Effect in Atomically Thin Carbon Films Supplementary. *Science (80-.).* **2004**, *5* (1), 1–12. https://doi.org/10.1126/science.aab1343.

(2) Parvez, K.; Wu, Z. S.; Li, R.; Liu, X.; Graf, R.; Feng, X.; Müllen, K. Exfoliation of Graphite into Graphene in Aqueous Solutions of Inorganic Salts. *J. Am. Chem. Soc.* **2014**, *136* (16), 6083–6091. https://doi.org/10.1021/ja5017156.

(3) Parvez, K.; Worsley, R.; Alieva, A.; Felten, A.; Casiraghi, C. Water-Based and Inkjet Printable Inks Made by Electrochemically Exfoliated Graphene. *Carbon N. Y.* **2019**, *149*, 213–221. https://doi.org/10.1016/j.carbon.2019.04.047.

(4) Tang, L.; Li, X.; Ji, R.; Teng, K. S.; Tai, G.; Ye, J.; Wei, C.; Lau, S. P. Bottom-up Synthesis of Large-Scale Graphene Oxide Nanosheets. *J. Mater. Chem.* **2012**, *22* (12), 5676–5683. https://doi.org/10.1039/c2jm15944a.

(5) Tung, T. T.; Yoo, J.; Alotaibi, F. K.; Nine, M. J.; Karunagaran, R.; Krebsz, M.; Nguyen, G. T.; Tran, D. N. H.; Feller, J. F.; Losic, D. Graphene Oxide-Assisted Liquid Phase Exfoliation of Graphite into Graphene for Highly Conductive Film and Electromechanical Sensors. *ACS Appl. Mater. Interfaces* **2016**, *8* (25), 16521–16532. https://doi.org/10.1021/acsami.6b04872.

(6) Suk, J. W.; Piner, R. D.; An, J.; Ruoff, R. S. Mechanical Properties of Monolayer Graphene Oxide. *ACS Nano* **2010**, *4* (11), 6557–6564. https://doi.org/10.1021/nn101781v.

(7) Cheng-An, T.; Hao, Z.; Fang, W.; Hui, Z.; Xiaorong, Z.; Jianfang, W. Mechanical Properties of Graphene Oxide/Polyvinyl Alcohol Composite Film. *Polym. Polym. Compos.* **2017**, *25* (1), 11–16. https://doi.org/10.1177/096739111702500102.

(8) Kim, J.; Kim, J.; Song, S.; Zhang, S.; Cha, J.; Kim, K.; Yoon, H.; Jung, Y.; Paik, K. W.; Jeon, S. Strength Dependence of Epoxy Composites on the Average Filler Size of Non-Oxidized Graphene Flake. *Carbon N. Y.* **2017**, *113*, 379–386. https://doi.org/10.1016/j.carbon.2016.11.023.

(9) Yoo, B. M.; Shin, H. J.; Yoon, H. W.; Park, H. B. Graphene and Graphene Oxide and Their Uses in Barrier Polymers. *J. Appl. Polym. Sci.* **2014**, *131* (1), 1–23. https://doi.org/10.1002/app.39628.

(10) Smith, A. T.; LaChance, A. M.; Zeng, S.; Liu, B.; Sun, L. Synthesis, Properties, and Applications of Graphene Oxide/Reduced Graphene Oxide and Their Nanocomposites. *Nano Mater. Sci.* **2019**, *1* (1), 31–47. https://doi.org/10.1016/j.nanoms.2019.02.004.

(11) Ghauri, F.; Raza, M.; Baig, M.; Ibrahim, S. Corrosion Study of the Graphene Oxide and Reduced Graphene Oxide-Based Epoxy Coatings. *Mater. Res. Express* **2017**, *4*. https://doi.org/10.1088/2053-1591/aa9aac.

(12) Hu, K.; Ohto, T.; Chen, L.; Han, J.; Wakisaka, M.; Nagata, Y.; Fujita, J. I.; Ito, Y. Graphene Layer Encapsulation of Non-Noble Metal Nanoparticles as Acid-Stable Hydrogen Evolution Catalysts. *ACS*

Energy Lett. **2018**, *3* (7), 1539–1544. https://doi.org/10.1021/acsenergylett.8b00739.

(13) Choi, J. Il; Abdelhafiz, A.; Buntin, P.; Vitale, A.; Robertson, A. W.; Warner, J.; Jang, S. S.; Alamgir, F. M. Contiguous and Atomically Thin Pt Film with Supra-Bulk Behavior Through Graphene-Imposed Epitaxy. *Adv. Funct. Mater.* **2019**, *1902274*, 1902274. https://doi.org/10.1002/adfm.201902274.

(14) Dong, L.; Yang, J.; Chhowalla, M.; Loh, K. P. Synthesis and Reduction of Large Sized Graphene Oxide Sheets. *Chem. Soc. Rev.* **2017**, *46* (23), 7306–7316. https://doi.org/10.1039/c7cs00485k.

(15) Su, C. Y.; Lu, A. Y.; Xu, Y.; Chen, F. R.; Khlobystov, A. N.; Li, L. J. High-Quality Thin Graphene Films from Fast Electrochemical Exfoliation. *ACS Nano* **2011**, *5* (3), 2332–2339. https://doi.org/10.1021/nn200025p.

(16) Gee, C. M.; Tseng, C. C.; Wu, F. Y.; Chang, H. P.; Li, L. J.; Hsieh, Y. P.; Lin, C. Te; Chen, J. C. Flexible Transparent Electrodes Made of Electrochemically Exfoliated Graphene Sheets from Low-Cost Graphite Pieces. *Displays* **2013**, *34* (4), 315–319. https://doi.org/10.1016/j.displa.2012.11.002.

(17) Tang, H.; He, P.; Huang, T.; Cao, Z.; Zhang, P.; Wang, G.; Wang, X.; Ding, G.; Xie, X. Electrochemical Method for Large Size and Few-Layered Water-Dispersible Graphene. *Carbon N. Y.* **2019**, *143*, 559–563. https://doi.org/10.1016/j.carbon.2018.11.058.

(18) Wu, L.; Li, W.; Li, P.; Liao, S.; Qiu, S.; Chen, M.; Guo, Y.; Li, Q.; Zhu, C.; Liu, L. Powder, Paper and Foam of Few-Layer Graphene Prepared in High Yield by Electrochemical Intercalation Exfoliation of Expanded Graphite. *Small* **2014**, *10* (7), 1421–1429. https://doi.org/10.1002/smll.201302730.

(19) Roscher, S.; Hoffmann, R.; Prescher, M.; Knittel, P.; Ambacher, O. High Voltage Electrochemical Exfoliation of Graphite for High-Yield Graphene Production. *RSC Adv.* **2019**, *9* (50), 29305–29311. https://doi.org/10.1039/c9ra04795f.

(20) Achee, T. C.; Sun, W.; Hope, J. T.; Quitzau, S. G.; Sweeney, C. B.; Shah, S. A.; Habib, T.; Green, M. J. High-Yield Scalable Graphene Nanosheet Production from Compressed Graphite Using Electrochemical Exfoliation. *Sci. Rep.* **2018**, *8* (1), 1–8. https://doi.org/10.1038/s41598-018-32741-3.

(21) Cai, C.; Sang, N.; Shen, Z.; Zhao, X. Facile and Size-Controllable Preparation of Graphene Oxide Nanosheets Using High Shear Method and Ultrasonic Method. *J. Exp. Nanosci.* **2017**, *12* (1), 1–16. https://doi.org/10.1080/17458080.2017.1303853.

(22) Chen, I. W. P.; Chen, Y. S.; Kao, N. J.; Wu, C. W.; Zhang, Y. W.; Li, H. T. Scalable and High-Yield Production of Exfoliated Graphene Sheets in Water and Its Application to an All-Solid-State Supercapacitor. *Carbon N. Y.* **2015**, *90*, 16–24. https://doi.org/10.1016/j.carbon.2015.03.067.

(23) No, Y.-S.; Choi, H. K.; Kim, J.-S.; Kim, H.; Yu, Y.-J.; Choi, C.-G.; Choi, J. S. Layer Number Identification of CVD-Grown Multilayer Graphene Using Si Peak Analysis. *Sci. Rep.* **2018**, *8* (1), 571. https://doi.org/10.1038/s41598-017-19084-1.

(24) Niu, L.; Li, M.; Tao, X.; Xie, Z.; Zhou, X.; Raju, A. P. A.; Young, R. J.; Zheng, Z. Salt-Assisted Direct

Exfoliation of Graphite into High-Quality, Large-Size, Few-Layer Graphene Sheets. *Nanoscale* **2013**, *5* (16), 7202–7208. https://doi.org/10.1039/c3nr02173d.

(25) Narayan, R.; Lim, J.; Jeon, T.; Li, D. J.; Kim, S. O. Perylene Tetracarboxylate Surfactant Assisted Liquid Phase Exfoliation of Graphite into Graphene Nanosheets with Facile Re-Dispersibility in Aqueous/Organic Polar Solvents. *Carbon N. Y.* **2017**, *119*, 555–568. https://doi.org/10.1016/j.carbon.2017.04.071.

(26) Xing, X.; Zhang, X.; Zhang, K.; Jin, L.; Cao, Q. Preparation of Large-Sized Graphene from Needle Coke and the Adsorption for Malachite Green with Its Graphene Oxide. *Fullerenes Nanotub. Carbon Nanostructures* **2019**, *27* (2), 97–105. https://doi.org/10.1080/1536383X.2018.1512099.

(27) Geng, X.; Guo, Y.; Li, D.; Li, W.; Zhu, C.; Wei, X.; Chen, M.; Gao, S.; Qiu, S.; Gong, Y.; Wu, L.; Long, M.; Sun, M.; Pan, G.; Liu, L. Interlayer Catalytic Exfoliation Realizing Scalable Production of Large-Size Pristine Few-Layer Graphene. *Sci. Rep.* **2013**, *3*, 1–6. https://doi.org/10.1038/srep01134.

(28) Zhu, Y.; Stoller, M. D.; Cai, W.; Velamakanni, A.; Piner, R. D.; Chen, D.; Ruoff, R. S. Exfoliation of Graphite Oxide in Propylene Carbonate and Thermal Reduction of the Resulting Graphene Oxide Platelets. *ACS Nano* **2010**, *4* (2), 1227–1233. https://doi.org/10.1021/nn901689k.

(29) Hu, Y.; Su, M.; Xie, X.; Sun, C.; Kou, J. Few-Layer Graphene Oxide with High Yield via Efficient Surfactant-Assisted Exfoliation of Mildly-Oxidized Graphite. *Appl. Surf. Sci.* **2019**, *494* (February), 1100–1108. https://doi.org/10.1016/j.apsusc.2019.07.111.

(30) Kim, H. R.; Lee, S. H.; Lee, K. H. Scalable Production of Large Single-Layered Graphenes by Microwave Exfoliation 'in Deionized Water.' *Carbon N. Y.* **2018**, *134*, 431–438. https://doi.org/10.1016/j.carbon.2018.04.014.

(31) Wu, W.; Xu, J.; Tang, X.; Xie, P.; Liu, X.; Xu, J.; Zhou, H.; Zhang, D.; Fan, T. Two-Dimensional Nanosheets by Rapid and Efficient Microwave Exfoliation of Layered Materials. *Chem. Mater.* **2018**, *30* (17), 5932–5940. https://doi.org/10.1021/acs.chemmater.8b01976.

(32) Wu, W.; Liu, M.; Gu, Y.; Guo, B.; Ma, H.; Wang, P.; Wang, X.; Zhang, R. Fast Chemical Exfoliation of Graphite to Few-Layer Graphene with High Quality and Large Size via a Two-Step Microwave-Assisted Process. *Chem. Eng. J.* **2020**, *381* (August 2019), 122592. https://doi.org/10.1016/j.cej.2019.122592.

(33) Chong, K. Y.; Chia, C. H.; Chook, S. W.; Zakaria, S.; Lucas, D. Simplified Production of Graphene Oxide Assisted by High Shear Exfoliation of Graphite with Controlled Oxidation. *New J. Chem.* **2018**, *42* (6), 4507–4512. https://doi.org/10.1039/c7nj04911k.

(34) Park, W. K.; Yoon, Y.; Song, Y. H.; Choi, S. Y.; Kim, S.; Do, Y.; Lee, J.; Park, H.; Yoon, D. H.; Yang, W. S. High-Efficiency Exfoliation of Large-Area Mono-Layer Graphene Oxide with Controlled Dimension. *Sci. Rep.* **2017**, *7* (1), 1–9. https://doi.org/10.1038/s41598-017-16649-y.

(35) Arao, Y.; Mizuno, Y.; Araki, K.; Kubouchi, M. Mass Production of High-Aspect-Ratio Few-Layer-Graphene by High-Speed Laminar Flow. *Carbon N. Y.* **2016**, *102*, 330–338.

https://doi.org/10.1016/j.carbon.2016.02.046.

(36) Wu, Z. S.; Ren, W.; Gao, L.; Liu, B.; Jiang, C.; Cheng, H. M. Synthesis of High-Quality Graphene with a Pre-Determined Number of Layers. *Carbon N. Y.* **2009**, *47* (2), 493–499. https://doi.org/10.1016/j.carbon.2008.10.031.

(37) Ogino, I.; Yokoyama, Y.; Iwamura, S.; Mukai, S. R. Exfoliation of Graphite Oxide in Water without Sonication: Bridging Length Scales from Nanosheets to Macroscopic Materials. *Chem. Mater.* **2014**, *26* (10), 3334–3339. https://doi.org/10.1021/cm501305c.

(38) Chuang, C. H.; Wang, Y. F.; Shao, Y. C.; Yeh, Y. C.; Wang, D. Y.; Chen, C. W.; Chiou, J. W.; Ray, S. C.; Pong, W. F.; Zhang, L.; Zhu, J. F.; Guo, J. H. The Effect of Thermal Reduction on the Photoluminescence and Electronic Structures of Graphene Oxides. *Sci. Rep.* **2014**, *4*, 1–7. https://doi.org/10.1038/srep04525.

(39) Aboutalebi, S. H.; Chidembo, A. T.; Salari, M.; Konstantinov, K.; Wexler, D.; Kun Liu, H.; Xue Dou, S. Comparison of GO, GO/MWCNTs Composite and MWCNTs as Potential Electrode Materials for Supercapacitors. *Energy Environ. Sci.* **2011**, *4* (5), 1855–1865. https://doi.org/10.1039/c1ee01039e.

(40) Xiang, C.; Li, M.; Zhi, M.; Manivannan, A.; Wu, N. A Reduced Graphene Oxide/Co3O4 Composite for Supercapacitor Electrode. *J. Power Sources* **2013**, *226*, 65–70. https://doi.org/10.1016/j.jpowsour.2012.10.064.

(41) Yang, X.; Zhang, F.; Zhang, L.; Zhang, T.; Huang, Y.; Chen, Y. A High-Performance Graphene Oxide-Doped Ion Gel as Gel Polymer Electrolyte for All-Solid-State Supercapacitor Applications. *Adv. Funct. Mater.* **2013**, *23* (26), 3353–3360. https://doi.org/10.1002/adfm.201203556.

(42) Sharma, B.; Frontiera, R. R.; Henry, A. I.; Ringe, E.; Van Duyne, R. P. SERS: Materials, Applications, and the Future. *Mater. Today* **2012**, *15* (1–2), 16–25. https://doi.org/10.1016/S1369-7021(12)70017-2.

(43) Huh, S.; Park, J.; Kim, Y. S.; Kim, K. S.; Hong, B. H.; Nam, J. M. UV/Ozone-Oxidized Large-Scale Graphene Platform with Large Chemical Enhancement in Surface-Enhanced Raman Scattering. *ACS Nano* **2011**, *5* (12), 9799–9806. https://doi.org/10.1021/nn204156n.

(44) Feng, S.; Cristina dos Santos, M.; Carvalho, B. R.; Lv, R.; Li, Q.; Fujisawa, K.; Elías, A. L.; Lei, Y.; Perea-López, N.; Endo, M.; Pan, M.; Pimenta, M. A.; Terrones, M. Ultrasensitive Molecular Sensor Using N-Doped Graphene through Enhanced Raman Scattering. *Sci. Adv.* **2016**, *2* (7), 1–13. https://doi.org/10.1126/sciadv.1600322.

(45) Das, R.; Parveen, S.; Bora, A.; Giri, P. K. Origin of High Photoluminescence Yield and High SERS Sensitivity of Nitrogen-Doped Graphene Quantum Dots. *Carbon N. Y.* **2020**, *160*, 273–286. https://doi.org/10.1016/j.carbon.2020.01.030.

(46) Xu, Y.; Konrad, M. P.; Trotter, J. L.; McCoy, C. P.; Bell, S. E. J. Rapid One-Pot Preparation of Large Freestanding Nanoparticle-Polymer Films. *Small* **2017**, *13* (2). https://doi.org/10.1002/smll.201602163.

(47) Le Ru, E. C.; Blackie, E.; Meyer, M.; Etchegoint, P. G. Surface Enhanced Raman Scattering Enhancement Factors: A Comprehensive Study. *J. Phys. Chem. C* **2007**, *111* (37), 13794–13803. https://doi.org/10.1021/jp0687908.

Chapter 4

Plasma Treated Graphene Oxide Surface for Trace Dye Detection using Surface-enhanced Raman Spectroscopy

In this **Chapter**, we employ plasma treatment for large lateral-size GO and RGO sheets to modify the surface, leading to structural change in the carbon skeleton. Various gas plasma environments were used during the treatment processes, such as Ar, N_2, O_2, and H_2 (diluted with Ar). Using Raman and FTIR spectroscopy, the resulting substrates were used to investigate the structural disorder and characteristics. The surface morphology of the synthesized GO and RGO was studied using FESEM, AFM, and FETEM. The functionality of the GO and RGO (with or without plasma treatments) in terms of their sensitivity to various dyes such as Methyl orange (MO), Methyl blue (MB), Rose Bengal (RB), and RhB were explored using surface-enhanced Raman spectroscopy technique. Further, the addition of noble metal (Au NPs) was examined to form a composite with GO and RGO, and its SERS performance to detect various dyes was studied.

4.1. Introduction

In recent times, trace detection for the various analyte (dyes, pesticides, food adulterants, etc.) has been enabled by employing surface-enhanced Raman spectroscopy (SERS). In most cases, gold or silver nanoparticles/nanostructured substrates are used to enhance the analyte's Raman signal in the SERS technique. Silver is a relatively better choice due to its lower cost than gold. However, the instability of the metals, susceptible to oxidation and sulfidation, could hinder the efficiency and consistency of the substrate for creating a plasmonic hotspot, thereby decreasing the sensitivity of the target molecules.

Graphene-based materials are promising applications in SERS sensors because they are low-cost, abundantly available raw materials (graphite), biocompatibility, tunable sheet layers, controllable lateral size, and tunable electronic properties. Furthermore, graphene exhibits a uniform surface, high absorptivity, and high stability. Ling et al.[1] first observed the effect of graphene in Raman signals in which many unknown peaks emerged when the graphene substrate was treated with organic solvent as compared to that of SiO_2/Si substrate. Graphene-based SERS substrates are enhanced predominantly by the chemical enhancement (CE)

mechanism through charge transfer processes[2]. Monolayer and a few layers of graphene were found to be more efficient in enhancing the Raman signals, and the intensities decrease as the number of layers increases. Ling et al.[1] reported the SERS effect for various dyes such as the phthalocyanine (Pc), R6G, protoporphyrin (PPP), and crystal violet (CV) dyes on the graphene. A composite of GO, silicon pyramid arrays, and Ag NPs has improved the SERS signals of R6G compared to GO, as demonstrated by Zhang et al.[3]. In most of the reports, the smaller lateral size of the graphene-based substrates was used for the SERS analysis. The effect of the large lateral size of graphene on the SERS enhancement is not reported yet. Moreover, it is challenging to locate the small-dimension graphene sheets using micro Raman spectroscopy due to their high optical transparency.

Recently, plasma treatment has been used to modify the properties of the graphene oxide for functionalization, etching, creating defects, and reduction of GO[4–7]. Plasma treatment is a simple, cost-effective, efficient, energy and time-saving, and clean process. The most commonly used gases in the plasma treatment system are N_2, O_2, H_2, CH_4, NH_3, and F. However, there are very few studies on modifying the GO materials using plasma treatment, specifically for SERS applications. The role of functional groups and defects on the SERS application of GO is little understood, and it is worth exploring since it enables a metal-free platform for cost-effective and reliable SERS detection.

4.2. Experimental Details

4.2.1. Synthesis of GO and RGO

GO is synthesized using the modified Hummer's method. 0.5g of graphite flakes (~ 1mm) and $KMnO_4$ were taken in the ratio of 1:8 and mixed in a conical flake. 100 ml of H_2SO_4 was added to the mixture along with 0.5 g $NaNO_3$ and stirred overnight. The pH of graphite oxide solution (brown color) was reduced up to 4.5 and vacuum dried at 45 °C for 24 hours. Further, graphite oxide was washed using de-ionized water (Milli-Q) and propanol. Graphite oxide was exfoliated to GO sheets using the mild heating method, as reported in **chapter 2** (**section 2.2.1**). All the chemicals were purchased from *Merck*. The GO solution is drop-casted on the SiO_2/Si substrate and heated at 85 °C on the hot plate (*AnTech*) overnight to remove the absorbed water.

RGO was synthesized from the GO using thermal treatment shown in **chapter 2** (**section 2.2.3**), in which the drop-casted GO on the SiO_2/Si substrate was placed on the quartz boat and inserted inside the quartz tube. The quartz tube was placed inside a muffle

furnace (*Kejia Furnace, China*) and heated at 150 °C (for analysis of the contribution of the SERS effect from functional groups) and 360 °C for 2 hours in a vacuum environment. The furnace was ramped up/down at 8 °C/minute.

4.2.2. Gas plasma treatment

Gas plasma treatment on GO-based materials is performed using a plasma cleaner chamber (PDC-32G-2) from Harrick Plasma, a rotary vacuum pump (VT-2015), and a Pirani gauge (VT-DHP-11) from VT vacuum technologies, a gas flow controller, and reader from MKS, and other essential equipment. The schematic diagram of the gas plasma treatment system is shown in **Fig. 4.1**. The drop-casted GO, RGO, and GQDs on the SiO_2/Si substrates are used for this measurement. The explore samples are placed inside the quartz chamber of the plasma cleaner and evacuated the inside pressure down to 2.5×10^{-2} mbar with support from the rotary vacuum pump. The chamber is kept for 30 minutes in the vacuum to remove any atmospheric particles. Then, 15 sccm of each analysed gas, such as Ar, N_2, O_2, and diluted H_2, is flown inside the plasma chamber. 18 Watts of RF power is applied for the plasma treatment.

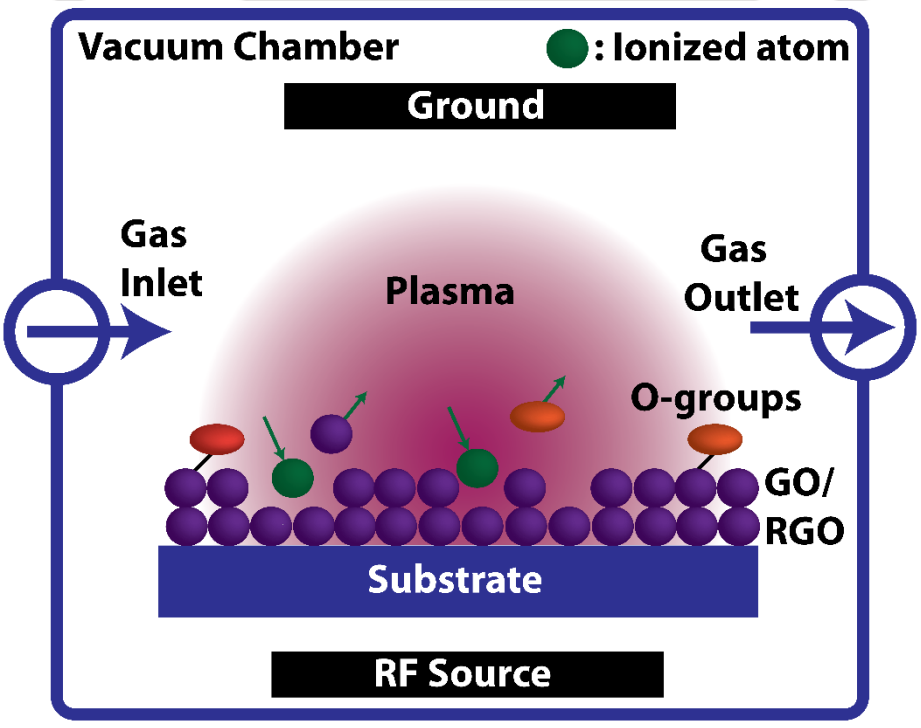

Fig. 4.1: Schematic diagram for gas plasma treatment on GO/RGO substrates.

The samples are analyzed for their characteristic change by varying the exposer duration. The analyzed duration of the exposers is 10s, 20s, 30s, 40s, 50s, 60s, and 90s for each of the gases. After exposure of each duration, the respective sample is characterized by Raman

spectroscopy with optical microscopy. Further, the same sample was exposed to another duration (like 10s + 10s: 20s) until the 90s. The samples are etched from the substrate after the 90s, and it is confirmed from the analysis of Raman spectra. The in-detail of the sample characteristic will be demonstrated in **section 4.5**. Based on the applied gases, the samples of the GO and RGO are named Ar-GO for Ar plasma-treated GO, N-GO for N_2 plasma-treated GO, and O-GO for O_2 plasma-treated GO, H-GO for diluted H_2 plasma-treated GO.

4.2.3. Synthesis of Au nanoparticles

The Au NPs were synthesized using a two-step process: deposition of the Au thin film using RF sputtering and forming Au NPs from Au thin film using RTA (rapid thermal annealing). SiO2/Si was used as the substrate for Au thin film deposition. The clean substrate was placed on the substrate holder of the sputtering system (*Excel Instrument*), and the chamber was evacuated down to 1.5 $\times 10^{-5}$ mbar using a diffusion pump supported by a rotary vacuum pump. 15 sccm of highly pure Ar (99.999%) was allowed to flow inside the vacuum chamber using a MFC, and the partial pressure was maintained at 8.6 $\times 10^{-2}$ mbar inside the chamber. 12 watts of RF power was applied to the Au sputtering target for 15 minutes, and the substrate was rotated at 2 rpm during the deposition of Au film for uniformity.

The Au thin-film deposited on SiO_2/Si substrate was treated with RTA to synthesize the Au NPs on SiO_2/Si substrate. The Au thin-film samples were placed inside the chamber of the RTA system (*ULVAC- RIKO, MILA-3000*), then evacuated to 2.2×10^{-2} mbar inside the chamber using a rotary vacuum pump. Highly pure Ar gas was allowed to flow into the system, and the pressure inside the chamber was maintained at 1 mbar. The sputtered samples were annealed at 600 °C for 3 minutes. The ramp-up and ramp-down times are the 30s and 60s, respectively. This process leads to the formation of Au NPs on the SiO_2 substrate. These samples were also analyzed for the SERS effect of the RhB molecules

4.3. Characterization techniques

The dye materials, such as Rhodamine B (RhB), Methyl blue (MB), Methyl orange (MO), and Rose Bengal (RB), were procured from *LOBA CHEMIE PVT. LTD.* The RhB, MB, MO, and RB concentrations at 10^{-4} M were prepared by adding 0.958 mg, 0.639 mg, 0.654 mg, and 1.947 mg in 20 ml of de-ionized water. Further, the dye's lower concentrations, such as (10^{-5} M, 10^{-6} M, 10^{-7} M, and 10^{-8} M) were made by adding the calculated volume of de-ionized water into the 10^{-4} M of the dye solution.

4.4. Results and discussions

4.4.1. Morphological analysis

The large-area, triangular shape of the GO sheet with slight folding is observed in the optical image, as shown in **Fig.4.2a**; the lateral dimension of the GO sheet is ~ 100 µm, which is quite large. Higher magnification images of the surface of the GO sheet obtained from the FESEM and AFM are shown in **Fig. 4.2b** and **Fig.4.2c**. The multiple folding at the edge of the GO sheet is obtained from the FETEM image (**Fig. 4.2d**), having a (002) plane as observed in the SAED pattern of **Fig. 4.2d** (**inset**). The SAED pattern is acquired from the circular-red spot on the GO sheet, as shown in **Fig. 4.2d**. The irregular fashion of the bright spots arrangement on the SAED pattern and wrinkles on the surface of the GO sheet indicates the attachment of oxygen functional groups with carbon atoms.

4.4.2. Structural analysis

The XRD pattern of GO and RGO is shown in **Fig. 4.2e.** GO and RGO peaks are located at $2\theta = 11.6°$ and $2\theta = 26.3°$, respectively, which correspond to the (002) plane of the lateral structure of carbon atoms. The graphite is located at $2\theta = 26.7°$; however, it has shifted to 11.6° after the oxidation of the graphite into graphite oxide. The interlayer spacing (d) of the GO and RGO is calculated using Bragg's law ($2d \sin\theta = n\lambda$) and found to be ~0.762 nm and ~0.34 nm, respectively. The full width at half maximum (FWHM) of the GO and RGO peaks are 4.82° and 1.05°, respectively. The GO's board peak indicates the GO's polycrystalline nature, which emerges due to the attachment of oxygen functional groups to the carbon atoms. Note that the peak position of RGO is shifted towards the graphitic peak at $2\theta = 26.3°$ with a sharper peak, depicting the restoration of the hexagonal carbon framework upon reduction from GO to RGO. However, the structural defects in RGO exist even after the de-oxidation treatment due to other stable oxygen functional groups.

The Raman spectra of the GO and RGO are shown in the range from 1100 cm^{-1} to 1700 cm^{-1} in **Fig. 4.2f**, displaying two typical broad peaks, such as D and G. The relative intensity of the D peak for RGO is less than that of GO. However, the relative intensity of the G peak of RGO is higher than that of GO, as shown in **Fig. 4.2f**. The intensity ratio (I_D/I_G) for GO and RGO are 0.89 and 1.1, respectively, and the position of the D peak is red-shifted from the GO peak at 1358 cm^{-1} to the RGO peak at 1348 cm^{-1}, which is attributed to the restoration of sp^2 carbon atoms from sp^3 carbon atoms [8]. The FWHM of the D band of GO and RGO is 161 and

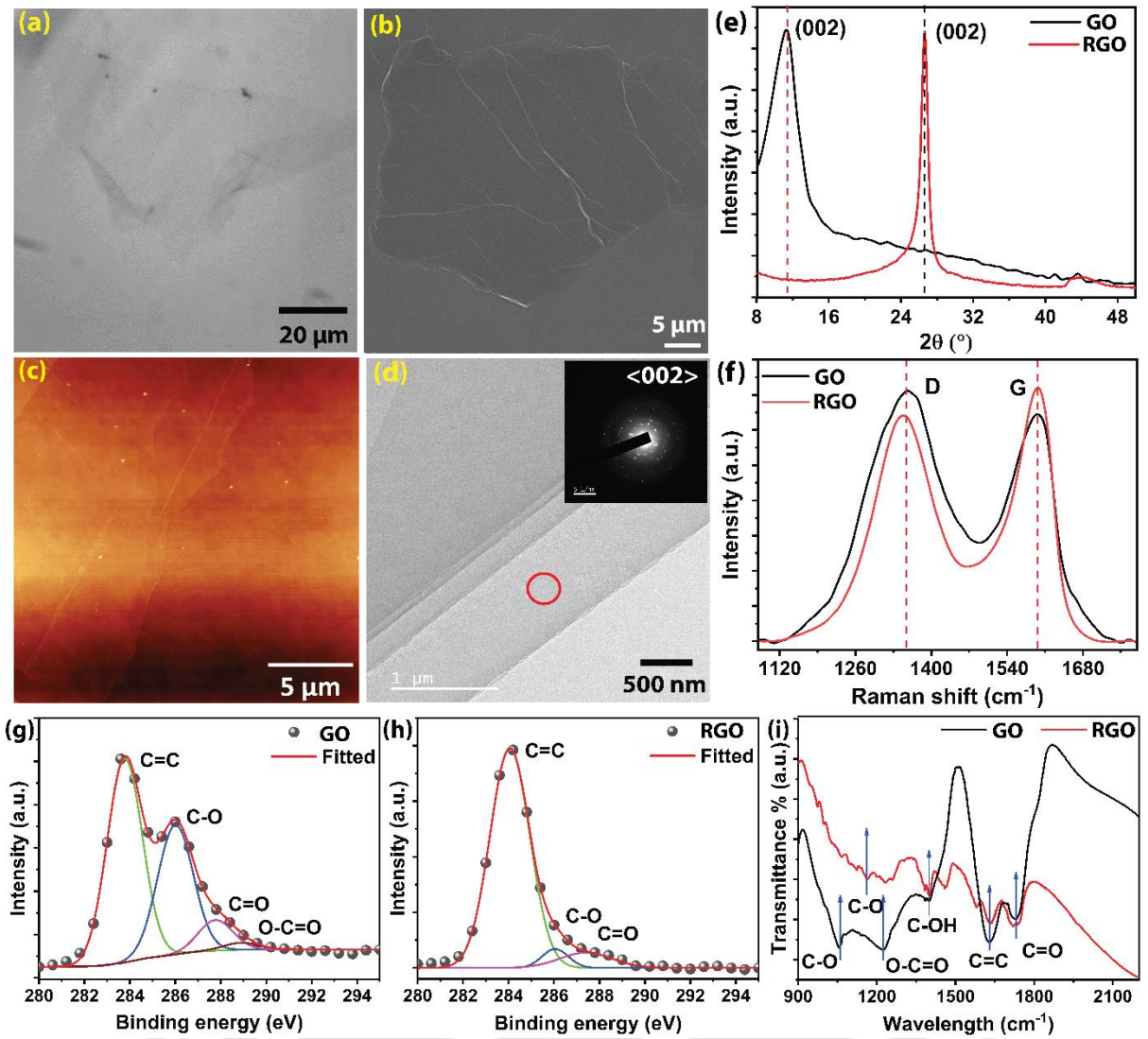

Fig. 4.2: (a) Optical microscopy image; (b) FESEM image; (c) AFM image; and (d) FETEM image (inset: SAED pattern) of GO sheet; (e) XRD pattern of GO and RGO; (f) Raman analysis of GO and RGO; XPS analysis of (g) GO, and (h) RGO; (i) FTIR analysis of GO and RGO (the respective modes are marked with arrows).

132, respectively, in which the FWHM value decreases in RGO, indicating the reduction of the oxygen functional groups attached to the skeleton of the sp^2 carbon atoms. Furthermore, the lower FWHM of the G band of RGO (90) is the characteristic of the restoration of hybridized sp^2 carbon bonds. Hence, the graphitic structure of the RGO is improved after the thermal treatment of the GO. Thus, the XRD and Raman analysis confirm that GO has a distorted graphitic structure (sp^2 hybridized carbon atoms) owing to its higher attached functional groups, and the RGO contains fewer functional groups resulting in the restoration of its graphitic structure.

The XPS analysis of the GO (**Fig. 4.2g**) and RGO (**Fig. 4.2h**) determines various oxygen functional groups attached to the basal plane of carbon atoms. The XPS spectra of C1s for the GO and RGO are plotted from 280 eV to 295 eV. The C1s band of GO and RGO is fitted with four Gaussian peaks and three Gaussian peaks, respectively. The peaks of GO at 283.8 eV, 286 eV, 287.8 eV, and 289 eV corresponded to the sp^2 carbon atoms (C=C), epoxy (C-O), carbonyl (C=O), and carboxyl (O-C=O) functional groups, respectively. The integral area of peaks for C1s of GO, related to C=C, C-O, C=O, and O-C=O bonds, are in the proportions of 55%, 35%, 8%, and 2%, respectively. In contrast, the integral area of C1s in RGO corresponding to C=C, C-O, and C=O are 87%, 5%, and 8%, respectively. Thus, the comparison between GO and RGO reveals that RGO has a much lower (3.46 times) percentage of oxygen functional groups than GO. Further, the O-C=O group has been removed from the RGO during the reduction process. For GO, the presence of higher asymmetric carbon atoms is obtained as compared to the RGO, evidenced by the lower shift of peak position for the C=C bond from 284 eV (RGO) to 283.8 eV (GO)[9].

The FTIR analysis of the GO and RGO is shown in **Fig. 4.2i**, in which the presence of oxygen functional groups (sp^3 and sp^2 carbon bonds) is exhibited. The transmittance peaks of FTIR for GO and RGO are concentrated in the range from 1000 to 2000 cm^{-1}. The peaks of C-O (alkoxyl group) at 1057 cm^{-1}, O-C=O at 1228 cm^{-1}, C-OH at 1391 cm^{-1}, C=C at 1630 cm^{-1}, and C=O at 1722 cm^{-1} are more prominent in GO. The intensity of the corresponding peaks for the C-O and O-C=O functional groups are suppressed in RGO compared to the GO. The peaks at 1391 cm^{-1} related to C-OH appear in the spectra for both GO and RGO; these may be due to the absorption of water from the atmosphere during the preparation of samples. The signature peak at 1630 cm^{-1} corresponding to C=C bonds is observed on both GO and RGO. The absorption peak from the carbonyl group (C=O) at 1740 cm^{-1} is present in both GO and RGO, which is very hard to remove even after thermal treatment. The XPS and the FTIR analyses show that the oxygen functional groups are reduced in RGO compared to the GO substrate.

4.4.3. PL analysis of RhB in graphene oxide and water solution

Photoluminescent (PL) characteristics of RhB molecules in GO and water solution are shown in figure Fig. 4.3. In the Fig. 4.3a, PL spectra for 10^{-7} M RhB solution, GO and their mixture in water are presented. Here, GO exhibits a broad PL emission with maximum intensity at ~ 570 nm. Whereas, 10^{-7} M RhB solution in water exhibits a PL emission peak at ~ 577 nm. It is observed that at low concentration of RhB, the PL emitted by the mixture is due to the combined effect of both RhB and GO. No charge transfer takes place as there is no interaction

between GO and RhB at 10^{-7} M concentration. In the Fig. 4.3b, the comparative PL spectra for 10^{-4} M RhB solution, GO and their mixture in water is displayed. The PL of GO is completely quenched when mixed with 10^{-4} M concentration of RhB. The PL emission of RhB is also reduced. This is due to the strong interaction between GO and RhB at higher concentration of the latter. There is a type 2 band alignment which aides in electron transfer from RhB to GO. This charge transfer plays a significant role in SERS enhancement and will be discussed in detail in section 4.6.3.

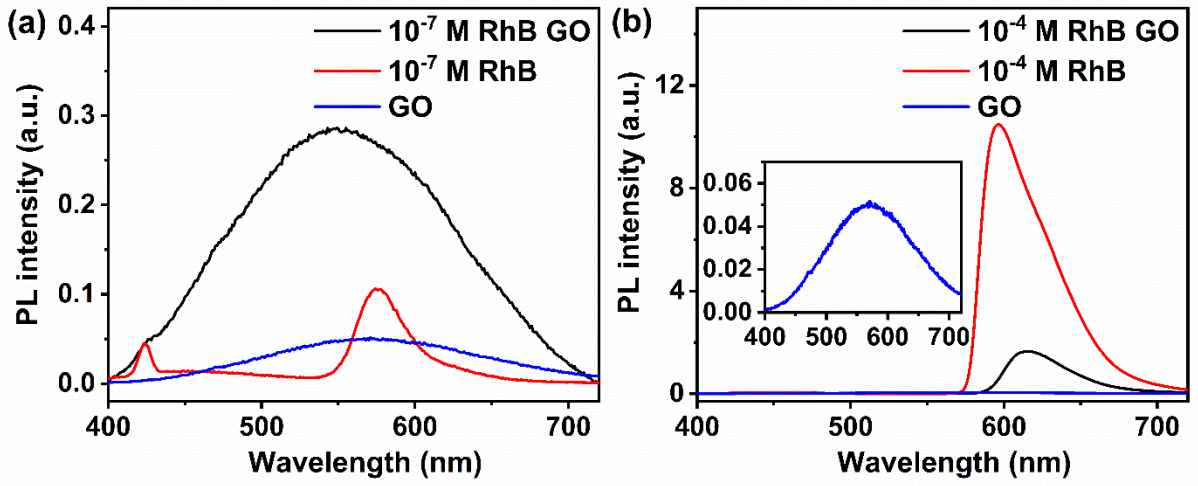

Fig. 4.3: PL analysis of different concentrations for RhB molecules dispersed in (a) GO solution; and (b) water solution with magnified (inset).

4.5. Gas plasma treatment on graphene oxide and reduced graphene oxide

4.5.1. Optimization of plasma treated duration

The gas plasma treatment on the GO is optimized by varying the duration of the RF exposer and retaining the RF power, working pressure, and gas flow rate constant. The effect of gas plasma treatment on GO is shown in **Fig. 4.4** and **Fig. 4.5**, with various gas applied to the GO. A mixer of H_2 (10%) and Ar plasma is treated on GO for 0s to 90s (**Fig.4.4**). The intensity for both the D and G bands of H-GO is reduced as increases the exposure time. This may be due to the removal of the carbon atoms and attached oxygen functional groups by the ion bombardment on the surface of GO. Raman spectra are measured on a separate GO sheet and captured an optical image before treated plasma, named 0s for all the samples. The Raman spectra are measured inside the yellow ring of the optical images, shown in **Fig. 4.5**. The intensity of the D and G bands are reduced as the duration of plasma exposure increases, and the GO is removed after the 90s. The GO etching rate depends on the exposure gas, presented in **Fig. 4.5**. In **Fig.4.5a**, the intensity of the D and G bands of Ar-GO has reduced after

increasing the duration. Thus, the characteristic of GO is losing after the 30s. The intensity of the bands is reduced as the exposure increases. Furthermore, the vanishing of the GO sheet from the optical images shows the etch of the sheet after the 90s.

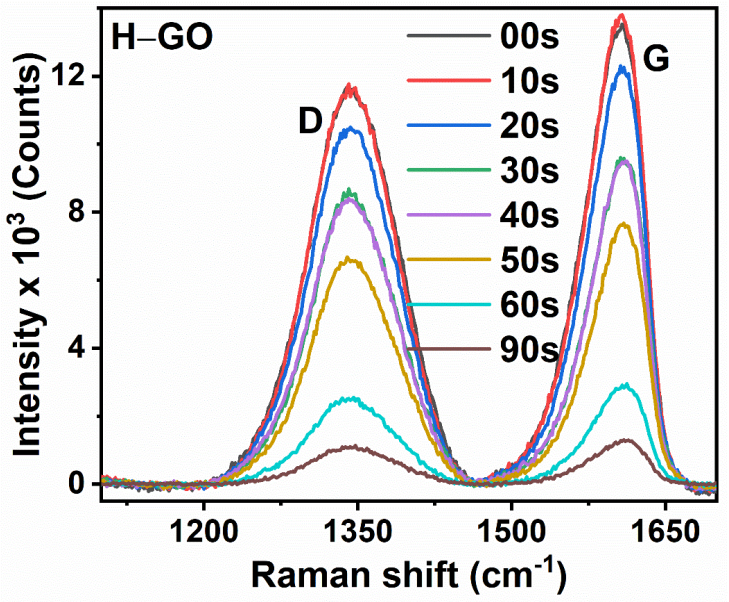

Fig. 4.4: Raman spectra of H-GO in different exposer time.

In **Fig. 4.5b**, the N_2 plasma-treated on the N-GO sheet reduced its normalized intensity of the D and G band as increased the exposure time. However, the changes in intensity for 10s and 20s, 30s and 40s are not much different, as observed in other samples. Similarly, the optical image of the 0s and 90s shows the etching of the sheet after nitrogen is exposed. The intensity of the bands is rapidly reduced after exposure to O_2 plasma for the 20s, shown in **Fig. 4.5c**. It is verified in the optical image of the GO sheet after the 90s. In **Fig. 3.7**, the O-GO sheet's D and G band is reduced as the exposure time increases, but the rate of reduction of the intensity of bands is less affected as compared to the other exposed gases. The D and G bands appeared after exposure to the 90s. So, the effect of the H-GO has less on the GO sheet than others such others such as Ar-GO, N-GO, and O-GO.as Ar-GO, N-GO, and O-GO.

4.5.2. Raman analysis of gas plasma treated graphene oxide/ reduced graphene oxide

The I_D/I_G of the Raman spectrum is used to determine the induced structure defects and disordered on the GO and RGO. The higher the value of I_D/I_G means, the increased the defects on the GO. I_D/I_G for Ar-GO, N-GO, O-GO, and H-GO are analyzed in **Fig. 4.6**. The I_D/I_G characterizes each sample for the exposure of plasma time. In the Ar-GO (Fig. 4.6a), I_D/I_G is increased from 0.85 for the 00s to 0.91 for the 30s. Afterward, it is reduced to 0.74 for the 90s.

It may be due to the creation of structural defects up to 30s and afterward the removal of carbon and functional groups from the GO by bombarding Ar ions. Similarly, the I_D/I_G of the N-GO (**Fig.4.6b**) is increased from 0.85 for 0s to 0.89 for the 30s, then reduced to 0.8 after the 90s.

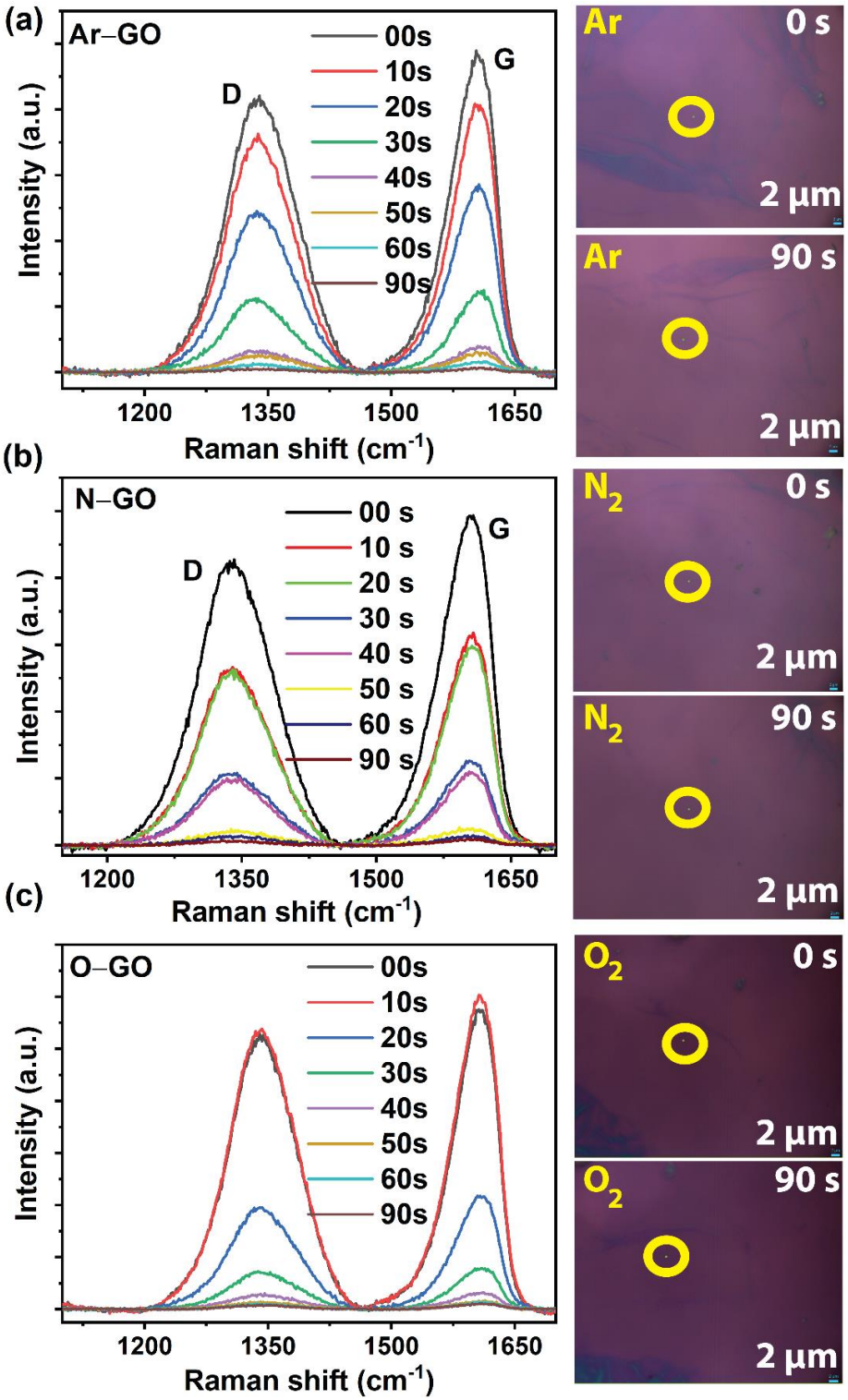

Fig. 4.5: Evolution of the Raman spectra of different gas plasma treated GO samples: (a) Ar-GO, (b) N-GO, (c) O-GO, with respective optical images.

The value of I_D/I_G of O-GO (**Fig.4.6c**) is 0.88 at 0s and increased to 0.91 after the 40s. The value of the I_D/I_G of O-GO is not consistent; its value is 0.88 after the 30s and 0.85 after the 90s. Again, in the H-GO, the value of I_D/I_G after the 30s is 0.92, which is the highest compared to other samples. The change I_D/I_G in the O-GO and H-GO fluctuated due to the extreme distortion of the structure of the GO sheet. The I_D/I_G of GO is decreased/increased after prolonged exposure of plasma on the GO; it does not imply the improvement of the distorted structure of GO. That is due to reducing the intensity of both D and G bands by etching the atoms (carbon and oxygen functional groups). So, it is required to set a particular duration for further optimization and studies for the SERS effect on GO after changing its structure and attached functional groups. The optimum exposure time for the gas plasma-treated on the GO/RGO is set at the 30s for further analysis of the effect of SERS and other applications. The rate of removal of functional groups and creation of structural defects are different based on the applied gases to the GO; this is one of the stimulating effects in this present study.

The structural changes in the GO can be studied by the parameters obtained from the Raman spectra, such as I_D/I_G, changing the peak position of G, D, D^1, and D^2 peaks. In **Fig. 4.7**, the Raman spectra of the 30s of plasma-treated GO and RGO samples are studied by de-convoluted them with five Gaussian peaks and three Gaussian peaks, respectively. D^1 peak at 1250 cm^{-1} emerged from the presence of oxygen functional groups in the GO samples[10]. D peak at 1350 cm^{-1} is due to the structural disorder. D^2 peak at 1570 cm^{-1} is represented the sp^2 sp3 bonded carbon atoms. G peak at 1600 cm^{-1} is due to the hybridized sp^2 carbon atoms. Furthermore, D' peak at 1622 cm^{-1} emerged from the defects and doping of atoms on the lattice structure of GO/RGO. D^1 and D^2 peaks are constituents in GO, including all the plasma-treated samples such as Ar-GO (**Fig. 4.7c**), N-GO (**Fig. 4.7e**), H-GO (**Fig. 4.8a)**, and O-GO (**Fig. 4.8b**). Plasma-treated on the RGO samples such as Ar-RGO (**Fig. 4.7d**) and N-RGO (**Fig. 4.7f)** are perfectly fitted without D^1 and D^2 peaks. It is proof of the reduction of oxygen functional groups attached to the carbon atoms and the restoration of the sp^2 hybridized carbon atoms (graphitic structure). Plasma treated on the GO samples has a disorder on the structure, attached oxygen functional groups, sp^3 carbons, and the creation of defects on the graphitic structure.

However, plasma treatment of the RGO samples created disorder and defects in the graphitic structure. It is correlated with the XPS and XRD analysis of the RGO, which explained the attachment of oxygen functional groups and the attachment of oxygen functional groups that altered sp^2 to sp^3 carbon atoms of GO. The changes in structural properties of GO and RGO are analyzed after plasma treatment using the shifting of the peak position of D, G,

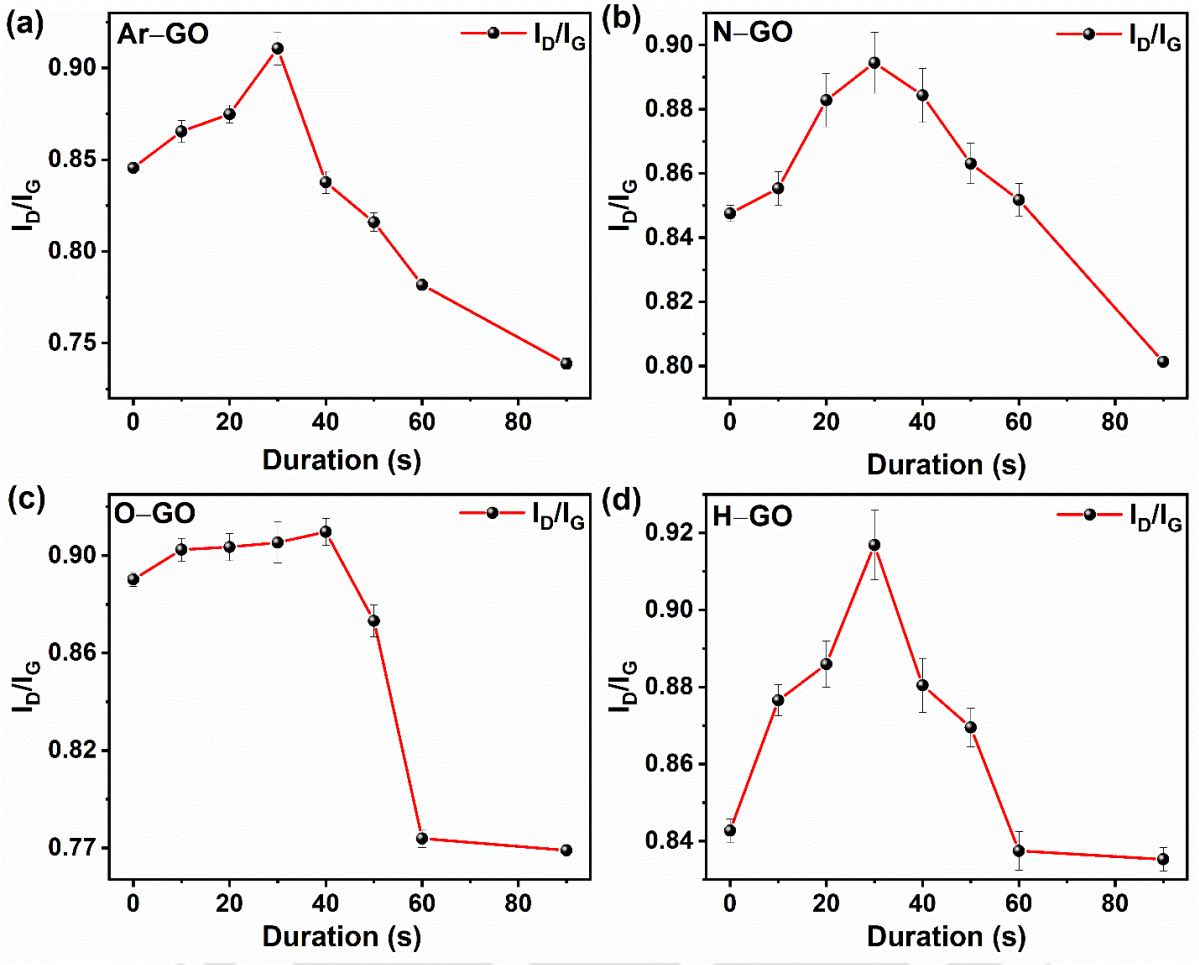

Fig. 4.6: I_D/I_G ratio of Raman spectra for (a) Ar-GO, (b) N-GO, (c) O-GO and (d) H-GO as a function of plasma exposure time.

D', D^1, and D^2; D'-G; FWHM of D, G, and D'; I_D/I_G; which are shown in **Table 4.1**. The changed of structural properties are studied, such as degree of disorder and defects in the structure, presence of oxygen functional groups, and crystallinity of sp^2 carbons[8]. The D^1 is 1243 cm^{-1} for N-GO, 1244 cm^{-1} for H-GO, 1247 cm^{-1} for Ar-GO, and 1267 cm^{-1} for O-GO. The peak position of D^1 is shifting to a higher wavelength, representing a high degree of functional groups attached to the GO.

Based on the analysis, N-GO contained high functional groups compared to other GO samples. The O-GO is removed from the oxygen functional groups by the bombardment of the oxygen ions instead of adding oxygen atoms to the structure of GO. The peak position of D^2 is at 1543 cm^{-1} for N-GO, 1556 cm^{-1} for O-GO, 1557 cm^{-1} for H-GO, and 1570 cm^{-1} for Ar-GO. Based on the study by Claramount et al.[8], Ar-GO has higher functional groups attached to it,

which is explained by the shifting of the D^2 peak position towards the lower wavelength and has formed sp^3 carbon atoms after the attached of functional groups. The D peak is 1347 cm^{-1}

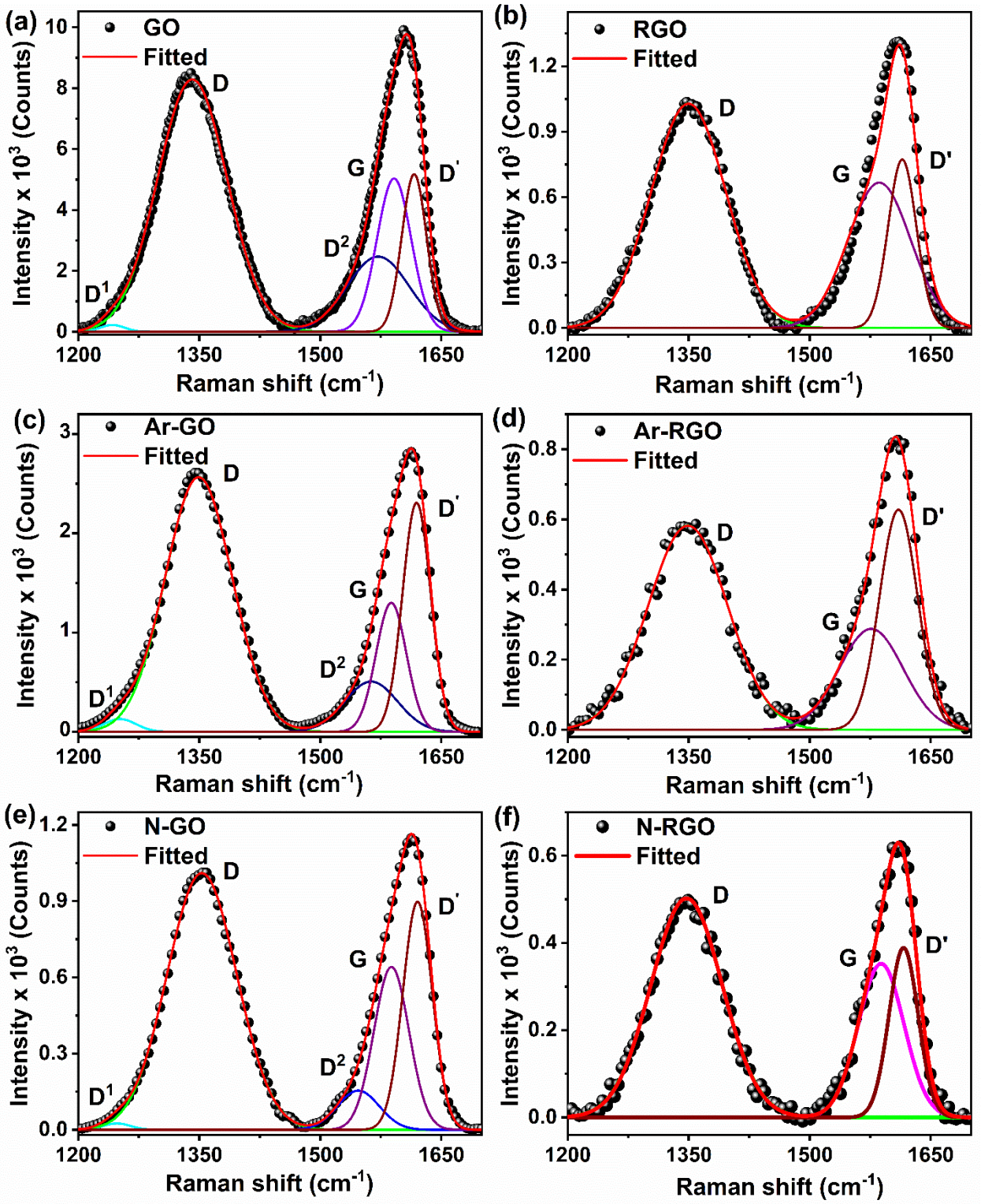

Fig. 4.7: Raman spectra and its deconvolution for (a) GO, (c) Ar-GO, & (e) N-GO, with five Gaussian peaks; and (b) RGO, (d) Ar-RGO, (f) N-RGO with three Gaussian peaks.

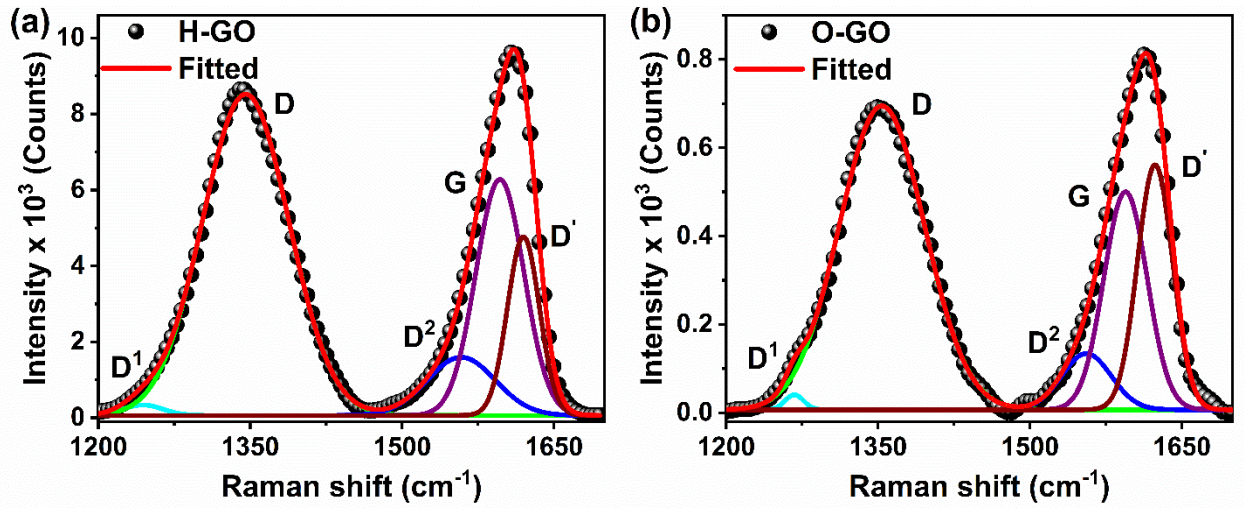

Fig. 4.8: Deconvolution of Raman spectra for (a) H-GO; and (b) O-GO by five Gaussian peaks.

for N-RGO, 1345 cm^{-1} for H-GO, 1348 cm^{-1} for Ar-RGO, 1349 cm^{-1} for Ar-GO, and 1352 cm^{-1} for O-RGO, 1353 cm^{-1} for N-GO and O-GO, that is observed. The blue shift of the D peak is due to the increasing disorder of the structure[11] by the plasma treatment. As a result, N-RGO has high disorder compared to the other samples; N_2 plasma on the RGO sheet has added extra disorder to the graphitic structure upon the thermally reduced RGO, which has inherently present structural defects after the removal of functional groups.

The peak shift of the G band is 1576 cm^{-1} for Ar-RGO, 1588 cm^{-1} for N-RGO, 1590 cm^{-1} for O-RGO, 1594 cm^{-1} for O-GO, 1596 cm^{-1} for H-GO, 1598 cm^{-1} for N-GO, and 1599 cm^{-1} for Ar-GO. The blue shift of the G peak position is indicated the presence of higher functional groups; Ar-RGO is obtained in the least functional groups, whereas, Ar-GO is attained in more functional groups. Interestingly, plasma-treated on the RGO samples is attached least. functional groups and plasma-treated GO samples are more functional groups based on the G band's analysis of the shift in the peak position. This result can be authenticated with the analysis of XRD and XPS data. The shift of peak position for D' peak is analyzed that blue shift of this peak position has due to the obtained of more functional groups, doping of atoms, and vacancies. As a result, plasma-treated RGO samples like Ar-RGO, O-RGO, and N-RGO peak positions at 1610 cm^{-1}, 1615 cm^{-1}, and 1616 cm^{-1}, respectively. The low functional groups are attached to it. However, the D' peak position for the plasma-treated the GO samples such as H-GO, N-GO, Ar-GO, and O-GO have their peak position at 1619 cm^{-1} and 1622 cm^{-1}, 1623 cm^{-1}, and 1623 cm^{-1}, respectively. Plasma-treated GO is created with more oxygen functional groups and structural defects than RGO. Ar-GO and O-GO obtained more functional groups and defects from the analysis of the D' position.

***Table 4.1**: Summary of the Raman modes of the gas plasma treated GO/RGO using peak position, FWHM, D`-G, and I_D/I_G.*

Peak position/FWHM (cm^{-1})	**Ar–GO**	**N–GO**	**O–GO**	**H–GO**	**Ar–RGO**	**N–RGO**	**O–RGO**
D band	1349	1353	1353	1345	1348	1347	1352
G band	1599	1598	1594	1596	1588	1576	1590
D` band	1623	1622	1623	1619	1610	1616	1623
D^1 band	1247	1242	1267	1244	-	-	-
D^2 band	1569	1542	1555	1558	-	-	-
FWHM of D	99	102	99	100	116	104	112
FWHM of G	55	65	55	55	94	66	94
FWHM of D`	35	36	40	37	56	42	41
D`-G	24	24	29	23	34	28	29
I_D/I_G ratio	2.55	1.77	2.75	2.43	2.47	2.28	2.75

Kondratowiczet al.[12] have explained graphene, RGO, and GO based on the value of D'-G (difference of the value of peak position between D' and G peak). The lower value of D'-G has determined the GO, meaning it contained more functional groups than the higher value of RGO and pristine graphene. Similarly, it is obtained that both H-GO, Ar-GO, and N-GO have values of 23 cm^{-1} and 24 cm^{-1} for both. The least contained functional groups are in the sequence of Ar-RGO of 34 cm^{-1}, N-RGO of 28 cm^{-1}, and O-RGO of 25 cm^{-1}, respectively. However, O-GO, which value is 29 cm^{-1}, does not follow this pattern. The FWHM of the D, G, and D peaks are analyzed.

The FWFM of the D peak is determined by creating structural defects/ distortion of the structure of the sp2 carbon atoms. More value of FWHM of D peak means higher structural defects; plasma treatment on the RGO samples are more structural defects than the GO

samples. The FWHM of the D peak is increased from 99 cm^{-1} to 116 cm^{-1}; in the sequence of 99 cm^{-1}, 99 cm^{-1},100 cm^{-1}, 102 cm^{-1}, 104 cm^{-1}, 112 cm^{-1}, and 116 $cm^{-1}$for the Ar-GO, O-GO, H-GO, N-GO, N-RGO, O-RGO, and Ar-RGO respectively. The graphitic structure determines the FWHM of the G peak; the increase in the graphitic structures[11] signifies the increase in the value of FWHM of the G peak. The value of FWHM of the G peak is increased from 55 cm^{-1}, 55 cm^{-1}, 55 cm^{-1}, 65 cm^{-1}, 66 cm^{-1}, 82 cm^{-1}, and 94 cm^{-1} for the Ar-GO, O-GO, H-GO, N-GO, N-RGO, O-RGO, and Ar-RGO respectively. Interestingly, the FWHM of the G peak for Ar-GO, O-GO, and H-GO have the same value of 55 cm^{-1}. The FWHM of the D' is determined by the degree of defect on the surface /presence of oxygen functional groups. The higher the value of FWHM for D, the more defects on the surface/ oxygen functional groups[12]. The FWHM of the D' for Ar-GO, N-GO, H-GO, O-GO, O-RGO, N-RGO, and O-RGO are 35 cm^{-1}, 36 cm^{-1}, 37 cm^{-1}, 40 cm^{-1}, 41 cm^{-1}, 42 cm^{-1}, and 56 cm^{-1} respectively. This analysis shows that Ar-GO has the least structural defects, but O-RGO has more.

The I_D/I_G of the N-GO, O-GO, N-RGO, H-GO, Ar-RGO, Ar-GO, and O-RGO are 1.77, 1.8, 2.28, 2.43, 2.47, 2.55, and 2.75 respectively. The higher the value of I_D/I_G is determined, the more structural defects on the sample. Based on the analysis, N-GO has the minimum structural defects, whereas O-RGO has the high structural defects. Ar-GO has a higher value of the I_D/I_G than the N-RGO and Ar-RGO, which shows the Ar plasma treated on the GO has created more structural defects than the RGO synthesized by thermal annealing. Most of the analyses are caused by the structural defects and functional groups of the GO/RGO. Plasma-treated RGO is presented with higher structural defects than the GO samples, which are explained in the study of peak positions of D, G, and D' peaks, and FWHM of D, G, and D'. Plasma-treated GO samples contained more functional groups than the RGO samples, which is explained by the study of peak positions, FWHM, D'-G, and I_D/I_G.

4.5.3. XPS and FTIR analysis of gas plasma treated graphene oxide/ reduced graphene oxide

The XPS analysis of the Ar-GO and N-GO is shown in **Fig. 4.9**; the survey spectra are measured from 220 eV to 550 eV. The bonding characteristics of the GO, RGO, and GQDs are studied using the XPS spectra in the previous chapters. The two prominent peaks are observed centered at 284 eV and 532 eV, which correspond to C1s and O1s of the Ar-GO (**Fig. 4.9a**)

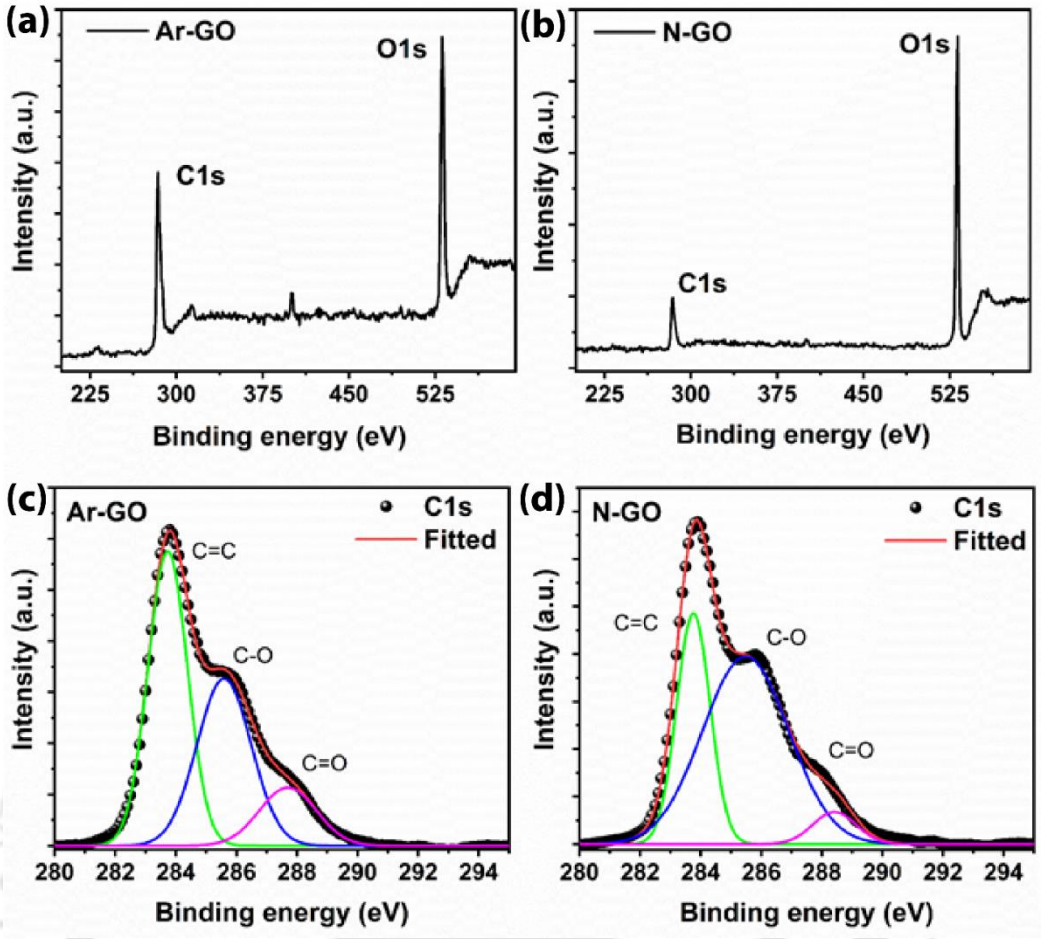

Fig. 4.9: Survey scan XPS spectra of (a) Ar-GO and (b) for N-GO; deconvoluted C 1s spectra for (c) Ar-GO; and (d) N-GO.

and N-GO (**Fig. 4.9b**). The intensity ratio of the O1s/C1s is obtained up to 1.8 for Ar-GO and 4.5 for N-GO. The C1s peak of Ar-GO and N-GO are fitted with three Gaussian peaks shown in **Fig. 4.9c** and **Fig.4.9d**, respectively. The fitted peaks are centered at 283.8 eV, 286.2 eV, and 288 eV, which are attributed to the C=C, C-O, and C=O, respectively. The first peak signified the retaining of the graphitic structure after the Ar plasma treatment, and the second and third peaks assigned the presence of oxygen functional groups, which is reduced relatively compared to the GO, but high as compared to the RGO. Similarly, N-GO retained the oxygen functional groups after N_2 plasma treatment on the GO. The oxygen functional group (O-C=O) is removed from both the Ar and N_2 plasma treatment on GO which is observed from the XPS analysis. The mildly bonded oxygen functional groups are removed from the gas plasma treatment on the GO, and the stable oxygen functional groups are attached to the GO. However, a detailed understanding of the elemental compositions, doping of atoms, and bonding characteristics is required to study.

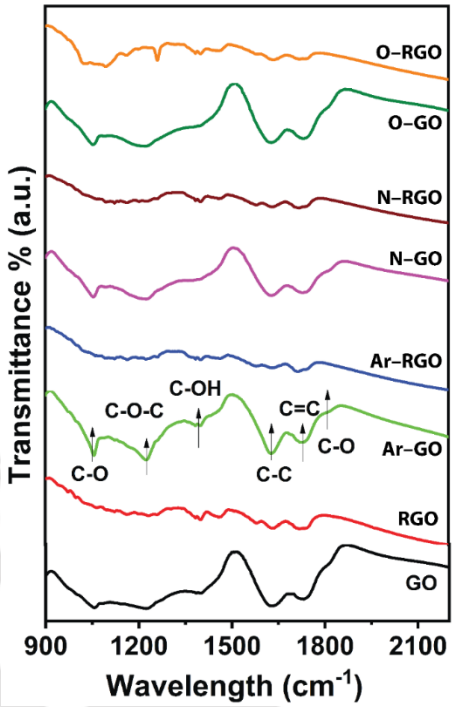

Fig. 4.10: FTIR spectra of the gas plasma treated GO and RGO.

After various gas plasma treatments, the bonding characteristics of the GO/RGO are analyzed using FTIR spectra shown in **Fig. 3.10**. Similar to the GO and RGO, which are analyzed in **chapter 3**, the transmittance peaks emerge between 1000 cm^{-1} and 2000 cm^{-1}. The plasma-treated GO samples such as Ar-GO, N-GO, and O-GO have distinct peaks at 1057 cm^{-1} for the C-O group, 1228 cm^{-1} for the O-C=O group, 1391 cm^{-1} for the C-OH group, 1630 cm^{-1} for C=C group, and 1722 cm^{-1} for C=O group. After the plasma treatment on GO, the characteristic peaks are retained that the oxygen functional groups exist on the GO even after the exposure to the gas plasma. The plasma-treated RGO exhibits reduced oxygen functional groups, which are observed from the disappearance of the C-O and C-OH groups. In O-RGO, a transmittance peak at 1265 cm^{-1} is observed, which is related to C-O-C. Thus, plasma-treated GO samples retain a rich amount of oxygen functional groups, whereas plasma-treated rGO samples possess a low amount of oxygen functional groups.

4.5.4. Analysis of Raman spectra on Ar plasma treated graphene quantum dots

The synthesized GQDs have analyzed the effect of Ar plasma treatment using Raman spectroscopy which is presented in **Fig. 4.11**. The Raman spectra (**Fig. 4.11a**) are measured from 1200 cm^{-1} to 1800 cm^{-1} in various exposer durations such as 10s, 30s, 60s, 90s, and 120s. Similar to the GO, the intensity of the corresponding Raman peaks (D and G) are reduced as increases the exposure duration of Ar plasma on the GQDs. After exposure of Ar plasma for 120s on GQDs, its characteristics of Raman peaks are not exhibited.

The I_D/I_G (**Fig. 4.11b**) of the synthesized GQDs is obtained at 0.57, much lower than GO; it shows the removal of the oxygen functional groups and restoration of sp2 carbon bonds in the GQDs. The presence of the large daggling bonds at the edge and a minimal amount of the highly stable oxygen functional groups of GQDs contributed to the emergence of the D band. Ar plasma treatment on the GQDs may create structural defects up to the 30s of exposure, leading to increases in the I_D/I_G up to 0.6.

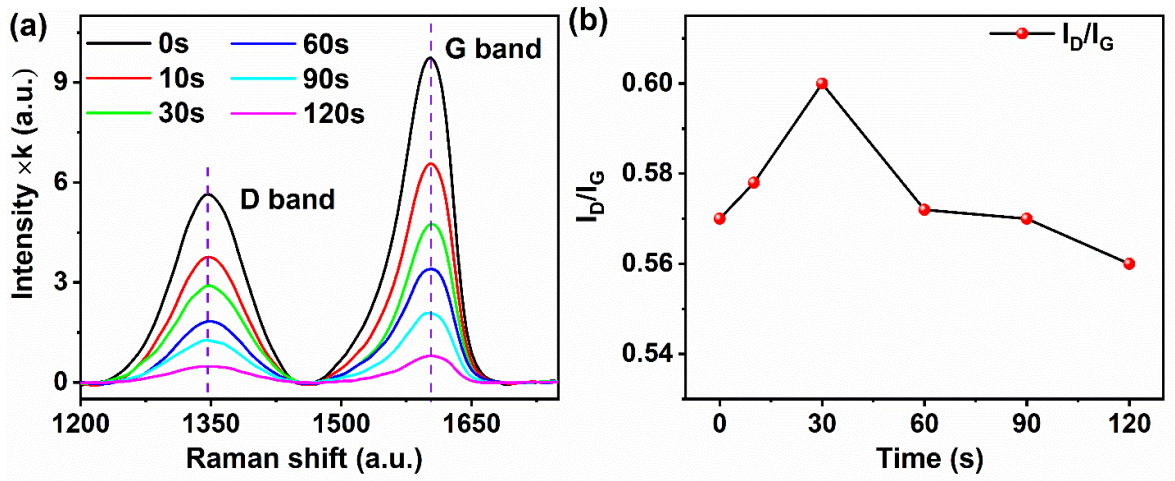

Fig. 4.11: (a) Raman spectra, (b) I_D/I_G analysis of Ar plasma treated on GQDs for different exposer times.

Afterward, the continuous exposure of Ar on GQDs has removed the graphitic structure of carbons and attached functional groups, which contributes to the reduction of the intensity of the significance Raman peaks (D and G) and the I_D/I_G. After analysis of the gas plasma treatment of GO/RGO, Ar plasma treatment is chosen for the GQDs and studied the effect of exposure duration. Similarly, 30s exposer duration exhibited higher structural defects based on the analysis of I_D/I_G. The 30s exposer of Ar plasma treated GQDs is studied for the SERS effect for detecting dye molecules.

4.6. Analysis of SERS effect on various graphene oxide-based substrates

4.6.1. UV absorbance of the various dyes

Fig. 4.12 shows UV absorbance of the RhB, MB, MO, and RB with their peak position, and the quenching of peaks is analyzed. GO shows a prominent absorbance peak at 230 nm, whereas the RhB peak is observed at 553 nm in water solution. The RhB peak is shifted to 562 nm, and the absorbance quenching is observed in the GO solution, shown in **Fig. 4.12a**. The MB has a prominent peak, centered at 603 nm in water, whereas the peak is shifted to 613 nm in GO solution (**Fig. 4.12b**). Similarly, MO (**Fig. 4.12c**) and RB (**Fig. 4.12d**) have shifted their absorbance peak from 469 nm to 491 nm & 485 nm to 500 nm, respectively. The shift of the

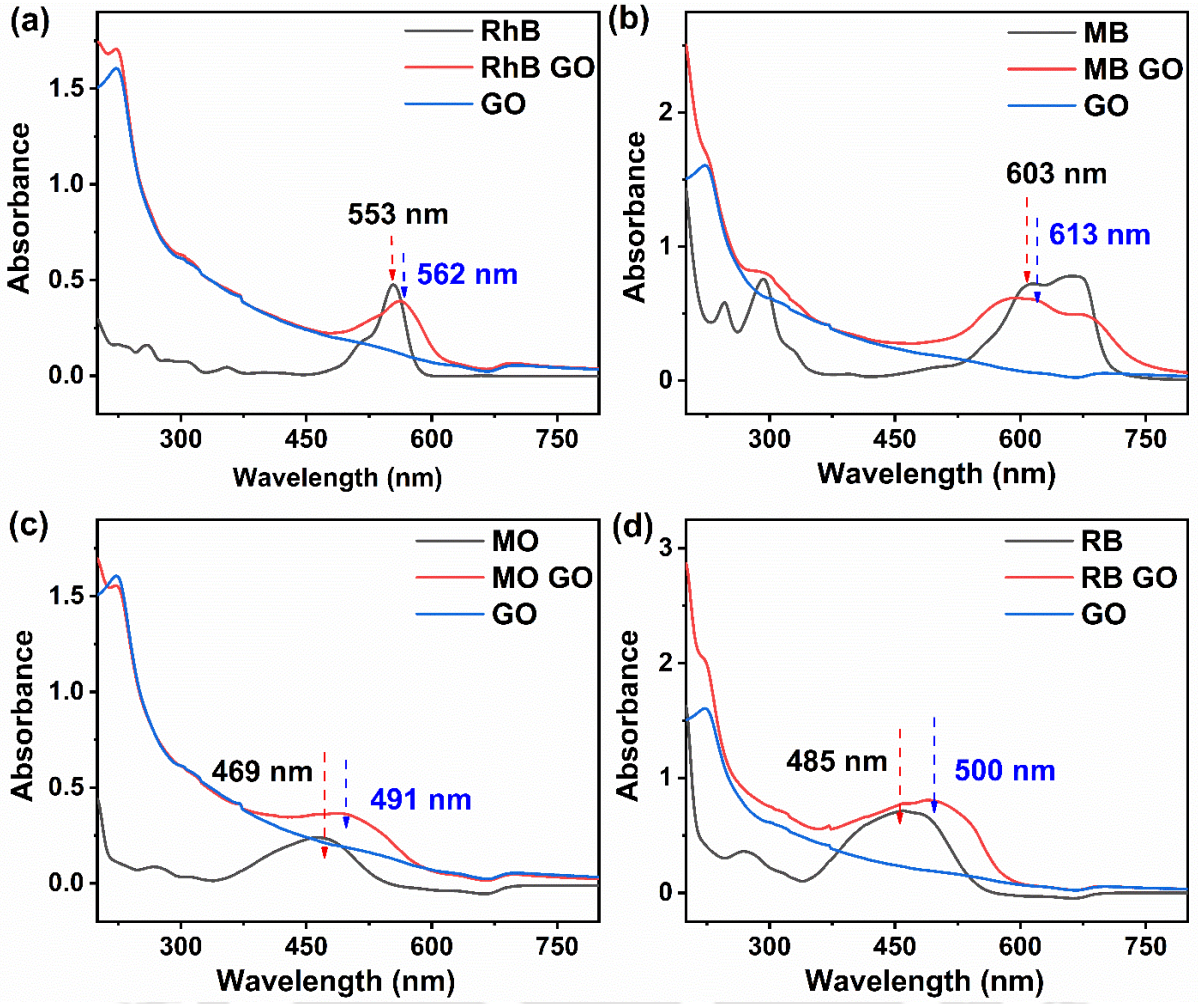

Fig. 4.12: UV absorption spectra of GO (a) with RhB and without RhB; (b) with MB and without MB; (c) with MO and without MO; and (d) with RB and without RB.

absorbance peak is due to the interaction between dye molecules and GO in water solution, which is observed in all the four dyes[13,14]. The quenching of UV absorbance of RhB and MB is due to the charge transfer effects between the aromatic dye molecules and the GO[15] by deactivating the pathway for charge transfer of the excited state from the π-π interactions.

4.6.2. SERS effect for various dye molecules on graphene oxide/ reduced graphene oxide

The SERS effects of various dye molecules such as MB, MO, RB, and RhB on the GO and RGO are shown in **Fig. 4.13**; each of the samples is studied in different concentrations from 10^{-4} M to 10^{-8} M in the aqueous solution. The corresponding details of the Raman signals for all the dyes are mentioned in **Table 4.2 and Table 3.2 (chapter 3)**. The MB molecules on the GO and RGO sheet show enhanced Raman signal, and the characteristic peaks for MB are at 1077 cm^{-1}, 1388 cm^{-1}, and 1627 cm^{-1}. The dominant peak at 1627 cm^{-1} is observed on the GO (**Fig. 4.13a**) and RGO (**Fig. 4.13b**) for both the concentrations of 10^{-4} M and 10^{-5} M;

further, this peak is 3.5 times stronger in intensity in the GO case than that of RGO at 10^{-4} M for MB. The SERS effect of the MO molecules on the GO and RGO sheet are analyzed, in **Fig. 4.13c** & **Fig. 4.13d**, respectively. The Raman peaks at 1115 cm^{-1}, 1141 cm^{-1}, and 1187 cm^{-1} are observed, and both 1115 cm^{-1} and 1141 cm^{-1} peaks obtain similar Raman intensity values on the GO substrate. Unlike on GO, the 1115 cm^{-1} of MO has enhanced higher Raman intensity compared to 1141 cm^{-1} at the same concentration on the RGO. The noticeable peak at 1115 cm^{-1} is observed on the GO and RGO from 10^{-4} M down to 10^{-7} M for MO; this peak has higher intensity (up to 1.4 times) on the GO than that of RGO for 10^{-4} M of MO.

***Table 4.2**: Description of Raman modes for MB[16], MO[17], and RB[18].*

Dyes	Raman peak (cm^{-1})	Details
MB	1077	Bending of C-H
	1388	Symmetrical stretching of C-N
	1627	Stretching of C-C
MO	1115	Stretching of Ph-N
	1141	Stretching of C-H
	1187	Stretching of Ph-N
	1445	Stretching of C-C
RB	1115	Stretching of C-OH
	1143	Deformation of C-H
	1193	Deformation of C=C
	1447	Asymmetric of C=C

However, the intensity of the Raman signals for the MO molecules on the GO and RGO sheets is significantly low. The RB molecules exhibit enhanced Raman signals when placed on the GO and RGO, as shown in **Fig. 4.13e** & **Fig. 4.13f**, respectively. A weak intensity peak at 1115 cm^{-1}, which corresponds to the stretching of C-OH of RB, has been detected on the GO and RGO from 10^{-4} M down to 10^{-6} M of RB. Similar to MO, the 1115 cm^{-1} enhanced its intensity higher than other RB peaks on RGO. This peak intensity increases to 2.8 times higher on the GO than RGO at 10-4 M for RB. A prominent peak at 1647 cm^{-1} is observed on the GO and RGO from 10^{-4} M down to 10^{-8} M of RhB (**Fig. 4.13g** & **Fig. 4.13h**, respectively); this peak intensity increases up to 1.9 times on the GO than that of RGO at 10^{-4} M for RhB.

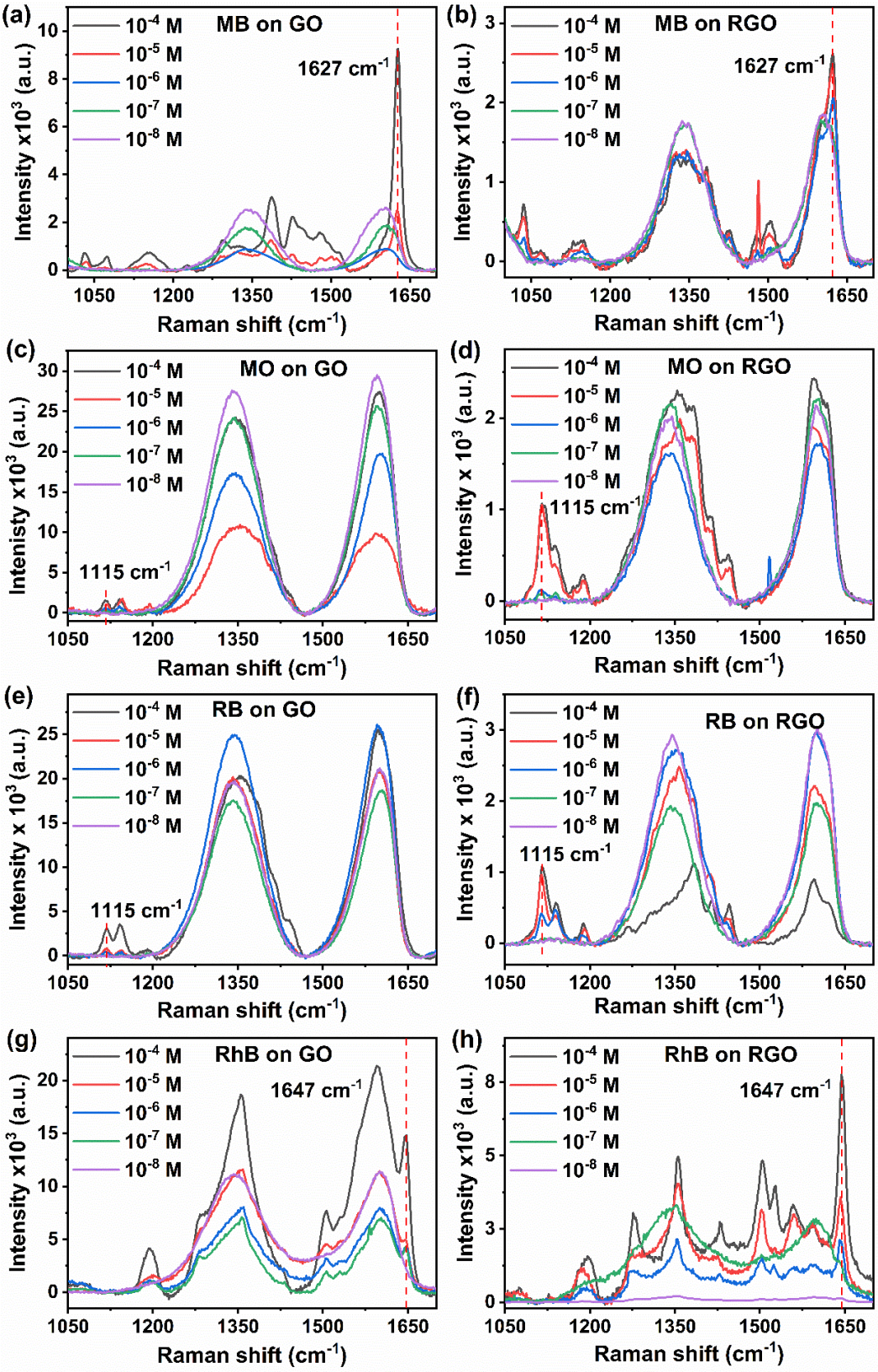

Fig. 4.13: Analysis of SERS effects with different concentration of various dyes such as MB on (a) GO; (b) RGO; MO on (c) GO; (d) RGO; on RB (e) GO; (f) RGO; and on RhB (g) GO; (h) RGO.

Interestingly, the Raman peaks correspond to the GO (D and G band) and are enhanced after interaction with the RhB and GO. These peaks (D and G) are suppressed after interaction

with the RhB and RGO, as shown in **Fig. 4.13h**. The comparative analysis of the various dyes at the different concentration of GO and RGO are shown in **Fig. 4.14.** In **Fig. 4.14a**, the significant difference in the Raman intensity is observed at 10^{-4} M of MB; further lower concentrations are not noticeable in GO and RGO.

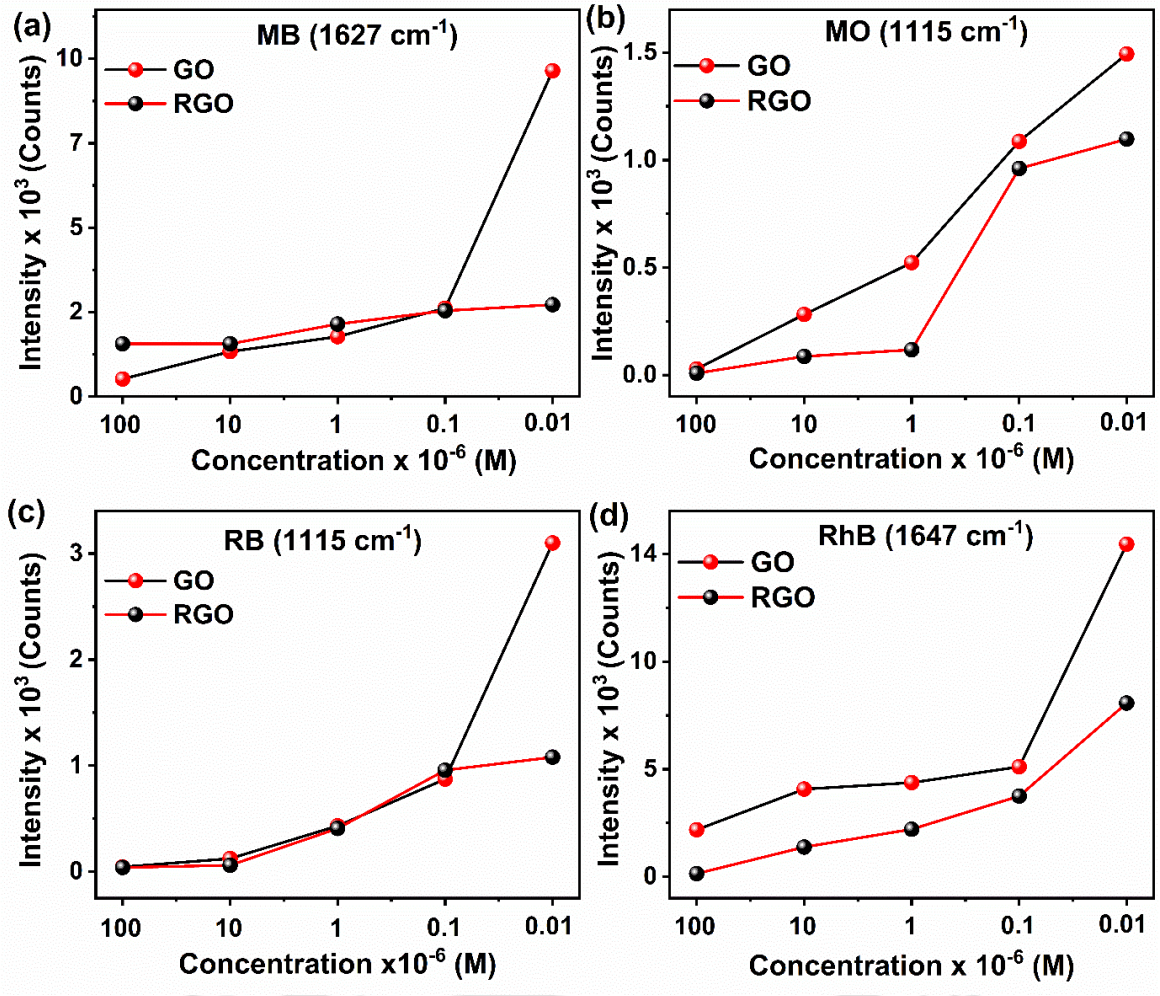

Fig. 4.14: SERS effect various dyes such as (a) MB; (b) MO; (c) RB; and (d) RhB on GO and RGO.

However, in **Fig. 4.14b**, the Raman intensity of the assigned peak (1115 cm^{-1}) is enhanced on GO compared to RGO down to the 10^{-7} M of MO. The narrow gap between the SERS intensity of MO at 10^{-5} M for GO and RGO is observed. The detection range of the RB is down to 10^{-4} M (**Fig. 4.14c**); the intensity of Raman is increasing as the concentration of RB in water solution is reduced. In **Fig. 4.14d**, the Raman intensity of the RhB peak (1647 cm^{-1}) is obtained highest SERS enhancement compared to discussed dyes. The intensity of the RhB is reduced as concentration dilution is higher. The increased intensity of MO and RB are much lower as compared to other dyes (MB and RhB). The Raman scattering cross-section of the RhB is more prominent than the other dyes; it is another result for RhB exhibiting a higher SERS effect than other dyes[19]. The sensitivity of both GO and RGO to detect RhB molecules

is very high, which can trace down to 10^{-8} M. So, the RhB dye is studied using the gas plasma-treated GO and RGO samples to improve its SERS sensitivity. In **Fig. 4.15**, the intensity of the Raman signals for 10^{-4} M RhB and GO (D and G

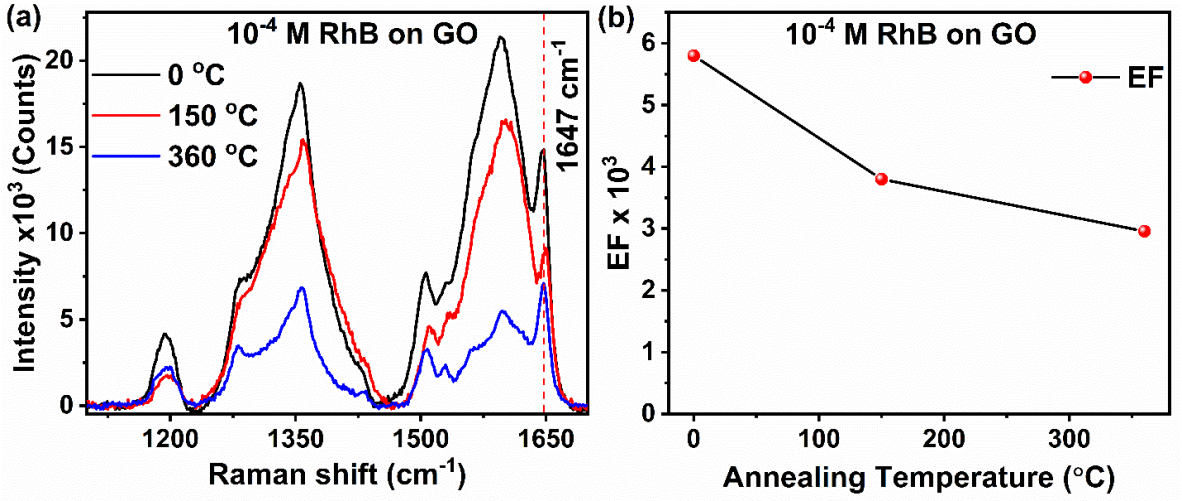

Fig. 4.15: SERS effect of 10^{-4} M RhB on various annealed temperature GO (a) Raman spectra; (b) its EF.

band) are reduced on the GO substrates which is annealed at higher the temperature. The Raman spectra shows in **Fig. 4.15a** is obtained with the combination of GO and RhB signals; The Raman signals related to RhB are suppressed/covered by the board and highly intense D and G band of GO before thermal annealed.

As the increased the applied annealed temperature, the Raman signals of RhB emerged on the Raman peaks of annealed GO at 150 °C. Interestingly, the intensity of the RhB signals is reduced as the annealed temperature of GO increases, which has shown that the contribution of oxygen functional groups to SERS enhancement decreases after the removal of attached functional groups from GO. At the annealed temperature of 360 °C, the rate of reduction for the intensity of Raman signals of RhB is slowly downed, showing that the role of functional groups in the SERS effect is minimized. The annealed temperatures (50 °C & 360 °C) of GO are set from the analysis of TGA and DTG. **Fig. 4.15b** shows the reduction of EF of thermal annealed GO at different temperatures after removing oxygen functional groups. The SERS enhancement after 360 °C annealed GO may be attributed to the structural defects on GO/RGO; it was created after removing oxygen functional groups.

4.6.3. Mechanism of SERS enhancement on graphene oxide/ reduced graphene oxide

The enhancement of the Raman signal for the dye molecules on GO/RGO-based material and SiO2/Si is usually explained by the chemical enhancement (CE) mechanism. In

contrast, electromagnetic enhancement is dominant for metallic nanoparticles. Besides, GO/RGO has suppressed the fluorescence of the dye molecules, which is emitted during the exposure of laser on it. The strong interaction between dye molecules and GO is observed from the shift of the peak position for the UV absorbance of the dye molecules in the GO solution. Further, charge transfer between the RhB and GO is obtained at the higher concentration (10-4 M) of RhB in GO solution; it is confirmed from the quenching of the intensity of PL spectra for RhB in GO solution.

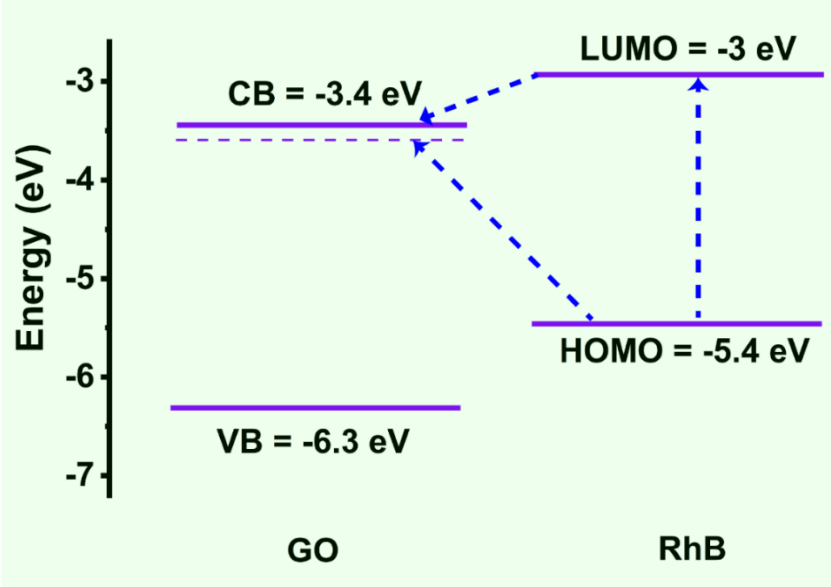

Fig. 4.16: Schematic illustration of charge transfer mechanism between GO and RhB.

To isolate the contribution of the functional groups, we performed vacuum annealing of the GO at two different temperatures. The reduction of the functional groups from GO by thermal annealing at 150 °C and 360 °C has gradually reduced the *EF* by a factor of 2 for the annealed samples, shown in **Fig.4.15**. Thus, the SERS effect on the GO/RGO arises from the attached functional groups and the presence of structural defects on it. The structural defects are not annealed at such a low temperature of annealing; hence, the remaining *EF* pertains to the structural defects. This is consistent with the higher enhancement factor of Ar plasma treated GO. In the Ar-GO case, it has created high defect sites on the GO20, which leads to an increase in the interaction of dye molecules and GO and efficient charge transfer. The CE mechanism using charge transfer is schematically illustrated in **Fig. 4.16**; the excitation of the laser (532 nm) on the GO/RGO leads to an increase in the transfer of electronic charge between the analyte molecules and GO/RGO sheet through the paths[21]. The energy value of the valence band (VB) and conduction band (CB) for GO is -6.3 eV and -3.4 eV, respectively[22]. Whereas,

the energy value for the highest occupied molecular orbital (HOMO) and lowest unoccupied molecular orbital (LUMO) for RhB is -5.4 eV and -3 eV, respectively[23].

The presence of the oxygen functional groups is facilitated energy level just below the CB of the GO, which is a more effortless charge transfer from HOMO of RhB to the CB of GO through functional groups that create energy levels. The removable oxygen functional groups reduce the charge transfer between them, resulting in the reduction of SERS enhancement in RGO compared to GO. The Ar–GO has exhibited more SERS enhancement due to the addition of controlled defect states in the GO that leads to an increase the charge transfer from RhB.

4.6.3. Mapping of Raman signals for RhB on GO

The mapping of the Raman signals for the RhB is measured in an area of 80 × 80 µm, shown in **Fig. 4.17(a-d)**.

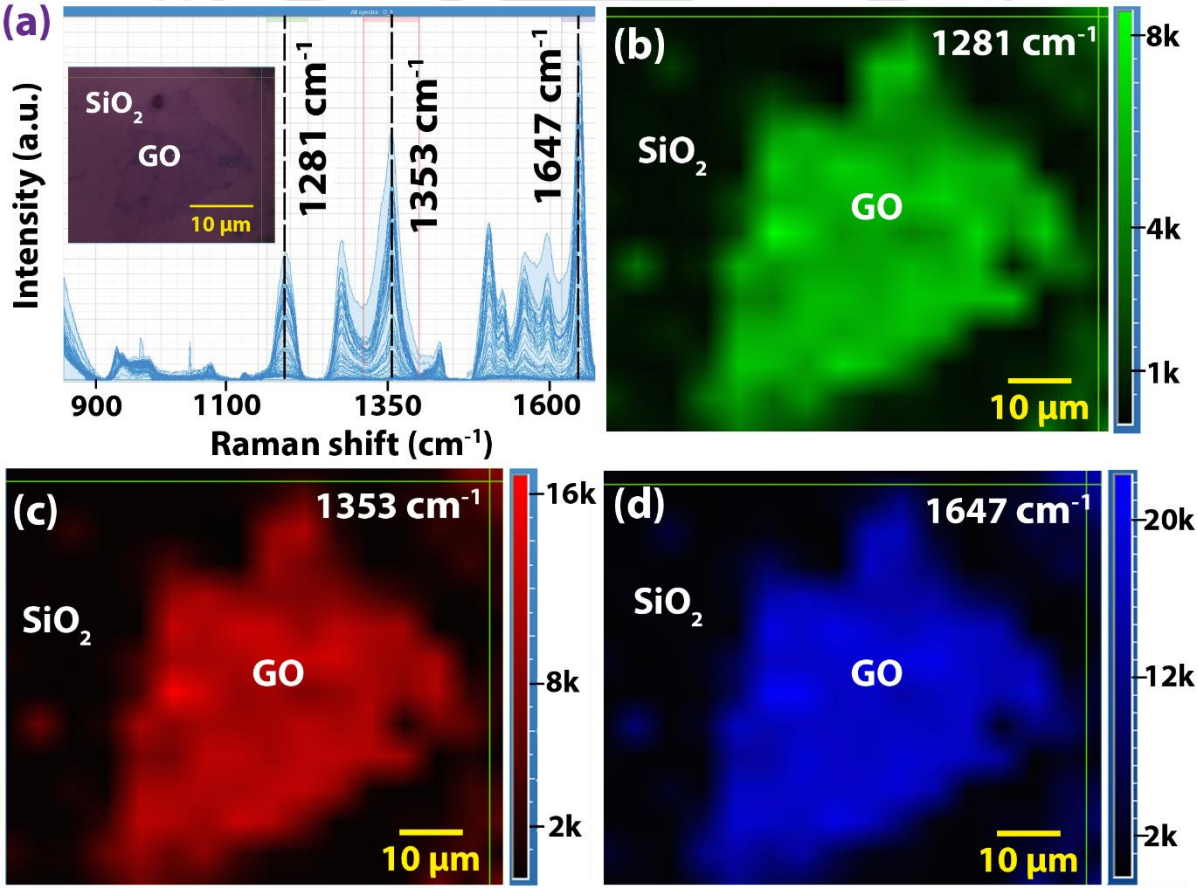

Fig. 4.17: (a) The Cumulative Raman spectra of RhB on RGO (inset: optical image of mapped area); Raman mapping/ intensity profile of the Raman peaks at (b) 1281 cm^{-1}; (c) 1353 cm^{-1}, and (d) 1647 cm^{-1}.

The Raman mapping is examined on GO and SiO_2/Si substrate to analyze the SERS effect of the GO and SiO_2. The cumulative Raman signals of the RhB are shown in **Fig. 4.17a**; it consists of various intensities of the Raman signals for RhB on the SiO_2 and GO sheet. In the GO sheet, folding at the edges and wrinkles leads to the variation of the intensities of Raman signals for the absorbed RhB molecules on the GO sheet.

Three Raman peaks, centered at 1281 cm^{-1}, 1353 cm^{-1}, and 1647 $cm^{-1,}$ are observed prominently for 10^{-4} M of RhB. The optical image of the GO sheet on the SiO_2/Si substrate is shown in **Fig. 4.17c** (**inset**); the optical image is captured after drop-casting the 10^{-4} M concentration of RhB on the substrate. In **Fig. 4.17b**, the green color is attributed to the Raman peak at 1281 cm^{-1} of RhB, which has an enhanced intensity up to 8×10^3 counts. The dark spot in **Fig. 4.17b** indicates that the Raman peak at 1281 cm^{-1} of RhB has no response on the SiO_2/Si. Similarly, the red color in **Fig. 4.17c** represents the Raman peak of the RhB at 1353 cm^{-1}; its intensity is enhanced up to 16×10^3 on the GO sheet, while there is no Raman signal on the SiO_2 substrate at this concentration, which is indicated by the dark spot. The blue color in **Fig. 4.17d** is the dominant peak of the Raman signal for RhB at 1647 $cm^{-1,}$ which has enhanced its intensity up to 22×10^3 on the GO; on the contrary, the Raman peak is not observed on the SiO_2 substrate, as indicated by dark spot. The mapping of the Raman peaks for the RhB is demonstrated the SERS effect of the dye molecules on the selected substrate, specially on the GO and its derivative materials. This technique is a fast and accurate technique used to determine the effectiveness of the SERS effect. From the Raman mapping of the RhB, it can be confirmed that the SERS effect of RhB is observed on the GO and its modified surface but not on the SiO_2 substrate.

4.6.4. Layer dependent study of the SERS effect on graphene oxide

The effect of the thickness of the GO layers on the SERS signal for RhB is next analyzed, as shown in **Fig. 4.18**. The concentration of 10^{-4} M of RhB solution is drop-casted on the different thicknesses of GO sheets with SiO_2/Si as the base substrate. The number of layers for the GO is observed from FETEM, and AFM images measured thickness from the height profile analysis, which is analyzed in **section 3.2.3** of **chapter 3**. The SERS effect of RhB is analyzed on the different layers such as mon-layer, bi-layer, <5-layer, <10-layer, <20-layer, and bulk-layer of GO (**Fig. 4.18a**). The Raman spectra of RhB are measured on the different thicknesses of GO sheets, and the signal from 1050 cm^{-1} to 1700 cm^{-1} is analyzed. The intensity of the Raman signals for RhB varies for the different sheets. The Raman peak at 1647 cm^{-1} is used as a reference peak for further analysis. In **Fig. 4.18b**, the Raman peak at

1647 cm^{-1} is plotted as *EF* vs the number of layers for GO. The *EF* of the RhB signal on the few layers (<5-layer) GO is enhanced up to 3.64 times than that of the monolayer GO; up to 2.86 times than that of the bi-layer GO; up to 1.2 times as compared to that of the <10-layer GO; up to 1.44 times than that of the <20-layer GO; up to 8.25 times as compared to the bulk GO.

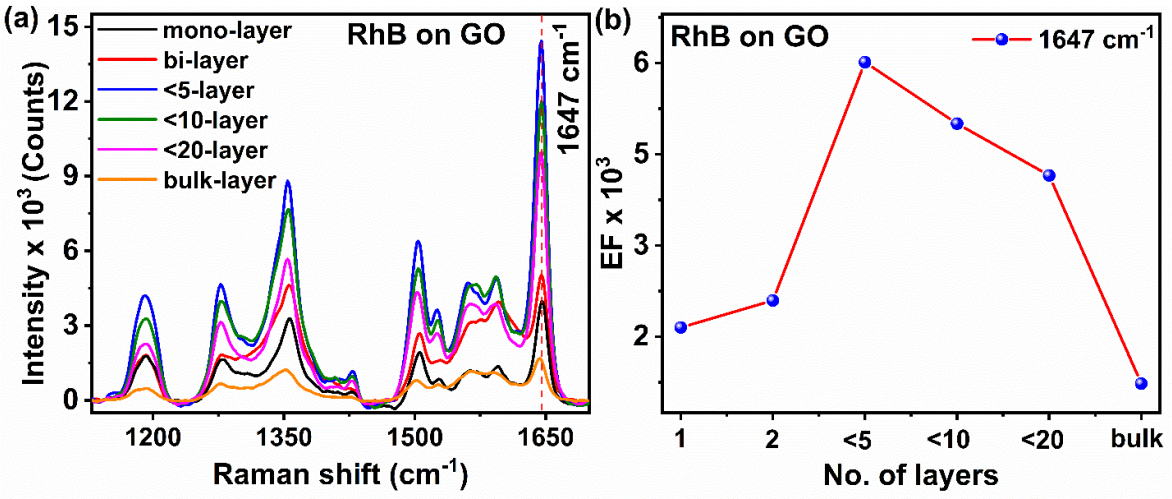

Fig. 4.18: (a) SERS spectra of RhB on different layers of GO; and (b) SERS intensity as a function to the number of GO layers.

Thus, the SERS enhancement for RhB is highest for the few-layer GO (<5 layers) compared to the monolayer GO and multilayer GO. It may be due to the multilayer interference of source laser on the few layers of the GO sheet and the multireflection of Raman signals in the GO[24].

4.6.5. SERS for RhB on plasma treated graphene oxide/ reduced graphene oxide

Raman signals for various concentrations from 10^{-4} M to 10^{-8} M of the RhB on the Ar, N_2, H_2, and O_2 plasma-treated GO/RGO are measured, shown in **Fig.4.19**. In **Fig. 4.19a,** the 10^{-4} M of RhB on Ar plasma treated on GO is enhanced the intensity of the 1647 cm^{-1} up to 32 $\times 10^3$ counts, which is improved by more than 50% as compared to the GO. Similarly, N_2 and O_2 plasma on GO are exhibited 23 $\times 10^3$ and 17 $\times 10^3$ counts, shown in **Fig. 4.19b** & **Fig. 4.19d**, respectively. The prominent Raman peaks (D and G band) of GO are suppressed for the Ar, N_2 and O_2 plasma-treated on GO; equally, Ar (**Fig. 4.19e**), and N_2 (**Fig. 4.19f**) plasma-treated on RGO whereas the O_2 plasma-treated on RGO is heavily distorted. Highly diluted H_2 plasma treated on GO is revealed an enhancement of intensity for both the Raman signals of GO with RhB (**Fig. 4.19c**).

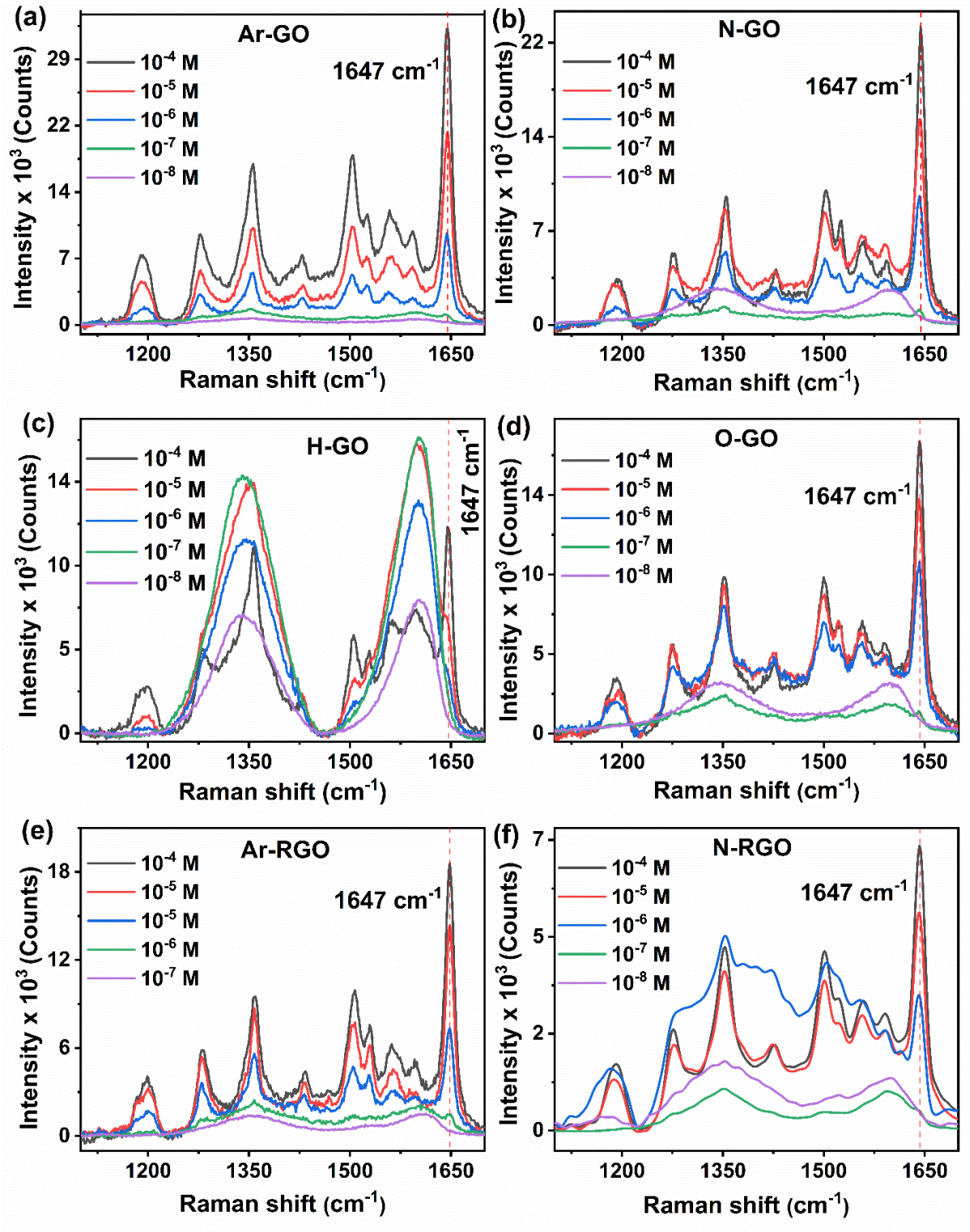

Fig. 4.19: Analysis of SERS effect of RhB on (a) Ar; (b) N_2; (c) diluted H_2; (d) O_2 plasma treated on GO, and (e) Ar; (f) N_2 plasma treated on RGO.

In **Fig. 4.20a**, the Raman signal for 10^{-4} M of RhB on the Ar-GO is deconvoluted with nine peaks, of which two are Gaussian peaks, and seven are Lorentz peaks. The two dominant peaks at 1353 cm^{-1} and 1647 cm^{-1} are observed for RhB molecules on the Ar-GO. The *EF* of the gas

plasma-treated samples is calculated using the equation used in **section 3.4.5** (chapter 3); *EF* of the RhB on the Ar-GO up to 1.3×10^4; the *EF* for the N-GO, Ar-RGO, O-GO, H-GO, and N-RGO, which are 9.4×10^3, 7.6×10^3, 7.3×10^3, 4.8×10^3, and 3.3×10^3, respectively, are shown in **Fig. 4.20b**. The *EF* of 10^{-4} M RhB on the various gas plasma-treated GO, and RGO are given in **Table 4.3**.

***Table 4.3**: SERS enhancement factors (EF) of 10^{-4} M RhB on the various gas plasma treated GO and RGO substrates.*

Gas plasma treatment	EF of GO	EF of RGO
Untreated	5.8×10^3	3.2×10^3
Ar	13.3×10^3	7.6×10^3
N_2	9.4×10^3	3.3×10^3
O_2	7.3×10^3	-
H_2	4.8×10^3	-

The *EF* of the plasma-treated samples Ar-GO, N-GO, Ar-RGO, O-GO, H-GO, N-GO, and RGO increases up to 2.15, 1.53, 1.25, 1.18, 0.79, 0.54, and 0.52 times than the *EF* of GO. For 10^{-8} M RhB, the peak at 1647 cm^{-1}, is noticeable on the H-GO and O-GO; its *EF* is about 0.4×10^3. However, the SERS enhancement of RhB on Ar-GO is the highest among all samples. The enhancement of the Raman signal of the RhB on GO and plasma-treated GO may be contributed from the oxygen functional groups attached to the GO/RGO and surface defects created during the gas plasma treatment.

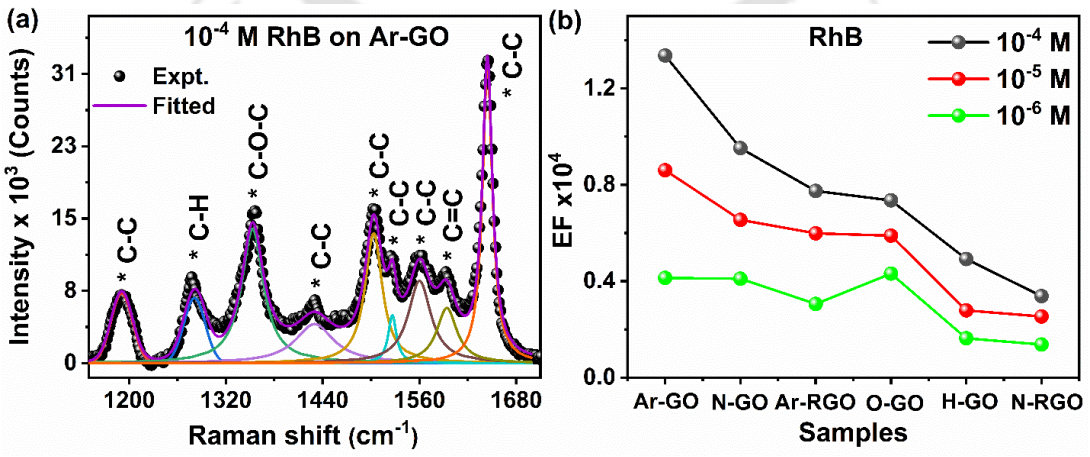

Fig. 4.20: (a) Raman spectrum and its deconvolution of 10^{-4} M RhB on GO; (b) analysis of the EF of 10^{-4}, 10^{-5}, and 10^{-6} M RhB on Ar-GO, N-GO, Ar-RGO, O-GO, H-GO, and N-RGO.

In the case of H-GO, the defects/ functional groups are passivated by the H ions during the H-plasma treatment on GO, which reduces the SERS signal for RhB molecules. Similarly, as the RGO contains fewer functional groups than GO after the thermal annealing, the corresponding SERS signal is reduced. So, the gas plasma treatment on GO improves the SERS *EF* for RhB molecules.

4.6.6. SERS effect on Au nanoparticles, nano-composite of Au and reduced graphene oxide, and nano-composite of Au and graphene oxide substrates

The SERS effect of RhB on Au NPs, AuRGO, and AuGO are studied in **Fig. 4.12**. The surface morphology of the Au NPs is analyzed in **Fig.4.12(a, b)**.

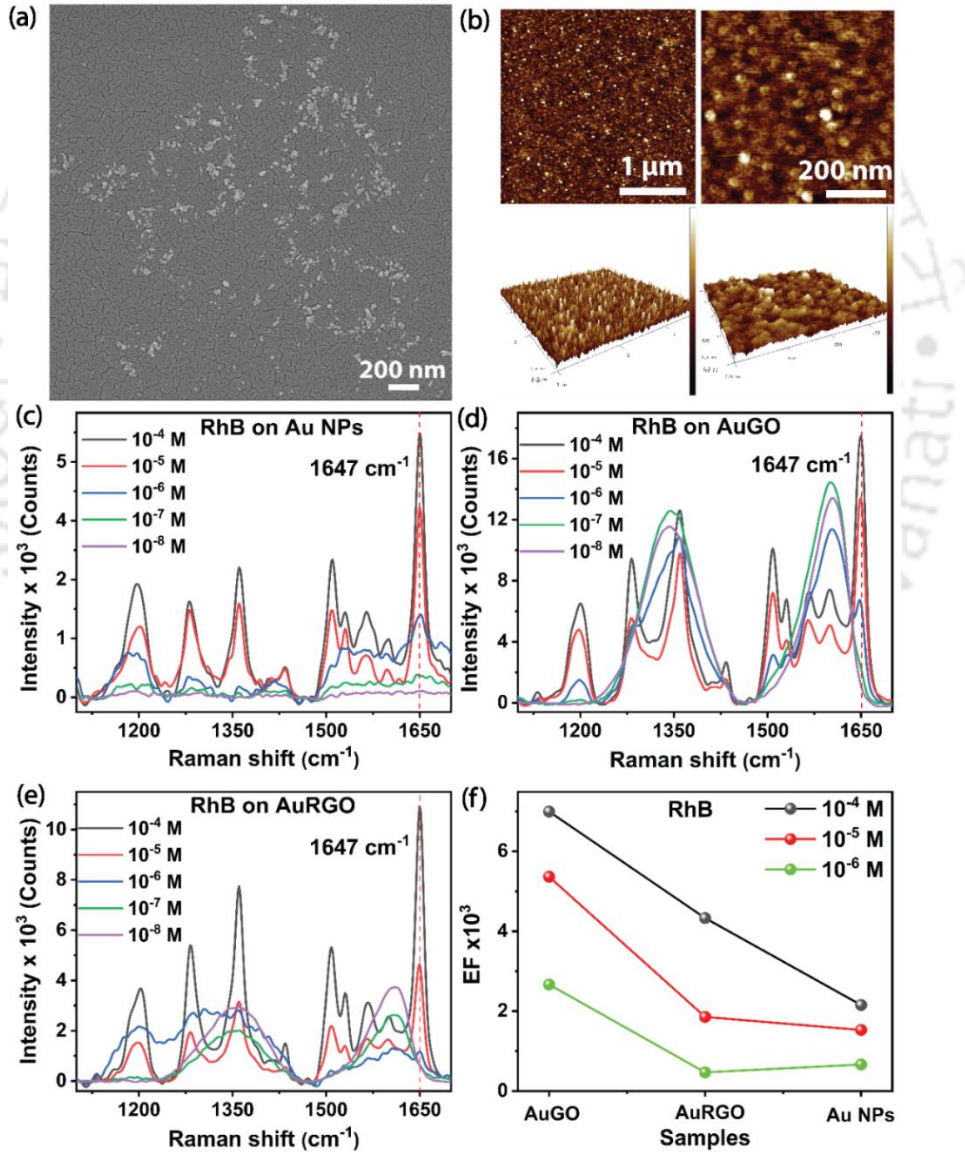

Fig. 4.22: (a) FESEM image of Au NPs; (b) Analysis of surface morphology using AFM image; SERS effect of RhB on the (c) Au NPs; (d) AuGO; (d) AuRGO; and (e) EF analysis of Au NPs and its nanocomposite of GO/RGO with different concentrations of RhB.

In **Fig.4.12a**, the FESEM image shows a random distribution of the Au NPs with sizes ranging from 25-80 nm. The surface roughness and distribution of the Au NPs are analyzed using an AFM image, as shown in **Fig.4.12b**. The root means square average (R_q) of the Au NPs is obtained as 0.319 nm, and the arithmetic average (R_a) of Au NPs is obtained as 0.325 nm. The SERS effect of the RhB is measured on the Au NPs, AuRGO, and AuGO, as shown in **Fig.4.12(c-e)**, respectively.

The SERS effect of dye molecules on the AuNPs is well explained using the mechanism of electromagnetic effect (EE)[25]. The SERS effect of RhB on the AuRGO and AuGO may be contributed both by the EE and CE; the CE is mainly due to the charge transfer from the GO/RGO to the RhB molecules and vice versa. The *EF* of the RhB on the Au NPs, AuRGO, and AuGO are calculated using the formula mentioned earlier. The *EF* of the RhB on the Au NPs, AuRGO, and AuGO are 2.2×10^3, 4.5×10^3, and 7.2×10^3, respectively. The contribution of the EE for the *EF* of the RhB on the Au NPs is 2.2×10^3. It is well known that the Au NPs enrich the *EF* from the EE mechanism. Further, the *EF* of the RhB on the composite of AuRGO and AuGO are 4.5×10^3 and 7.2×10^3, respectively. Thus, the *EF* of the composite of AuRGO and AuGO is higher than the individual Au NPs or RGO/GO due to the former's combined effect on the EE and CE. Whereas the lower concentration at 10^{-6} M of RhB on the AuRGO has a lower enhancement factor than on Au NPs; this may be due to the non-uniform distribution of the Au NPs concerning their size and shape as well as the tendency to coagulate, which cause undesired variation in the SERS signals[26]. However, the *EF* on the Au NPs depends on the size, shape, and distribution of the Au NPs on the substrate[27]. In the present case, Ar plasma treated GO is found to possess the highest EF among all the samples. Thus, the plasma-treated GO can be explored further and exploited in low-cost SERS sensing applications.

4.7. Conclusion

In summary, extra-large GO sheets are exfoliated using a cost-effective mild heating technique. Subsequently, the attached oxygen functional groups are removed using thermal treatment without changing their size. The microscopic structure of the GO is studied using the optical microscope, FESEM, AFM, and FETEM imaging. The signature of the GO and RGO has been confirmed from the XRD, Raman, XPS, and FTIR analyses. The structure of GO and RGO is modified using gas plasma treatment on the GO and RGO, which is evidenced from the Raman analysis with shifting of peak positions, FWHM of peaks, D`-G, and I_D/I_G, and substantiated by FTIR analysis. We have shown that the SERS effect of the RhB on the

GO/RGO is selectively more enhanced than the MO, MB, and RB dyes due to the high charge transfer between the RhB molecules and GO/RGO samples. The *EF* of the GO and RGO are obtained as 6.2 $\times 10^3$ and 3.22 $\times 10^3$, which are increased to 1.33 $\times 10^4$, 9.52 $\times 10^3$, 7.74 $\times 10^3$, 7.35 $\times 10^3$ for Ar-GO, N-GO, Ar-RGO, O-GO, respectively. Ar plasma treated GO substrate exhibits the highest *EF* among all the substrates for RhB detection, owing to the strong coupling dye molecules on the defect sites of GO. The SERS effect is also improved on the composite AuGO than the individual Au NPs or GO/RGO owing to the contribution of *EF* from both EE and CE for RhB dye detection. This study unveils the application of large-area graphene-based sheets for SERS application and the role of low-power plasma treatment on the metal-free substrates for its exploitation in low-cost SERS sensing applications.

Reference

(1) Ling, X.; Xie, L.; Fang, Y.; Xu, H.; Zhang, H.; Kong, J.; Dresselhaus, M. S.; Zhang, J.; Liu, Z. Can Graphene Be Used as a Substrate for Raman Enhancement? *Nano Lett.* **2010**, *10* (2), 553–561. https://doi.org/10.1021/nl903414x.

(2) Liang, W.; Chen, X.; Sa, Y.; Feng, Y.; Wang, Y.; Lin, W. Graphene Oxide as a Substrate for Raman Enhancement. *Appl. Phys. A Mater. Sci. Process.* **2012**, *109* (1), 81–85. https://doi.org/10.1007/s00339-012-7051-y.

(3) Zhang, C.; Jiang, S. Z.; Huo, Y. Y.; Liu, A. H.; Xu, S. C.; Liu, X. Y.; Sun, Z. C.; Xu, Y. Y.; Li, Z.; Man, B. Y. SERS Detection of R6G Based on a Novel Graphene Oxide/Silver Nanoparticles/Silicon Pyramid Arrays Structure. *Opt. Express* **2015**, *23* (19), 24811. https://doi.org/10.1364/oe.23.024811.

(4) Wang, X.; Shi, G. An Introduction to the Chemistry of Graphene. *Phys. Chem. Chem. Phys.* **2015**, *17* (43), 28484–28504. https://doi.org/10.1039/c5cp05212b.

(5) Alam, S. N.; Sharma, N.; Kumar, L. Synthesis of Graphene Oxide (GO) by Modified Hummers Method and Its Thermal Reduction to Obtain Reduced Graphene Oxide (RGO)*. *Graphene* **2017**, *06* (01), 1–18. https://doi.org/10.4236/graphene.2017.61001.

(6) Chen, D.; Feng, H.; Li, J. Graphene Oxide: Preparation, Functionalization, and Electrochemical Applications. *Chem. Rev.* **2012**, *112* (11), 6027–6053. https://doi.org/10.1021/cr300115g.

(7) Kumar, N. A.; Choi, H. J.; Shin, Y. R.; Chang, D. W.; Dai, L.; Baek, J. B. Polyaniline-Grafted Reduced Graphene Oxide for Efficient Electrochemical Supercapacitors. *ACS Nano* **2012**, *6* (2), 1715–1723. https://doi.org/10.1021/nn204688c.

(8) Claramunt, S.; Varea, A.; López-Díaz, D.; Velázquez, M. M.; Cornet, A.; Cirera, A. The Importance of Interbands on the Interpretation of the Raman Spectrum of Graphene Oxide. *J. Phys. Chem. C* **2015**, *119* (18), 10123–10129. https://doi.org/10.1021/acs.jpcc.5b01590.

(9) Díaz, J.; Paolicelli, G.; Ferrer, S.; Comin, F. Separation of the and Components in the C1s Photoemission Spectra of Amorphous Carbon Films. *Phys. Rev. B - Condens. Matter Mater. Phys.* **1996**, *54* (11), 8064–8069. https://doi.org/10.1103/PhysRevB.54.8064.

(10) Lee, A. Y.; Yang, K.; Anh, N. D.; Park, C.; Lee, S. M.; Lee, T. G.; Jeong, M. S. Raman Study of D* Band in Graphene Oxide and Its Correlation with Reduction. *Appl. Surf. Sci.* **2021**, *536* (September 2020), 147990. https://doi.org/10.1016/j.apsusc.2020.147990.

(11) Saleemi, A. S.; Singh, R.; Luo, Z.; Zhang, X. Structure Dependent Negative Magnetoresistance of Amorphous Carbon Thin Films. *Diam. Relat. Mater.* **2017**, *72*, 108–113. https://doi.org/10.1016/j.diamond.2017.01.009.

(12) Kondratowicz, I.; Nadolska, M.; Şahin, S.; Łapiński, M.; Prześniak-Welenc, M.; Sawczak, M.; Yu, E. H.; Sadowski, W.; Żelechowska, K. Tailoring Properties of Reduced Graphene Oxide by Oxygen Plasma

Treatment. *Appl. Surf. Sci.* **2018**, *440*, 651–659. https://doi.org/10.1016/j.apsusc.2018.01.168.

(13) Khalil, I.; Ali, A.; Sina, I. Dual Platform Based Sandwich Assay Surface- Enhanced Raman Scattering DNA Biosensor for the Sensitive Detection of Food Adulteration †. **2020**, 1414–1426. https://doi.org/10.1039/c9an02106j.

(14) Liu, Z.; Li, S.; Hu, C.; Zhang, W.; Zhong, H.; Guo, Z. PH-Dependent Surface-Enhanced Raman Scattering of Aromatic Molecules on Graphene Oxide. *J. Raman Spectrosc.* **2013**, *44* (1), 75–80. https://doi.org/10.1002/jrs.4142.

(15) Sun, S.; Zhang, Z.; Wu, P. Exploring Graphene Nanocolloids as Potential Substrates for the Enhancement of Raman Scattering. *ACS Appl. Mater. Interfaces* **2013**, *5* (11), 5085–5090. https://doi.org/10.1021/am400938z.

(16) Chae, M. S.; Kim, J.; Jeong, D.; Kim, Y. S.; Roh, J. H.; Lee, S. M.; Heo, Y.; Kang, J. Y.; Lee, J. H.; Yoon, D. S.; Kim, T. G.; Chang, S. T.; Hwang, K. S. Enhancing Surface Functionality of Reduced Graphene Oxide Biosensors by Oxygen Plasma Treatment for Alzheimer's Disease Diagnosis. *Biosens. Bioelectron.* **2017**, *92* (August 2016), 610–617. https://doi.org/10.1016/j.bios.2016.10.049.

(17) Si, M. Z.; Kang, Y. P.; Zhang, Z. G. Surface-Enhanced Raman Scattering (SERS) Spectra of Methyl Orange in Ag Colloids Prepared by Electrolysis Method. *Appl. Surf. Sci.* **2009**, *255* (11), 6007–6010. https://doi.org/10.1016/j.apsusc.2009.01.055.

(18) Rodríguez-Torres, M. del P.; Díaz-Torres, L. A.; Romero-Servin, S. Heparin Assisted Photochemical Synthesis of Gold Nanoparticles and Their Performance as SERS Substrates. *Int. J. Mol. Sci.* **2014**, *15* (10), 19239–19252. https://doi.org/10.3390/ijms151019239.

(19) Chen, Y.; Liu, H.; Jiang, J.; Gu, C.; Zhao, Z.; Jiang, T. Immunoassay of Tumor Markers Based on Graphene Surface-Enhanced Raman Spectroscopy. *ACS Appl. Bio Mater.* **2020**, 0–10. https://doi.org/10.1021/acsabm.0c01098.

(20) Mohai, M.; Bertóti, I. Modification of Graphene-Oxide Surface in Nitrogen and Argon Glow Discharge Plasma. *Surf. Interface Anal.* **2016**, *48* (7), 461–464. https://doi.org/10.1002/sia.5929.

(21) Liu, D.; Chen, X.; Hu, Y.; Sun, T.; Song, Z.; Zheng, Y.; Cao, Y.; Cai, Z.; Cao, M.; Peng, L.; Huang, Y.; Du, L.; Yang, W.; Chen, G.; Wei, D.; Wee, A. T. S.; Wei, D. Raman Enhancement on Ultra-Clean Graphene Quantum Dots Produced by Quasi-Equilibrium Plasma-Enhanced Chemical Vapor Deposition. *Nat. Commun.* **2018**, *9* (1), 1–10. https://doi.org/10.1038/s41467-017-02627-5.

(22) Chao, H.; Yuan, F. Y.; Wu, H.; Deng, N.; Yu, Z. Z.; Wei, R. Graphene Oxide and TiO2 Nano-Particle Composite Based Nonvolatile Memory. *2015 15th Non-Volatile Mem. Technol. Symp. NVMTS 2015* **2016**, 18–21. https://doi.org/10.1109/NVMTS.2015.7457487.

(23) Qiu, H.; Wang, M.; Zhang, L.; Cao, M.; Ji, Y.; Kou, S.; Dou, J.; Sun, X.; Yang, Z. Wrinkled 2H-Phase MoS2 Sheet Decorated with Graphene-Microflowers for Ultrasensitive Molecular Sensing by Plasmon-Free SERS Enhancement. *Sensors Actuators, B Chem.* **2020**, *320* (October 2019), 128445.

https://doi.org/10.1016/j.snb.2020.128445.

(24) Wang, Y. Y.; Ni, Z. H.; Shen, Z. X. Interference Enhancement of Raman Signal of Graphene. **2008**, *043121* (November 2007). https://doi.org/10.1063/1.2838745.

(25) Moskovits, M. Surface-Enhanced Raman Spectroscopy: A Brief Retrospective. *J. Raman Spectrosc.* **2005**, *36* (6–7), 485–496. https://doi.org/10.1002/jrs.1362.

(26) Cong, S.; Liu, X.; Jiang, Y.; Zhang, W.; Zhao, Z. Surface Enhanced Raman Scattering Revealed by Interfacial Charge-Transfer Transitions. *Innov.* **2020**, *1* (3), 100051. https://doi.org/10.1016/j.xinn.2020.100051.

(27) Sharma, B.; Frontiera, R. R.; Henry, A. I.; Ringe, E.; Van Duyne, R. P. SERS: Materials, Applications, and the Future. *Mater. Today* **2012**, *15* (1–2), 16–25. https://doi.org/10.1016/S1369-7021(12)70017-2.

Chapter 5

Fabrication and Analysis of Photodetector Devices based on Surface Modified Graphene Oxide and SnO_2-Graphene Oxide Hybrid

This chapter deals with the fabrications of interdigitated electrodes (IDE) for photodetector devices using the UV lithography technique. As-grown graphene oxide (GO) and GO annealed at different temperatures, such as 50 ˚C, 85 ˚C, 120 ˚C, and 230 ˚C are characterized using the XRD, Raman, and I-V measurements. The characteristics of photo response are analyzed on the as-grown and annealed GO, Ar plasma treated GO and nano hybrid of GO and SnO_2. Various features of photocurrent are compared among the different samples and device parameters such as photo-response, response time, responsivity, and detectivity are studied. It is shown that Ar plasma treated GO has the best photo detection performance among all samples.

5.1. Introduction

GO[1] and its derivative materials ((reduced graphene oxide (RGO)[2] and graphene quantum dots (GQDs)[3]) have potential applications in almost every field of applied science and engineering; due to the tunable properties such as electrical conductivity[4,5], surface defects[6,7], bandgaps[8,9], optical transparency[10], lateral size[11], etc[12,13]. The photodetector is one of the applications used in military surveillance[2], self-control vehicles, self-power photosensor[14], wearable devices[15], bio-sensing[3], flexible sensors[16], and home uses[12]. The existing semiconductor-based photodetectors exhibited various drawbacks such as cost, complex fabrication process, fixed bandgap, a hazard to environments, and limited availability of materials[17]. The properties of the semiconductor materials are not flexible as compared to the GO-based materials in terms of the tunable bandgap, sensitivity, fast responsivity, flexible, self-bias, etc[18].

The property of pristine graphene is limited to use as a good photodetector device due to the high transparency, no band gap, and fast carrier recombination. However, these limitations are overcome by oxidation of graphene into GO/RGO and the creation of structural defects used as charge carrier trappers, which are low cost, easily dispersible in solution, and

easily fabricated into the device. The bandgap of the GO (~2.2 eV) and RGO (1.1 eV to 1.9 eV) can be altered by changing the concentration of oxygen functional groups[19]. RGO-based photodetectors detect a large spectrum of wavelengths from IR to UV regions. The structural defects on the surface of RGO enhance the performance of the IR-detector[20].

Further, photodetectors made with heterostructures and nano hybrids of GO can enhance their photo responsivity and detection spectrum. A cost-effective, reproducible, high-quality, easily modifiable, and adjustable photodetector is required. It can be solved by using hybrid of GO-based materials with SnO_2 NPs. SnO_2 NPs are basically semiconducting with large surface area materials, and their absorbance is observed in the UV regions. The combination of GO/RGO with SnO_2 NPs has enhanced the UV response. Due to the low photoresponse of GO and RGO, the photoresponse of the hybrid material using SnO_2/GO can be enhanced. The photodetector performance of the SnO_2 NP and GO/RGO can be improved after various treatments such as gas plasma treatment and thermal annealing.

5.2. Experimental Details

5.2.1. Synthesis of graphene oxide, reduced graphene oxide, and graphene quantum dots

The previous chapters explain the synthesized large lateral size GO and further reduced the oxygen functional groups from the drop-casted GO using thermal treatment. Again, GQDs

Table 5.1*: Description of the samples with sample codes.*

Sample code	Descriptions
GO-RT	GO dried at room temperature
GO-50	GO dried at 50 ˚C
GO-85	GO dried at 85 ˚C
GO-120	GO dried at 120 ˚C
GO-230	GO dried at 230 ˚C
Ar-GO	Ar plasma treated on GO-85
SO	Nanoparticles (NPs) of SnO_2
SO-GO	Nano hybrid of SnO_2 NPs on GO layer
SO-RGO	Nano hybrid of SnO_2 NPs on RGO layer
GQDs-SO	Nano hybrid of GQDs on SnO_2 NPs

are synthesized from the GO solution using a hydrothermal method assisted by a tip-sonication process that was discussed in **chapter 2**.

5.2.2. Fabrication of Inter digitated electrode (IDE)

The 10 µm channel-IDE electrodes are fabricated using UV lithography techniques shown in **Fig. 5.1**. A 300 nm thick SiO_2 on Si substrate is cleaned using three steps: (a) the substrate is deep in the Piranha solution (8:1 of H_2SO_4 in H_2O_2 solution) for 15 minutes to remove the unwanted particles present on the substrate. The substrate is rinsed in the de-ionized water and then dry it using N_2 gas. (b) The substrate is sonicated for 15 minutes in the ethanol

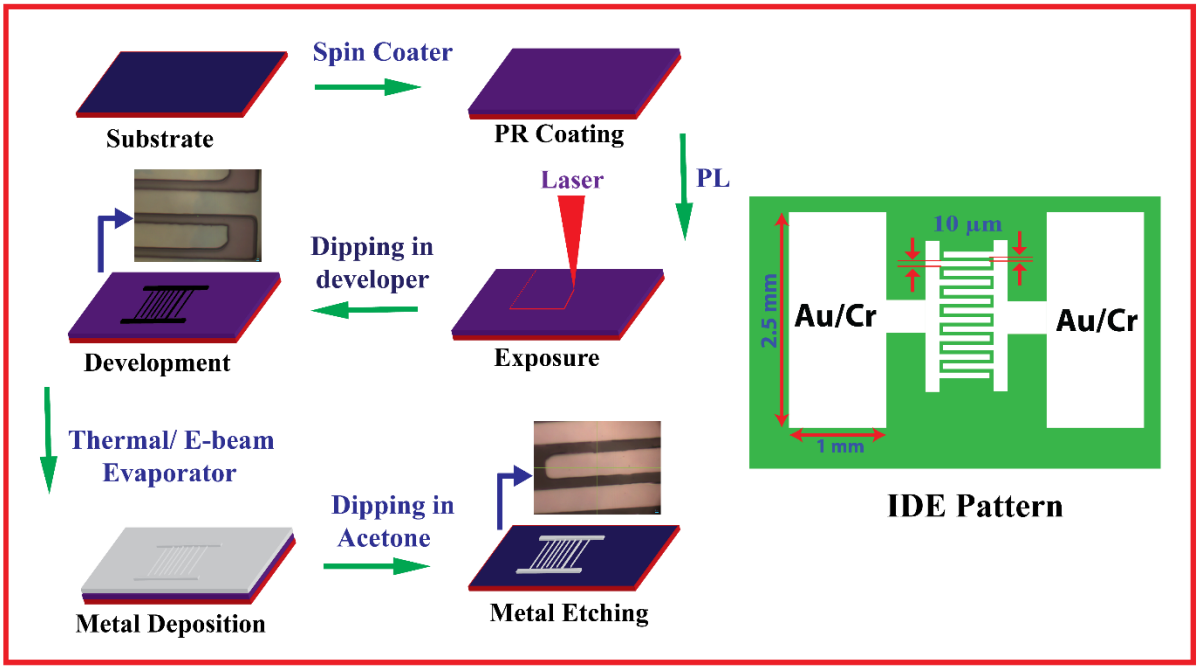

Fig. 5.1: Schematic illustration for fabrication of IDE pattern on SiO_2/Si substrate.

solution. Finally, (c) the substrate is sonicated in acetone solution for 15 minutes and dried after being rinsed in water. Positive photoresist (MicroChemicals GmbH: S1813) is deposited on the cleaned SiO_2/Si at 3500 RPM for 60 s by using spin coater (Apex instruements: spinNXG-M1). Moreover, the positive photoresist (PR) thickness is at~1 µm. The deposited substrate is baked on a hot plate for 3 minutes at 130 ˚C and slowly reduced to 60 ˚C after 3 minutes. The substrate is placed inside the UV exposer stage, just below the microscopic optical lens (20x) for exposing the UV light. The desired IDE pattern is designed in K-layout (software tool) and executed program in the system software (DilaseSoft).

After completion of the exposure, the substrate is removed from the system to develop the pattern. The substrate is dipped in the developer solution for 60 s, and then rinsed with de-ionized water. Once the patterns are developed, the metallization process is done in the

thermal/E-beam evaporator system. The substrate is placed on the sample holder inside the evaporator chamber; the inside pressure of the chamber is evacuated up to 5.8×10^{-6} mbar using a turbo-molecular vacuum pump (Pfeiffer vacuum) supported by a rotary vacuum pump. The wanted vacuum pressure is achieved after 6 hours of a continuous run of the vacuum system. The substrate is deposited by 10 nm thick Cr using an E-beam evaporator and then by 20 nm of Au using a thermal evaporator. After metal deposition, the substrate is taken for the metal lift-off process; the 130 ˚C baked substrate is dipped into the acetone solution for 3 minutes and shaken in the container gently. Thus, the 10 µm channel IDE pattern is fabricated using UV lithography.

Now, the IDE pattern is composed of two parts: fringes and two metal pads. Fringes are made in dimensions of 10 µm width of a metal fringe and 10 µm of the minimum gap between two adjacent metal fringes. Each dimension of the metal pad is 2.5×1 mm^2 in width and length, sufficient for electrical probing with metal tips.

5.2.3. Synthesis of nano hybrid of SnO_2 on graphene oxide

A composite of GO and NPs of SnO_2 (Aldrich) is synthesized using drop-casting NPs of SnO_2 on the GO sheets. At first, 2 µl of GO solution is drop-casted on the pattern and dried in an open environment. 3mg of ~100 nm NPs of SnO_2 are dispersed in the 20 ml of de-ionized water using the tip-sonication process for 30 minutes. 2 µl of dispersed NPs are drop-casted on the GO sheets where they are placed on the IDE pattern. The device is dried for 45 minutes at 85 ˚C on the hot plate.

5.2.4 Characterization Techniques

The morphology of the GO, annealed GO, and IDE pattern on the SiO_2/Si was observed using a field emission scanning electron microscope (FESEM) (*JEOL, JSM-7610F*). The thickness of the IDE patterns was studied using an atomic force microscope AFM (*Bruker, Innova*), and data were analyzed using analysis software (*NanoScope Analysis 1.5*). The structural analysis of the GO and annealed GO was studied using XRD (Rigaku, *RINT 2500 TTRAX-III*), with Cu Kα radiation as a source of x-ray and a scanning speed of 3 °/min. The structural defects and functional groups attached to the graphitic carbons of GO and annealed GO were studied using Raman spectroscopy (*Horiba, LabRam HR*) with the wavelength of 532 nm as a laser source using a 100× optical lens. The functional groups attached to the GO and annealed GO were studied using an X-ray photoelectron spectroscopy (XPS) (*PHI X-tool, ULVAC-PHI INC*) with Al K_α as an X-ray energy source at 20 kV and 54 W. The functional groups of the GO/annealed

GO were studied using the transmittance mode of the Fourier transform infrared (FTIR) spectroscopy (*Perkin Elmer, spectrum BX*). The photoluminescence (PL) of GO solution was measured using the fluorimeter (*Horiba, Fluromax-4*) using 360 nm excitation.

5.2.5 Photodetector set-up

A customized photodetector system is used for the photo-response measurement, shown in **Fig. 5.2**. It consists of a microprobe station (ECOPIA, EPS-500), a source-measure unit (Keithley 2401), a 405 nm diode laser (CNI Laser), a monochromator (Oriel Instruments), a pulse generator (Scientific), and a focusing lens.

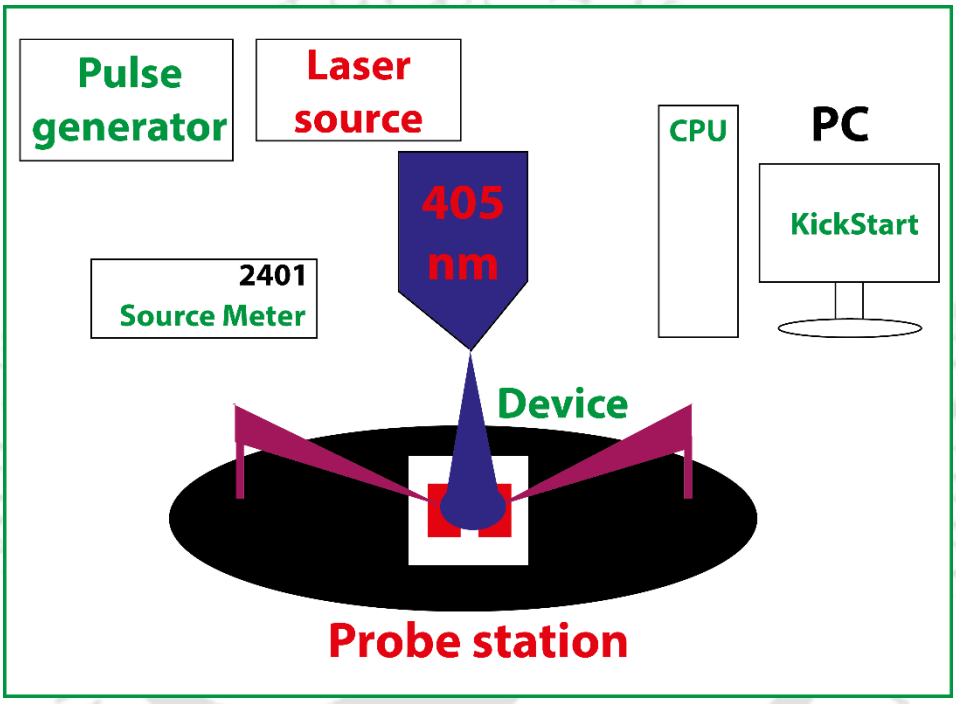

Fig. 5.2: Illustrated schematic diagram of a photodetector measurement system.

At first, the device is placed on the micro-probe station, and two gold-coated micro-tips are engaged on both sides of the metal pads of the device. The metal probes are connected to a source-measure unit (Keithley 2401) which is further connected to the personal computer through a GPIB cable. A laser source is focused on the device to measure its photo-response; it has an adjustable laser power. A pulse generator is connected to the laser source to provide a pulse form of laser to the device to measure the ON/OFF response. All the response activities are controlled and acquired using KickStart software.

5.3. Results and discussions

5.3.1. Morphological and structural analysis

A cross-section area of (120 ×100) μm^2 of GO sheet with wrinkles is observed in the FESEM image, shown in **Fig. 5.4a**. A magnified image of the wrinkled is shown in the **inset** of **Fig. 5.4a.** The structural analysis of the GO and different annealed GO samples are studied using XRD (**Fig. 5.4b**) and Raman spectra (**Fig. 5.4c**). XRD pattern of the GO samples dried at room temperature (GO-RT) is obtained in the (002) plane at 10.9˚ of 2θ, which is owing to the highly oxidized GO/ highly oxygen functional groups attached to GO sheets[21,22]. Similarly, GO annealed at 50 ˚C (GO-50) is also attained at 10.9 ˚. GO annealed above 50 ˚C suppressed the significant GO peaks at 10.9˚ and shifted towards the graphitic peak at 26.3˚. Interestingly, GO-85 (GO annealed at 85 ˚C) is flattered on both peaks (10.9˚ and 25.6˚). The

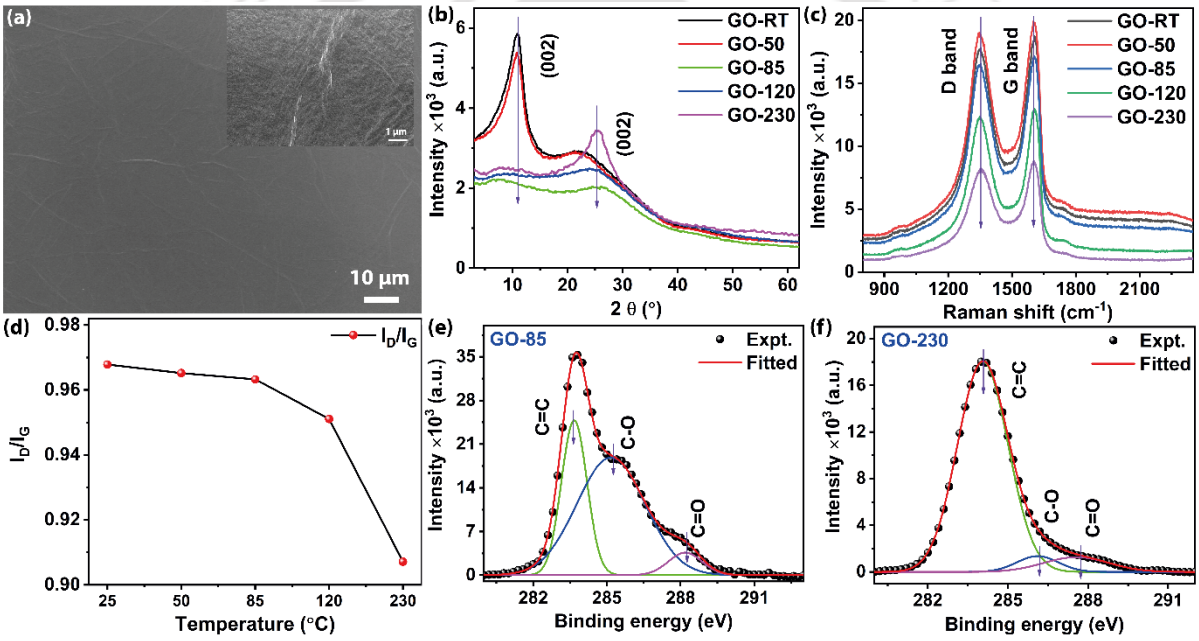

Fig. 5.3: (a) FESEM image; (b) XRD pattern and (c) Raman spectra of GO and different temperature annealed GO; (d) I_D/I_G of the different temperature of GO samples; XPS analysis of (e) annealed GO at 85 ˚C, and (f) annealed GO at 230 ˚C.

peak at 25.6˚ is enhanced as the annealing temperature increases from 120 ˚C (GO-120) to 230 ˚C (GO-230). The GO samples' interlayer spacing (*d*) is calculated using Bragg's law ($2d \sin\theta = n\lambda$). The interlayer spacing (*d*) of the GO-RT and GO-50 was found to be ~0.81 nm; for GO-85, GO-120, and GO-230 it was ~0.34 nm.

The Raman spectra of GO and annealed GO samples are analyzed in **Fig. 5.4c**. The Raman spectra are measured from 800 cm^{-1} to 2400 cm^{-1}; two prominent bands (D and G bands) are[23] centered at 1350 cm^{-1} and 1600 cm^{-1}. The intensity of the D and G bands are reduced as

the annealing temperature of GO samples increase, but the position of the peaks is retained as constant after different heat treatments. The change in the intensity of the Raman signals may be influenced by the presence of oxygen functional groups on GO. Raman spectra are measured on the different GO samples, which are complex to justify the nature of the GO from the intensity of the peak alone.

I_D/I_G analysis of the Raman signal is one parameter to define the GO samples' quality (**Fig. 5.4d**). The reduction of I_D/I_G value indicates the restoration of the sp^2 hybridized structure of thermal annealed GO. Due to the removal of oxygen functional groups attached to the graphitic structure and the presence of the functional groups, it leads to a change in the sp^2 to sp^3. The I_D/I_G ratio of the annealed sample was negligibly changed from 0.968 to 0.964 for GO-RT to GO-85; it may be because the 85 ˚C annealing cannot remove the oxygen functional groups in GO. At higher temperatures, its value is reduced to 0.95 for GO-120 and 0.91 for GO-230. The reduction of the I_D/I_G value is shown by removing the loosely bounded oxygen functional groups from the GO, which is supported by the TGA analysis of GO and RGO, analyzed in **section 3.2.2** (**chapter 3**).

The XPS analysis of the thermal annealed GO at 85 ˚C and 230 ˚C is shown in **Fig. 5.3e** and **Fig. 5.3f**. The strong presence of C-O and C=O functional groups in the GO-85 is indicated in the 286 eV and 288.9 eV, respectively[24]. Moreover, the signified oxygen functional group (C-O) at 286 eV is flatted after thermal annealing of GO at 230˚C. This shows that removal of C-O functional groups from GO after thermal annealing at 230 ˚C leads to restoring the GO's graphitic structure.

FTIR spectra of the GO and thermal annealed GO are studied in the presence of oxygen functional groups and graphitic structure (sp^3 and sp^2 carbon bonds), which is shown in **Fig. 5.4**. The transmittance peaks of FTIR for GO and annealed GOs are concentrated in the range from 900 to 3600 cm^{-1}. The peaks range from 950 cm^{-1} to 1480 cm^{-1} are comprised of the oxygen functional groups. The peaks of C-O (alkoxyl group) at 1057 cm^{-1}, O-C=O at 1228 cm^{-1}, C-OH at 1391 cm^{-1}, C=C at 1630 cm^{-1}, and C=O at 1722 cm^{-1} are more prominent in GO-RT, GO-50, and GO-85[25,26].

The intensity of the corresponding peaks for the C-O and O-C=O functional groups are suppressed in GO-120 and GO-230 compared to the previous case. The peaks at 3400 cm^{-1} related to -OH appears in the spectra for both GO and all annealed GO samples except GO-230; these may be due to the absorption of water from the atmosphere during the preparation of samples. The signature peak at 1630 cm^{-1} corresponding to C=C bonds is observed on all

the samples. The absorption peak arising from the carbonyl group (C=O) at 1740 cm^{-1} are present in all the samples, which is very hard to remove even after thermal treatment. From the XPS and the FTIR analyses, it is evident that the oxygen functional groups are reduced in GO-230 compared to the other GO samples.

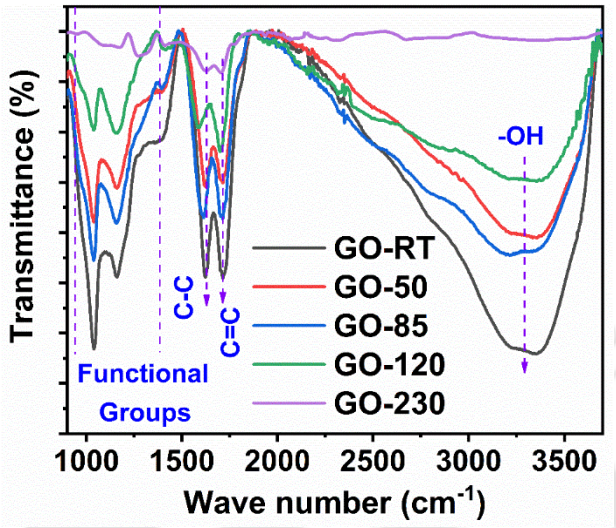

Fig. 5.4: FTIR analysis of as-grown GO and different temperature annealed GO.

5.3.2. UV absorption and PL studies of graphene oxide

UV absorption and Photoluminescent (PL) characteristics of GO-RT are shown in **Fig. 5.5.** UV absorption spectra of the GO-RT are analyzed in **Fig. 5.5a**. Two notable peaks at 235 nm and 300 nm are observed. A peak at 235 nm can be assigned to $\pi \rightarrow \pi^*$ transition or π-plasmon resonance common for extended sp^2 conjugated carbon sheet (C═C present within the aromatic sp^2 hybridized carbon framework)[12]. A slight hump-like shoulder is also seen at 300 nm, corresponding to $n \rightarrow \pi^*$ from oxygen-containing functional groups.

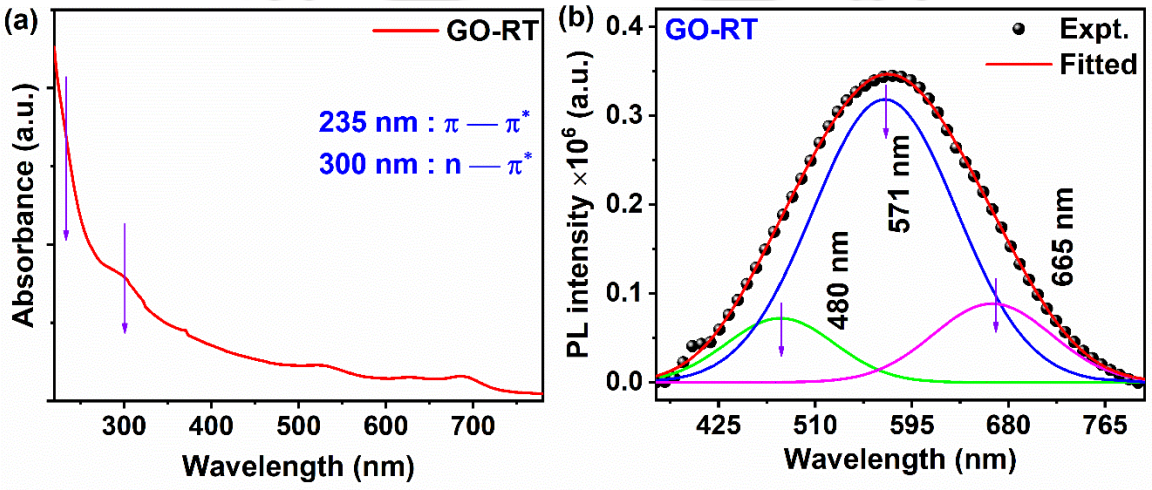

Fig. 5.5: (a) UV absorption of GO RT; and (b) PL analysis of GO RT.

The presence of oxygen-containing functional groups is evident from the absorption spectra of GO. A broader band in the range 400-780 nm is observed in the PL spectrum of GO-RT (**Fig. 5.5b**). This band consists of three peaks, centered at 480 nm, 571 nm, and 665 nm, arising from the disorder-induced defect states due to the sp^3 character of carbon with oxygen-containing functional groups attached to graphene carbons. The presence of oxygen can increase the number of (C─OH) and (C─O─C) bonds due to the rearrangement of oxygen and oxygen-containing functional groups with carbons. This consequently enhances the transfer of resonance energy from O sites to the sp^2 clusters in the graphene lattice, contributing to a broad PL emission[13].

5.3.3. Analysis of interdigitated electrode pattern

Fabricated 10µm channel IDE studied the microstructure using FESEM and AFM images, shown in **Fig. 5.6**. In **Fig. 5.6a**, a low magnification image of the IDE pattern with the large metal pad is observed; this large area (2.5 × 1) mm is sufficient for probing the 0.5 mm diameter probe for the measurement of photo I-V characteristics. The magnified image on the metal fringes are shown in **Fig. 5.6b**; the clear separation of the metal fringes is observed in the image, and the spacing between the consecutive metal fringes is obtained at ~10 µm. The IDE is fabricated on the clean SiO_2/Si substrate to confirm that it is essential for the fabrication and working of a device.

An AFM image is shown in **Fig. 5.6c**, which is captured between two consecutive metal fringes of the IDE pattern. The gap in the spacing is measured ~10 µm; this is similarly attained from the analysis of FESEM images. The thickness of the deposited metal is measured using the height profile of the AFM image; it is obtained ~ 30 nm (**Fig. 5.6d**). This thickness is sufficient for measuring the device's I-V characteristic and sustaining the probing multi-times on the same metal pad.

FESEM image of the GO sheets deposited on the IDE pattern is studied and viewed in **Fig. 5.6e** and magnified image in **Fig. 5.6f**. Due to the extremely thin and transparent nature of the GO sheets, the microscopic imaging of a GO sheet is difficult to spot and observe. However, the presence of wrinkles and folds on the surface of GO determines the GO sheet on the IDE pattern. In **Fig. 5.6e**, a large number of non-fashioned bright-line spots on the IDE pattern are observed. The spots are spread across the metal fringes, which shows the GO sheet is connected across the metal fringes, or GO sheets connect two electrodes. The magnified image of the GO deposited IDE is monitored, and found the GO sheets are lying on top of the metal fringes and connected to the electrodes.

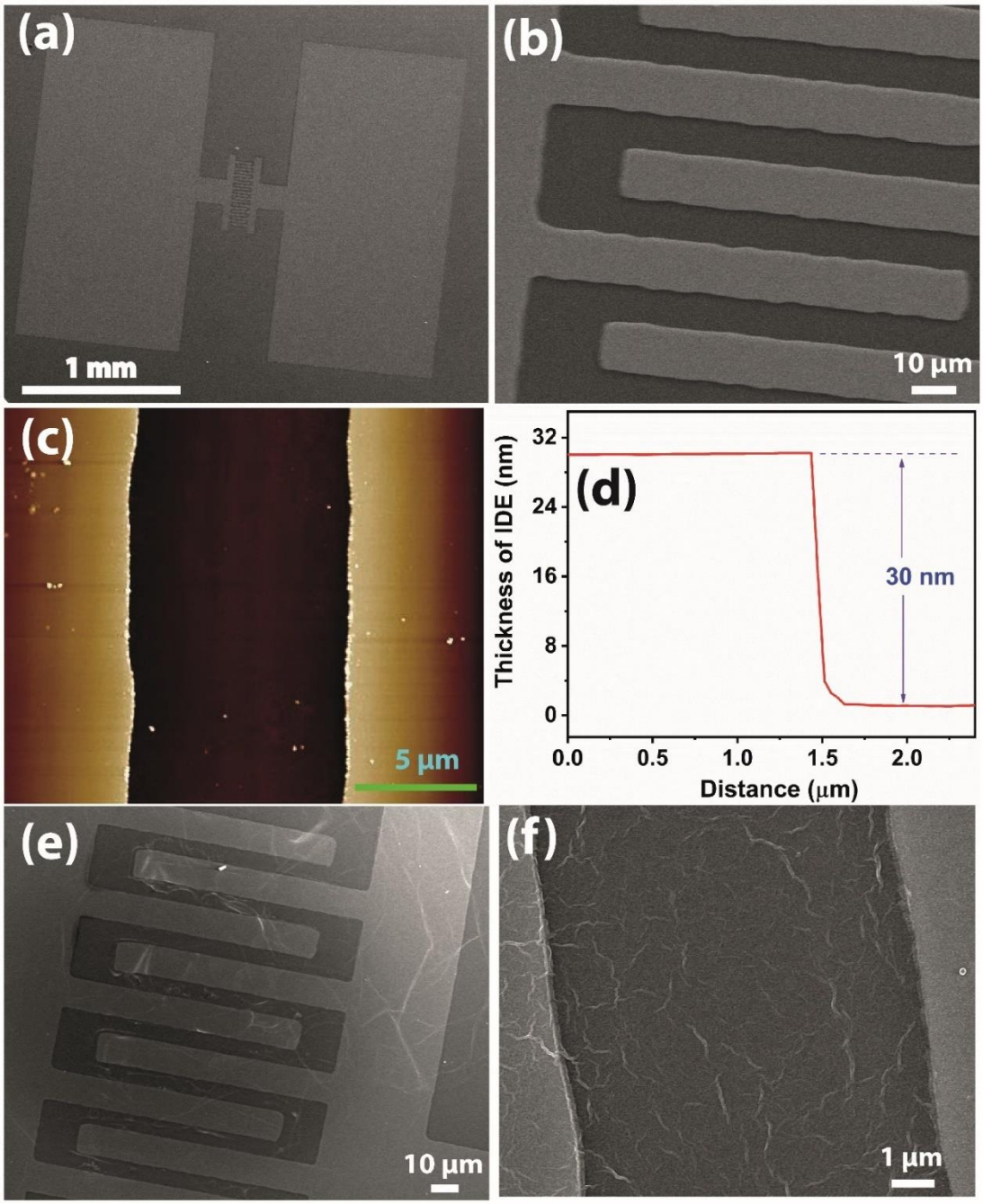

Fig. 5.6: (a) FESEM image of IDE (a) low magnification image; (b) high magnification image on fringes; (c) AFM image on the two consecutive fringes; (d) Height profile of electrode thickness; (e) GO sheets on IDE; and (f) GO sheets in between the metal fringes.

5.4. Electrical characterizations

5.4.1. IV characteristics of graphene oxide and different temperature annealed graphene oxide

IV characteristics of the GO samples such as GO-RT, GO-50, GO-85, GO-120, and GO-230 in **Fig. 5.7**. The current of the GO samples is measured from -2 V to 2V; observed the

variation of current flow based on the annealed temperature of GO. The characteristics of the IV seem like non-ohmic nature and semiconducting behavior[27]. GO-RT is highly insulating and obtained a very low current compared to the other annealed GO samples. The flow of current is increasing as we increase the temperature of annealing in GO; when 1 V is applied in the GO-based devices, the flow of the current in the GO-RT, GO-50, GO-85, GO-120, and GO-230 is 29 nA, 1.6 µA, 7.4 µA, 14 µA, and 0.6 mA, respectively shown in **Fig. 5.7a**. **Table 5.2** explains the flow of current on the different temperature annealed GO samples concerning the applied voltage.

The improvement of current for the GO samples is obtained; such as the current of GO-50 is enhanced up to 55 times from GO-RT; GO-85 is improved 4.6 times from GO-50; GO-120 is enhanced 4.6 times from GO-85, and GO-230 is increased 42 times. The highest current improvement is observed from GO-RT to GO-50; it may be due to the removal of moistures contained in the GO-RT after being heated at 50 ˚C. The FTIR analysis supports it.

***Table 5.2**: I-V characteristics of different temperature annealed GO samples*

Voltage (V)	**Dark current (A)**				
	GO-RT	**GO-50**	**GO-85**	**GO-120**	**GO-230**
-2	-1.9×10^{-7}	-4.1×10^{-6}	-9.3×10^{-6}	-6.3×10^{-5}	-1.2×10^{-3}
-1	-5.4×10^{-9}	-3.8×10^{-7}	-1.2×10^{-6}	-1.2×10^{-5}	-6.7×10^{-4}
1	2.9×10^{-8}	1.6×10^{-6}	7.4×10^{-6}	1.4×10^{-5}	6.1×10^{-4}
2	1×10^{-7}	3.1×10^{-6}	8.2×10^{-6}	8.2×10^{-5}	6.1×10^{-4}

Similarly, GO-230 has 42 times enhanced flow of current compared to GO-120 (**Fig. 5.7b**) due to the removal of the oxygen functional groups attached to the GO-120 and restoration of the sp^2 graphitic structures. The removal of oxygen functional groups from GO-230 compared to GO the XPS, and FTIR analysis confirm 120. The IV characteristics of the GO and annealed GO samples confirmed that the attached oxygen functional groups disturbed the graphitic structure of the GO and induced structural defects.

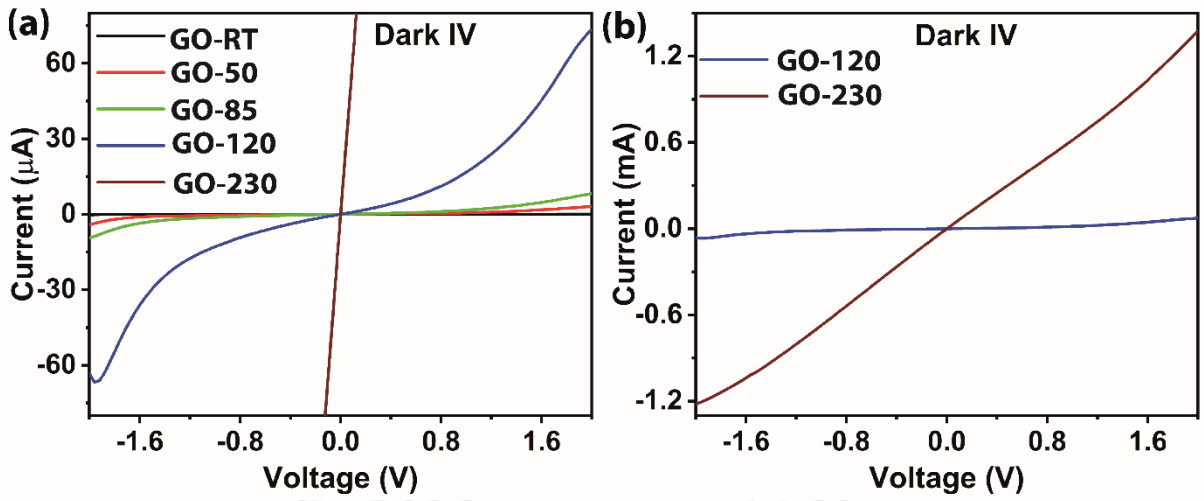

Fig. 5.7: Dark IV characteristics of (a) GO and annealed GO, and (b) Comparison of GO-120 and GO-230.

5.4.2. IV characteristics of graphene oxide (GO) under dark and light

The IV characteristics in the dark and under light on the annealed GO samples are analyzed in **Fig. 5.8**.

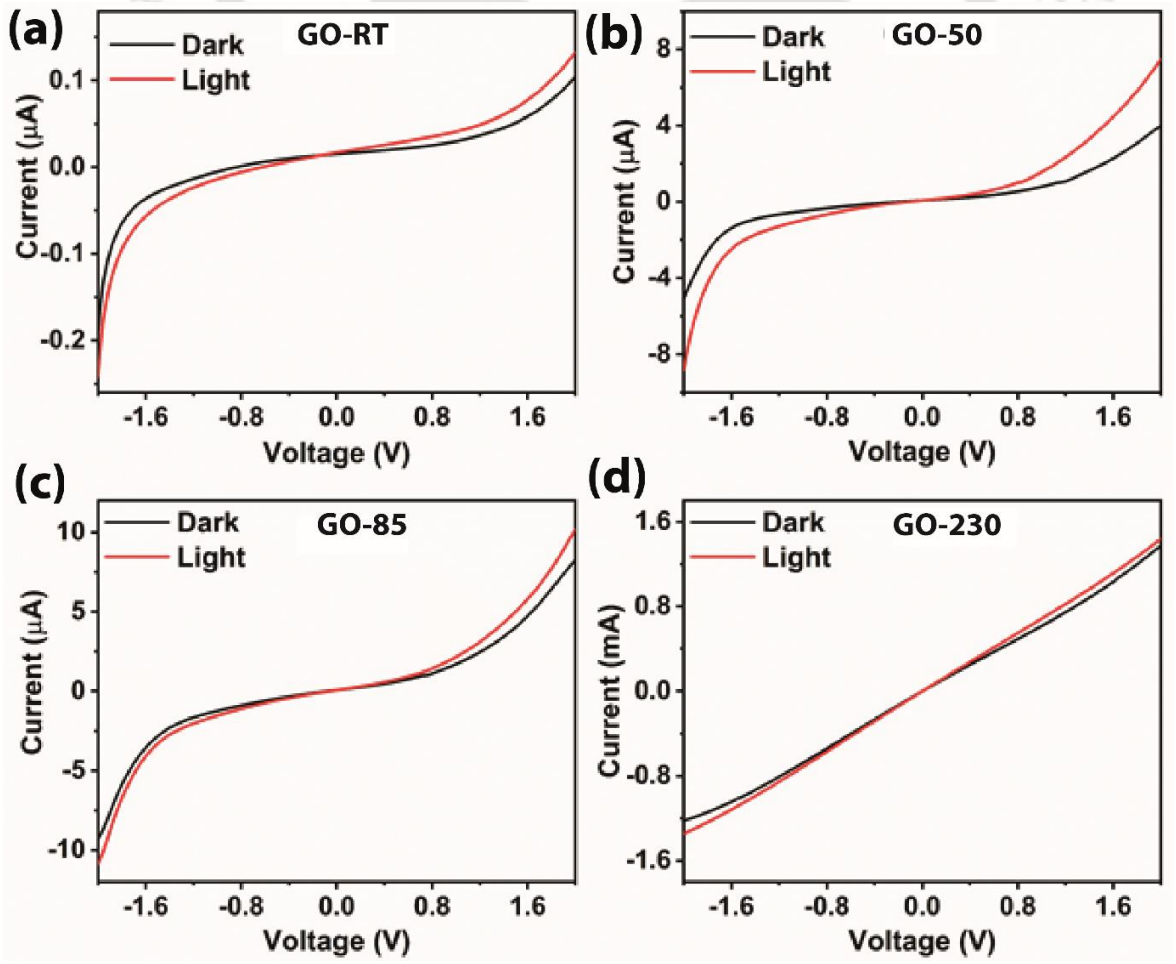

Fig. 5.8: IV characteristics of dark and light (405 nm) of (a) GO-RT; (b) GO-50; (c) GO-85; and (d) GO-230.

In the light condition, the GO-based two-electrode device is exposed by laser (405 nm); the applied power of the laser is calculated to be 16.5 mW/cm^2. The current flow is improved for all the devices under the photo environment. The IV curve is measured from -2V to 2V. In **Fig. 5.8a**, the change of current flow in the GO-RT is increased up to 21 nA after being exposed to the laser and the applied bias voltage is 2V; the change in the current is still very low. In the case of GO-50, the enhanced current is 0.76 µA after being exposed to the laser, which is observed in **Fig. 5.8b**.

The flow of the photo-induced current is much improved in GO-50 compared to GO-RT. Likewise, the increased photocurrent of GO 85C is 0.61 µA (**Fig. 5.8c**), which is as compared with the GO 50C. A similar pattern of change in the dark current is observed in the previous discussion in **section 5.5.1**. Besides, the flow of current in the GO-230 (**Fig.5.8d**) is increased up to 85 µA under the light condition. The GO-230 is like ohmic contact, which behaved most likely as a metal other than a semiconductor. So, use of GO-230 is not favoured use in photodetector devices. The stability of the photodetector device is better in GO-85 due to the removal of unstable oxygen functional groups from the GO. As a result, GO-85 is chosen as GO for the photodetector device and its relevant studies.

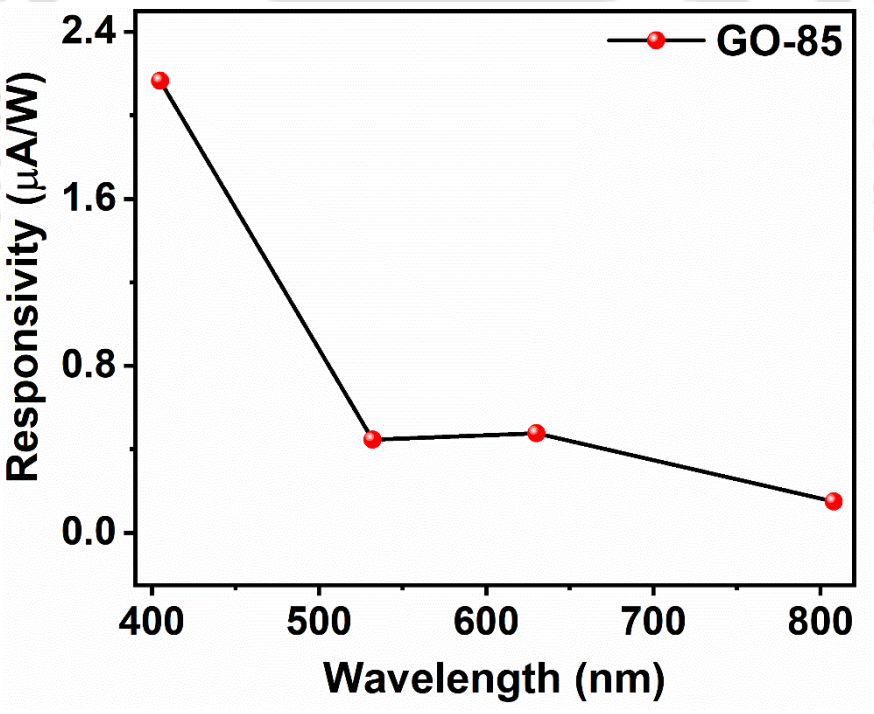

Fig. 5.9: Wavelength dependent photoresponsivity of GO-85.

The responsivity of the GO-85 is studied in a different wavelength of the laser source, shown in **Fig. 5.9**. Responsivity is the amount of photocurrent generated by a unit of optical power.

The highest photo response of GO-85 is 2.4 when exposed by 405 nm, as compared to the other wavelengths such as 532 nm, 630 nm, and 808 nm.

5.4.4. Photo and dark I-V characteristics of Ar plasma treated GO, and nano hybrid of SnO_2 NPs on GO-85

The I-V characteristics of the Ar-plasma treated GO (Ar-GO) and nano hybrid of SnO_2 NPs and GO (SO-GO) samples are measured in dark and light (405 nm laser), as shown in **Fig. 5.10**. The Ar-GO photodetector is fabricated by: GO solution is dropped cast on the 10 µm channel IDE pattern, the sample is dried at 85 ˚C for 45 minutes; then it is exposed to the Ar plasma for 30 s. The photodetector device is placed on the micro-probe stage and probes the two micro tips on the electrode pads. And the micro-tips are connected to the source meter (Keithley, 4201); the source meter is connected to the personal computer through GPIB to USB cable. The measurement of the IV characteristics is done by using LabTracer 2.9 software. The laser vertically falls on the devices. The power of the laser can be controllable and automatic ON/OFF the laser power by using a function generator. The voltage is measured from 0 V to 2.5 V. In **Fig. 5.10a**, Ar-GO is measured for its I-V characteristics with and without a light source. The flow of current on the Ar-GO is increased from 1.2 µA to 1.96 µA after exposure to light. The change of current is measured at 0.75 µA. In **Fig. 5.10b**,

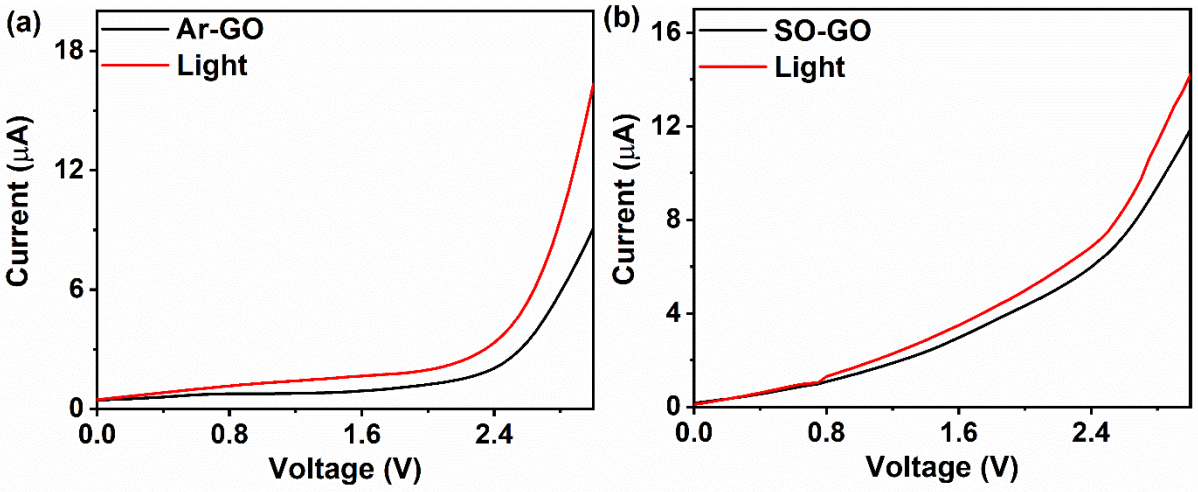

Fig. 5.10: IV characteristics of dark and light environment of (a) Ar plasma treated GO (Ar-GO); (b) Nano hybrid of GO and NPs of SnO_2.

the nano hybrid of the SnO_2 NPs and GO-85 is obtained at 4.32 µA for dark and 4.98 µA for light. The change of current is 0.65 µA. The applied power of the laser is calculated to be 15.8 mW/cm^2.

5.4.5. Photocurrent of GO-85, Ar plasma treated GO, and nano hybrid of SnO_2 NPs on GO-85

Photocurrent of the GO-85, Ar-GO, and SO-GO are analyzed in **Fig. 5.11**. The photocurrent (I_{ph}) is defined as the current difference between light current (I_{light}) and dark current (I_{dark}). Hereby, I_{light} is defined as the amount of current flow to the device when the illumination of light on it; I_{dark} is defined as the amount of current flow to the device in a dark environment. The illuminated wavelength of the laser is 405 nm and the density power of the incident laser is 16.5 mW/cm^2. In **Fig. 5.11a**, the GO-85's dark current is increasing as the number of ON/OFF cycles increases. The origin of the continuous increase in the baseline/dark current is not very clear. However, a change in the dark current with time is commonly observed in photodetectors[28–30]. The magnitude of the photocurrent is almost constant for many ON/OFF cycles, which is unrelated to the reduction in GO due to light illumination[31]. The Iph of the GO-85 is 81 nA. In the case of Ar-GO, the dark current is almost retained constant at 5.7 µA for all the NO/OFF cycles shown in **Fig. 5.11b**.

The Iph of the Ar-GO is 1120 nA. The dark current of the Ar-GO is increased after plasma treatment on the GO-85. The I_{ph} of Ar-GO is equal for all the number of ON/OFF cycles which frequency is set to 0.05 Hz. The SO-GO obtained the I_{ph} of 362 nA, the photo-induced current on the nano hybrid of SnO_2 NPs on GO-85 shown in **Fig. 5.11c**. Three different GO-based materials are exhibited different photo-induced currents such as 81 nA, 362 nA, and 1120 nA for GO-85, SO-GO, and Ar-GO, respectively. The SO-GO is improved the I_{ph} may be due

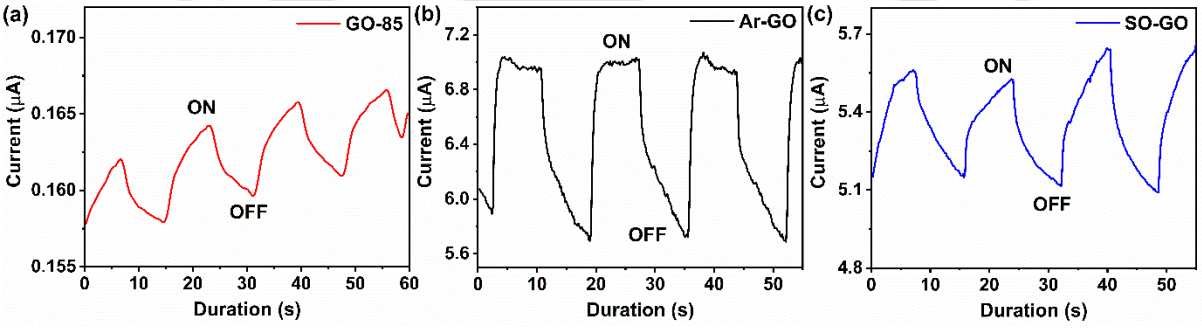

Fig. 5.11: Photo-response of (a) GO-85; (b) Ar-GO; and (c) SO-GO.

to the increasing of charge carriers into the GO-85 after light illumination. In contrast, the surplus increase of I_{ph} for Ar-GO may be due to the creation of defects and removal of a certain amount of oxygen functional groups leading to an increased photo-induced current.

5.4.6. Time response of GO-85, Ar plasma treated GO, and nano hybrid of SnO_2 NPs on GO-85

The time response is an important parameter to calibrate the quality of a photodetector device. It is investigated from the photocurrent presented in the above **section 5.5.5**. A photodetector's response time is divided into two: rise time or response time (τ_{rise}) and decay time or recovery time (τ_{dec}). τ_{rise} is the amount of time required to reach the I_{light} from I_{dark}. It is calculated from 10% of the I_{dark} to 90% of I_{light} of time. Similarly, τ_{dec} is defined as the amount of time required by a device to return the dark current from the light current; the amount of time required from 90% of I_{light} to 10% of I_{dark}.

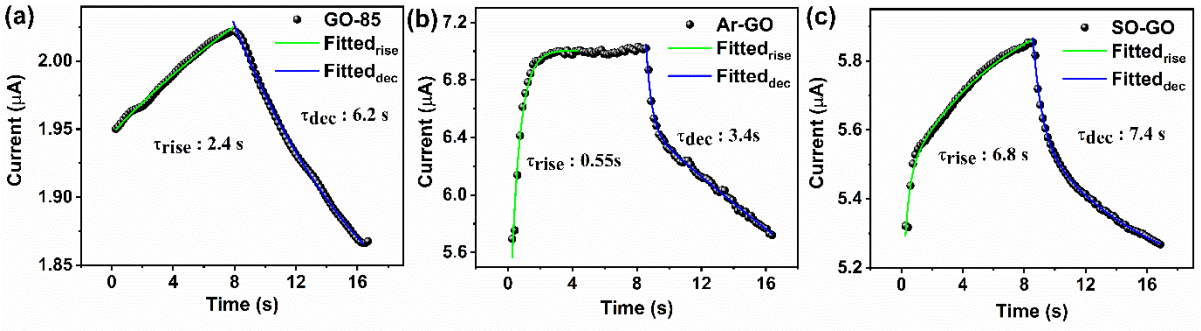

Fig. 5.12: Time response analysis of (a) GO; (b) Ar-GO; and (c) SO-GO.

In **Fig. 5.12a**, the τ_{rise} and τ_{dec} of the GO-85 are 2.4 s and 6.2 s. The value of τ_{rise} is calculated from the slope of a fitted exponential growth curve of an ON/OFF cycle of the photocurrent graph, shown in **Fig. 5.12a**. Similarly, the value of τ_{dec} is calculated from a slope of a fitted exponentially decay curve of an ON/OFF cycle of the photocurrent graph. The fitting of the related curves is drawn in the Origin 8.5 tool. From **Fig. 5.12b**, the τ_{rise} and τ_{dec} of the Ar-GO is 0.55 s and 3.4 s. Furthermore, **Fig. 5.12c** is shown that the τ_{rise} and τ_{dec} of the SO-GO is 6.8 s and 7.4 s, respectively. Thus, Ar-GO is improved the τ_{rise} to 4.3 times from the GO-85, and 12.3 times from the SO-GO. The τ_{dec} to 1.8 times from the GO-85 and 2.1 times from the SO-GO. As a result, Ar-GO has obtained a fast response and recovery time compared to others. The analysis of τ_{rise} and τ_{dec} for GO-85, Ar-GO, and SO-GO, it is confirmed the response time are not equal. It may be due to the creation of structure defects by plasma treatment and the creation of nano hybrid affected the photo response of the devices. The slower response time of the GO and related materials may be due to the trapping charge carriers[32]; the presence of rich oxygen functional groups in GO may trap charge carriers which result slow response time[31]. And, Trapping increases the recombination lifetime of the charge carrier[33], which manifests as a significantly longer response time.

5.4.7. Voltage-dependent study of GO-85, Ar plasma treated GO, and nano hybrid of SnO_2 NPs on GO-85

The change of response current with respect to the bias voltage on the GO-85, SO-GO, and Ar-GO is analyzed in **Fig. 5.13**. The photo response of current is studied by varying the bias voltage from 0 to 2.5 V for all the samples. In **Fig. 5.13a**, the photo response at the 0V and 0.1 V is nil; but the response is increases as increasing the bias voltage up to 2.5 V. A prominent change of current from 38 nA to 81 nA then 118 nA after applying the bias voltage of 1.5 V, 2V and 2.5 V, respectively. This enhancement of response current may be due to the bias voltage are suppressed the activation voltage to flow the current on GO-85.

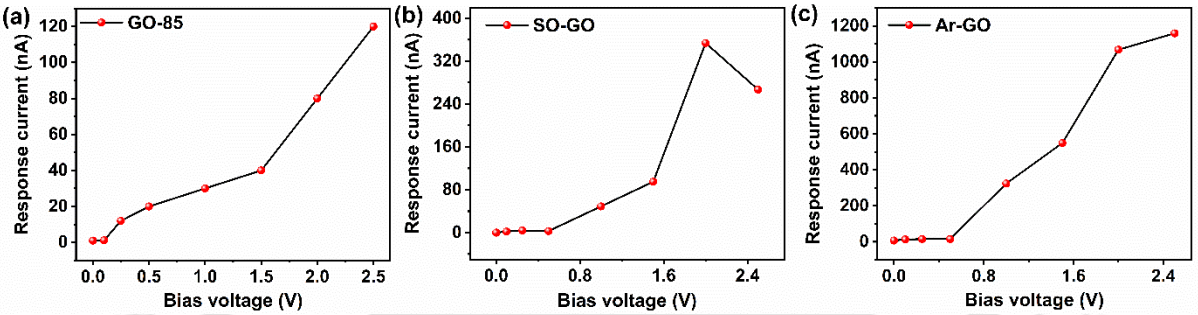

Fig.5.13: Voltage-dependent studied on (a) GO-85; (b) SO-GO; and (c) Ar-GO.

In **Fig. 5.13b**, the response current is nil for the bias voltage from 0 to 0.5 V; the flow of current is increases as the applied voltage increases afterward. The prominent change of response current is observed from the 1.5 V to 2 V of bias voltage which is 220 nA. The reduction of the response current down to 280 nA after applying the bias voltage of 2.5V unusual. In **Fig. 5.13c**, the response current is not observed up to the bias voltage of 0.5 V for the Ar-GO; the response current is enhanced after applying the bias voltage of 0.5V and above. A drastic increase in response current is detected linearly. 380 nA of current is flown after applied bias voltage of 1V, which is nearly negligible when applied bias voltage of 0.5 V. Again, 620 mA of response current is increased from the applied bias of 1.5 v to 2V. Thus, Ar-GO has obtained a higher flow of response current compared to the GO-85 and SO-GO, which may be due to the creation of surface defects and restoration of the graphitic structure after Ar plasma treatment. The dark current of the photodetector device can be reduced further using various processes. Such as the formation of heterostructure layers, composite with different bandgap materials, increase in the thickness of the active layer, blocking the charge recombination during the operation, and increasing the charge trapping sites[34–36]. Thus, the photo-response can be improved by forming multi-layer active materials decorated with Au nanoparticles.

5.4.8. Excitation power study of GO-85, Ar plasma treated GO, and nano hybrid of SnO_2 NPs on GO-85

Excitation power study on GO and its related materials is analyzed in **Fig. 5.14**. The density power of the 405 nm laser is analyzed from 0 to 16.5 mW/cm^2. The change in the exposed laser's power density has affected the devices' photocurrent while the applied bias voltage is kept at 2V for all devices.

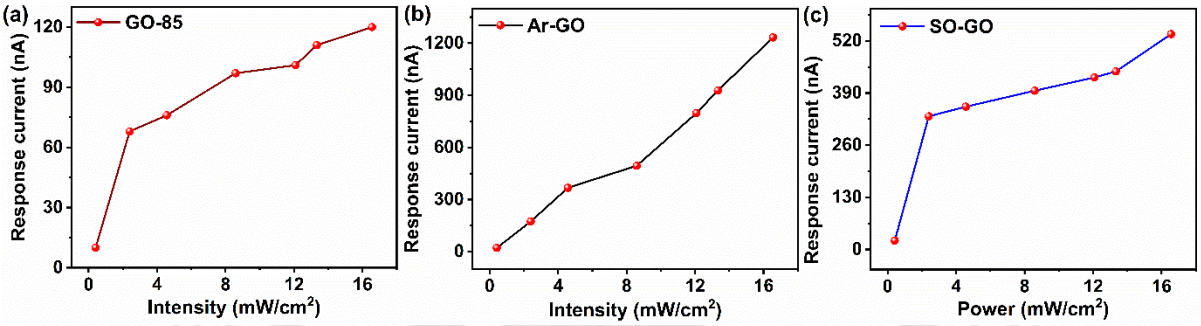

Fig. 5.14: Analysis of power density effect on the photocurrent of (a) GO; (b) Ar-GO; (c) SO-GO.

In **Fig. 5.14a**, the photocurrent of the GO-based device is responded to after the power density of 0.42 mW/cm^2 exposed on the GO-85. Thus, the photocurrent intensity increases with the illuminated laser power density. The photocurrent of GO-85 is obtained to 68 nA at 3.6 mW/cm^2 and 118 nA at 16.5 mW/cm^2. Further, the effect of laser power density on Ar-GO is analyzed in **Fig. 5.14b**; 0.42 mW/cm^2 and above generate photocurrent for all the devices. The photocurrent of the Ar-GO is attained to 160 nA at 3.6 mW/cm^2 and 1120 nA at 16.5 mW/cm^2. In SO-GO (**Fig. 5.14c**), the photocurrent is more sensitive at a lower power density than at higher power. 320 nA of photocurrent is generated at 3.6 mW/cm^2, and afterward, the photocurrent response is saturated even if the power density is increased up to 16.5 mW/cm^2. Ar-GO based photodetector device exhibited higher photocurrent as the illuminated laser's power density increased on the sample. The curve can be fitted with two linear lines, one in the low-power density region and another in the high-power density region.

5.4.9 Responsivity (R) and Detectivity (D)

The responsivility (R) and detectivity (D) of GO-85, Ar-GO, and SO-GO are calculated, which is used to determine the performance of the fabricated devices. R can be calculated by using the formula given below[37]:

$$R = \frac{Iph}{PA}$$

Whereas, I_{ph} is the photo-induced current; $I_{ph} = I_{light}-I_{dark}$. And *P* is the incident power density of the illuminated light on the sample, and *A* is the effective area of the device. The value of *PA* is calculated to be 0.31×10^{-3} W^{-1}. The value of the R (**Table 5.3**) for GO-85, SO-GO, and Ar-GO is obtained to 0.39 mAW^{-1}, 1.07 mAW^{-1}, and 3.7 mAW^{-1}, respectively. The R of the Ar-GO is improved 3.5 times of the GO-85 and 2.7 time of the SO-GO. Ar-GO is better responsivity as compared to SO-GO and GO-85. The performance of the photodetector device can be improved by the Ar plasma treatment or synthesis of nano hybrid of SnO_2 NPs.

***Table 5.3**: Responsivity and detectivity of GO-85, Ar-GO, and SO-GO devices.*

Devices	Responsivity (mAW^{-1})	Detectivity (Jones)
GO-85	0.39	0.22×10^{10}
SO-GO	1.07	0.37×10^{10}
Ar-GO	3.7	1.22×10^{10}

D of a photodetector device is a figure of merit and it is defined as the ability to detect weak signals. Higher the value of D of a device is more suitable to detect a weak signal. D of the GO-85, SO-GO, and Ar-GO devices can be calculated by using the formula given below[38]:

$$D = R\left(\frac{A}{(2qIdark)}\right)^{1/2}$$

Whereas, *q* is the electronics charge. The value of the D for GO-85, SO-GO, and Ar-GO are 0.22×10^{10} Jones, 0.37×10^{10} Jones, and 1.22×10^{10} Jones, respectively.

***Table 5.4**: A Comparative study of GO-based photodetector devices*

Active material	Responsivity (mAW^{-1})	Reference
RGO (film)	0.0043	[39]
Bilayer graphene	1	[40]
RGO (thin film)	2.7	[41]
Graphene	0.4	[42]
RGO (thick film)	0.27	[43]
SO-GO	1.07	Present work
Ar-GO	3.7	Present work

The D of the Ar-GO is improved to 5.5 times of the GO-85 and 3.3 times of the SO-GO. Herein, the Ar-GO-based photodetector is exhibited better detectivity compared to other GO-85 and

SO-GO. The R of the graphene oxide and its related materials are studied in **Table 5.4**. Ar-GO is improved the R as compared to the other reported materials. The R and D analysis of the GO-85, SO-GO, and Ar-GO devices, it is confirmed that surface-modified using the simplest and easiest method, Ar plasma treated on the GO-85 can improve the performance of GO-based photodetector devices.

5.5. Conclusion

In this chapter, we discussed the successful fabrication of an interdigitated electrode (IDE) pattern on GO sheets using the UV lithography process. The channel width or minimum distance between the two electrodes is made as 10 µm, confirmed by the AFM and FESEM images. The thickness of the metal electrode is 30 nm, measured from the height profile analysis of the AFM image. The FESEM images observe the fabrication of the GO-based IDE pattern. The changes in characteristics and properties of the GO after different temperatures annealing, such as 50 ˚C, 85 C, 120 ˚C, and 230 ˚C are studied. The restoration of the graphitic structure after annealing at 230 ˚C is authenticated from the XRD and Raman spectra analysis; the shifting of 2θ peak towards the 25.6˚ of the XRD spectra and reducing the value of I_D/I_G Raman spectra. The presence of oxygen functional groups is studied using XPS and FTIR analysis; flattening of C-O peak at 286 eV after 230 C annealing of GO and removal of oxygen functional groups related peaks from 950 cm^{-1} to 1480 cm^{-1} in the FTIR spectra. PL and UV absorption also fortified the rich presence of oxygen functional groups in the GO-RT.

I-V measurement of the GO and different annealed GO are studied and concluded that higher the oxygen functional groups attached to GO disturbed the flow of current in the GO, which leads to behaving like an insulator. The attached oxygen functional groups can regulate the electrical properties of the GO on the GO. Three photodetectors are made by using GO-85, Ar-GO, and SO-GO. The performances of the devices are compared, such as photocurrent (I_{ph}), response time (τ_{rise} and τ_{dec}), responsivity (R), and detectivity (D). Ar-GO photodetector performs better than the other two, showing that the surface modification using the Ar-plasma treatment improves the GO-based photodetector performance.

Reference:

(1) Tang, L.; Li, X.; Ji, R.; Teng, K. S.; Tai, G.; Ye, J.; Wei, C.; Lau, S. P. Bottom-up Synthesis of Large-Scale Graphene Oxide Nanosheets. *J. Mater. Chem.* **2012**, *22* (12), 5676–5683. https://doi.org/10.1039/c2jm15944a.

(2) Khan, M. A.; Kumar, A.; Zhang, J.; Kumar, M. Recent Advances and Prospects in Reduced Graphene Oxide-Based Photodetectors. *J. Mater. Chem. C* **2021**, *9* (26), 8129–8157. https://doi.org/10.1039/d1tc01306h.

(3) Chen, W.; Lv, G.; Hu, W.; Li, D.; Chen, S.; Dai, Z. Synthesis and Applications of Graphene Quantum Dots: A Review. *Nanotechnol. Rev.* **2018**, *7* (2), 157–185. https://doi.org/10.1515/ntrev-2017-0199.

(4) Wang, L.; Kang, J.; Nam, J. Do; Suhr, J.; Prasad, A. K.; Advani, S. G. Composite Membrane Based on Graphene Oxide Sheets and Nafion for Polymer Electrolyte Membrane Fuel Cells. *ECS Electrochem. Lett.* **2015**, *4* (1), F1–F4. https://doi.org/10.1149/2.0021501eel.

(5) Wei, Z.; Wang, D.; Kim, S.; Kim, S. Y.; Hu, Y.; Yakes, M. K.; Laracuente, A. R.; Dai, Z.; Marder, S. R.; Berger, C.; King, W. P.; De Heer, W. A.; Sheehan, P. E.; Riedo, E. Nanoscale Tunable Reduction of Graphene Oxide for Graphene Electronics. *Science (80-.).* **2010**, *328* (5984), 1373–1376. https://doi.org/10.1126/science.1188119.

(6) Yu, X.; Cai, H.; Zhang, W.; Li, X.; Pan, N.; Luo, Y.; Wang, X.; Hou, J. G. Tuning Chemical Enhancement of SERS by Controlling the Chemical Reduction of Graphene Oxide Nanosheets. *ACS Nano* **2011**, *5* (2), 952–958. https://doi.org/10.1021/nn102291j.

(7) Dong, L.; Yang, J.; Chhowalla, M.; Loh, K. P. Synthesis and Reduction of Large Sized Graphene Oxide Sheets. *Chemical Society Reviews*. Royal Society of Chemistry December 7, 2017, pp 7306–7316. https://doi.org/10.1039/c7cs00485k.

(8) Das, P.; Mandal, B.; Gumma, S. Applied Surface Science Engineering of Structural and Surface Functional Characteristics of Graphite Oxide Nanosheets by Controlling Oxidation Temperature. *Appl. Surf. Sci.* **2020**, *504* (October 2019), 144444. https://doi.org/10.1016/j.apsusc.2019.144444.

(9) Jiang, X.; Nisar, J.; Pathak, B.; Zhao, J.; Ahuja, R. Graphene Oxide as a Chemically Tunable 2-D Material for Visible-Light Photocatalyst Applications. *J. Catal.* **2013**, *299*, 204–209. https://doi.org/10.1016/j.jcat.2012.12.022.

(10) Chang, S.; Zhou, X.; Palacios, T.; Gradečak, S.; Kong, J.; Park, H. Flexible Graphene Electrode-Based Organic Photovoltaics with Record-High Efficiency. *Nano Lett.* **2014**, *14* (9), 5148–5154. https://doi.org/10.1021/nl501981f.

(11) Chong, K. Y.; Chia, C. H.; Chook, S. W.; Zakaria, S.; Lucas, D. Simplified Production of Graphene Oxide Assisted by High Shear Exfoliation of Graphite with Controlled Oxidation. *New J. Chem.* **2018**, *42* (6), 4507–4512. https://doi.org/10.1039/c7nj04911k.

(12) Jiang, J.; Wen, Y.; Wang, H.; Yin, L.; Cheng, R.; Liu, C.; Feng, L.; He, J. Recent Advances in 2D

Materials for Photodetectors. *Adv. Electron. Mater.* **2021**, *7* (7), 1–27. https://doi.org/10.1002/aelm.202001125.

(13) Xiao, N.; Dong, X.; Song, L.; Liu, D.; Tay, Y.; Wu, S.; Li, L.; Zhao, Y. ACS Nano 2011 Xiao N.Pdf. **2011**, No. 4, 2749–2755.

(14) Zheng, L.; Zhongzhu, L.; Guozhen, S.; Zhang, K.; Zhang, L.; Han, L.; Wang, L.; Chen, Z.; Xing, H.; Chen, X.; Qiao, H.; Huang, Z.; Ren, X.; Liu, S.; Zhang, Y.; Qi, X.; Zhang, H.; Long, M.; Wang, P.; Fang, H.; Hu, W.; Jiang, J.; Wen, Y.; Wang, H.; Yin, L.; Cheng, R.; Liu, C.; Feng, L.; He, J.; Huo, N.; Konstantatos, G.; Ezhilmaran, B.; Patra, A.; Benny, S.; M. R., S.; V. V., A.; Bhat, S. V.; Rout, C. S. Recent Progress and Future Prospects of 2D-Based Photodetectors. *Adv. Funct. Mater.* **2021**, *7* (19), 1–27. https://doi.org/10.1088/1674-4926/37/9/091001.

(15) Huang, X. M.; Liu, L. Z.; Zhou, S.; Zhao, J. J. Physical Properties and Device Applications of Graphene Oxide. *Front. Phys.* **2020**, *15* (3). https://doi.org/10.1007/s11467-019-0937-9.

(16) Torrisi, F.; Hasan, T.; Wu, W.; Sun, Z.; Lombardo, A.; Kulmala, T. S.; Hsieh, G. W.; Jung, S.; Bonaccorso, F.; Paul, P. J.; Chu, D.; Ferrari, A. C. Inkjet-Printed Graphene Electronics. *ACS Nano* **2012**, *6* (4), 2992–3006. https://doi.org/10.1021/nn2044609.

(17) Li, G.; Liu, L.; Wu, G.; Chen, W.; Qin, S.; Wang, Y.; Zhang, T. Self-Powered UV–Near Infrared Photodetector Based on Reduced Graphene Oxide/n-Si Vertical Heterojunction. *Small* **2016**, *12* (36), 5019–5026. https://doi.org/10.1002/smll.201600835.

(18) Zheng, L.; Zhongzhu, L.; Guozhen, S. Photodetectors Based on Two Dimensional Materials. *J. Semicond.* **2016**, *37* (9). https://doi.org/10.1088/1674-4926/37/9/091001.

(19) Ezhilmaran, B.; Patra, A.; Benny, S.; M. R., S.; V. V., A.; Bhat, S. V.; Rout, C. S. Recent Developments in the Photodetector Applications of Schottky Diodes Based on 2D Materials. *J. Mater. Chem. C* **2021**, *9* (19), 6122–6150. https://doi.org/10.1039/d1tc00949d.

(20) Abid; Sehrawat, P.; Islam, S. S.; Mishra, P.; Ahmad, S. Reduced Graphene Oxide (RGO) Based Wideband Optical Sensor and the Role of Temperature, Defect States and Quantum Efficiency. *Sci. Rep.* **2018**, *8* (1), 1–13. https://doi.org/10.1038/s41598-018-21686-2.

(21) Krishnamoorthy, K.; Veerapandian, M.; Yun, K.; Kim, S. J. The Chemical and Structural Analysis of Graphene Oxide with Different Degrees of Oxidation. *Carbon N. Y.* **2013**, *53*, 38–49. https://doi.org/10.1016/j.carbon.2012.10.013.

(22) Sreeja, V. G.; Vinitha, G.; Reshmi, R.; Anila, E. I.; Jayaraj, M. K. Effect of Reduction Time on Third Order Optical Nonlinearity of Reduced Graphene Oxide. *Opt. Mater. (Amst).* **2017**, *66*, 460–468. https://doi.org/10.1016/j.optmat.2017.01.042.

(23) Li, X. Preparation of Graphene Oxide and Its Application as Substrates for SERS. *J. Chem.* **2018**, *2018*. https://doi.org/10.1155/2018/8050524.

(24) Zhao, H.; Fan, S.; Chen, Y.; Feng, Z.; Zhang, H.; Pang, W.; Zhang, D.; Zhang, M. Oxygen Plasma-Treated Graphene Oxide Surface Functionalization for Sensitivity Enhancement of Thin-Film Piezoelectric Acoustic Gas Sensors. *ACS Appl. Mater. Interfaces* **2017**, *9* (46), 40774–40781. https://doi.org/10.1021/acsami.7b09547.

(25) Aliahmad, M.; Dehbashi, M. Synthesis and Characterization of Thermally-Reduced Graphene. *Iran. J. Energy Environ.* **2013**, *4* (1), 53–59. https://doi.org/10.5829/idosi.ijee.2013.04.01.

(26) Deemer, E. M.; Paul, P. K.; Manciu, F. S.; Botez, C. E.; Hodges, D. R.; Landis, Z.; Akter, T.; Castro, E.; Chianelli, R. R. Consequence of Oxidation Method on Graphene Oxide Produced with Different Size Graphite Precursors. *Mater. Sci. Eng. B Solid-State Mater. Adv. Technol.* **2017**, *224* (March 2019), 150–157. https://doi.org/10.1016/j.mseb.2017.07.018.

(27) Smith, A. T.; LaChance, A. M.; Zeng, S.; Liu, B.; Sun, L. Synthesis, Properties, and Applications of Graphene Oxide/Reduced Graphene Oxide and Their Nanocomposites. *Nano Mater. Sci.* **2019**, *1* (1), 31–47. https://doi.org/10.1016/j.nanoms.2019.02.004.

(28) Lai, S. K.; Tang, L.; Hui, Y. Y.; Luk, C. M.; Lau, S. P. A Deep Ultraviolet to Near-Infrared Photoresponse from Glucose-Derived Graphene Oxide. *J. Mater. Chem. C* **2014**, *2* (34), 6971–6977. https://doi.org/10.1039/c4tc01175a.

(29) Zheng, K.; Meng, F.; Jiang, L.; Yan, Q.; Hng, H. H.; Chen, X. Visible Photoresponse of Single-Layer Graphene Decorated with TiO 2 Nanoparticles. *Small* **2013**, *9* (12), 2076–2080. https://doi.org/10.1002/smll.201202885.

(30) Liu, N.; Tian, H.; Schwartz, G.; Tok, J. B. H.; Ren, T. L.; Bao, Z. Large-Area, Transparent, and Flexible Infrared Photodetector Fabricated Using P-N Junctions Formed by N-Doping Chemical Vapor Deposition Grown Graphene. *Nano Lett.* **2014**, *14* (7), 3702–3708. https://doi.org/10.1021/nl500443j.

(31) Qi, X.; Zou, X.; Huang, Z.; Ren, L.; Hao, G.; Liu, Y.; Wei, X.; Zhong, J. Ultraviolet, Visible, and near Infrared Photoresponse Properties of Solution Processed Graphene Oxide. *Appl. Surf. Sci.* **2013**, *266*, 332–336. https://doi.org/10.1016/j.apsusc.2012.12.020.

(32) Chang, H.; Sun, Z.; Saito, M.; Yuan, Q.; Zhang, H.; Li, J.; Wang, Z.; Fujita, T.; Ding, F.; Zheng, Z.; Yan, F.; Wu, H.; Chen, M.; Ikuhara, Y. Regulating Infrared Photoresponses in Reduced Graphene Oxide Phototransistors by Defect and Atomic Structure Control. *ACS Nano* **2013**, *7* (7), 6310–6320. https://doi.org/10.1021/nn4023679.

(33) Konstantatos, G.; Howard, I.; Fischer, A.; Hoogland, S.; Clifford, J.; Klem, E.; Levina, L.; Sargent, E. H. Ultrasensitive Solution-Cast Quantum Dot Photodetectors. *Nature* **2006**, *442* (7099), 180–183. https://doi.org/10.1038/nature04855.

(34) Simone, G.; Dyson, M. J.; Meskers, S. C. J.; Janssen, R. A. J.; Gelinck, G. H. Organic Photodetectors and Their Application in Large Area and Flexible Image Sensors: The Role of Dark Current. *Adv. Funct. Mater.* **2020**, *30* (20). https://doi.org/10.1002/adfm.201904205.

(35) Wei, Y.; Chen, H.; Liu, T.; Wang, S.; Jiang, Y.; Song, Y.; Zhang, J.; Zhang, X.; Lu, G.; Huang, F.; Wei, Z.; Huang, H. Self-Powered Organic Photodetectors with High Detectivity for Near Infrared Light Detection Enabled by Dark Current Reduction. *Adv. Funct. Mater.* **2021**, *31* (52). https://doi.org/10.1002/adfm.202106326.

(36) Eun, H. J.; Kye, H.; Kim, D.; Jin, I. S.; Jung, J. W.; Ko, S. J.; Heo, J.; Kim, B. G.; Kim, J. H. Effective Dark Current Suppression for High-Detectivity Organic Near-Infrared Photodetectors Using a Non-Fullerene Acceptor. *ACS Appl. Mater. Interfaces* **2021**, *13* (9), 11144–11150. https://doi.org/10.1021/acsami.0c22808.

(37) Kumawat, K. L.; Singh, D. K.; Nanda, K. K.; Krupanidhi, S. B. Solution-Processed SnSe2-RGO-Based Bulk Heterojunction for Self-Powered and Broadband Photodetection. *ACS Appl. Electron. Mater.* **2021**, *3* (7), 3131–3138. https://doi.org/10.1021/acsaelm.1c00352.

(38) Parveen, S.; Das, M.; Ghosh, S.; Giri, P. K. Experimental and Theoretical Study of Europium-Doped Organometal Halide Perovskite Nanoplatelets for UV Photodetection with High Responsivity and Fast Response. *Nanoscale* **2022**, 6402–6416. https://doi.org/10.1039/d2nr01063a.

(39) Cao, Y.; Zhu, J.; Xu, J.; He, J. Tunable Near-Infrared Photovoltaic and Photoconductive Properties of Reduced Graphene Oxide Thin Films by Controlling the Number of Reduced Graphene Oxide Bilayers. *Carbon N. Y.* **2014**, *77*, 1111–1122. https://doi.org/10.1016/j.carbon.2014.06.029.

(40) Yin, J.; Wang, H.; Peng, H.; Tan, Z.; Liao, L.; Lin, L.; Sun, X.; Koh, A. L.; Chen, Y.; Peng, H.; Liu, Z. Selectively Enhanced Photocurrent Generation in Twisted Bilayer Graphene with van Hove Singularity. *Nat. Commun.* **2016**, *7*, 1–8. https://doi.org/10.1038/ncomms10699.

(41) Freitag, M.; Low, T.; Avouris, P. Increased Responsivity of Suspended Graphene Photodetectors. *Nano Lett.* **2013**, *13* (4), 1644–1648. https://doi.org/10.1021/nl4001037.

(42) Patil, V.; Capone, A.; Strauf, S.; Yang, E. H. Improved Photoresponse with Enhanced Photoelectric Contribution in Fully Suspended Graphene Photodetectors. *Sci. Rep.* **2013**, *3*, 1–5. https://doi.org/10.1038/srep02791.

(43) Moon, I. K.; Ki, B.; Yoon, S.; Oh, J. Lateral Photovoltaic Effect in Flexible Free-Standing Reduced Graphene Oxide Film for Self-Powered Position-Sensitive Detection. *Sci. Rep.* **2016**, *6* (August), 1–12. https://doi.org/10.1038/srep33525.

Chapter 6

Fabrication of CO_2 Sensors Based on Graphene Oxide Based 2D Materials and its Nano Hybrid with SnO_2

This chapter concentrates on the fabrication and optimization of gas sensing devices using RGO, GQDs, and its nano hybrid with SnO_2 NPs.. The I-V characteristics of the sensing material are measured and the change of current with an increase in temperature is analyzed. The sensing response of the CO_2 gas is measured from 250 ppm to 5000 ppm, as the presence of CO_2 in the atmosphere is 410 ppm whereas the harmful concentration of CO_2 is above 5000 ppm. The sensing properties such as response time, sensitivity, repeatability, etc. are studied in this chapter. The sensitivity of the RGO/SnO_2 is 9% and 4% for 5000 ppm and 1000ppm of CO_2 gas. The response and recovery times for RGO/SnO_2 is the 20s and 40s at 5000 ppm of CO_2. The RGO/SnO_2 nano hybrid improved the sensing response by up to 50% as compared to bare SnO_2.

6.1. Introduction

Growing concerns about environmental conditions motivate researchers worldwide to focus attention on developing effective methods for environmental monitoring and efficient devices that run on low-power and are portable for on-site measurement. In particular, CO_2 detection in ambient air has continued to be a challenge due to the stability of the compound and interferences from several species, such as nitrogen dioxide (NO_2) and carbon monoxide (CO)[1]. Further, a CO_2 sensor can be greatly beneficial to a wide range of applications, including breath and blood analysis for medical diagnosis, portable gas detectors for personal protection, and gas monitoring for climate control[2]. The increased emission of carbon dioxide (CO_2) and other greenhouse gases since the mid-20th century has been thought to be the cause of the increase in the average near-surface air and ocean temperature of the earth, a phenomenon known as global warming. Efforts are being undertaken to mitigate the greenhouse gas concentration by monitoring and subsequently reducing CO_2 emissions from the combustion of fuel in vehicles and the burning of coal in power plants[3]. Therefore, it is important to develop low-cost, sensitive, resettable sensors that can be used to monitor the CO_2 concentration in industrial exhaust gases.

Since the discovery of graphene in 2004, immense efforts have been focused on GO[4]. This is because it is the most promising precursor to obtaining mass production of graphene compared to micromechanical exfoliation and catalytic decomposition of hydrocarbons on transition metals[5]. The presence of oxygen functional groups on the graphene sheets reduces electron mobility typically becoming an insulator and thus removal of these functional groups to restore its conductivity is a challenging task. Several approaches for a reduction process have been reported such as hydrazine chemical treatment, thermal reduction, and gas plasma treatment.

Besides, oxygen is known to have better charge transfer to planar defected graphite due to the presence of defects, which results in stronger semiconducting characteristics for GO[6]. GO containing numerous oxygen functional groups was too electrically insulated to be used in a resistance-based sensor. As a kind of chemically/thermally derived graphene, RGO, containing many dangling oxygen atoms which act as binding sites for gas analytes, was appreciated to be studied and used for gas sensors[7]. Interestingly, change in the RGO by adsorption/desorption of molecule may give rise to a significant effect on sensing behaviours[8].

6.2. Experimental Details

6.2.1. Synthesis of RGO and GQDs

The graphite oxide was synthesized by using the simplified Hummer's method and further, exfoliated into GO sheets using a mild heating technique. The exfoliated GO sheets are drop-casted on the SiO_2/Si substrate and dried on the hotplate at 85 ˚C. Subsequently, GO sheets are converted into RGO using thermal annealing at 360 ˚C. GQDs are synthesized from the GO solution using a hydrothermal method assisted by a tip-sonication process. More details of the synthesis process of graphite oxide, exfoliation of GO, and GQDs were presented in **Chapter 2**.

Table 6.1*: Summary of the samples studied and sample codes.*

Sample codes	Descriptions
SO	SnO_2 Nanoparticles
SO-GO	SnO_2 on GO nano hybrid
SO-RGO	SnO_2 on RGO nano hybrid
GQDs-SO	GQDs on SnO_2 nano hybrid

6.2.2. Fabrication of SnO_2 NPs, nano hybrids of RGO, and GQDs devices

The interdigitated electrode (IDE) is fabricated using UV lithography. A 10 µm channel IDE is made together of multiple numbers of metal fringes; the minimum distance between the two electrodes is 10 µm. After the patterned IDE on the SiO_2/Si substrate by UV lithography, Au/Cr are deposited by a thermal/e-beam evaporator. The detailed process steps for the fabrication of IDE are explained in **section 5.2.2** of **chapter 5**.

The SO sensor is made by depositing the SnO_2 NPs on the IDE pattern. An average of 100 nm size SnO_2 NPs is purchased from Sigma Aldrich. 5mg of SnO_2 NPs is added to a 50 ml beaker containing 30 ml of de-ionized water. A bath-sonicator disperses the solution for 30 minutes. Then, 10 µl of the solution is drop-casted on the IDE pattern and dried at 85 ˚C for 60 minutes. Thus, the SnO_2 sensor (SO) is made and characterized for further analysis.

SO-RGO sensor is fabricated by deposition of SnO_2 NPs on the RGO, which was placed on the IDE pattern. The exfoliated GO sheets are drop-casted on the IDE pattern and dried on the device on the hot plate at 85 ˚C for 60 minutes. Afterward, the device is placed inside a quartz tube using a quartz boat for vacuum annealing. The device is heated at 360 ˚C for 60 minutes to remove oxygen functional groups attached to the GO sheets. The process of vacuum annealing followed the same steps to synthesize RGO from GO using the thermal annealing method explained in **chapter 2**.

GQDs-SO sensor is fabricated using 10 µl of GQDs dispersed in the water solution and drop-casted on the SO sensor. The synthesis of the GQDs is explained in **chapter 2**. The device is dried at 85 ˚C on the hot plate for 60 minutes. This is the simplest method to fabricate the SnO_2 NPs, RGO, and GQDs hybrid devices.

6.2.3. Characterization techniques

The morphology of the RGO, GQDs, SnO_2 NPs and their nano hybrids on the SiO_2/Si were observed using a field emission scanning electron microscope (FESEM) (*JEOL, JSM-7610F*). High resolution image and selected area electron diffraction (SAED) pattern of the SnO_2 NPs was examined using a field emission transmission electron microscopy (FETEM) (*JEOL, JEM-2100F*), operated at an accelerating voltage of 200 kV. The structural analysis of the RGO, GQDs, SnO_2 NPs and their nano hybrids were studied using XRD (Rigaku, *RINT 2500 TTRAX-III*), with Cu Kα radiation as a source of x-ray and a scanning speed of 3 °/min. The structural and functional groups attached to the RGO, GQDs, SnO_2 NPs and their nano hybrids were studied using Raman spectroscopy (*Horiba, LabRam HR*) with the 532 nm laser

using a 100X optical lens. The functional groups attached to the RGO, GQDs, SnO_2 NPs and their nano hybrids were studied using an X-ray photoelectron spectroscopy (XPS) (*PHI X-tool, ULVAC-PHI INC*) with Al Kα as an X-ray energy source at 20 kV and 54 W. The functional groups of the nano hybrids of SnO_2 and RGO was studied using the transmittance mode of the Fourier transform infrared (FTIR) spectroscopy (*Perkin Elmer, spectrum BX*). The photoluminescence (PL) of SnO_2 NPs was measured using the fluorimeter (*Horiba, Fluromax-4*) using 360 nm excitation. I-V measurements for CO_2 sensors were performed using a home-made set-up with a source measure unit (*Keithley 2400*, Germany) and the data were retrieved using *KickStart* Instrument control software (version 1.9.8).

6.2.4. Gas sensing set-up

A CO_2 gas sensing system is a set-up by assembling various parts such as a probe station with a temperature controller, a source-measure unit (Keithley 2401), a gas flow reader and controllers (MKS), high purity gas cylinders (5000 ppm of CO_2, and 99.999% of N_2), a vacuum system, and a personal computer with KickStart tool. The schematic illustration of the customized system is shown in **Fig. 6.1**. The vacuum supported probe station with substrate holder is heated at 120 ˚C for 6 hours by using the metal hot plate placed inside the vacuum chamber. This process removes the attached water vapors and humidity inside the chamber with the support of a rotary vacuum pump. The pressure inside the chamber is reduced to 1.6 × 10^{-2} mbar.

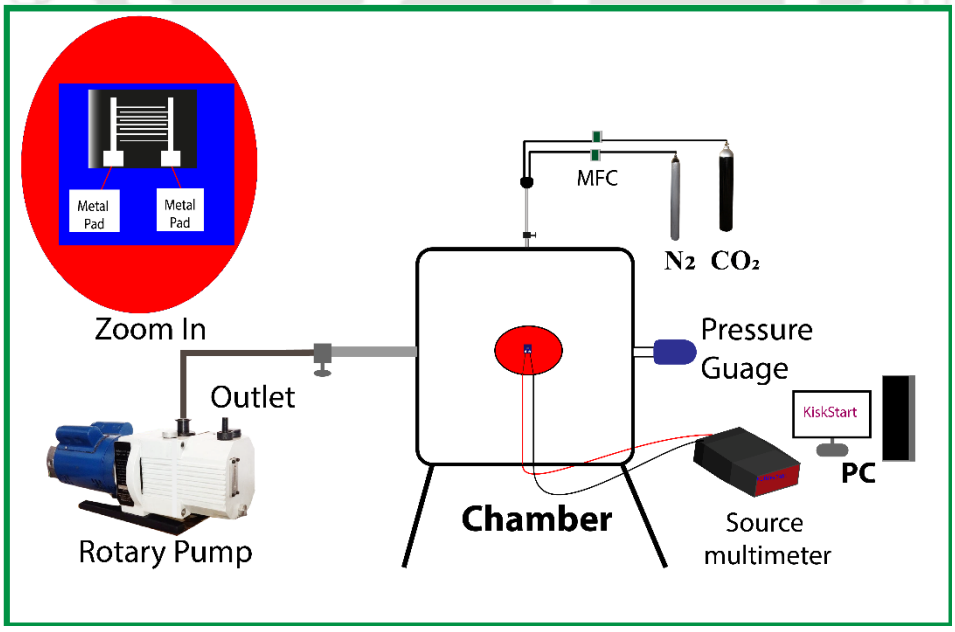

Fig. 6.1: Schematic diagram of the CO_2 gas sensing system.

Then N_2 is pursued inside the chamber for over 30 minutes to remove the impurities/ unwanted gas presence inside the gas line tube. Similarly, CO_2 (5000 ppm) is pursed inside the chamber for 30 minutes to remove the other gases trapped inside the tubes. The pursing of the gas process is done in vacuum environments. After that, the main gas valve is closed, and the sample is loaded inside the chamber. The fabricated device is placed on the probe station and probed the tips to measure the electrical characteristics.

Before measuring the gas sensing parameters, removing water vapors and flushing the impurity gas are done. Thus, the device is placed on the micro-probe station, and two gold-coated micro-tips are engaged on the metal pads of the device. The metal probes are connected to a source measure unit (Keithley, 2401) which is further connected to the personal computer through a GPIB cable. The ON/OFF response of the CO_2 sensor is controlled by manually stopping the flow of CO_2 gas supplied into the chamber. All the response activities are controlled and acquired using KickStart software.

6.3. Results and discussions

6.3.1. Morphological analysis

The morphological studied of the SnO_2 NPs using FESEM and FETEM is disclosed in **Fig. 6.2**. A uniform distribution of SnO_2 NPs on the SiO_2/Si is observed in the FESEM image

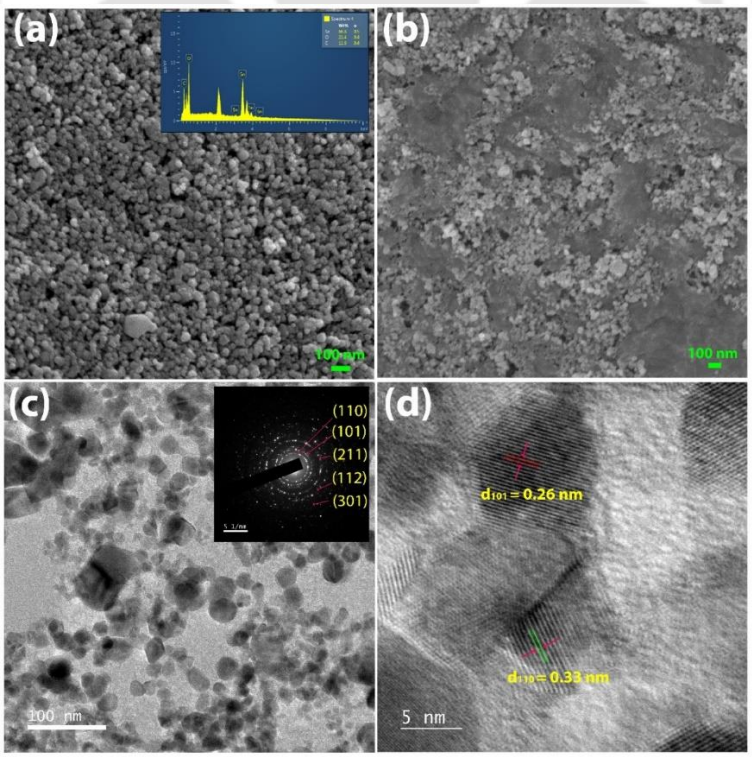

Fig. 6.2: FESEM image of (a) SnO_2 NPs; (b) nano hybrid of SnO_2 and RGO. (c) FETEM image of SnO_2 NPs (inset: SAED pattern); and (d) HRTEM image of SnO_2 NPs.

(**Fig. 6.2a**). In **Fig. 6.2b**, RGO sheets and the SnO_2 NPs are seen; a random scatter of NPs, and RGO sheets (dark color) are associated. The FETEM image of the SnO_2 NPs is shown in **Fig. 6.2c**, and the size of the NPs is obtained down to 50 nm. The SAED pattern on the NPs shows a number of large circular rings decorated with non-uniform bright spots. Each of the rings represents the planes of the NPs. Several planes of the SnO_2 NPs are detected in the SAED patterns (**Fig.6.2c (inset)**), such as (110), (101), (211), (112), and (301)[9]. Thus, NPs are confirmed as polycrystalline from the bright spots and multiple rings. In **Fig. 6.2d**, a high-resolution HRTEM image of the SnO_2 NPs is observed with their lattice fringes, and inter-planar spacing is d_{110} = 0.33 nm and d_{101}= 0.29 nm, which are obtained from the analysis of HRTEM image.

6.3.2. Structural analysis

XRD pattern of the nano hybrids of SnO_2 NPs (SO) and GO (SO-GO) and nano hybrids of SnO_2 NPs and RGO (SO-RGO) are plotted in **Fig. 6.3**. The lattice plane (002) of the GO and RGO is observed around 10.8˚ and 21.3˚, discussed in **previous chapters**. Diffraction peaks (2θ) of SO are observed at 26.28˚, 33.72˚, 37.64˚, 51.66˚, 54.79˚, 64.44˚, 71.04˚, and 78.56˚ are related to the lattice plane of (110), (101), (200), (211), (220), (112), (202), and (301)[10].

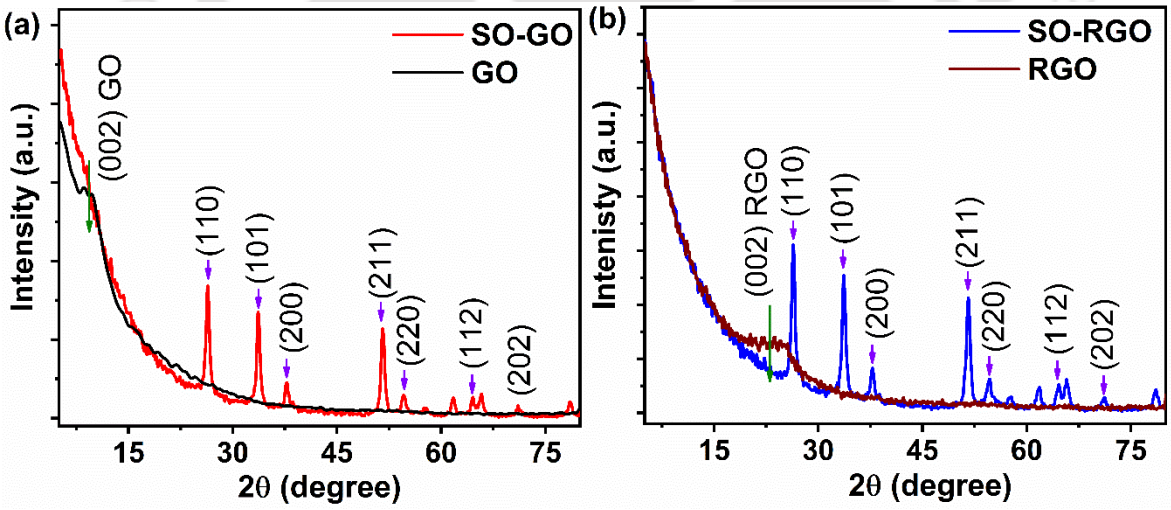

Fig. 6.3: XRD pattern of (a) GO and SO-GO; (b) RGO and SO-RGO.

he interplanar spacing (d) of the NPs is calculated using Bragg's law ($2d \sin\theta = n\lambda$). The interplanar spacing for d_{110} and d_{101} of the NPs are ~0.33 nm and ~0.26 nm. The interplanar spacings observed in the XRD agreed with the HRTEM image of SO. The XRD pattern of the SO-GO has reflected the composite of the SnO_2 and GO, shown in **Fig. 6.3a**. The diffraction

peak of the GO and RGO is insignificant due to the presence of less GO/RGO. The XRD pattern of the SO-RGO is analyzed in **Fig. 6.3b**. Thus, the nano hybrids of the SO-GO and SO-RGO are analyzed using XRD analysis, including their lattice plane.

Raman spectra of the SO, SO-RGO, and GQDs-SO are analyzed from 550 cm^{-1} to 1800 cm^{-1} in **Fig. 6.4a**. The significant peaks of the SO are observed at 645 cm^{-1} (A_{1g}) and 720 cm^{-1} (B_{2g}), which area corresponds to the vibration of Sn-O bonds and the presence of oxygen atoms, respectively[11]. The B_{2g} peak of the SO is miniature as compared to A_{1g} of SO, which shows the Sn-O is mainly contained. In SO-RGO, three noticeable peaks are observed, which are A_{1g} for SO, D, and G band for RGO. The D band at 1350 cm^{-1} corresponds to the defects and oxygen functional groups present in the GO. The G band at 1600 cm^{-1} is the signature of the graphitic structure of GO. The B_{2g} at 720 cm^{-1} is suppressed in the nano hybrids of SO-GO. In GQDs-SO, the D and G band of the GQDs is famous, but A_{1g} signified for SnO_2 is weak. Interestingly, the A_{1g} is shifted to 632 cm^{-1} in SO-RGO, and GQDs-SO shows the interaction of SnO_2 and RGO/GQDs.

The FTIR analysis of SO-RGO is measured from 400 cm^{-1} to 4000 cm^{-1} showed in **Fig. 6.4b**. A famous peak at 522 cm^{-1} regrads to the Sn-O-Sn; various peaks are observed from 1000 cm^{-1} to 1800 cm^{-1} related to the functional groups[12]. A significant peak at 1645 cm^{-1} is correlated to the C=C of the RGO and other peaks such as 1262 cm^{-1}, 1414 cm^{-1}, and 1558

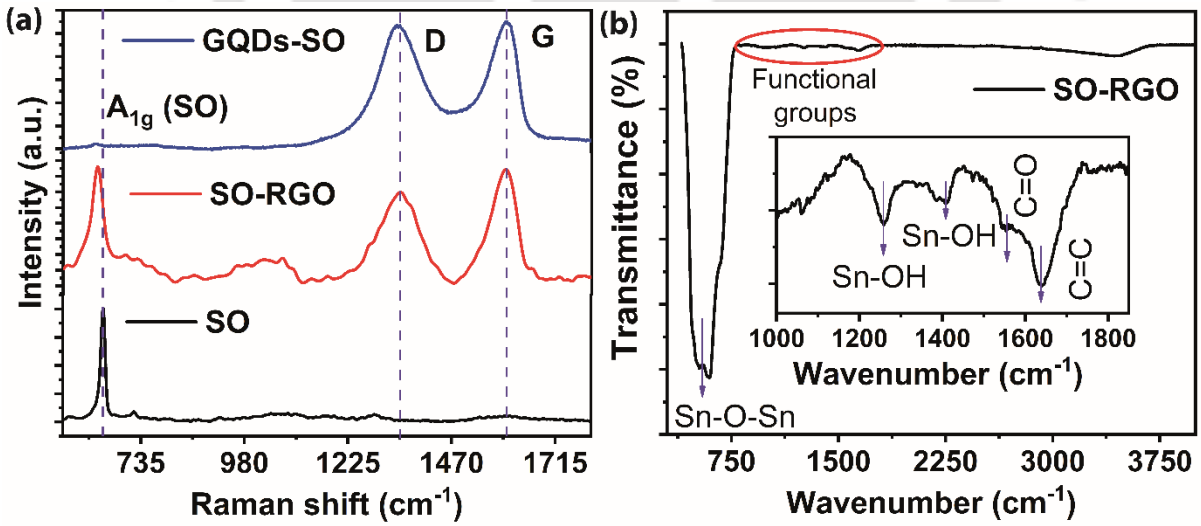

Fig.6.4: (a) Raman spectra of SnO_2 NPs (SO), SO-RGO, GQDs-SO; (b) FTIR analysis of SO-RGO.

cm^{-1} are linked to the Sn-O, Sn-OH, Sn-OH, and C=O, respectively[13]. The appearance of C=O peak may be contributed from the SnO_2 NPs and RGO, because both peaks are observed in the FTIR analysis. And, a peak at 3450 cm^{-1} is emerged from the humidity (-OH) absorbed in the

sample. From the FTIR analysis, SO-RGO confirmed the presence of functional groups associated with the SnO_2 and RGO.

The XPS spectra characterize the nano hybrids of SnO_2 NPs and RGO/GQDs from 220 nm to 580 nm, shown in **Fig. 6.5**. The XPS spectrum of SO-RGO is measured on the SnO_2 NPs on the RGO sheets; the signified peaks for SnO_2 NPs and RGO are observed in **Fig. 6.5a**. A tiny peek at 284 nm corresponds to C1s; two prominent peaks[14] at 485 nm and 494 nm are related to the $Sn3d_{5/2}$ and $Sn3d_{3/2}$, and the 532 nm peak is assigned O1s. The C1s and O1s peaks may be contributed from the RGO, it is observed and studied in the **previous chapters**. The $Sn3d_{5/2}$ and $Sn3d_{3/2}$ have signified peaks of the SnO_2 NPs (**Fig.6.5a (inset)**); the $Sn3d_{5/2}$ is intensified up 1.3 times from the $Sn3d_{3/2}$, shows the $Sn3d_{5/2}$ is higher contained in the SnO_2 NPs.

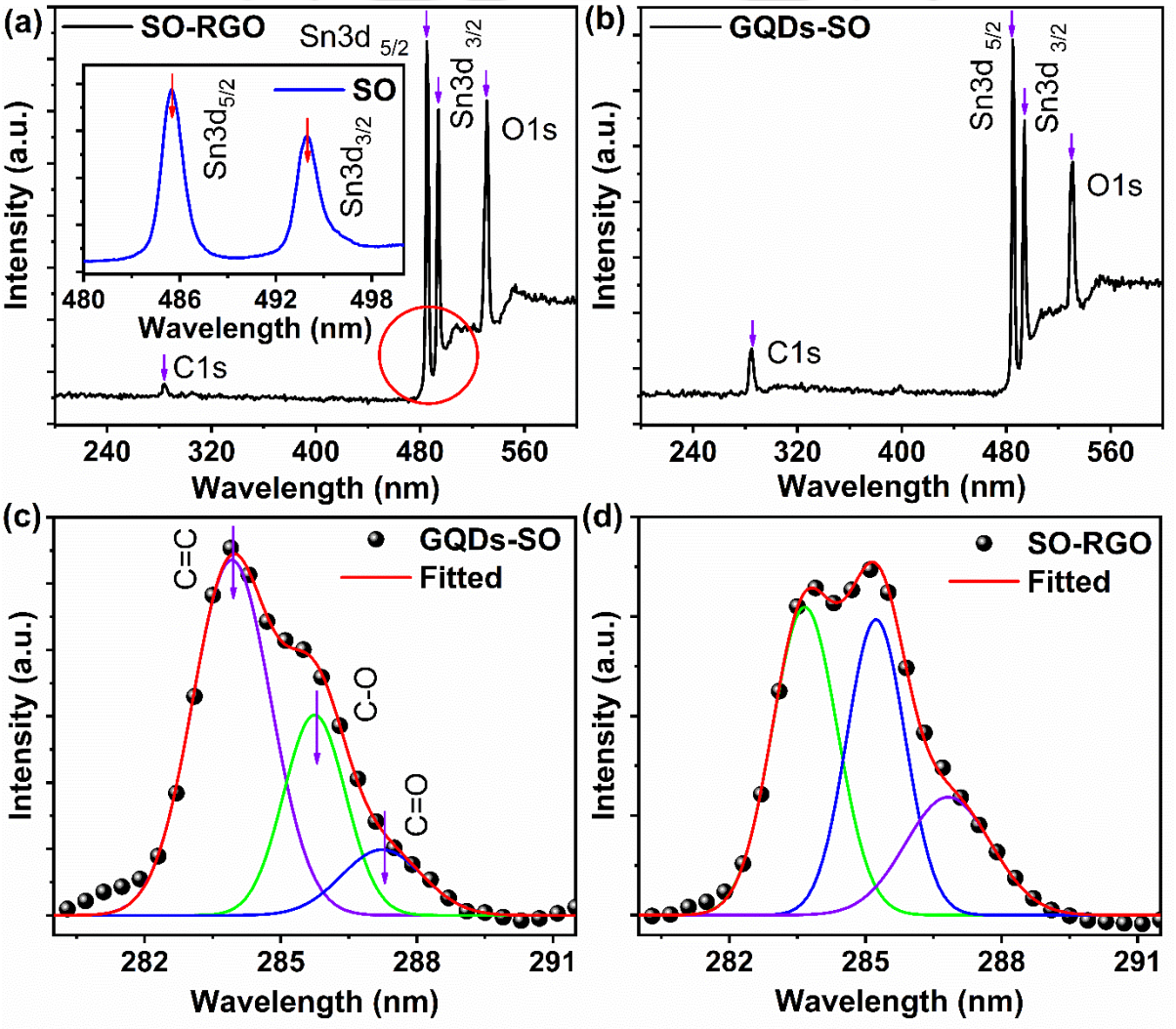

Fig.6.5: XPS (a) survey analysis of SO-RGO (inset: magnified spectrum of SO); (b) survey analysis of GQDs-SO; deconvolution of XPS analysis for (c) GQDs-SO; and (d) SO-RGO.

In **Fig.6.5b**, the GQDs are deposited on the SnO_2 NPs. The XPS spectrum is surveyed, and the assigned peaks such as C1s, $Sn3d_{5/2}$, and $Sn3d_{3/2}$, O1s are observed. The ratio of O1s to C1s is 8.14 for So-RGO and 3.45 for GQDs-SO. The presence of oxygen in SO-RGO is 2.35 times high than in GQDs-SO. The oxygen functional groups presented in the SO may be contributed to the O1s, which leads to increased unexpected oxygen functional groups in the SO-RGO and GQDs-SO. Three Gaussian peaks deconvolute the GQDs-SO and SO-RGO at 284 nm, 285.7 nm, and 287 nm, shown in **Fig. 6.5c** and **Fig.6.5d**, respectively. The GQDs-SO, the peak at 284 nm assigned to C=C, 285.7 nm related to C-O, and 287 nm linked to C=O. The integral area of the fitted peaks is contributed as C=C, C-O, and C=O to 57%, 32%, and 11%, respectively; the main contribution in the C1s is from the graphitic structure (sp^2 hybridized bonds). Similarly, the SO-RGO peak was analyzed based on the integral area of the fitted peaks. The C=C, C-O, and C=O contributed 42%, 41%, and 17%, respectively. The oxygen-related functional groups are mainly contained in C1s of SO-RGO.

6.3.3. UV absorption and PL analysis

UV absorption characteristics for RGO, SO, and SO-RGO, PL analysis of SO are shown in **Fig. 6.6.** A peak at 263 nm can be assigned to $\pi \rightarrow \pi^*$ transition or π-plasmon resonance common for extended sp^2 conjugated carbon sheet (C═C present within the aromatic sp^2 hybridized carbon framework)[15]. Two prominent peaks at 226 nm, and 282 nm are observed for SO in **Fig.6.6a,** which are corresponds to the intrinsic transition from the valence band to

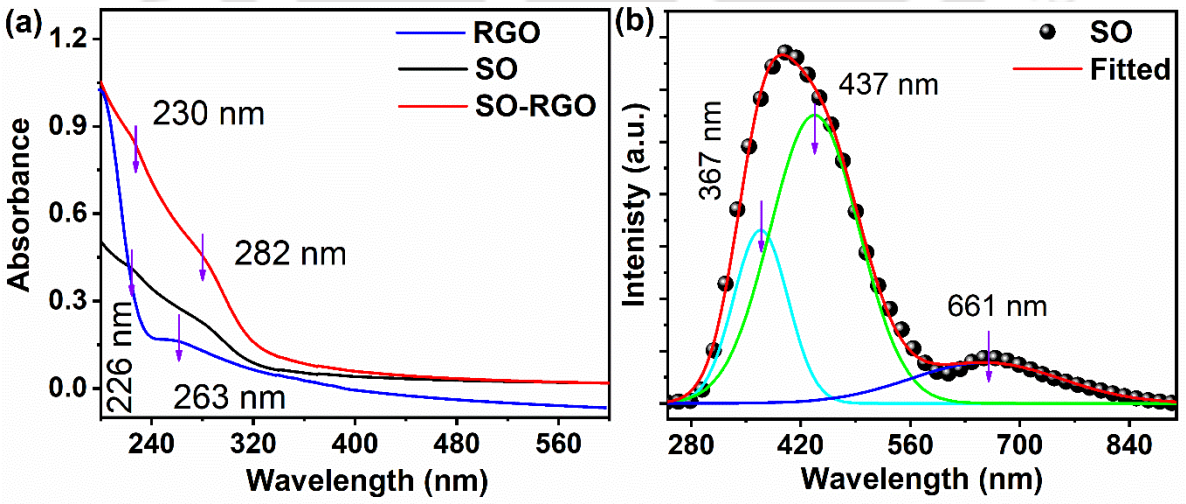

Fig. 6.6: (a) UV absorption spectra of SO and SO-RGO; and (b) PL analysis of SO.

conduction band ($\pi \rightarrow \pi^*$), and transition between the functional groups and defects at the edge of the NPs ($n \rightarrow \pi^*$), respectively[16,17]. The peak position shift corresponds to $\pi \rightarrow \pi^*$ from 226

nm to 230 nm due to the charge transfer between the RGO and SO. Thus, the formation of nano hybrids with the SnO_2 NPs and RGO is confirmed from the peak shifting[18].

The PL analysis of the SO (SnO_2 NPs) is shown in **Fig. 6.6b**; it can determine the presence of oxygen and Sn vacancies, defects on the surface, and impurities. The broad PL spectrum is measured from 260 nm to 860nm and deconvoluted with three peaks. These peaks, centered at 367nm, 437 nm, and 667 nm, are assigned to the disorder-induced defect states from the oxygen and Sn vacancies, presence of impurities, formation of trapping states, and daggling bonds from the edge[19]. The UV absorbance and PL analysis confirmed that the presence of defective sites helps attract the sensing gas molecules.

6.4. Electrical characterizations

6.4.1. IV characteristics of SO and SO-RGO

The electrical measurement of the RGO in different temperatures in **Fig. 6.7a**, and IV measurement of SO and SO-RGO is shown in **Fig. 6.7b**. In **Fig. 6.7a**, an RGO-based device is measured its current by increasing the temperature; the applied temperature is varied from RT to 290 ˚C. The device's temperature increases at 5 ˚C per minute, and 5V is applied as a bias voltage. The current of the RGO device is linearly increased from 0.93 mA at RT to 2.4 mA at 290 ˚C; the current improvement may be due to the removal of attached oxygen functional groups leading to restoring the graphitic structure of RGO. From this measurement, the fabricated IDE pattern using Au/Cr has sustained the temperature up to 300 ˚C without affecting the electrical conductivity. RGO is retained in contact with the metal electrode.

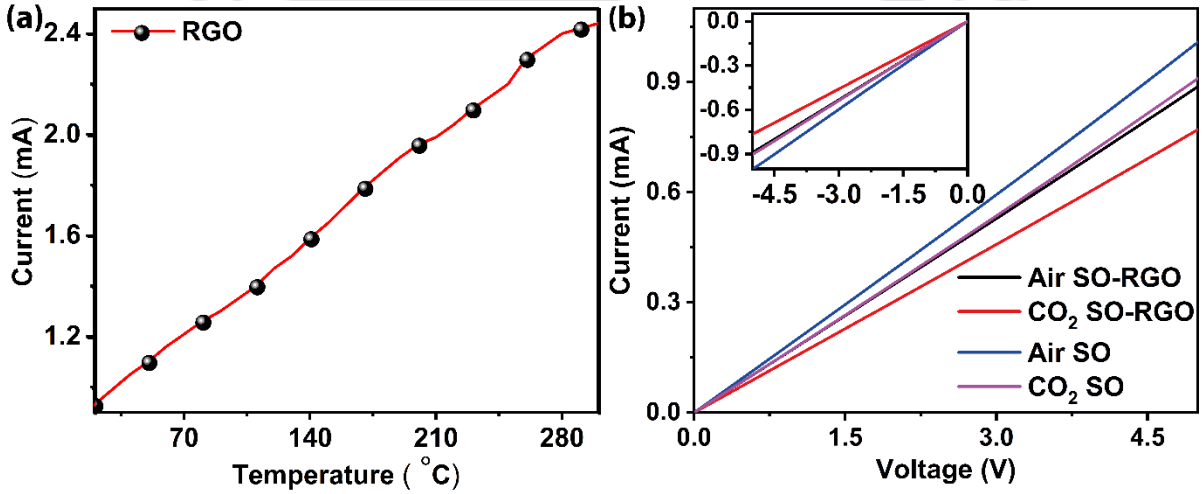

Fig. 6.7: (a) Measurement of current with respect to temperature of RGO, and (b) IV characteristics of SO and SO-RGO.

The IV of the SO and SO-RGO device is measured with and without CO_2 environments, shown in **Fig.6.7b**. The devices' current is measured from -5V to 5V; -5V to 0V in RT is shown in **Fig. 6.7b(inset)**. Both the devices reduced their conductivity during the exposure to CO_2; it may be due to the charge transfer from the device's material to the sensing gas. In the SO device, the current is 1.01 mA in the air and 0.91 mA in the 5000 ppm CO_2 environment. The reduction of the current during exposure to CO_2 is 0.10 mA, equal to 10% of the current. The values of the current vs. devices are shown in **Table 6.2**. Whereas the current of the SO-RGO is 0.887 mA in air and 0.770 mA in 5000 ppm of CO_2. The current reduction during exposure to CO2 is 0.101 mA, equal to 12.5%. The current of the SO and SO-RGO are varied linearly in both the negative and positive of the voltage.

6.4.2. Analysis of CO_2 sensor of SO and SO-RGO

The sensitivity of CO_2 is measured on the SO and SO-RGO devices, shown in **Fig. 6.8**. The SO-based devices are probed inside the vacuum chamber; it measures the sensitivity of the CO_2 in the form of resistance. When 5000 ppm of CO_2 is pursing inside the vacuum chamber, the device's resistance increases from 3339.7 Ω to 3559 Ω. It returns to the original resistance after removing the gas from the chamber. Similarly, the SO-RGO-based device is placed inside the vacuum probe station and measures resistance change by pursuing CO_2. The resistance of the SO-RGO is increased from its base value of 3319 Ω to 3636 Ω. The SO-RGO is low resistance compared to SO, which may be contributed by the formation of nano hybrids with RGO sheets (**Fig. 6.8a**). Furthermore, the sensing resistance is increased up to 77 Ω. The sensitivity of the CO_2 on the SO-RGO is improved compared to SO.

***Table 6.2**: The change of current at 5V for SO and SO-RGO device in different environments*

Sensors	SO	SO-RGO
Air	1.01 mA	0.88 mA
5000 ppm CO_2	0.91 mA	0.77 mA
Change of Current	0.10 mA	0.11 mA

In **Fig. 6.8b**, the SO-RGO sensor is measured for the sensing response in different concentrations of CO_2 such as 5000 ppm, 1000 ppm, 500 ppm, and 250 ppm. The concentration of CO_2 in the atmosphere is 410 nm, which is not harmful to living things and is a highly stable gas[20]. The measurement of 250 ppm is sufficient for CO_2 based sensor device. The resistance

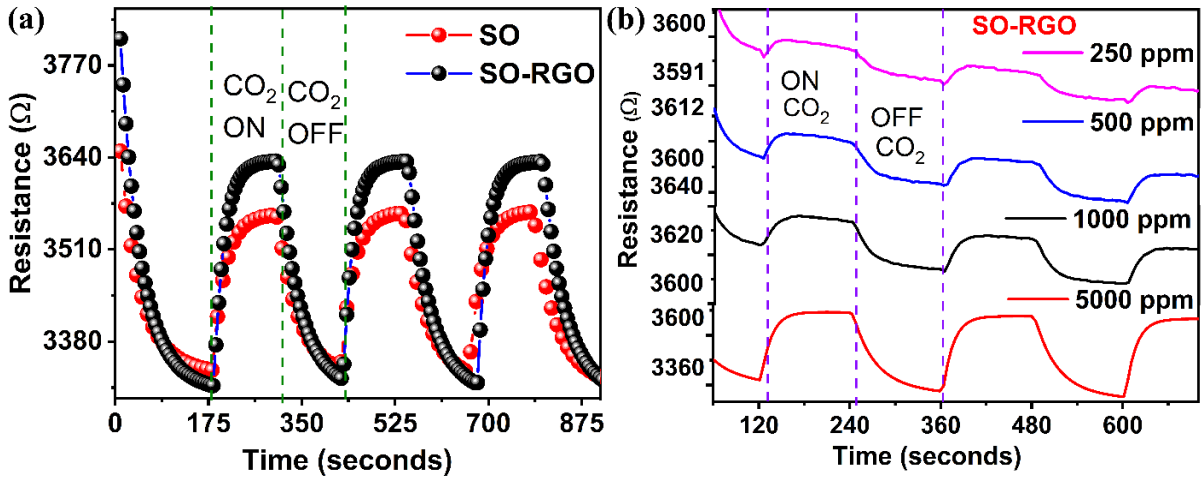

Fig. 5.8: CO_2 flow ON/OFF on (a) SO and SO-RGO; and (b) SO-RGO in different flow rate.

is changed from 3613 Ω to 3627 Ω for 1000 ppm, 3601 Ω to 3607 Ω for 500 ppm, and 3591 Ω to 3594Ω for 250 ppm. The device response is reduced while increasing the pursing of N_2; 5000 ppm of CO_2 has given the best response to the devices.

6.4.3. Mechanism of resistive-based CO_2 sensor

The sensing mechanism of a resistive-based gas sensor depends on the roughness of the surface, structural defects, vacancies of atoms, and daggling bonds of the active material[21–23]. The SO, SO-RGO, and GQDs-SO are characterized by their surface morphology using FESEM and FETEM images. The structural analysis is performed using XRD and Raman measurements. The presence of functional groups, bonding of atoms were studied using FTIR and XPS spectra, and the existence of defect state using UV absorbance and PL spectra. Thus, the presence of surface defects and dangling bonds in the SO, SO-RGO, and GQDs-SO are used as an active material for the CO_2 sensor. Semiconductor materials require a range of temperature from 100 ˚C to 450 ˚C for sensing the required gas. As a result of heating, semiconductor materials produce oxygen vacancies, which are attractive sites for analyte gas molecules. The continuous heating of the semiconductor material at high temperature leads to thermal motion of charge carrier, defects which caused the intrinsic resistance. Whereas RGO presents intrinsic defects during the reduction process from the GO, it has a large surface area for interacting with the analyte gas molecules. Similarly, as GQDs are synthesized from the hydrothermal and tip sonication process, it produces large edge defects which can be used as a trapping site for target gas molecules.

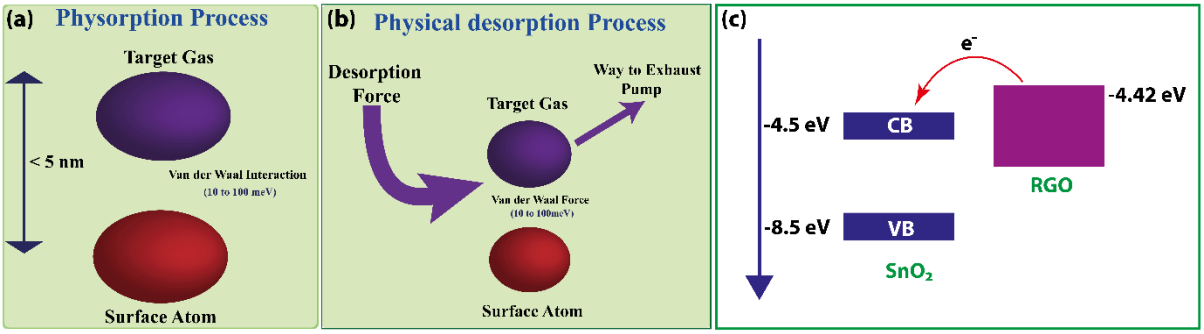

Fig. 6.9: An illustration of the mechanism of resistive-based CO_2 sensor (a) Physorption process; (b) Physical desorption process; and (c) Charge transfer process.

In general, the gas sensors work in three mechanisms: adsorption, absorption, and ion exchange. Sorption is a process of interaction of one state with another state. Moreover, adsorption is a process of interaction of target gas (CO_2) on the surface of the SnO_2 NPs, nano-composite of SnO_2 NPs with RGO/GQDs, and it works at RT. The SO and nano hybrid materials interacted by the physisorption process (Fig. 6.9a & Fig. 6.9b) and interacted with the target CO_2 with van der Waals forces on the surface of the active material. The CO_2 molecules are closer than 5 nm on the defect surface of SO/SO-RGO/GQDs-SO by the gas pressure during the exposure of CO_2 into the vacuum chamber[24]. Thus, the interaction of CO_2 and active materials occurs at the defect sites, leading to charge transfer from the active material to the CO_2. This process caused the reduction of charge carriers on the surface of the active materials, which led to increased resistance of the devices. The charge transfer process is illustrated in Fig. 6.9c, electrons from the RGO is transfer to the SnO_2 NPs which leads to increase the interaction of the CO_2 (target gas).

Further, the interaction of CO_2 and active material can be terminated by providing an external pressure force such as the opening of vacuum valves for a rotary pump. This process is called as physical desorption process. Thus, the CO_2 molecules are departed from the van der Waals interaction and return the transferred electron to the active materials, which decreases the resistance of the device after removal of the CO_2 from the vacuum chamber. These devices do not require heating for physisorption and physical desorption processes.

6.4.4. Response and recovery time for CO_2 sensors

The SO device was measured for the response and recovery time of the sensing by applying 5V bias and 5000 ppm of concentration of CO_2. The sensing response in shown in **Fig. 6.10** and it show exponential rise and decay in the sensing response. The response time (τ_{res}) is computed from the fitting of an exponential growth curve using the iteration algorithm

of Levenberg Marquartdt. The τ_{res} is obtained as 23 s; it is the time needed by the sensor to arrive at a stable value in response to a stimulus. If a step change is introduced in the input, response time is the time required for the sensor to reach 95% of the final value. Recovery time (τ_{rec}) is the time required for the sensor to reach 95% of its final value when the source of the stimulus is removed. The τ_{rec} is calculated from an exponential decay curve fitted. Thus, the recovery

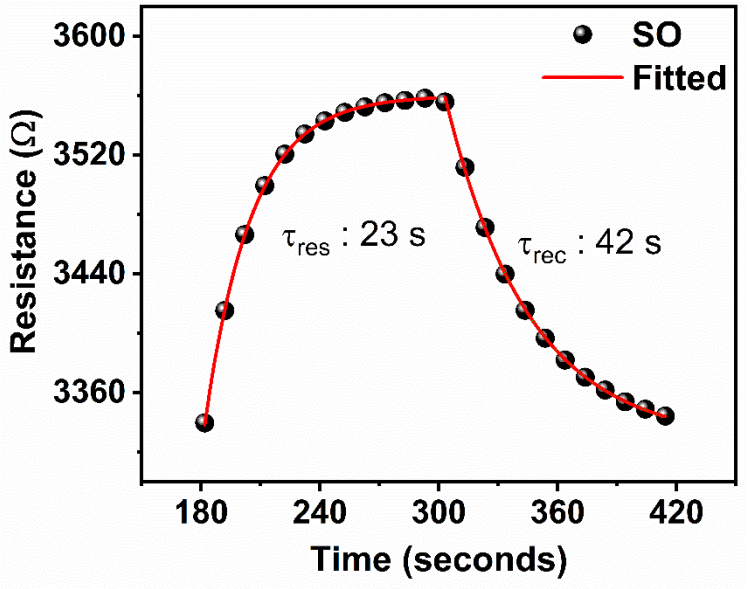

Fig. 6.10: Response and recovery time of SO device.

time is obtained to 42 s. The τ_{res} and τ_{rec} of the SO-RGO are studied in **Fig. 6.11**; it is calculated using exponential growth and exponential decay curves, respectively. The response time for 500 ppm of CO_2 is 12 s, as shown in Fig. 6.11a. Afterward, the response resistance is reduced to base resistance during the desorption process, which takes ~23 s. The τ_{res} and τ_{rec} for the 1000 ppm of CO_2 are 13 s and 31 s, respectively (**Fig. 6.11b**). Moreover, the pursing of the 5000 ppm of CO_2 in the SO-RGO device can detect the gas within 20 s and 40 s is required to return to the base resistance, as shown in **Fig. 6.11c**. The τ_{res} is increased as the concentration of CO_2 increases, like 500 ppm, 1000 ppm, and 5000 ppm, which take 12 s, 13 s, and 20 s, respectively. It may be due to the more analyte gas molecules are available for interaction with the defect sites on the surface of the active material. Similarly, the τ_{rec} is increased as the concentration of the analyte gas increases, such as 500 ppm, 1000 ppm, and 5000 ppm taken 23 s, 31 s, and 40 s, respectively (**Fig. 6.11d**). The τ_{res} required less time than τ_{rec} because removing interaction between the analyte gas molecules and materials required an external force like sucking pressure from the vacuum pumps.

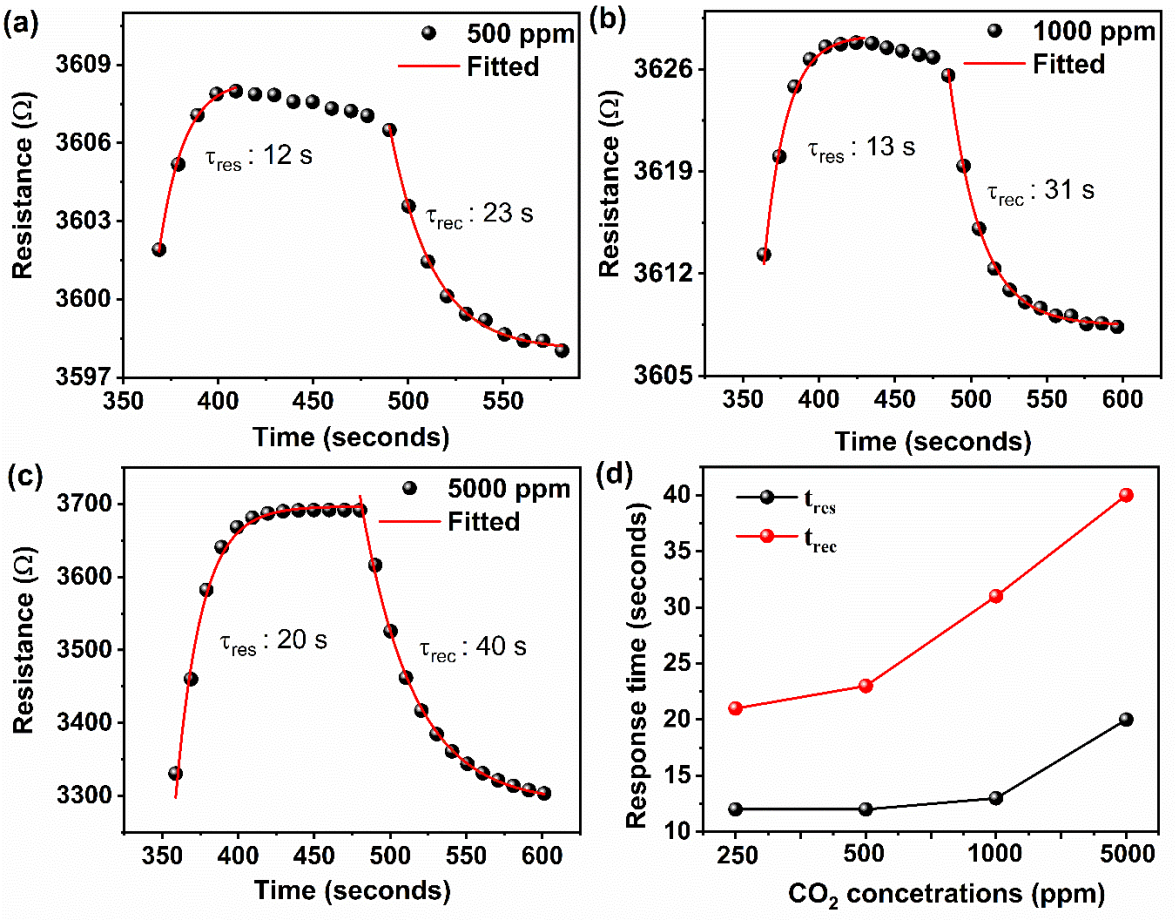

Fig. 6.11: Response and recovery time for different concentration (a) 500 ppm, (b) 1000 ppm, and (c) 5000 ppm CO_2 exposer to SO-RGO device; (d) Analysis of τ_{res}, and τ_{rec} for CO_2.

6.4.5. CO_2 sensing in GQDs-SO

The ON/OFF response of CO_2 on the GQDs-SO is analyzed in **Fig. 6.12**. The base resistance of the GQDS-SO is 4960 Ω, and the response resistance is 6105 Ω when 5000 ppm of CO_2 is exposed to the GQDs-SO. The device's-based resistance is changed slightly during repeated experiments, which is observed and acceptable for any sensor device. The ON/OFF cycle is repeated 3 times within the 900 s. The change of the base resistance is negligible if the response resistance is significant. The based resistance and response resistance are 4764 Ω and 4778 Ω for 1000 ppm and 4744 Ω and 4753 Ω for 500 ppm, respectively.

In GQDS-SO, different concentration of the CO_2 is measured by increasing the dilute gas flowing inside the chamber. The base resistance of the GQDS-SO is varied such as 4960 Ω for 5000 ppm, 4764 Ω for 1000 ppm, and 4744 Ω for 500 ppm. And, the change of base resistance in every cycle of 5000 ppm CO_2 flow ON/OFF are 4920 Ω for the first cycle, 4946 Ω for the second cycle, 4957 Ω for the third cycle, and 4960 Ω for the fourth cycle.

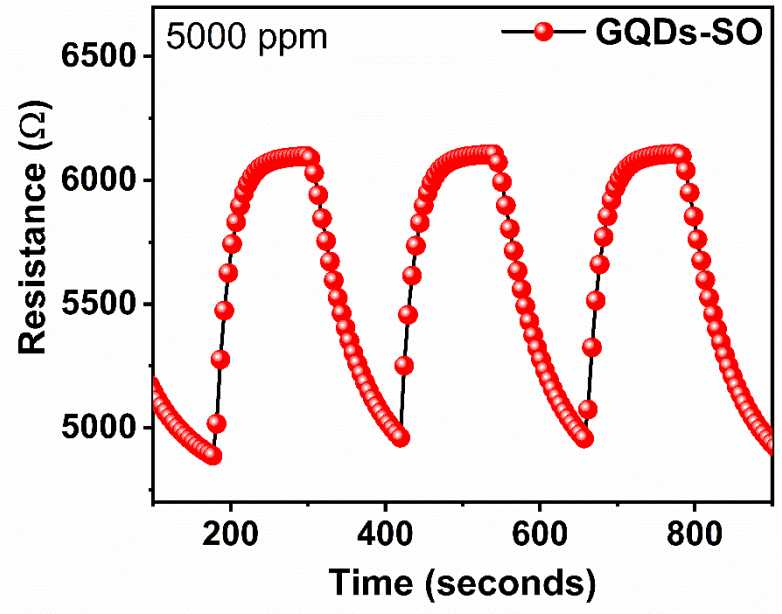

Fig. 6.12: 5000 ppm of CO_2 responses on the GQDS-SO.

6.4.6. Response and recovery time of GQDS-SO device

The τ_{res} and τ_{rec} of the GQDs-SO are calculated by fitting the exponential curve, shown in **Fig. 6.13**. The analysis of the fitted curves for 500 ppm, 1000 ppm, and 5000 ppm of CO_2 are shown in **Fig. 6.13a**, **Fig. 6.13b**, and **Fig. 6.13d**, respectively. The τ_{res} of the sensing response is fitted with a exponential growth curve using Origin Pro 8.5. The τ_{res} of the GQDs-SO are 14 s, 15 s, and 17 s for 500 ppm, 1000 ppm, and 5000 ppm, respectively. The τ_{rec} of the GQDs-SO is 15 s, 24 s, and 67 s for 500 ppm, 1000 ppm, and 5000 ppm, respectively. As a result, the τ_{res} of the GQDs-SO is 2 s more than SO-RGO in 500 ppm. Whereas the τ_{res} of the GQDs-SO is 3 s less than SO-RGO in 5000 ppm. The response resistance of CO_2 on GQDs-SO is higher than SO-RGO. The τ_{res} of GQDs-SO is higher than other devices, possibly due to the high number of trapping sites provided by the GQDs.

Thus, the τ_{res} and τ_{rec} for GQDS-SO in different concentrations of CO_2 are shown in **Fig. 6.13d**. Interestingly, the τ_{res} increased from 14 s for 500 ppm to 17 s for 5000 ppm; it shows an improvement of the τ_{res} as compared to the SO-RGO at 5000 ppm. The τ_{rec} of the GQDS-SO is increased from 15 s to 67 s; it requires more time in the recovery process after removing CO_2 gas from the chamber. The fast interaction of the GQDs-SO with the exposer CO_2 molecules at 5000 ppm may be due to the extra dangling bonds, and defects are expanded across the GQDs-SO. Removing CO_2 analyte molecules from the interaction with the defect sites requires extra time even after opening the pressure valves to evacuate the chamber.

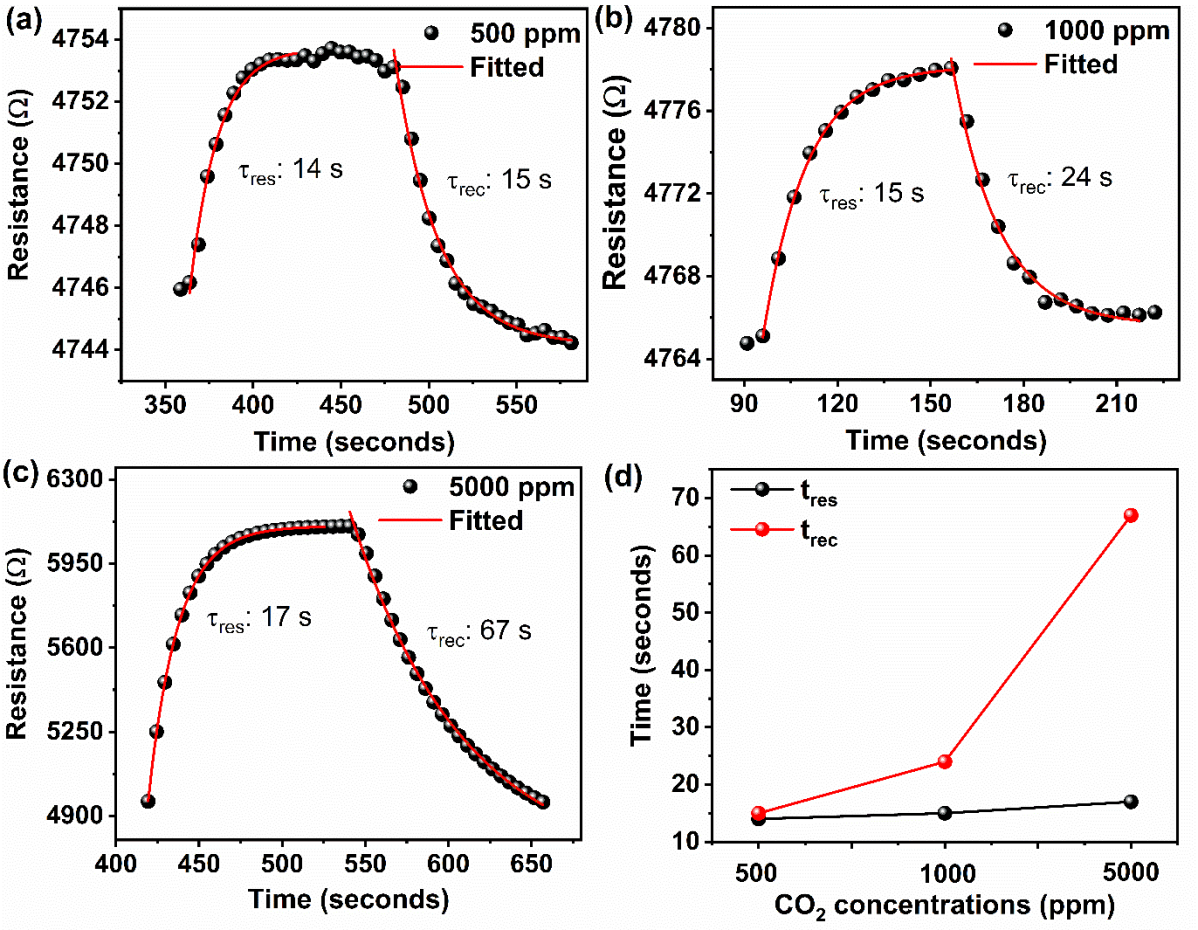

Fig. 6.13: The τ_{res} and τ_{rec} of the GQDS-SO in different concentration (a) 500 ppm, (b) 1000 ppm, and (c) 5000 ppm of CO_2; (d) Analysis of the τ_{res} and τ_{rec} for GQDS-SO device.

6.4.7. Sensitivity of CO_2 sensors

The sensitivity (*S*) of the CO_2 sensor is one of the important parameters for determining the quality of the sensor. Base resistance (Ro) is defined as the value of a sensor device's resistance obtained before exposure to the target gas molecules. The response resistance (Rs) is defined as the value of a sensor device's resistance obtained after exposure to target gas molecules in a controlled environment. The *S* of the devices, such as SO, SO-RGO, and GQDs-SO, are calculated by using the formula[25]:

$$S = \frac{Rs-Ro}{Rs} \times 100$$

Whereas S: sensitivity of the CO_2; Rs: maximum value of resistance during the exposer of CO_2 to the sensor device; Ro: value of resistance before exposer of CO_2 to the sensor device. Thus, the R of the SO, SO-RGO, and GQDs-SO are mentioned in **Table 6.3**.

***Table 6.3**: Sensitivity of the different concentration of SO, SO-RGO, and GQDs-SO.*

	Sensitivity (S)		
Conc. of CO_2 (ppm)	**SO**	**SO-RGO**	**GQDs-SO**
5000	6%	9%	19%
1000	-	4%	3%
500	-	2%	2%
250	-	1%	-

The GQDs-SO improved the sensitivity of the 5000 ppm of CO_2 by 3 times from SO and 2 times from the SO-RGO. The nano hybrids SO-RGO improved the sensitivity by 50% as compared to bare SnO_2 NPs. Moreover, the nano hybrids of the GQDs-SO improved the sensitivity > by 300% compared to the SnO_2 NPs. Thus, the improvement of the CO_2 sensing is mainly contributed to the intrinsic defects present after thermal annealing of RGO and hydrothermal treatment during the synthesis of the GQDs from GO. Moreover, the large surface defects and edge states are generated after reduction from the large lateral size GO to ultra-small size GQDs. The presence of oxygen vacancies in the SnO_2 NPs also attracts sites for the CO_2 in the SO sensor. The combined effect of the nano hybrids materials (SO-RGO and GQDs-SO) thus exhibited higher sensitivity than SO. Finally, the fabricated CO_2 sensors are less effective at the lower concentrations below 1000 ppm of CO_2, which is observed from the analyzed results.

***Table 6.4**: A comparative study of GO-based CO_2 sensors.*

Material	**Response time (s)**	**Recovery time (s)**	**Reference**
RGO	82	77	[26]
H_2 plasma treated RGO	240	240	[23]
Composite of VO_2 and GO	150	250	[27]
Composite of RGO and PEI	43	120	[28]
Nano hybrid of SnO_2 on RGO	20	40	Present work
Nano hybrid of GQDs on SnO_2	17	67	Present work

In agreement with the report, CO_2 is a highly stable gas, and the sensitivity of this gas is very low. Sensing semiconductor-based gas sensors requires a minimum operating temperature range from 100 ˚C to 450 ˚C. In this study, the sensitivity of the CO_2 is analyzed at room temperature (RT). The response time and recovery time of the synthesized nano hybrid of SnO_2 and RGO/GQDs are improved compared to some of the reported analyses, shown in **Table 6.4**.

6.5. Conclusion

SnO_2 NPs and their nano hybrid with RGO/GQDs are analyzed by their surface morphology by FESEM and FETEM imaging. The crystalline structure of the SnO_2 is studied using SAED pattern, HRTEM image, and XRD pattern. The interplanar spacing (d_{101} and d_{110}) of the NPs are 0.26 nm and 0.33 nm, which is agreed with the HRTEM images. The structural defects and signature of the material are confirmed from the Raman spectra. The structural bonds such as Sn-O-Sn, Sn-OH, Sn-O, C=O, and C=C are analyzed from the FTIR spectra. The elemental composition of the materials is examined using EDS and XPS spectra. Defects, daggling bonds, and oxygen vacancies are known from the PL and UV absorbance.

Further, SnO_2 NPs (SO) and their nano hybrid with RGO/GQDs -based device are fabricated on the IDE pattern. The CO_2 sensing is measured and calibrated in a customized gas sensing system. I-V characteristics of the SO and SnO_2-RGO (SO-RGO) are measured in CO_2 and air environments. The ON/OFF analysis of the SO-RGO and the sensitivity of the CO_2 are studied in different concentrations such as 250 ppm, 500 ppm, 1000 ppm, and 5000 ppm. The response and recovery time of the SO, SO-RGO, and GQDs-SnO_2 (GQDs-SO) are compared. The sensitivity of the devices is calculated using the commonly used formula; GQDs-SO based sensor show 3 times higher sensitivity than the SO based sensor and 2 times higher than the SO-RGO based sensor at room temperature (RT). Finally, derivatives of GO such as RGO and GQDs with SnO_2 NPs are more efficient for detecting higher concentrations (>5000 ppm) of CO_2.

Reference

(1) Guo, L.; Hao, Y. W.; Li, P. L.; Song, J. F.; Yang, R. Z.; Fu, X. Y.; Xie, S. Y.; Zhao, J.; Zhang, Y. L. Improved NO2 Gas Sensing Properties of Graphene Oxide Reduced by Two-Beam-Laser Interference. *Sci. Rep.* **2018**, *8* (1), 1–7. https://doi.org/10.1038/s41598-018-23091-1.

(2) Zhou, Y.; Jiang, Y.; Xie, T.; Tai, H.; Xie, G. A Novel Sensing Mechanism for Resistive Gas Sensors Based on Layered Reduced Graphene Oxide Thin Films at Room Temperature. *Sensors Actuators, B Chem.* **2014**, *203*, 135–142. https://doi.org/10.1016/j.snb.2014.06.105.

(3) Srinives, S.; Sarkar, T.; Hernandez, R.; Mulchandani, A. A Miniature Chemiresistor Sensor for Carbon Dioxide. *Anal. Chim. Acta* **2015**, *874*, 54–58. https://doi.org/10.1016/j.aca.2015.03.020.

(4) Geim, A. K.; Novoselov, K. S. The Rise of Graphene. *Nat. Mater.* **2007**, *6* (3), 183–191. https://doi.org/10.1038/nmat1849.

(5) Abdolhosseinzadeh, S.; Asgharzadeh, H.; Kim, H. S. Fast and Fully-Scalable Synthesis of Reduced Graphene Oxide. *Sci. Rep.* **2015**, *5*, 1–7. https://doi.org/10.1038/srep10160.

(6) Ganguly, A.; Sharma, S.; Papakonstantinou, P.; Hamilton, J. Ganguly_J Phys Chem C_2011_probing the Thermal Deoxygenation of Graphene Oxide Using High Resolution XPS.Pdf. **2011**, 17009–17019.

(7) Silva, D. L.; Machado, L. R. P.; Soares, E. M.; Miquita, D. R.; Miranda, H.; Rabelo, C.; Vilela, O. P.; Jorio, A.; Gustavo, L. Raman Spectroscopy Analysis of Number of Layers in Mass-Produced Graphene Fl Akes. **2020**, *161*, 181–189. https://doi.org/10.1016/j.carbon.2020.01.050.

(8) Zhou, Y.; Lin, X.; Huang, Y.; Guo, Y.; Gao, C.; Xie, G.; Jiang, Y. Impact of Further Thermal Reduction on Few-Layer Reduced Graphene Oxide Film and Its n-p Transition for Gas Sensing. *Sensors Actuators, B Chem.* **2016**, *235*, 241–250. https://doi.org/10.1016/j.snb.2016.05.078.

(9) Celina Selvakumari, J.; Nishanthi, S. T.; Dhanalakshmi, J.; Ahila, M.; Pathinettam Padiyan, D. Bio-Active Synthesis of Tin Oxide Nanoparticles Using Eggshell Membrane for Energy Storage Application. *Appl. Surf. Sci.* **2018**, *441*, 530–537. https://doi.org/10.1016/j.apsusc.2018.02.043.

(10) Nipa, S. T.; Akter, R.; Raihan, A.; Rasul, S. bin; Som, U.; Ahmed, S.; Alam, J.; Khan, M. R.; Enzo, S.; Rahman, W. State-of-the-Art Biosynthesis of Tin Oxide Nanoparticles by Chemical Precipitation Method towards Photocatalytic Application. *Environ. Sci. Pollut. Res.* **2022**, *29* (8), 10871–10893. https://doi.org/10.1007/s11356-021-17933-1.

(11) Diéguez, A.; Romano-Rodríguez, A.; Vilà, A.; Morante, J. R. The Complete Raman Spectrum of Nanometric SnO2 Particles. *J. Appl. Phys.* **2001**, *90* (3), 1550–1557. https://doi.org/10.1063/1.1385573.

(12) Mu, J.; Chen, B.; Guo, Z.; Zhang, M.; Zhang, Z.; Shao, C.; Liu, Y. Tin Oxide (SnO2) Nanoparticles/Electrospun Carbon Nanofibers (CNFs) Heterostructures: Controlled Fabrication and High Capacitive Behavior. *J. Colloid Interface Sci.* **2011**, *356* (2), 706–712. https://doi.org/10.1016/j.jcis.2011.01.032.

(13) Pavitra, V.; Udayabhanu; Harini, R.; Viswanatha, R.; Praveen, B. M.; Nagaraju, G. Sonochemical Synthesis of SnO2–CuO Nanocomposite: Diverse Applications on Li-Ion Battery, Electrochemical Sensing and Photocatalytic Activity. *J. Mater. Sci. Mater. Electron.* **2020**, *31* (11), 8737–8749. https://doi.org/10.1007/s10854-020-03408-5.

(14) An, G.; Na, N.; Zhang, X.; Miao, Z.; Miao, S.; Ding, K.; Liu, Z. SnO_2/Carbon Nanotube Nanocomposites Synthesized in Supercritical Fluids: Highly Efficient Materials for Use as a Chemical Sensor and as the Anode of a Lithium-Ion Battery. *Nanotechnology* **2007**, *18* (43), 435707. https://doi.org/10.1088/0957-4484/18/43/435707.

(15) Jiang, J.; Wen, Y.; Wang, H.; Yin, L.; Cheng, R.; Liu, C.; Feng, L.; He, J. Recent Advances in 2D Materials for Photodetectors. *Adv. Electron. Mater.* **2021**, *7* (7), 1–27. https://doi.org/10.1002/aelm.202001125.

(16) Saleem, H.; Haneef, M.; Abbasi, H. Y. Synthesis Route of Reduced Graphene Oxide via Thermal Reduction of Chemically Exfoliated Graphene Oxide. *Mater. Chem. Phys.* **2018**, *204*, 1–7. https://doi.org/10.1016/j.matchemphys.2017.10.020.

(17) Ghugal, S. G.; Umare, S. S.; Sasikala, R. A Stable, Efficient and Reusable CdS-SnO2 Heterostructured Photocatalyst for the Mineralization of Acid Violet 7 Dye. *Appl. Catal. A Gen.* **2015**, *496* (December 2017), 25–31. https://doi.org/10.1016/j.apcata.2015.02.035.

(18) Ahmed, A.; Siddique, M. N.; Ali, T.; Tripathi, P. Influence of Reduced Graphene Oxide on Structural, Optical, Thermal and Dielectric Properties of SnO2 Nanoparticles. *Adv. Powder Technol.* **2018**, *29* (12), 3415–3426. https://doi.org/10.1016/j.apt.2018.09.026.

(19) Maestre, D.; Cremades, A.; Piqueras, J. Growth and Luminescence Properties of Micro- and Nanotubes in Sintered Tin Oxide. *J. Appl. Phys.* **2005**, *97* (4). https://doi.org/10.1063/1.1851602.

(20) Muhammad Hafiz, S.; Ritikos, R.; Whitcher, T. J.; Md. Razib, N.; Bien, D. C. S.; Chanlek, N.; Nakajima, H.; Saisopa, T.; Songsiriritthigul, P.; Huang, N. M.; Rahman, S. A. A Practical Carbon Dioxide Gas Sensor Using Room-Temperature Hydrogen Plasma Reduced Graphene Oxide. *Sensors Actuators, B Chem.* **2014**, *193* (January), 692–700. https://doi.org/10.1016/j.snb.2013.12.017.

(21) Smith, A. D.; Elgammal, K.; Fan, X.; Lemme, M. C.; Delin, A.; Råsander, M.; Bergqvist, L.; Schröder, S.; Fischer, A. C.; Niklaus, F.; Östling, M. Graphene-Based CO2 Sensing and Its Cross-Sensitivity with Humidity. *RSC Adv.* **2017**, *7* (36), 22329–22339. https://doi.org/10.1039/c7ra02821k.

(22) Wei, Y.; Chen, C.; Yuan, G.; Gao, S.; י, גרינבלט.; Ansari, A. R.; Hussain, S.; Imran, M.; Al-Ghamdi, A. A.; Chandan, M. R.; Muhammad Hafiz, S.; Ritikos, R.; Whitcher, T. J.; Md. Razib, N.; Bien, D. C. S.; Chanlek, N.; Nakajima, H.; Saisopa, T.; Songsiriritthigul, P.; Huang, N. M.; Rahman, S. A. No Titleענף מצב תמונת: הקיווי. *Sensors Actuators, B Chem.* **2014**, *36* (2), 37–39. https://doi.org/10.1016/j.snb.2013.12.017.

(23) Zaki, S. E.; Basyooni, M. A.; Shaban, M.; Rabia, M.; Eker, Y. R.; Attia, G. F.; Yilmaz, M.; Ahmed, A. M. Role of Oxygen Vacancies in Vanadium Oxide and Oxygen Functional Groups in Graphene Oxide for

Room Temperature CO2 Gas Sensors. *Sensors Actuators, A Phys.* **2019**, *294*, 17–24. https://doi.org/10.1016/j.sna.2019.04.037.

(24) Sevanthi, R.; Irin, F.; Parviz, D.; Andrew Jackson, W.; Green, M. J. Electrical Current Stimulated Desorption of Carbon Dioxide Adsorbed on Graphene Based Structures. *RSC Adv.* **2016**, *6* (49), 43401–43407. https://doi.org/10.1039/c6ra01792d.

(25) Muhammad Hafiz, S.; Ritikos, R.; Whitcher, T. J.; Md. Razib, N.; Bien, D. C. S.; Chanlek, N.; Nakajima, H.; Saisopa, T.; Songsiriritthigul, P.; Huang, N. M.; Rahman, S. A. A Practical Carbon Dioxide Gas Sensor Using Room-Temperature Hydrogen Plasma Reduced Graphene Oxide. *Sensors Actuators, B Chem.* **2014**, *193*, 692–700. https://doi.org/10.1016/j.snb.2013.12.017.

(26) Lee, Z. Y.; Hawari, H. F. Bin; Djaswadi, G. W. Bin; Kamarudin, K. A Highly Sensitive Room Temperature Co2 Gas Sensor Based on Sno2-Rgo Hybrid Composite. *Materials (Basel).* **2021**, *14* (3), 1–16. https://doi.org/10.3390/ma14030522.

(27) Fan, X.; Elgammal, K.; Smith, A. D.; Östling, M.; Delin, A.; Lemme, M. C.; Niklaus, F. Humidity and CO2 Gas Sensing Properties of Double-Layer Graphene. *Carbon N. Y.* **2018**, *127*, 576–587. https://doi.org/10.1016/j.carbon.2017.11.038.

(28) Yu, C. H.; Huang, C. H.; Tan, C. S. A Review of CO2 Capture by Absorption and Adsorption. *Aerosol Air Qual. Res.* **2012**, *12* (5), 745–769. https://doi.org/10.4209/aaqr.2012.05.0132.

Chapter 7

Summary and Outlook

Chapter 7 highlights the contributions of the presented thesis and the future scopes of the presented work. A new technique is proposed to exfoliate the large lateral size of graphene oxide (GO); it is a low-cost process and a simple technique. A new method is introduced to synthesize reduced graphene oxide (RGO) without losing its lateral size. Ultra-small graphene quantum dots (GQDs) are synthesized using hydrothermal and tip-sonication methods. Further, synthesized materials are utilized for SERS sensing, photodetector, and CO_2 sensor applications.

7.1. Highlights of the Thesis

The studies present a large lateral size GO and RGO; it is synthesized by modifying Hummer's method by omitting continuous starring of solution during the oxidation process. We have demonstrated a cost-effective and facile approach using mild heating to exfoliate GO sheets with ultra-large lateral sizes using a simplified technique, superior to the commonly used ultrasonic method. And, we have synthesized RGO without losing its lateral size from GO using thermal, and chemical methods. Lastly, the ultra-small size (1.53 nm) of GQDs is synthesized successfully (Chapter 2). The quality of the GO, RGO, and GQDs is analyzed using various techniques. GO is analyzed for the structural defects and numbers of layers using Raman spectra and FETEM images. The presence of oxygen functional groups in GO, RGO, and GQDs are studied using FTIR, and XPS. The electrical properties of the GO and RGO are elucidated (Chapter 3). The surface structure of the GO and RGO is modified by using gas plasma treatment. Modified surfaces are used as a substrate for the detection of various dyes, such as methyl orange (MO), methylene blue (MB), rose Bengal (RB), and Rhodamine B (RhB). This study unveils the application of large-area graphene-based sheets for SERS application and the role of low-power plasma treatment on the metal-free substrates for its exploitation in low-cost SERS sensing applications (Chapter 4). The photodetector device is fabricated using GO deposited on the interdigitated electrode (IDE). The changes in characteristics and properties of the GO after different temperatures such as 50 ˚C, 85 C, 120 ˚C, and 230 ˚C are studied. The performance of the devices is compared with device parameters, such as photocurrent (I_{ph}), response time (τ_{rise} and τ_{dec}), responsivity (R), and

detectivity (D) (Chapter 5). SnO_2 NPs and their nanocomposite with RGO/GQDs are analyzed for their surface morphology, crystalline structure, and structural defects. SnO_2 NPs and their nanocomposite with RGO/GQDs -based device are fabricated on the IDE pattern. The characteristics of the SnO_2 and SnO_2-RGO are measured in CO_2 and air environments. Through the ON/OFF analysis of the SnO_2-RGO sensor, we have studied its sensitivity and response time for CO_2 sensing in gas different concentrations and it shows superior performance as compared to the individual counterparts (Chapter 6).

The important contributions of the present thesis are summarized as follows:

A. Synthesis and Characterization of Large Lateral-size Graphene Oxide and its Derivative Materials

Firstly, graphite oxide is synthesized using the simplified Hummer's method; we have omitted continuous starring of solution during the oxidation process, which controls the lateral size of the graphite oxide flakes. We have demonstrated a cost-effective and facile approach using mild heating to exfoliate GO sheets with ultra-large lateral sizes up to 104 µm using a simplified technique, superior to the commonly used ultrasonic method. Further, GO is confirmed from the XRD and Raman analysis. Subsequently, the reduction was carried out to obtain RGO with fewer defects as indicated by I_D/I_G ratio from the Raman studies. The highly uniform and small size of the GQDs after 60 minutes of tip-sonication is validated from the FETEM imaging and its size distribution analysis. The structure of GQDs is analyzed using XRD and Raman spectroscopy. Finally, we successfully synthesized high-quality, super large lateral size GO and its derivative materials such as RGO and GQDs.

B. A Detailed Study of Layer Dependent Properties of Large Lateral-size Graphene Oxide and Reduced Graphene Oxide

Large lateral size GO as obtained from the mild heating technique is confirmed from the FESEM image and Raman analysis. Correlation between the number of GO layers and the I_D/I_G ratio was obtained from Raman spectra in which the I_D/I_G ratio decreases linearly with an increase in the number of layers in GO (monolayer, bilayer, <5, <10, and > 10 layers). Results from FTIR, XPS, UV-vis absorption, PL, and TGA/DTG confirmed the partial removal of oxygen-containing functional groups in RGO, suggesting the minimization of defect-induced disorder in graphitic carbon framework, which results in restoration of sp^2 hybridized honeycomb skeleton. In RGO, the current flow was significantly improved from micro-ampere to milli-ampere, which is 3 orders of magnitude change, arising from the good ohmic contact

formation on RGO as confirmed by the linear I-V curve, indicating the high quality of the graphene-based sheets. The electrochemical impedance results corroborate with the I-V characteristics, exhibiting much lower charge transfer resistance for RGO than that of GO, which depicts the higher conductivity across the liquid/solid interface for the former as compared to the latter electrode materials. The large area GO and RGO sheets have been utilized for SERS application for detecting Rhodamine B (RhB) down to a concentration of 10 nM, and a large SERS enhancement factor of 10^4 is reported, which is significantly high considering its semiconducting nature. Thus, the present simplified and economical approach of large-area graphene oxide could potentially open up a new strategy for industrial-scale production for cutting-edge sensing applications. *This work has been published in "RSC Advance, 2021, 11,9488".*

C. Plasma Treated Graphene oxide surface for Trace Dye Detection using Surface-enhanced Raman Spectroscopy

The structure of GO and RGO is modified using gas plasma treatment on the GO and RGO, which was evidenced from the Raman analysis with shifting of peak positions, FWHM of peaks, D`-G, and I_D/I_G, and substantiated by FTIR analysis. We have shown that the SERS effect of the RhB on the GO/RGO is selectively more enhanced than the MO, MB, and RB dyes due to the high charge transfer between the RhB molecules and GO/RGO samples. Ar plasma-treated GO substrate exhibits the highest *EF* among all the substrates for RhB detection, owing to the strong coupling dye molecules on the defect sites of GO. The SERS effect is also improved on the composite AuGO than the individual Au NPs or GO/RGO owing to the contribution of *EF* from both electromagnetic enhancement (EE) and chemical enhancement (CE) for RhB dye detection. This study unveils the application of large-area graphene-based sheets for SERS application and the role of low-power plasma treatment on the metal-free substrates for its exploitation in low-cost SERS sensing applications. *This work has been published in "ACS Appl. Nano Mater.2022, 5,5, 6352-6364".*

D. Fabrication and Analysis of Photodetector Devices based on Surface Modified Graphene Oxide and SnO_2- Graphene Oxide Hybrid

We demonstrated the fabrication of an interdigitated electrode (IDE) pattern using the UV lithography technique on various substrates including GO. The channel width or minimum distance between the two electrodes is made of 10 µm, confirmed by the AFM and FESEM images. The thickness of the metal electrode is 30 nm, measured from the height profile analysis of the AFM image. Through the FESEM imaging, we observed the fabrication of the

GO-based IDE pattern. The changes in characteristics and properties of the GO after different temperatures treatment (such as 50 ˚C, 85 C, 120 ˚C, and 230 ˚C) are studied. The restoration of the graphitic structure after annealing at 230 ˚C is authenticated from the XRD and Raman spectra analysis. It shows the shifting of the 2θ peak towards the 25.6˚ of the XRD pattern and the reduction of the value of the I_D/I_G ratio in the Raman spectra. The presence of oxygen functional groups is studied using XPS and FTIR analysis; flattening of C-O peak after 230 ˚C annealing of GO and removal of oxygen functional groups related peaks in the FTIR spectra. PL and UV absorption also fortified the rich presence of oxygen functional groups in the GO RT. I-V measurement of the GO and different annealed GO are studied and it was concluded that higher oxygen functional groups attached to GO disturbed the flow of current in the GO, which leads to its insulator-like behavior. The attached oxygen functional groups can regulate the electrical properties of the GO. Three photodetectors are made by using GO, Ar-GO, and SO-GO. The performance of the devices was evaluated and compared in terms of photocurrent (I_{ph}), response time (τ_{rise} and τ_{dec}), responsivity (R), and detectivity (D). Ar-GO based photodetector performs better than the other two, showing that the surface modification by the Ar plasma treatment is beneficial for the improved photodetector performance.

E. Fabrication of CO_2 Sensors Based on Graphene Oxide Based 2D Materials and its Nano Hybrid with SnO_2

SnO_2 NPs and their nanocomposite with RGO/GQDs are analyzed for their surface morphology by FESEM and FETEM images; The crystalline structure of the SnO_2 is studied using SAED pattern, HRTEM image, and XRD spectra. The structural defects and signature of the material are confirmed by the Raman spectra. The structural bonds such as Sn-O-Sn, Sn-OH, Sn-O, C=O, and C=C are analyzed from the FTIR spectra. The elemental composition of the materials is examined using EDS and XPS spectra. Defects, daggling bonds, and oxygen vacancies are evaluated from the PL and UV absorbance data. Further, SnO_2 NPs (SO) and their nanocomposite with RGO/GQDs -based device are fabricated on the IDE pattern. The CO_2 sensing is measured and calibrated in a customized gas sensing system. IV characteristics of the SO and SnO_2-RGO (SO-RGO) are measured in CO_2 and air environments. The ON/OFF analysis of the SO-RGO and the sensitivity were studied for CO_2 gas at different concentrations, such as 250 ppm, 500 ppm, 1000 ppm, and 5000 ppm. The response and recovery time of the SO, SO-RGO, and GQDs-SnO_2 (GQDs-SO) are compared. The sensitivity of the devices is calculated using the commonly used formula; The sensitivity of the GQDs-

SO is 3 times higher than that of SO and 2 times higher than that of SO-RGO at room temperature (RT). Finally, the derivatives of GO such as RGO and GQDs with SnO_2 NPs are efficient for detecting higher concentrations (>5000 ppm) of CO_2.

7.2. Scope for Future Work

In the present thesis, we have successfully synthesized large lateral-size GO and RGO; exfoliated large lateral-size GO using a simple and cheap mild-heating technique. Additionally, we have made an IDE pattern using the UV lithography technique, which is required for further applications such as photodetector and gas sensors. There is enormous scope to extend the present work to fabricate devices on the GO and RGO sheets for a broad range of applications, such as:

1. GO and modified GO can be used to detect dye molecules produced by garment industries that are hazardous to our environment and pollutes the drain, rivers, ponds, etc. It will be one of the cheapest and low-cost methods.
2. Structurally modified large-area GO/RGO can be used for photodetector devices on a single sheet, and the sensor's performance will be increased due to the elimination of overlapping resistance. GO/RGO may be used in a self-bias photodetector because laser power is sufficient to change the electrical properties of the material.
3. Nano-composite of the RGO/GQDs can be used in gas sensors due to the presence of intrinsic surface defects, vacancies, dangling bonds, and edge defects trapping sites for target gas molecules.
4. Super large lateral-size GO/RGO sheets are potential in water-splitting applications; they can be used as an electrode or membranes. The costly Platinum is used as an electrode; researchers are looking for an alternative electrode which much cheaper and more efficient than Platinum. The GO and its derivative materials are the best options for replacing Platinum.
5. Plasma treatment of graphene-based 2D materials came out to be a powerful approach to alter its properties. Based on our findings, further application of plasma-treated GO/RGO and diverse applications of the plasma-treated other 2D materials can be explored.
6. Various applications such as super-capacitor, flexible electrodes, detection of cancer cells, lightweight building materials, etc., are usable by GO and its surface-modified materials.